Advancing Non-Gaussian states and measurements - an experimental test bed for heterogeneous quantum networks

Beate Elisabeth Asenbeck

Thèse de doctorat de Sorbonne Université

pour l'obtention du grade de
Docteur de Sorbonne Université
sur le sujet:

Advancing Non-Gaussian states and measurements

an experimental test bed for heterogeneous quantum networks

présentée par

Beate Elisabeth Asenbeck

le 28 juin 2024

Membres du jury :

Prof. Yvonne Gao	Rapporteuse
Prof. Christoph Marquardt	Rapporteur
Dr. Nadia Belabas	Examinatrice
Prof. Gwendal Feve	Président du jury
Dr. Damian Markham	Invité/ Co-encadrant
Prof. Julien Laurat	Directeur de thèse

Laboratoire Kastler Brossel
Physique quantique et applications

Acknowledgements

Reflecting on my PhD years, I'm truly thankful for all the people who guided and enriched my academic experience.

First and foremost, I would like to express my sincere gratitude to my supervisors, Professor Julien Laurat and Dr. Damian Markham, for their unwavering support, invaluable guidance, and constant encouragement throughout this research. Julien, I deeply appreciate the trust you placed in me, as well as the freedom you gave me to explore different paths in both experiment and theory. Second, I want to thank my PhD jury, Professor Gwendal Feve, Professor Christoph Marquardt, Professor Yvonne Gao, and Dr. Nadia Belabas. Thank you so much for giving me the opportunity to discuss my work with you. I know that reading a manuscript, especially if it is a bit long, can be a tiresome task in your busy lives, and I am deeply thankful that you shared your knowledge with me.

Of course, research is always a team effort, and I am fortunate to have had such exceptional colleagues by my side. Tom, thank you for teaching me everything about our experiment and making me feel welcome from day one. I also appreciate your introduction to non-Bavarian beer, which you have somewhat converted me to. Alban, your solutions and ideas have been invaluable; I don't think this PhD would have been possible without you, and I admire you greatly. Tridib, thank you for always being there when I needed you; your skills, knowledge, and readiness to tackle any problem are deeply inspiring. Félix, Jeremy and Thomas thank you for your kindness and incredible ideas. Hadriel, thank you for your ongoing support and our deep discussions. Adrien, thank you for your enthusiasm in helping others. Ambroise, thank you for all the fun we had both in and out of the lab; I am happy to see you continuing the experiment and feel lucky to have worked with you. Lukáš and Priyanka, thank you for our exchanges about life, locking and Non-Gaussianity. Ioanna, thank you for being such a ray of sunshine in the lab. Anaïs, thank you for your advocacy for minorities and your DJ skills. Félix and Jean-Gabriel, thank you for guiding me on the next journey of discovering atoms. Huazhuo, David, Mingxin, Sukanya, Albane, Idriss, and Lucas, thank you for adding so much value to my experience in our team. I also want to thank the whole support team of the LKB, especially David and Stéphanie, for always caring!

During my time at LKB, I was fortunate to make many friends both within my group and beyond, largely thanks to QICS. I'm especially grateful to Khamsa for her constant support of all the projects we came up with as young PhD students. I also want to thank David for our long hours of discussions, often over a beer, and for his many hours of DJing. Niels, thank you for trying to get me to go to psytrance concerts; you have a way of brightening people's spirits, and I will always remember your amazing treehouse pre-party with the Jacuzzi. Of course, I want to thank Clémentine and Francesca, without whom I would have missed out on a great friendship, many hours of cooking, drinking beer by the Seine, watching Bollywood movies, and many other experiences. I am so happy that we had each

other's support during this time and am glad that we will stay in touch in the future.
Thank you so much, Alex, Kristina, Volha, and Dounia, for sharing the lockdown experience on the second floor with me. I will never forget our amazing evenings together and am excited to create new memories with you!

Next, I want to thank my friends from before Paris. Special thanks go to Valeria; you showed me how much fun research can be and gave me a lot of the confidence that led to my decision to start a PhD. You are someone I really look up to in science, and I am happy to have worked with you.
Natürlich will ich auch meiner Wiener-Gang danken! Sophie, Leo, Philipp, Klara, Michi, Herbert, Mati, Luca, Dodo, Gregor und Ben – ich bin so glücklich, dass unsere Freundschaft fest steht, auch wenn wir uns inzwischen weniger sehen. Meine Jahre in Wien waren wunderschön, und ich will zunächst besonders Leo danken für die extrem schöne Zeit und unseren Zusammenhalt, der mich besonders warm an die Anfangsjahre unseres Studiums denken lässt! Ich danke auch Sophie, mit der ich praktisch den gesamten Master durchgemacht habe. Dank unseres ständigen mehrstimmigen Gesanges in den Laboren hast du meine Motivation auf deine aufaddiert, und ich finde, wir waren ein Traumteam im Studium und sind es heute auch noch außerhalb.
Un grand merci à Martin et Célestine, avec qui j'ai fait le tour de l'orchestre, mais surtout de Vienne. Je suis incroyablement heureuse que nous nous rencontrions désormais presque aussi souvent à Paris qu'à Vienne et je me réjouis déjà de nos prochaines excursions sportives. Je tiens également à remercier Raphaël, tu as vraiment facilité mes débuts à Paris, même si nous avons peut-être mangé un peu trop de crêpes.
Moni und Andrea, ich weiß gar nicht richtig, wie ich euch danken soll, weil wir uns einfach schon so lange kennen, dass der Dank nicht nur den letzten vier Jahren gelten sollte. Ihr wisst es eh, aber das Studieren habt ihr mir so ein bisschen in den Kopf gesetzt. Es ist extrem selten, so gute Freundschaften zu finden, zu behalten und weiterzuentwickeln, und ich bin stolz auf uns drei, dass wir das schaffen. Vielen Dank einfach fürs Dasein!
Mama und Papa, bei euch gilt das Gleiche. Natürlich wart ihr es, die mir alles ermöglicht habt, und ich bin unendlich dankbar dafür. Papa, ohne deine frühen Mathe-Nachhilfestunden wäre aus mir wohl nie eine Physikerin geworden, vielen Dank fürs Nicht-Lockerlassen. Die Liebe zum Tüfteln im Labor kommt sicherlich von dir. Mama, du hast mir dafür beigebracht, wie man auf die Bedürfnisse anderer eingeht und sich in sie hineinfühlt, das ist eine sehr gute Fähigkeit in so großen Teams. Beide habt ihr mir gezeigt, dass es Spaß macht, sich in etwas reinzufuchsen, und dafür, aber auch für all die Jahre, will ich euch danke sagen.
Mein finales Danke gilt dir, Pierre-Emmanuel. Ich kann nicht in Worte fassen, wie viel mir deine Unterstützung bedeutet und wie wichtig du für mich bist. Dein unerschütterlicher Glaube daran, dass ich den PhD meistere, und dein beeindruckendes Vorbild von Ruhe und Gelassenheit haben mich durch diese Zeit getragen.

Abstract

This thesis focuses on the creation and manipulation of Non-Gaussian states with the goal of testing emerging heterogeneous quantum networks. These networks are envisioned to host multiple physical platforms, that are connected by optical communication lines. The optical states used for this communication will have to be adapted to the encoding of the physical platform they connect to, leading to a variety of possible encoding strategies. In this work, we develop criteria to test the quality of different encodings and benchmark tools that ensure faithful information transfer. Moreover, we show that multiple encodings can simultaneously be used in the same quantum network without losing their quantum properties through conversion.

We use high-quality optical parametric oscillators, producing single- or two-mode squeezed states. Together with heralding via superconducting nanowire single-photon detectors, we create two different optical encodings representing a two-level system and a harmonic oscillator. The two-level system corresponds to superpositions of photon-number excitations, while the harmonic oscillator state translates to optical Schrödinger cats. By creating entanglement between those two different encodings, its use in network protocols is possible. Network protocols are intrinsically limited by the success rate and fidelity of Bell-state measurements. We present an improvement in output state fidelity and projectivity of an all-optical linear Bell-state measurement by combining single photon detection with field quadrature selection. Employing hybrid entanglement together with this hybrid Bell-state measurement enables a two-level input qubit to be converted into its harmonic oscillator counterpart in a teleportation-based setup. After thorough analysis of the results of the converter experiment, we develop a criterion to judge the Non-Gaussianity of quantum coherences. This criterion is applied to two different experimental two-level systems. Finally, a stimulative study of the possible generation of error-correctable Non-Gaussian states points the way towards the future of this experiment.

This work promotes the use of multiple encodings in quantum networks and advances measurements and state creation methods that expand the capability of optical systems for quantum communication.

Résumé

Cette thèse porte sur la création et la manipulation d'états non gaussiens dans le but de tester les réseaux quantiques hétérogènes émergents. Ces réseaux sont envisagés pour héberger de multiples plateformes physiques, connectées par des lignes de communication optiques. Les états optiques utilisés pour cette communication devront être adaptés à l'encodage de la plateforme physique à laquelle ils sont connectés, ce qui conduit à une variété de stratégies d'encodage possibles. Dans ce travail, nous développons des critères pour tester la qualité des différents encodages et des outils de référence qui garantissent un transfert d'informations fidèle. En outre, nous montrons que plusieurs encodages peuvent être utilisés simultanément dans le même réseau quantique sans perdre leurs propriétés quantiques lors de la conversion.

Nous utilisons des oscillateurs paramétriques optiques de haute qualité, produisant des états comprimés monomodes ou bimodes. Grâce à des détecteurs à photons uniques supraconducteurs, nous créons deux encodages optiques différents représentant un système à deux niveaux et un oscillateur harmonique. Le système à deux niveaux correspond à des superpositions d'excitations de nombres de photons, tandis que l'état de l'oscillateur harmonique à des chats de Schrödinger optiques. En créant une intrication entre ces deux encodages différents, il est possible de les utiliser dans des protocoles de réseau. Ces derniers sont intrinsèquement limités par le taux de réussite et la fidélité des mesures de l'état de Bell. Nous présentons une amélioration de la fidélité de l'état de sortie et de la projectivité d'une mesure linéaire tout-optique de l'état de Bell en combinant la détection de photons uniques avec la sélection en quadrature du champ. L'utilisation de l'intrication hybride avec cette mesure hybride de l'état de Bell permet de convertir un qubit d'entrée à deux niveaux en son équivalent en oscillateur harmonique dans une configuration basée sur la téléportation. Après une analyse approfondie des résultats de l'expérience du convertisseur, nous développons un critère pour juger de la non-gaussianité des cohérences quantiques. Ce critère est appliqué à deux systèmes à deux niveaux expérimentaux différents. Enfin, des simulations démontrent qu'une future version de l'expérience pourra comprendre de la génération d'états non gaussiens corrigeables d'erreur.

Ce travail encourage l'utilisation de plusieurs encodages dans les réseaux quantiques et fait progresser les méthodes de mesure et de création d'états qui élargissent les capacités des systèmes optiques pour la communication quantique.

Zusammenfassung

Diese Arbeit konzentriert sich auf die Erzeugung und Manipulation von nicht-Gaußschen Zuständen mit dem Ziel, neue heterogene Quantennetze zu testen. Diese Netze sollen mehrere physikalische Plattformen beherbergen, die durch optische Kommunikationsleitungen verbunden sind. Die optischen Zustände, die für diese Kommunikation verwendet werden, müssen an die Kodierung der physikalischen Plattform, mit der sie verbunden sind, angepasst werden, was zu einer Vielzahl von möglichen Kodierungsstrategien führt. In dieser Arbeit entwickeln wir Kriterien zur Prüfung der Qualität verschiedener Kodierungen und Benchmarking-Tools, die eine getreue Informationsübertragung gewährleisten. Darüber hinaus zeigen wir, dass mehrere Kodierungen gleichzeitig in ein und demselben Quantennetzwerk verwendet werden können, ohne dass ihre Quanteneigenschaften durch Umsetzung verloren gehen.

Wir verwenden hochwertige optische parametrische Oszillatoren, die ein- oder zweimodige gequetschte Zustände erzeugen. Indem wir die Präsenz eines Zustandes über supraleitende Nanodraht-Einzelphotonendetektoren ankündigen, erzeugen wir zwei verschiedene optische Kodierungen, die ein Zwei-Niveau-System und einen harmonischen Oszillator darstellen. Das Zwei-Niveau-System entspricht einer Überlagerung von Photonen-Anregungen, während der Zustand des harmonischen Oszillators optische Schrödinger-Katzen beschreibt. Durch die Erzeugung von hybriden Verschränkung zwischen diesen beiden unterschiedlichen Kodierungen ist ihre Verwendung in Netzwerkprotokollen möglich. Netzprotokolle sind von Natur aus durch die Erfolgsrate und die Fidelität von Bell-Zustandsmessungen begrenzt. Wir präsentieren eine Verbesserung der Fidelität des Ausgabezustandes und der Projektivität einer rein optischen linearen Bell-Zustandsmessung durch die Kombination von Einzelphotonendetektion und Feldquadraturauswahl. Die Verwendung hybrider Verschränkung zusammen mit dieser hybriden Bell-Zustandsmessung ermöglicht die Umwandlung eines Zwei- Level-Input- Qubits in sein harmonisches Oszillator- Gegenstück in einem teleportationsbasierten Aufbau. Nach einer gründlichen Analyse der Ergebnisse dieses Konverterexperiments entwickeln wir ein Kriterium zur Beurteilung der nicht-Gaußschen Eigenschaft von Quantenkohärenzen. Dieses Kriterium wird auf zwei verschiedene experimentelle Zwei-Niveau-Systeme angewendet. Schließlich weist eine Studie über die mögliche Erzeugung von fehlerkorrigierbaren nicht-Gaußschen Zuständen den Weg in die Zukunft dieses Experiments.

Diese Arbeit bewirbt die Verwendung von Mehrfachkodierungen in Quantennetzwerken und bringt Messungen und Methoden zur Erzeugung von Zuständen voran, die die Möglichkeiten optischer Systeme für die Quantenkommunikation erweitern.

Contents

Chapter 1

Introduction and context

> Physics is mathematical not because we know so much
> about the physical world, but because we know so little;
> it is only its mathematical properties that we can discover.
>
> *Bertrand Russell, An Outline of Philosophy, 1927*

1.1 A short story of quantum information

The first half of the 20th century witnessed two major scientific revolutions that changed our understanding of physics and are known as the relativist and quantum revolutions. They arose from the search to better match scientific results, and driven by observations, were both more or less established around the 1920s. While relativity was innovative but could be accepted for its time, quantum mechanics was shocking. Two striking examples are for instance Born's rule, leading to a modification of the state through measurement, and Heisenberg's uncertainty principle, intrinsically limiting the precision in the measurement result of two conjugate variables, such as position and momentum or time and energy. This is especially clear when reading the conclusion of Heisenberg's paper about uncertainty, where he writes (translated from German)

"But in the sharp formulation of the law of causality: "If we know the present exactly, we can calculate the future", it is not the conclusion that is wrong, but rather the premise. In principle, we cannot get to know the present in all its determinants. Therefore, all perception is a selection from an abundance of possibilities and a limitation of what is possible in the future. Since the statistical character of quantum theory is so closely linked to the imprecision of all perception, one could be tempted to assume that behind the perceived statistical world there is still a "real" world in which the law of causality applies. But such speculations seem to us, we emphasize explicitly, unfruitful and pointless. Physics should only formally describe the connection between perceptions. Rather, the true facts can be characterized much better in this way: Because all experiments are subject to the laws of quantum mechanics [...], the invalidity of the law of causality is definitively established by quantum mechanics." - W. Heisenberg 1927 [1]

Heisenberg discusses the implication of quantum mechanics being a probabilistic theory, which was for many physicists at the time a weakness. They saw it as a sign, that there should be an underlying, hidden variable, theory that can explain the results of quantum mechanics in a deterministic way and thereby preserve our understanding of causality. Instead of getting caught up in the philosophical ramifications of quantum mechanics, he urges

the reader not to equate a physical model with reality, as models only explain what you observe. This idea should later on form the foundation of one of the leading philosophical interpretations of quantum physics, the Copenhagen interpretation. This interpretation was once, a bit harshly, framed as "Shut up and calculate!" by N. D. Mermin [2] and indeed, this is what physicists did. Much of the significant technological development we use today is based on the principles of quantum mechanics, first and foremost the semiconductor technology, enabling me to write this thesis on a computer, and the development of lasers, enabling worldwide communication such that you can download this thesis on your computer. These developments are often called the *first quantum revolution* and it is quite ironic, that the *second quantum revolution* [3] should be fueled by physicists in the second half of the 20th century who refused to just calculate.

By then, quantum mechanics was an established theory, but part of its implications were not well understood. A famous example is the EPR-paradox of 1935 [4], asking how to keep reality and locality in quantum mechanics, which was answered by J. Bell in 1964, showing that you have to choose one or the other [5]. This new wave of research under the slogan "Shut up and contemplate!" [6], asked questions about why macroscopic superpositions don't exist [7] or showed in 1986 that quantum jumps, transitions between energy levels, really do occur [8]. Counter-intuitive features of quantum mechanics were further elaborated: understanding strong quantum correlations or entanglement [9–11], reformulating the discussion about causality in terms of contextuality [12–14], as well as the impossibility to formulate a probability distribution for quantum systems [15] or the no-cloning theorem [16] that showed that an unknown quantum state cannot be copied. Experimentally testing these concepts did not serve to expand nor revolutionize quantum mechanics but rather to fully understand it and thereby create a new way in which to think about it. In theoretical quantum mechanics, this led to the merging of quantum and information theory, giving birth to *quantum information science*. In quantum experiments, single quanta of light and matter were able to be controlled, which had been a theoretical idea, discussed in 1958 by Feynman [17]. It was experimentally realized for atoms in 1978 via laser cooling and trapping [18] and for light with squeezed light sources in 1983 [19] followed since the 2000s by cavity QED [20] and circuit QED [21]. These high-precision experimental techniques could then react to new advances in quantum theory, which proclaimed that *information is physical* and showed the advantage of a quantum Turing machine over a classical one [22]. A Turing machine is a mathematical model of a computer and can be used to show which kind of algorithms are in principle possible. If the Turing machine is allowed to use quantum mechanics, its main advantage lies in *quantum parallelism*, by which probabilistic tasks can be performed faster than with any classical Turing machine. This promise of a powerful quantum computer is one of the goals of this second quantum revolution. Another branch of quantum information science asked questions about measurement precision and

defined a new limit of parameter estimation with the quantum Fisher informational bound [23]. It was shown how to approach this limit by using quantum states in *quantum-enhanced metrology* [24–26]. Finally, the inability to clone quantum states has given rise to a whole field of *quantum encryption* [27], which is unconditionally mathematically secure, be it for banking [28] or communication. These three promises of quantum advances in computation, metrology, and encryption are advancing steadily, in both experiment and theory and have already expanded beyond the university sphere to branch out into start-ups.

In order to connect all those different devices, a worldwide quantum communication network, the *quantum internet* [29], is envisioned. Similar to today's internet, it will have to deal with different physical devices that will be used in the context of computation, metrology, or encryption on a variety of physical platforms. Nonetheless, the unchanged preferred system to send and exchange information is optical states. This is the starting point for this thesis, which explores the quality of optical states and measurements, as well as the feasibility of harnessing multiple degrees of freedom of light in a network, that is envisioned to be heterogeneous in both platforms and encodings.

1.2 Context of this thesis

The research of combining multiple encodings in optical states was started in the Quantum Networks Team at LKB by Olivier Morin [30], who defended his thesis in 2014. He experimentally demonstrated one of our basic tools, which is a *hybrid entanglement* between two fundamentally different encodings in light, creating correlations between the particle and wave properties of quantum light [31]. The three following PhD students Hanna Le Jeannic, Kun Huang and Adrien Cavaillès improved both the experimental resource states [32, 33] and measurements [34], such that non-locality, an important quality feature of entanglement, could be proven via quantum steering in 2018 [35]. With those resources at hand, one of the two cornerstone protocols of sending information through quantum networks could be realized in 2020 [36] by the PhD-student and Post-doc at the time, Tom Darras and Giovanni Guccione, who performed entanglement swapping using hybrid entanglement. The clear goal of this group was then to show that the second key protocol, quantum teleportation, is reachable as well. In this context, I joined the group in October 2020 and worked together with Tom Darras towards the goal of quantum teleportation. Measurement and data analysis were finished in the spring of 2022 and the paper was published in early 2023 [37]. After Tom Darras graduated in June 2021, I was joined by Ambroise Boyer in February 2022 first as an intern and then as a PhD student on the project. Together with Akito Kawasaki, who joined the group in September 2022 as a visiting PhD student from Professor Akira Furusawa for three months, we worked on understanding the performance of the measurement that enabled both the quantum teleportation and entanglement swapping

experiment: a boosted version of the liner-optical Bell-state measurement[1]. Active collaboration with Lukáš Lachman, who is a Post-doc in the group of and in collaboration with professor Radim Filip in the Palacký University Olomouc, led to the development of a tool to quantify an important property of quantum states: their coherences[2]. Lately, we started working towards the creation of error-correctable states in our setup and are working on improved lock stabilization and state quality with the help of Priyanka Giri, who joined our team as a Post-Doc in 2023. This work is being continued together with Albane Lapras, who joined the team as an intern in March 2024.

1.3 Thesis structure

This manuscript is structured into eight chapters, including this introduction and the appendix. First, we will recapture important aspects of quantum theory in chapter 2. This chapter is written as a thorough introduction to quantum optics, where we will focus on two aspects that are especially important for us: the multi-modal property of light, that we want to suppress in our experiment, and the purely quantum counter-intuitive features of light, that we want to highlight with our experiments. This is why we choose to introduce quantum mechanics via the Koopman–von Neumann representation of classical mechanics. It formulates classical mechanics in a Hilbert space, such that it looks formally equivalent to quantum mechanics. In this framework, it is easier to see which features are necessary in order to deviate from classical and towards quantum mechanics, which turns out to be purely Heisenberg's uncertainty. We furthermore introduce the density matrix and Wigner function formalism, which are two equivalent ways to describe the states and measurements of a quantum system. Moreover, the important concept of Non-Gaussianity is introduced as an emerging property due to Heisenberg's uncertainty, where deviation from Gaussianity marks the beginning of quantum features that cannot be simulated by classical states. Different Non-Gaussian and Gaussian states, operations, and measurements are introduced. The last section of the theory chapter gives a motivation why Non-Gaussianity is interesting beyond its fundamental aspect by framing it in the context of quantum error correction, which is necessary for any quantum computation algorithm. In the following chapter 3 we introduce the main tools in our laboratory, enabling us to create high-quality single-mode states. Specifically, the optical parametric oscillators (OPO) and heralding, both at the heart of our experiments, are explained. Furthermore, our two detection methods, homodyne detection and superconducting nanowire single-photon detection are presented. The experimental output states of all three OPOs are analyzed by the end of this chapter, before describing how we record and reconstruct data. After those more general chapters, the main results of this thesis follow. In chapter 4, the hybrid Bell-state measurement, enabling a boost in measurement quality of all-linear Bell-state measurements, is analyzed and pre-

[1] Paper in preparation.
[2] Paper in preparation.

sented together with the creation process of hybrid entanglement. Entangled states and Bell-state measurements are essential cornerstones of any quantum network and ensuring a high quality of both is crucial to enable those networks. In chapter 5 the quantum teleportation with hybrid entanglement, i.e. a quantum converter of encodings, is presented. This experimental result shows that a quantum network can support different encodings without losing its quantum properties. Those properties are further analyzed in chapter 6 with a very stringent criterion on the off-diagonal matrix elements, or coherences, of states. In order to be considered quantum, we test them against all Gaussian states and apply this criterion to two sets of experimental states. We show where to improve the quality of our states further to create a next generation of Non-Gaussian states, which are discussed in chapter 7. In this final chapter, we give first encouraging simulation results, suggesting that our experiment can create error-correctable states if losses in the system can be reduced by a reasonable amount.

Chapter 2

Theory

Contents

This chapter serves as a rigorous introduction to quantum optics that establishes notions, formalism, and approximations that we will use throughout the thesis. It redraws the red line from classical mechanics over quantum state representation to experimentally used states, measurements, and operations and gives a thorough argument as to why non-Gaussianity is an important feature in quantum optics. Consequently, it is tailored to suit readers with varying levels of familiarity with the topic. For those well-versed in the field, it can serve as a recapitulation of the key concepts, providing an opportunity to re-visit and reinforce their understanding. Conversely, for readers who are relatively new to the topic, this chapter offers a comprehensive, step-by-step exploration of the fundamental

principles. To ensure comprehension and retention of the material, each section concludes with a summary of takeaway messages.

The **first section** of this chapter introduces classical light as a multi-modal field and develops its quantization using the Koopman-von Neumann representation, which highlights two key aspects of our experimental work. Firstly, we state that the multi-modal field in our experiment can be reduced to a single mode, an approximation that ensures high state purity in our experiment. Secondly, by using the Koopman-von Neumann representation, we can focus on the truly quantum aspects of our light field, independent of the mathematical framework, and represent states, operations, and measurements in both phase-space and Hilbert space. We then discuss the naming convention of discrete- and continuous variables, cast purely quantum aspects into the framework of Non-Gaussianity, and explain why is valid and useful, and how it allows us to classify and characterize quantum states and operations in a meaningful way. The **second section** of this chapter outlines different Gaussian and non-Gaussian states that have been or could be studied experimentally with our setup. The **third section** turns to operations, drawing a parallel distinction between Gaussian and non-Gaussian scenarios. This section encompasses both gates and measurements, and further explores cases that are not yet experimentally feasible. The **fourth section** elaborates on the previously introduced concept of Non-Gaussianity, highlighting its importance in the context of quantum advantage. We focus on quantum error correction within the stabilizer formalism and examine bosonic encodings. Although this discussion may seem distant from our current experimental capabilities, it sheds light on why generating non-Gaussian states is a key objective. This motivates a study in the final chapter of this thesis, chapter 7 , where we explore the potential for experimentally approaching error-correctable states.

2.1 Description of light in quantum optics

In the **first subsection**, we develop the multi-modal aspects of classical light fields and recast them into a modal Hilbert space. We then use this Hilbert space to describe classical mechanics in the Koopman-von Neumann representation and elaborate on the main ingredient to make quantum aspects appear: the Heisenberg uncertainty relation. As this formulation is rather general, we refocus on its implications for quantum light in the next subsection and elaborate on commutator relations and the resulting photon-number Hilbert space. Finally, we revisit Heisenberg's uncertainty relation. In the **second subsection**, we explore two distinct methods for representing quantum states using the formalism established in the previous subsection. The first method involves constructing density matrices from the eigenvectors of the Hilbert space, while the second method utilizes the conjugate variables of the light field to describe a state as a quasi-probability distribution via the Wigner function. We introduce the concepts of pure and mixed states, define purity and

fidelity, and examine these two methods in the context of composite systems, enabling us to define entanglement and its measures. Furthermore, we demonstrate the equivalence of these two approaches and discuss alternative formulations beyond the Wigner function. In the **third subsection**, we discuss how to formulate operations as unitary evolution of quantum systems within the framework of density matrices. We introduce the general matrix formulation of measurement, known as positive operator-valued measures (POVMs), and elaborate on how the impact of operations on the Wigner function can be assessed via changes in its phase-space coordinates. In the **fourth subsection**, we explain how the two equivalent approaches to describing quantum states, presented in the previous subsections, have historically led to two distinct communities focusing on either the continuous or discrete aspects of quantum light. This historical division has led to different naming conventions in our experiment, where states are distinguished based on whether they are described in small or larger Hilbert spaces. In the **fifth subsection**, we use the Heisenberg limit to compute all possible states that have minimal uncertainty. We demonstrate that these states can be described by a product of Gaussian phase-space distributions, showing that they can be generated using classical light. To conclude the section, in the **sixth subsection** we will summarize the key concepts that we have developed.

2.1.1 From Maxwell's equations to Heisenberg's uncertainty

2.1.1.1 Classical light description

Here, we will recall the orthonormal mode basis solution to Maxwell's equations in free space, following the approach of C. Fabre and N. Treps [38] and G. Grynberg et al. [39]. Maxwell's equations are the basis for classical and quantum electrodynamics. Classically, light is electromagnetic radiation, described as a real-valued electrical field $\vec{E}(\vec{r},t)$. This field can be decomposed into two complex fields, containing the sums of positive frequency components $\vec{E}^{+}(\vec{r},t)$ and negative frequency components $\vec{E}^{-}(\vec{r},t)$. As they carry the same information, such that $\vec{E}(\vec{r},t)=\vec{E}^{+}(\vec{r},t)+\vec{E}^{-}(\vec{r},t)=\vec{E}^{+}(\vec{r},t)+(\vec{E}^{+}(\vec{r},t))^{*}$, we will further only consider the positive complex field component $\vec{E}^{+}(\vec{r},t)$. This field can be further decomposed into different orthonormal mode bases $\vec{f}_m(\vec{r},t)$. Each mode is a normalized solution to Maxwell's equations in vacuum, obeying Maxwell's wave equation (2.1), with the electric field being orthogonal/transverse to its propagation direction through eq. (2.2) and normalized at all times through eq. (2.3)

$$(\Delta-\frac{1}{c^2}\frac{\partial}{\partial t^2})\vec{f}_m(\vec{r},t)=0, \tag{2.1}$$

$$\nabla\cdot\vec{f}_m(\vec{r},t)=0, \tag{2.2}$$

$$\frac{1}{V}\int_V d^3r|\vec{f}_m(\vec{r},t)|^2=1, \tag{2.3}$$

where the volume V contains the entire physical system. This volume is taken to be large but finite[1], such that the complex electric field can be written as [41] as a *sum of discrete modes*

$$\vec{E}^{+}(\vec{r},t) = \sum_{m} \mathcal{E}_m \vec{f_m}(\vec{r},t), \tag{2.4}$$

where $\mathcal{E}_m$ is the complex amplitude of each mode, whose real and imaginary parts are called the field quadratures $\mathcal{E}_m = E_m^X + iE_m^P$.

We can interpret the vector of field quadratures $\vec{Q} = (E_1^X, ..., E_N^X, E_1^P, ..., E_N^P) \in \mathcal{R}^{2N}$ as the optical phase-space coordinates of the field. Note that the electromagnetic field $\vec{E}^{+}$ itself verifies Maxwell's wave equation (2.1). The simplest orthonormal mode basis are plane wave modes

$$\vec{f_m}(\vec{r},t) = \vec{\epsilon}_m e^{i(\vec{k}_m\vec{r}-\omega_m t)}, \tag{2.5}$$

where $\vec{\epsilon}_m$, $\vec{k}_m$ and ω_m are the polarization vector, wave vector, and frequency of the mode.

In order to see the main components of optical modes let us consider an electrical field in the narrow-band and paraxial approximation [2], where the carrier plane wave is considered to propagate along z such that

$$\vec{f_m}(\vec{r},t) = \vec{\epsilon}_m e^{i(k_0 z-\omega_0 t)} f^{(T)}(x,y,z) f^{(L)}(z,t). \tag{2.6}$$

Here k_0 is the mean value, close to which each mode's wave vector lies, and ω_0 is the central frequency. Each mode is factorized into its spatial (or transverse) component $f^{(T)}(x,y,z)$ and its temporal (or longitudinal) component $f^{(L)}(z,t)$ in addition to the polarization vector $\vec{\epsilon}_m$. Each of those components can be used to define a polarization, temporal, or spatial mode basis. Those degrees of freedom can be coupled if the above approximations are violated, as for ultrashort laser pulses [42, 43]. In the non-pulsed, continuous wave approximation that we are working with here, those effects can be ignored.
As the choice of orthonormal mode basis is not unique, we can define a unitary operator U mapping one basis $\vec{f_m}(\vec{r},t)$ into another $\vec{g_n}(\vec{r},t)$ via

$$\vec{f_m}(\vec{r},t) = \sum_{n=1}^{N} U_{nm} \vec{g_n}(\vec{r},t), \tag{2.7}$$

$$\vec{g_m}(\vec{r},t) = \sum_{n=1}^{N} U_{nm}^{\dagger} \vec{f_n}(\vec{r},t), \tag{2.8}$$

[1] This assumption stems from the fact that Maxwell's equations imply the conservation of charge (continuity equation), which is defined in a finite volume [40].
[2] The narrow-band approximation assumes that mostly one frequency component is dominant, with a small bandwidth, while the paraxial approximation assumes small divergence of the mode.

where U is defined via

$$U_{nm} = \frac{1}{V}\int_V d^3r \vec{g}_n(\vec{r},t)^* \vec{f}_m(\vec{r},t). \tag{2.9}$$

If we expand the electromagnetic field in the new basis we importantly also have to transform the complex field amplitude $\mathcal{E}'_m = \sum_n U_{mn}\mathcal{E}_n$, thereby also transforming the phase-space coordinates as seen in [41]. We therefore conclude that each mode has its proper optical phase-space.

Let us now focus on the complex field amplitude $\mathcal{E}_m$ and the idea of the coherence of an electromagnetic field. The level of coherence of a field describes how well-defined it is in time and space. The above modal decomposition allows for a perfectly coherent field if the complex field amplitudes are complex coefficients. More realistically we have to consider amplitude and phase fluctuations of the field, which leads to the complex field amplitudes to be described as probability distributions. The coherence is then defined by those fluctuations and correlations between them [38]. A prominent measure of the coherence of a field is the quadrature covariance matrix Γ_Q, defined as the expectation value of the quadrature vector with its transpose

$$\Gamma_Q = E[\vec{Q}\vec{Q}^T], \tag{2.10}$$

containing the second moment or variance of each mode on the diagonal and their correlation in the off-diagonal elements.

2.1.1.2 Underlying assumptions of classical light and mechanics

Before we formulate a quantum description of light let us examine the mathematical structure we have placed the classical light field into. The electromagnetic wave lives in a vector space, spanned by its modes, called the modal Hilbert space [38]. Generally, a Hilbert space is a vector space over the complex or real numbers such that its inner product $\langle .,. \rangle$ is linear, positive definite, and conjugate symmetric, and defines a norm $|x| = \sqrt{\langle x,x\rangle}$. The norm helps to define a distance measure $d(x,y) = |x-y|$ that is invariant under basis change.
In the case of the electromagnetic field, we have already defined the inner product in eq. (2.3) as the complex dot product $\langle \vec{f},\vec{g}\rangle = \vec{f}^\dagger \cdot \vec{g}$. This is indeed the spatial overlap between $\vec{f}$ and $\vec{g}$.

Let us now define when an electromagnetic field $\vec{E}$ is normalized: it is only possible if there exists an eigenmode-decomposition of the field in which only one mode is populated. We can therefore define the state of the system to be in a single-mode approximation.
For simplicity let us keep this approximation to investigate the dynamics of the system. The state of the system is now described by the complex amplitude $\mathcal{E}$ of the single mode, and its trajectory in phase-space. We have stated before that the complex amplitude can be a normalized probability distribution $\mathcal{P}(X,P)$ over the phase-space coordinates X and

P. Now, we can define a *pure state*, which is the limiting case in which the state exists in only one point $\mathcal{P}_{X',P'}(X,P) = \delta(X - X', P - P')$, considered to be perfectly coherent.

The evolution of any such phase-space distribution is governed by the Liouville equation, assuring that the density of the system is time-independent,

$$\frac{\partial \mathcal{P}}{\partial t} = -\{\mathcal{P}, H\}, \tag{2.11}$$

where the effect of any Hamiltonian H is described by the Poisson bracket [44]. The expectation value of function $A(X,P)$ is then defined as $E[A] = \int \mathcal{P}(X,P)A(X,P)dxdp$.
We can translate this phase-space formulation of the evolution of the complex amplitude of the electromagnetic field into a Hilbert space. Note that this is not the same Hilbert space as our previously defined modal Hilbert space, but rather in a tensor product with it.

2.1.1.3 From classical to quantum mechanics

There exist many ways to describe what happens in the quantization process of quantum mechanics: One can start from Hilbert space and commutators, phase-space and Moyal product or path integrals, and the Dirac notation. All of them have in common that there is no physical intuition that leads to the formulation of quantum mechanics, rather axioms are found that fit perfectly the experimental results of their time. This is why here we will start from a basic set of axioms, which elegantly show the main difference between classical and quantum mechanics, formulated in the same mathematical language. We closely follow Bondar et al. [45] and use the Koopman–von Neumann representation of classical mechanics. Those axioms are

Axiom 1. *The states of a system are represented by normalized vectors* $|\Psi\rangle$ *of a complex Hilbert space.*

Axiom 2. *The measurables or observables* $\hat{A}$ *of a system are defined as self-adjoined operators acting on this space and its expectation value at time* t *is defined as* $\langle A(t)\rangle = \langle\Psi(t)|\,\hat{A}\,|\Psi(t)\rangle$.

Axiom 3. *The probability that measuring* $\hat{A}$ *at time* t *yields the value* A *is given by* $|\,\langle A|\Psi(t)\rangle\,|^2$ *where* A *is an eigenvalue of* $\hat{A}$*:* $\hat{A}\,|A\rangle = A\,|A\rangle$.

Axiom 4. *The Hilbert space of a composite system is written as the tensor product of its subsystems Hilbert spaces.*

We immediately see that those axioms are the usual postulates of quantum mechanics [46]. The equation of motion with kinetic energy $V(p)$ and potential energy $U(x)$ for a system $x(t)$ are

$$\frac{d}{dt}x(t) = V'(p)(t) \quad \xrightarrow{\text{Axioms}} \quad \frac{d}{dt}\langle\Psi(t)|\,\hat{x}\,|\Psi(t)\rangle \quad = \langle\Psi(t)|\,V'(\hat{p})\,|\Psi(t)\rangle\,, \tag{2.12}$$

$$\frac{d}{dt}p(t) = -U'(x)(t) \quad \xrightarrow{\text{Axioms}} \quad \frac{d}{dt}\langle\Psi(t)|\,\hat{p}\,|\Psi(t)\rangle = \langle\Psi(t)|\,-U'(\hat{x})\,|\Psi(t)\rangle\,, \tag{2.13}$$

and can be written straightforwardly with those axioms, where $V'(p) = \frac{\partial V(p)}{\partial p}$ and $U'(x) = \frac{\partial U(x)}{\partial x}$.

Until here we have not specified whether we are talking about quantum or classical mechanics. For this, we will add one more assumption, differentiating those two cases. For classical mechanics, we add the assumption that the observables of phase-space $\hat{x}$ and $\hat{p}$ commute, such that

$$[\hat{x}, \hat{p}] = 0. \tag{2.14}$$

This describes the assumption that classical measurements are non-invasive, meaning that further statistics of the system are not affected by whether or not another measurement was conducted [47, 48]. Indeed we will see that with the above axioms and the non-invasive assumption we can recover the Liouville equation. The chain rule can be applied to equations (2.12) and (2.13) such that

$$\langle\frac{d}{dt}\Psi(t)|\,\hat{x}\,|\Psi(t)\rangle + \langle\Psi(t)|\,\hat{x}\,|\frac{d}{dt}\Psi(t)\rangle = \langle\Psi(t)|\,V'(\hat{p})\,|\Psi(t)\rangle\,, \tag{2.15}$$

$$\langle\frac{d}{dt}\Psi(t)|\,\hat{p}\,|\Psi(t)\rangle + \langle\Psi(t)|\,\hat{p}\,|\frac{d}{dt}\Psi(t)\rangle = \langle\Psi(t)|\,-U'(\hat{x})\,|\Psi(t)\rangle\,. \tag{2.16}$$

If we now assume that observable smoothly depends on time (Stone's theorem [3]) we can introduce a motion generator operator $\hat{L}$ such that

$$i\,|\frac{d}{dt}\Psi(t)\rangle = \hat{L}\,|\Psi(t)\rangle\,. \tag{2.17}$$

With this we can rewrite eq. (2.15) and (2.16) as

$$i\,\langle\Psi(t)|\,[\hat{L}, \hat{x}]\,|\Psi(t)\rangle = \langle\Psi(t)|\,V'(\hat{p})\,|\Psi(t)\rangle\,, \tag{2.18}$$

$$i\,\langle\Psi(t)|\,[\hat{L}, \hat{p}]\,|\Psi(t)\rangle = -\,\langle\Psi(t)|\,U'(\hat{x})\,|\Psi(t)\rangle\,, \tag{2.19}$$

which gives for all states the commutator relations

$$i[\hat{L}, \hat{x}] = V'(\hat{p}), \qquad i[\hat{L}, \hat{p}] = -U'(\hat{x}). \tag{2.20}$$

[3] Stone's theorem states that every self-adjoint operator T in Hilbert space has a one-to-one correspondence to a strongly continuous unitary operator $U(t) = \exp(-iTt)$ [49].

We can see that the if the motion generator operator $\hat{L}$ would be a function that depends only on $\hat{x}, \hat{p}$ then we would contradict eq. (2.20) and (2.14): $i[L(\hat{x},\hat{p}),\hat{x}] = 0 = V'(\hat{p})$ and $i[L(\hat{x},\hat{p}),\hat{p}] = 0 = -U'(\hat{x})$. Therefore we will introduce two new operators $\hat{\lambda}_x = -i\frac{\partial}{\partial x}$ and $\hat{\lambda}_p = -i\frac{\partial}{\partial p}$ such that

$$[\hat{x},\hat{\lambda}_x] = [\hat{p},\hat{\lambda}_p] = i, \tag{2.21}$$

$$[\hat{x},\hat{p}] = [\hat{x},\hat{\lambda}_p] = [\hat{p},\hat{\lambda}_x] = [\hat{\lambda}_x,\hat{\lambda}_p] = 0. \tag{2.22}$$

Note here that in this formulation $\hat{x}, \hat{p}$ are not the canonical coordinates and we thus have to add operators to fully describe the evolution in phase-space, which is why their counterparts $\hat{\lambda}$ were added. Now the motion generating operator $L(\hat{x},\hat{\lambda}_x,\hat{p},\hat{\lambda}_p)$ is defined by the commutator relations (2.20) to be

$$\hat{L} = V'(\hat{p})\hat{\lambda}_x - U'(\hat{x})\hat{\lambda}_p + f(\hat{x},\hat{p}), \tag{2.23}$$

where $f(\hat{x},\hat{p})$ is an arbitrary real-valued function. This follows from Theorem 1 in the supplementary of [45]. We can now use eq. (2.17) to write the equation of motion for $\hat{L}$ in $\hat{x}, \hat{p}$ by using the eigenvector $|x,p\rangle$ (as they commute, they share common eigenvectors):

$$\langle x,p|\, i\,|\frac{d}{dt}\Psi(t)\rangle = \langle x,p|\,\hat{L}\,|\Psi(t)\rangle\,, \tag{2.24}$$

$$\begin{aligned} i\frac{\partial}{\partial t}\langle x,p|\Psi(t)\rangle =& \langle x,p|\,V'(\hat{p})\hat{\lambda}_x\,|\Psi(t)\rangle \\ &- \langle x,p|\,U'(\hat{x})\hat{\lambda}_p\,|\Psi(t)\rangle \\ &+ \langle x,p|\,f(\hat{x},\hat{p})\,|\Psi(t)\rangle\,, \\ i\frac{\partial}{\partial t}\langle x,p|\Psi(t)\rangle =& \left(-iV'(p)\frac{\partial}{\partial x} + iU'(x)\frac{\partial}{\partial p} + f(x,p)\right)\langle x,p|\Psi(t)\rangle\,, \end{aligned} \tag{2.25}$$

which indeed yields the Louville equation for the density function $\mathcal{P}(x,p,t) = |\,\langle px|\Psi(t)\rangle\,|^2$ such that

$$\frac{\partial}{\partial t}\mathcal{P}(x,p,t) = \left(-V'(p)\frac{\partial}{\partial x} + U'(x)\frac{\partial}{\partial p}\right)\mathcal{P}(x,p,t), \tag{2.26}$$

$$\frac{\partial}{\partial t}\mathcal{P}(x,p,t) = -\{\mathcal{P}(x,p,t), H\}, \tag{2.27}$$

with the Poisson bracket as in eq. (2.11). We have therefore *retrieved classical dynamics.*

Let us now move to the derivation of *quantum mechanics.* We will now state that there is the Heisenberg uncertainty

$$[\hat{x},\hat{p}] = i\hbar, \tag{2.28}$$

which implies that quantum measurements can interfere [4]. If we compare the commutation relation of eq. (2.28) with the one of eq. (2.21) we see that

$$\hat{p} := -i\hbar\frac{\partial}{\partial x}, \tag{2.29}$$

meaning that $\hat{p}$ can be viewed as the Fourier transform of $\hat{x}$.
We can treat the derivation analogously until eq. (2.20), where we rename the motion generation operator $\hat{H}$. Now indeed we can simply set $\hat{H} = H(\hat{x}, \hat{p})$ and get

$$\hat{H} = V(\hat{p}) + U(\hat{x}), \tag{2.30}$$

which is any general quantum Hamiltonian. Via axiom 3 we can define the probability of measuring the state $|\Psi(t)\rangle$ as a probability density $\hat{\rho} = |\Psi(t)\rangle\langle\Psi(t)|$ such that Stone's equation (2.17) becomes

$$i\hbar\frac{d}{dt}|\Psi(t)\rangle\langle\Psi(t)| = i\hbar|\frac{d}{dt}\Psi(t)\rangle\langle\Psi(t)| + i\hbar|\Psi(t)\rangle\langle\frac{d}{dt}\Psi(t)|, \tag{2.31}$$

$$= \hat{H}\hat{\rho} - \hat{\rho}\hat{H}, \tag{2.32}$$

$$i\hbar\frac{d}{dt}\hat{\rho} = [\hat{H}, \hat{\rho}], \tag{2.33}$$

such that we recover the *von Neumann equation for time evolution.*
Let us now try to investigate the phase-space behavior of such a system. Importantly we note that as $\hat{x}$ and $\hat{p}$ do not commute, they each form their own orthonormal basis such that they do not have common eigenvectors and the projection of eq. (2.24) cannot be applied to eq. (2.30). However, due to axiom 3 we can deduce the probability densities of the eigenvalues of $\hat{x}$ and $\hat{p}$

$$\mathcal{P}(x,t) = |\langle x|\Psi(t)\rangle|^2, \tag{2.34}$$

$$\mathcal{P}(p,t) = |\langle p|\Psi(t)\rangle|^2. \tag{2.35}$$

Equally, using axiom 2 we can find the average value of any function that depends on $\hat{x}$ and/or $\hat{p}$

$$\langle f(\hat{x},\hat{p})\rangle = \langle\Psi(t)|f(\hat{x},\hat{p})|\Psi(t)\rangle, \tag{2.36}$$

$$\langle\Psi(t)|f(\hat{x})|\Psi(t)\rangle = \int dx\mathcal{P}(x,t)f(x), \tag{2.37}$$

$$\langle\Psi(t)|f(\hat{p})|\Psi(t)\rangle = \int dp\mathcal{P}(p,t)f(p), \tag{2.38}$$

[4] The Planck constant $\hbar$ has to be added to Stone's theorem here and can be any constant, used for normalization.

where in eq. (2.37) the function solely depends on $\hat{x}$ or in eq. (2.38) on $\hat{p}$. Stone's theorem of eq. (2.17), which is equivalent to the Schrödinger equation, therefore governs the evolution of the state $|\Psi(t)\rangle$ such that we can indeed calculate the mean value of any function on the quantum phase-space at any time.

The next step would be to find an equation governing the dynamics of $\mathcal{P}(x,t)$ and $\mathcal{P}(p,t)$, but as in classical mechanics, there is no equation describing the evolution of marginal distributions [50]. We are left with trying to find a joint probability distribution $\mathcal{P}(x,p,t)$ as in classical mechanics such that we can find a quantum equivalent to the Liouville equation. We already note here that any joint probability distribution would require joint eigenvectors $|x,p\rangle$, which do not exist due to the operators not commuting. Therefore we will search for a quasi-probability distribution $\mathcal{W}(x,p,t)$ such that

$$\mathcal{P}(x,t) \propto \int_{-\infty}^{\infty} dx \mathcal{W}(x,p,t), \tag{2.39}$$

$$\mathcal{P}(p,t) \propto \int_{-\infty}^{\infty} dp \mathcal{W}(x,p,t). \tag{2.40}$$

Let us come back to the definition of the classical phase-space, where we have defined four phase-space variables with commutator relations as in eq. (2.21) and (2.22). Indeed we can construct our quantum mechanical operators via those four classical operators. For this let us denote the classical operators $\hat{x}_c, \hat{p}_c, \hat{\lambda}_{xc}, \hat{\lambda}_{pc}$ as to avoid confusion. We can now write our quantum mechanical operators as

$$\hat{x} = \hat{x}_c - \frac{\hbar}{2}\hat{\lambda}_{pc}, \tag{2.41}$$

$$\hat{p} = \hat{p}_c + \frac{\hbar}{2}\hat{\lambda}_{xc}, \tag{2.42}$$

and preserve the commutator relation of eq. (2.28). We can now use the von Neumann eq. of (2.33) and project it onto the eigenvectors of the two positions x, x', where $\hat{x}' = \hat{x}_c + \frac{\hbar}{2}\hat{\lambda}_{pc}$. This is equivalent to asking for the probability that the state of the system is on average in the position $x_c = \frac{x'+x}{2}$ and can pass a distance $\lambda_{pc} = x' - x$ in a certain time interval. We find

$$i\hbar \frac{d}{dt} \langle x| \hat{\rho} |x'\rangle = \langle x| \left[\hat{H}, \hat{\rho}\right] |x'\rangle \tag{2.43}$$

$$= \langle x| \hat{H}\hat{\rho} |x'\rangle - \langle x| \hat{\rho}\hat{H} |x'\rangle \tag{2.44}$$

$$= \left[H\left(\hat{x}, -i\hbar\frac{\partial}{\partial x}\right) - H\left(\hat{x'}, i\hbar\frac{\partial}{\partial x'}\right)\right] \langle x| \hat{\rho} |x'\rangle \tag{2.45}$$

$$= \left[H\left(x_c - \frac{\hbar\lambda_{pc}}{2}, -\frac{i\hbar}{2}\frac{\partial}{\partial x_c} + i\frac{\partial}{\partial \lambda_{pc}}\right) - H\left(x_c + \frac{\hbar\lambda_{pc}}{2}, \frac{i\hbar}{2}\frac{\partial}{\partial x_c} + i\frac{\partial}{\partial \lambda_{pc}}\right)\right] \times \langle x| \hat{\rho} |x'\rangle . \tag{2.46}$$

This already gives us an equation of motion, but dependent on x_c and λ_{pc}, whereas we want x_c and p_c. Now, as we know that $\hat{\lambda}_{pc}$ is defined as the conjugate variable to $\hat{p}_c$, we can obtain the quasi-probability $\mathcal{W}$ via the inverse Fourier transform of $\langle x_c - \frac{\hbar\lambda_{pc}}{2}| \hat{\rho} |x_c + \frac{\hbar\lambda_{pc}}{2}\rangle$

$$\mathcal{W}(x_c, p_c) = \frac{1}{2\pi}\int d\lambda_{pc} \langle x_c - \frac{\hbar\lambda_{pc}}{2}| \hat{\rho} |x_c + \frac{\hbar\lambda_{pc}}{2}\rangle e^{ip_c\lambda_{pc}} \tag{2.47}$$

$$= \langle x_c + \frac{i\hbar}{2}\frac{\partial}{\partial p_c}| \hat{\rho} |x_c - \frac{i\hbar}{2}\frac{\partial}{\partial p_c}\rangle , \tag{2.48}$$

and as such we can see that the Wigner function is the Fourier transform of the density matrix.
This important concept shows the equivalence between those two representations of quantum states. As required, this quasi-probability function normalizes to one $\int \mathcal{W}(x,p)dxdp = 1$ and fulfills eq. (2.39) and (2.40) but is not strictly positive. This shows an important difference between classical and quantum states. We can then write the equation of motion for $\mathcal{W}(x_c, p_c)$ as

$$i\hbar\frac{d}{dt}\mathcal{W}(x_c, p_c) = \left[H(x_c + \frac{i\hbar}{2}\frac{\partial}{\partial p_c}, p_c - \frac{i\hbar}{2}\frac{\partial}{\partial x_c}) - H(x_c - \frac{i\hbar}{2}\frac{\partial}{\partial p_c}, p_c + \frac{i\hbar}{2}\frac{\partial}{\partial x_c})\right]\mathcal{W}(x_c, p_c). \tag{2.49}$$

This is called the *Moyal's equation* and describes the dynamical evolution of the joint probability distribution $\mathcal{W}$ of the quantum phase-space [51].

We have seen that for each mechanical system, there exists a *phase-space* x, p which can be mapped to a *complex Hilbert space*. The difference between quantum and classical dynamics finds itself in the *commutator relation*. In classical mechanics we can see that the commutator relation necessitates four phase-space operators to define the motion of a state. This shows that the pure states $|x, p\rangle$ are not to be associated with the vectors $|\Psi\rangle$ spanning the Hilbert space. This prevents the classical states from being in superpositions. Different expectation values of density functions are simultaneously sharp [47] due to all observables commuting. In the quantum phase-space, on the other hand, enforcing a joint description of the phase-space coordinates leads to a *quasi-probability* distribution that can take *negative values*.

2.1.1.4 Quantum Light

Let us now transition from the general description of quantum mechanics above to our case of a quantum electromagnetic wave. For this, we will write the Hamiltonian of the EM field, for which we need the electric and magnetic fields. We recall eq. (2.4) of the complex electric field, written as a sum of discrete modes. We can use Maxwell's equation (2.50),

where it is clear that $\vec{B}$ will depend on the orthonormal mode basis we choose for $\vec{E}$. Here, we proceed with the plane wave modes of eq. (2.5), such that $\vec{B}$ takes the form of eq. (2.52)

$$\nabla \times \vec{E}^{+} = -\frac{\partial \vec{B}^{+}}{\partial t}, \tag{2.50}$$

$$\nabla \times \vec{E}^{+} = \sum_{m} \mathcal{E}_m \vec{k}_m \times \vec{\varepsilon}_m e^{i(\vec{k}_m \vec{r} - \omega_m t)}. \tag{2.51}$$

We can see that in order for the equation to account for the right side of eq. (2.50), we need to add a factor $-i\omega_m$ to the electric field, resulting in the new fields

$$\vec{B}^{+} = i \sum_{m} \mathcal{E}_m \vec{k}_m \times \vec{\varepsilon}_m e^{i(\vec{k}_m \vec{r} - \omega_m t)}, \tag{2.52}$$

$$\vec{E}^{+} = -i \sum_{m} \omega_m \mathcal{E}_m \vec{\varepsilon}_m e^{i(\vec{k}_m \vec{r} - \omega_m t)}. \tag{2.53}$$

This added pre-factor comes from the fact that the modal decomposition used for eq. (2.50), although using the Coulomb gauge, omitted $i\omega_m$, as it is specific to the orthonormal basis chosen and can be described by the complex field amplitude $\mathcal{E}$.

We can now write the classical Hamiltonian of the free radiating field H_c^R as

$$H_c^R = \frac{\varepsilon_0}{2} \int_V d^3 r \left[|\vec{E}(\vec{r}, t)|^2 + c^2 |\vec{B}(\vec{r}, t)|^2 \right] \tag{2.54}$$

$$= V \frac{\varepsilon_0}{2} \sum_{m} \left(\omega_m^2 |\mathcal{E}_m|^2 + c^2 |\vec{k}_m|^2 |\mathcal{E}_m|^2 \right). \tag{2.55}$$

If we insert $\vec{E}^{+}$ in eq. (2.1), we find $|\vec{k}_m| c = \omega_m$ and as such we define the Hamiltonian

$$H_c^R = \sum_{m} \epsilon_0 V \omega_m^2 |\mathcal{E}_m|^2 \tag{2.56}$$

$$= \sum_{m} \epsilon_0 V \omega_m^2 ((\mathcal{E}_m^X)^2 + (\mathcal{E}_m^P)^2), \tag{2.57}$$

where we set $\mathcal{E}_m = \mathcal{E}_m^X + i\mathcal{E}_m^P$ as quadratures.

Let us now verify if the quadratures can be used as phase-space coordinates $\{x, p\} \stackrel{!}{=} \{x, \frac{dx}{dt}\}$ such that p is the canonical momentum. Using the Hamiltonian equations, we find that

$$\frac{d\mathcal{E}_m^X}{dt} = \frac{\partial H}{\partial \mathcal{E}_m^P} = 2\varepsilon_0 V \omega_m^2 \mathcal{E}_m^P, \tag{2.58}$$

with the results that $\{\mathcal{E}_m^X, \mathcal{E}_m^P\} \stackrel{!}{=} \{\mathcal{E}_m^X, \frac{d\mathcal{E}_m^X}{dt}\} = \{\mathcal{E}_m^X, 2\varepsilon_0 V \omega_m^2 \mathcal{E}_m^P\}$. This can be easily solved by introducing a normalization constant $\mathcal{E}_m^{(1c)}$ for the two new coordinates $\{x, p\}$, such that

$$\mathcal{E}_m^{(1c)} = \sqrt{2\omega_m \epsilon_0 V}, \tag{2.59}$$

$$x_m = \mathcal{E}_m^{(1c)} \mathcal{E}_m^X, \tag{2.60}$$

$$p_m = \mathcal{E}_m^{(1c)} \mathcal{E}_m^P, \tag{2.61}$$

$$H_c^R = \sum_m \frac{\omega_m}{2}(x_m^2 + p_m^2), \tag{2.62}$$

where we left ω_m in the Hamiltonian to ensure that the condition of Stone's theorem of eq. (2.17) is met. We can now quantize the canonical coordinates

$$\{x_m, p_m\} \xrightarrow{\text{quantization}} \{\hat{x}_m, \hat{p}_m\}, \tag{2.63}$$

leading to m uncoupled harmonic oscillators describing the quantized EM radiation Hamiltonian

$$H_c^R \xrightarrow{\text{quantization}} H_q^R = \sum_m \frac{\omega_m}{2}(\hat{x}_m^2 + \hat{p}_m^2). \tag{2.64}$$

To make sure that the commutator relation is fulfilled, as we will see in the next subsubsection, the normalization constant becomes $\mathcal{E}_m^{(1)} = \sqrt{2\omega_m \epsilon_0 V/\hbar}$. If we now rewrite the quantized electrical field vector in the plane wave modal basis, we find

$$\hat{E}^+(\vec{r}, t) = \sum_m \mathcal{E}_m^{(1)} \frac{\hat{x}_m + i\hat{p}_m}{\sqrt{2}} \vec{\epsilon}_m e^{i(\vec{k}_m \vec{r} - \omega_m t)}, \tag{2.65}$$

such that in an arbitrary mode basis, we write

$$\hat{E}^+(\vec{r}, t) = \sum_m \mathcal{F}_m^{(1)} \frac{\hat{x}_m + i\hat{p}_m}{\sqrt{2}} \vec{f_m}(\vec{r}, t). \tag{2.66}$$

The phase-space quadrature operators can be arbitrarily rotated by θ in a manner that

$$\hat{x}_m^\theta = \cos(\theta)\hat{x}_m + \sin(\theta)\hat{p}_m \tag{2.67}$$

$$\hat{p}_m^\theta = \hat{x}_m^{\theta+\pi/2}, \tag{2.68}$$

can also form the phase-space. The choice of θ is arbitrary.

The normalization constant $\mathcal{E}_m^{(1)}$ can be seen as the electric field per photon, which is transformed with a mode basis change similar to eq. (2.9). The general electrical field per mode $\mathcal{F}_m^{(1)}$ can be written as

$$(\mathcal{F}_m^{(1)})^2 = \sum_n (\mathcal{E}_m^{(1)})^2 |U_{nm}|^2. \tag{2.69}$$

In general, this dependence of the quantum quadrature operators on the orthonormal mode basis shows one part of the *wave-particle duality*. Even though there is a Hilbert space, defined as a quantum mechanical oscillator for each modem and an optical phase-space can be formed, these two are still dependent on the underlying physical system, which is the mode the light lives in [38].

2.1.1.5 Commutator relations

Let us now verify that our treatment of the electromagnetic field has a normalization that is consistent with the general commutator relation of conjugate variables in quantum mechanics, eq. (2.28). For this we start with the classical normalization $\mathcal{E}_m^{(1c)}$

$$[\hat{x}, \hat{p}] = [\mathcal{E}_m^{(1c)}\hat{\mathcal{E}}_m^X, \mathcal{E}_m^{(1c)}\hat{\mathcal{E}}_m^P] \tag{2.70}$$

$$= (\mathcal{E}_m^{(1c)})^2[\hat{\mathcal{E}}_m^X, \hat{\mathcal{E}}_m^P], \tag{2.71}$$

$$[\hat{\mathcal{E}}_m^X, \hat{\mathcal{E}}_m^P] = \frac{i}{(\mathcal{E}_m^{(1)})^2} \quad \text{to obey eq. (2.21) and (2.28)} \tag{2.72}$$

$$[\hat{x}, \hat{p}] = \frac{(\mathcal{E}_m^{(1c)})^2}{(\mathcal{E}_m^{(1)})^2} i \tag{2.73}$$

$$= i\hbar. \tag{2.74}$$

Therefore, we justified the choice of $\mathcal{E}_m^{(1c)} \to \mathcal{E}_m^{(1)}$ with the normalization of the commutator relation in quantum mechanics. Moreover, we remind ourselves, that the complex amplitude operator has been defined as $\hat{\mathcal{E}}_m = \hat{\mathcal{E}}_m^X + i\hat{\mathcal{E}}_m^P$. It can now be rewritten with eq. (2.65) as

$$\hat{\mathcal{E}}_m = \mathcal{E}_m^{(1)} \frac{\hat{x}_m + i\hat{p}_m}{\sqrt{2}} = \mathcal{E}_m^{(1c)} \frac{\hat{x}_m + i\hat{p}_m}{\sqrt{2\hbar}},$$

$$\hat{a} = \frac{\hat{\mathcal{E}}_m}{\mathcal{E}_m^{(1c)}} = \frac{\hat{x}_m + i\hat{p}_m}{\sqrt{2\hbar}}.$$

Here, we can see that we can redefine the quantized complex field amplitude operator as a dimensionless[5] operator $\hat{a}_m$. By defining its complex conjugate $\hat{a}_m^\dagger$, we can write the complex set of dimensionless operators for any m in phase-space

$$\hat{x} = \sqrt{\frac{\hbar}{2}}(\hat{a}^\dagger + \hat{a}), \tag{2.75}$$

$$\hat{p} = i\sqrt{\frac{\hbar}{2}}(\hat{a}^\dagger - \hat{a}), \tag{2.76}$$

$$\hat{a} = \frac{1}{\sqrt{2\hbar}}(\hat{x} + i\hat{p}), \tag{2.77}$$

$$\hat{a}^\dagger = \frac{1}{\sqrt{2\hbar}}(\hat{x} - i\hat{p}), \tag{2.78}$$

[5] If $\hbar$ has no dimension, which is always the case for us.

such that the commutator relations are

$$[\hat{a}_m, \hat{a}_n^\dagger] = \delta_{mn}, \tag{2.79}$$

$$[\hat{x}_m, \hat{p}_n] = i\hbar\delta_{mn}. \tag{2.80}$$

Here $\hat{a}$ is called annihilation and $\hat{a}^\dagger$ creation operator, for reasons we will see in the next subsubsection. As in the classical case, an orthonormal mode change is performed as

$$\hat{b}_m^\dagger = \sum_n U_{nm}\hat{a}_n^\dagger, \tag{2.81}$$

by once again using the transformation matrix of eq. (2.9).

2.1.1.6 Hilbert space of photons

Let us now have a closer look at the energy levels of the quantum harmonic oscillator defined in eq. (2.64), where we will look at one mode only, therefore omitting the subscript m

$$H = \frac{\omega}{2}(\hat{x}^2 + \hat{p}^2) \tag{2.82}$$

$$= \frac{\omega}{2}(\hat{x}\hat{x}^\dagger + \hat{p}\hat{p}^\dagger) \tag{2.83}$$

$$= \frac{\hbar\omega}{2}(\hat{a}^\dagger\hat{a} + \hat{a}\hat{a}^\dagger) \tag{2.84}$$

$$= \hbar\omega(\hat{a}^\dagger\hat{a} + \frac{1}{2}) \tag{2.85}$$

$$= \hbar\omega(\hat{n} + \frac{1}{2}), \tag{2.86}$$

such that we can see that the discrete energy levels depend on the number of excitations in the system, shown by the newly defined number operator $\hat{n} := \hat{a}^\dagger\hat{a}$ with a minimal energy of $\hbar\omega/2$. We can define a Hilbert space, spanned by vectors that correspond to all excitation states of the quantum harmonic oscillator. As such we can define the vacuum state as $|0\rangle = (1, 0, 0, 0, ...)$ and in fact any number-of-excitation-state like $|1\rangle = (0, 1, 0, ..., 0)$ or $|3\rangle = (0, 0, 0, 1, 0..., 0)$. If we now reconsider the creation and annihilation operator, we find that their action on the number operator is

$$[\hat{n}, \hat{a}] = [\hat{a}^\dagger\hat{a}, a] = -\hat{a}, \qquad [\hat{n}, \hat{a}^\dagger] = \hat{a}^\dagger, \tag{2.87}$$

such that we can find the action of annihilation and creation operator with the help of the eigenvalue equation $\hat{n}\,|n\rangle = n\,|n\rangle$ to be

$$\begin{aligned}\hat{n}\hat{a}\,|n\rangle &= (\hat{a}\hat{n} + [\hat{n}, \hat{a}])\,|n\rangle \\ &= \hat{a}n\,|n\rangle - \hat{a}\,|n\rangle \\ &= (n-1)\hat{a}\,|n\rangle\,.\end{aligned} \tag{2.88}$$

This shows, that if $|n\rangle$ is an eigenvector of $\hat{n}$ with eigenvalues n, then $\hat{a}\,|n\rangle$ is an eigenvector of $\hat{n}$ with eigenvalues $n-1$. We can reformulate this statement in the following equation

$$\hat{n}\hat{a}\,|n\rangle = (n-1)\hat{a}\,|n\rangle \equiv (n-1)\,|n-1\rangle = \hat{n}\,|n-1\rangle\,. \tag{2.89}$$

Applying the annihilation operator therefore destroys or annihilates one excitation in the system, thereby explaining its naming. The creation operator, being its conjugate transpose counterpart, creates one excitation in the system. The action of those operators adapted to respect the eigenvalue equation of the number operator, is most commonly formulated as

$$\hat{a}^\dagger\,|n\rangle = \sqrt{n+1}\,|n+1\rangle\,, \tag{2.90}$$

$$\hat{a}\,|n\rangle = \sqrt{n}\,|n-1\rangle\,, \tag{2.91}$$

$$\hat{n}\,|n\rangle = n\,|n\rangle\,. \tag{2.92}$$

The eigenvectors of the number operator, we have used in this subsubsection, are called *Number states* and are also known as *Fock states*. Now, it becomes evident that if n is indeed the number of excitations in the system, then in the case of an EM field, this corresponds to the *number of photons* in the mode of interest.

2.1.1.7 Revisiting the Heisenberg's uncertainty

The commutator relation $[\hat{x},\hat{p}] = i\hbar$ leads to an uncertainty of the measurement precision, or standard deviation, of $\hat{x}$ and $\hat{p}$. Let us define the standard deviation as $\Delta\hat{x} = \sqrt{\langle\hat{x}^2\rangle - \langle\hat{x}\rangle^2}$ and similar for Δp. Using the Cauchy-Schwartz inequality we write

$$(\Delta\hat{x})^2(\Delta\hat{p})^2 = \langle\Psi|\hat{x}^2|\Psi\rangle\,\langle\Psi|\hat{p}^2|\Psi\rangle \tag{2.93}$$

$$\geq |\,\langle\Psi|\hat{x}\hat{p}|\Psi\rangle\,|^2, \tag{2.94}$$

where we assumed without loss of generality that the means vanish, corresponding to a shift towards the phase-space origin. Now we can further use that the modulus square of a complex number is $|z|^2 \geq (\frac{z-z^*}{2i})^2$ such that we continue with

$$(\Delta\hat{x})^2(\Delta\hat{p})^2 \geq |\,\langle\Psi|\hat{x}\hat{p}|\Psi\rangle\,|^2 \tag{2.95}$$

$$\geq |\frac{1}{2i}[\langle\Psi|\hat{x}\hat{p}|\Psi\rangle - \langle\Psi|\hat{p}\hat{x}|\Psi\rangle]|^2 \tag{2.96}$$

$$\geq |\frac{1}{2i}\,\langle[\hat{x},\hat{p}]\rangle\,|^2 \tag{2.97}$$

$$\geq \frac{\hbar^2}{4}. \tag{2.98}$$

We can therefore see that the product of the standard deviation of position and momentum are bound $\Delta\hat{x}\Delta\hat{p} \geq \hbar/2$.

We note that for this derivation, pure states are assumed. Indeed if it is applied to mixed states the variance will consist of a classical and quantum part, where the quantum variance is dominating the limit [52].

2.1.2 How to describe states

2.1.2.1 The density matrix

We have seen in the previous subsection that each quantized light mode has a Hilbert space associated with it that can be described by a quantum harmonic oscillator. The Hilbert space is spanned by the eigenstates of the number operator $\hat{n}$, called Fock states $\hat{n}$, where $n \in [0, N]$ for the Hilbert space size N. This suggests that the set of all possible states is convex with the Fock states at its surface. As such we can define a matrix representation of those pure states

$$\hat{\rho}_{pure,n} = |n\rangle \langle n| . \tag{2.99}$$

Consequently, if a state is impure it can be described as a statistical mixture of pure states with probabilities p_n to find the state in a pure state, which leads to the general density matrix formalism of quantum states

$$\hat{\rho} = \sum_{l=0}^{L} p_l |l\rangle \langle l| , \tag{2.100}$$

where we take $|l\rangle$ to be any basis in the Fock Hilbert space including superpositions of Fock states. Each density matrix is written in a finite dimension N, dependent on the maximal Fock excitation in the system.
The density matrix is a Hermitian positive semi-definite matrix and fulfills

$$\mathrm{Tr}[\hat{\rho}] = 1, \tag{2.101}$$

$$\hat{\rho} = \hat{\rho}^{\dagger}, \tag{2.102}$$

$$\mathrm{Tr}[\hat{\rho}^2] \leq 1, \tag{2.103}$$

such that with eq. (2.101) we ensure the normalization of the state, with eq. (2.102) it is defined as hermitian or self-adjoined and eq. (2.103) defines its eigenvalues to be non-negative and therefore the matrix to be positive semi-definite. Indeed here we can see that if $\mathrm{Tr}[\hat{\rho}^2] = 1$ then the matrix $\hat{\rho}$ is a projection. In this way we can define the purity of a density matrix:

$$\mathcal{P}(\hat{\rho}) = \mathrm{Tr}[\hat{\rho}^2], \tag{2.104}$$

$$\frac{1}{N} \leq \mathcal{P}(\hat{\rho}) \leq 1, \tag{2.105}$$

which thereby shows, that the purity of a state lies between a completely mixed state, bound by its dimension N, and a pure state such that

$$\mathcal{P}(\hat{\rho}_{pure}) = \mathrm{Tr}[\hat{\rho}_{pure}^2] = \mathrm{Tr}[\hat{\rho}_{pure}] = 1. \tag{2.106}$$

Here we notice one key feature of quantum states: they can be statistical mixtures, akin to classical statistical mixtures, but indeed can also exist as a superposition of pure states

$$|\Psi\rangle = \sum_n c_n |n\rangle \quad \text{where} \quad \sum c_n^2 = 1, \tag{2.107}$$

which unlike the statistical mixture of eq. (2.100) will have correlations between the different Fock states and are themselves pure. This of course means that any superposition of Fock states can lead to a new vector basis of the Hilbert Space, which are the already defined $|l\rangle$ of eq. (2.100), which will be crucial in chapter 6. Moreover, we can now view the purity $\mathcal{P}$ as an eigenanalysis, where a pure state has only one non-zero eigenvalue.
Let us now define the *Fidelity* as the overlap between two states. If those states are pure, we simply write $\mathcal{F}(|\psi\rangle, |\phi\rangle) = |\langle\psi|\phi\rangle|^2$. For mixed state this equation becomes[6]

$$\mathcal{F}(\hat{\rho}_1, \hat{\rho}_2) = \left(\mathrm{Tr}\left[\sqrt{\sqrt{\hat{\rho}_1}\hat{\rho}_2\sqrt{\hat{\rho}_1}}\right]\right)^2, \tag{2.108}$$

which is a symmetric measure $\mathcal{F}(\hat{\rho}_1, \hat{\rho}_2) = \mathcal{F}(\hat{\rho}_2, \hat{\rho}_1)$ bound to be $0 \leq \mathcal{F}(\hat{\rho}_1, \hat{\rho}_2) \leq 1$ and preserved under unitary transformation on both states. In all the following chapters, the quality of both states and measurements will be evaluated using the criteria of purity and fidelity.

2.1.2.2 Density matrix of composite systems

As defined in axiom 4, two quantum systems can be written as their tensor product. Take a system of dimension N_1 and another of dimension N_2. The combined Hilbert space of those two systems $\mathcal{H}_{N_1N_2} = \mathcal{H}_{N_1} \otimes \mathcal{H}_{N_2}$ has dimension N_1N_2.

Here, we can see that in quantum mechanics "the whole is greater than the sum of its parts" [7] as $N_1 \times N_2 > N_1 + N_2$ (except if $N_1 = N_2 = 2$). The basis that spans this Hilbert space $\mathcal{H}_{N_1N_2}$ is the tensor product of the basis vectors of the individual systems $|m\rangle_{\mathcal{H}_{N_1}} \otimes |n\rangle_{\mathcal{H}_{N_2}} = |m\rangle_{\mathcal{H}_{N_1}} |n\rangle_{\mathcal{H}_{N_2}}$, where the sign $\otimes$ is often omitted. We can see that the basis vectors are products of vectors of the individual systems. The larger size of the composite systems stems from the fact, that we can now create superpositions in this new vector

[6] The Fidelity for mixed states can be derived via minimizing over any POVM that maximizes the indistinguishability between the measurement outcomes of the two density matrices. As we have not introduced POVMs yet, we will omit the derivation.
[7] Hermann Weyl

basis. Each possible pure state of the composite system can then be written as a tensor product of the eigenvectors of the two systems or as a superposition of those tensor products.

If a state in the composite system cannot be expressed as a product of vectors of the individual system it is said to be *entangled*. Note that we can compose a system out of infinitely many Hilbert spaces. For simplicity here we will work with *bipartite systems* where only two Hilbert spaces are considered. An operator $\hat{A}$ applied to the density matrix of the whole system $\hat{\rho}_{12}$ is then written as

$$\hat{A}_{mn,\mu\nu} = \langle m| \langle n| \hat{A} |\mu\rangle |\nu\rangle , \tag{2.109}$$

where m, μ are the indices of the first and n, ν of the second subsystem. We can recover the density matrices of the subsystems $\hat{\rho}_1$ and $\hat{\rho}_2$ via the partial trace

$$\hat{\rho}_1 = \mathrm{Tr}_2 \hat{\rho}_{12} \quad \text{where} \quad (\hat{\rho}_1)_{m,\mu} = \sum_{\nu}^{N_2} (\hat{\rho}_{12})_{m\nu,\mu\nu}, \tag{2.110}$$

where the resulting matrix is called *reduced density matrix*. If the operator $\hat{A}$ is only acting on the first subsystem we write

$$\hat{A} = \hat{A}_1 \otimes \mathbb{1} \quad \text{with} \quad \hat{A}_{mn,\mu\nu} = (A_1)_{m,\mu} \delta(n - \nu). \tag{2.111}$$

The partial trace is interesting, as it transforms a pure entangled state $\hat{\rho}_{12}$ into a mixed state $\hat{\rho}_1$. It is always possible to describe a mixed state as taking the partial trace over a pure state in a larger Hilbert space. The partial trace therefore can be described as *informational ignorance*, where part of the information about the system is not considered. We will use the partial trace in the next chapters to apply losses to a system and to omit already measured modes.

Moreover, we can now connect this to our notion of entanglement. If tracing out the system $\mathcal{H}_{N_2}$ leads to a mixed state $\hat{\rho}_1$ then clearly the state $\hat{\rho}_{12}$ could not be expressed by a product of vectors of the individual systems. Therefore the information about $\hat{\rho}_1$ was not only in $\mathcal{H}_{N_1}$ but *delocalized* over the composite system $\mathcal{H}_{N_1 N_2}$. This points to the fact that the two systems are correlated and we can easily see that this is achieved by a superposition of the new basis vectors $|mn\rangle$

$$|\psi_{12}\rangle = \sum_{m}^{N1} \sum_{n}^{N2} c_{mn} |mn\rangle \quad \text{where} \quad \sum c_{mn}^2 = 1. \tag{2.112}$$

This kind of state is indeed pure and taking the partial trace leads to completely mixed reduced density matrices. We can therefore define entanglement as the correlation between

the subsystems of composite systems, where a state is said to be *maximally entangled* if the partial trace leads to maximally mixed subsystems. As was the case for single quantum systems, an arbitrary basis change can be performed on the state 2.112, which cannot increase its entanglement. This fact can be used to quantify the degree of entanglement in a system, by performing the singular value decomposition of the matrix c of complex numbers c_{mn}, such that $c = udv$ where d is a positive semi-definite diagonal matrix and u, v are unitary matrices. We can rewrite eq. (2.112) as

$$|\psi_{12}\rangle = \sum_{imn} u_{mi} d_{ii} v_{in} |mn\rangle \,, \tag{2.113}$$

such that we can write the subsystem basis vectors as

$$|i\rangle_1 = \sum_m u_{mi} |m\rangle \,, \tag{2.114}$$

$$|i\rangle_2 = \sum_n v_{in} |n\rangle \,. \tag{2.115}$$

In this way, eq. (2.113) becomes

$$|\psi_{12}\rangle = \sum_i^s \lambda_i |i\rangle_1 |i\rangle_2 \,, \tag{2.116}$$

where $d_{ii} := \lambda_i$. The bases $|i\rangle_1$ and $|i\rangle_2$ are called the Schmidt basis and the number of non-zero values λ_i is called the *Schmidt number* s of the state $|\psi_{12}\rangle$. Trivially the reduced density matrices are of the form

$$\hat{\rho}_{1/2} = \sum_i^s \lambda_i^2 |i\rangle_{1/2} \langle i|_{1/2} \,, \tag{2.117}$$

and therefore both reduced-density matrices have identical eigenvalues. We can connect this to our notion of maximal entanglement and say that a state is maximally entangled if $s = N_1$ (assuming $N_1 = N_2$) such that $\lambda_i = \sqrt{1/s} \quad \forall \quad i$ and not entangled if $\lambda_i = 0 \quad \forall \quad i \neq 0$, in which case the subsystems will be pure. The Schmidt number is preserved under unitary transformations applied to the subsystem(s). Of course, a state of the composite Hilbert space will be generally written as a density matrix, being a mixture of pure states. The Schmidt rank of a density matrix is then defined as the maximal Schmidt coefficient of the ensemble of pure states. Even though the Schmidt coefficient provides us with an intuition about entanglement, it is not the most used measure of entanglement.

2.1.2.3 Entanglement measures

In the last subsubsection, we have connected entanglement to the purity of a composite system. Experimentally, we will find ourselves in between pure and mixed composite sys-

tems. To be able to quantify entanglement a threshold is used, where we limit ourselves to bipartite entanglement here.

When analyzing a two-mode state, we can separate it into three classes: fully separable, bound entangled, and distillable entangled. Fully separable states can be written as a (sum) of tensor products, as explained in the last subsubsection. Distillable entanglement coincides with the usual notion of entanglement: it is typically verified via the positive partial transpose (PPT) criterion, developed in 1996 [53], where at least one eigenvalue of the density matrix after partial transpose of one subsystem has to be negative, to witness entanglement in the system. The most common measure/witness constructed from the PPT criterion is either the negativity $\mathcal{N}$ or logarithmic negativity $E_{\mathcal{N}} = \log_2(2\mathcal{N}+1)$. Given a bipartite state ρ with modes A and B, the partial transpose taken on subsystem A (or B), ρ^{Γ_A}, leads to the negativity and logarithmic negative to be defined as [54]

$$\mathcal{N} = \frac{||\rho^{\Gamma_A}|| - 1}{2} = |\sum_{\lambda_i<0} \lambda_i| \quad \text{for a bipartite system} \quad 0 \leq \mathcal{N} \leq 0.5 \tag{2.118}$$

$$E_{\mathcal{N}} = \log_2(||\rho^{\Gamma_A}||) \quad \text{for a bipartite system} \quad 0 \leq E_{\mathcal{N}} \leq 1, \tag{2.119}$$

where $||O|| = \mathrm{Tr}(\sqrt{O^\dagger O})$ is the trace-norm of a density matrix O. The negativity can either be written with this trace norm or can be seen as the absolute value of the sum of all negative eigenvalues $\lambda_i < 0$ of the partially transposed state ρ^{Γ_A}. Any measure of entanglement has to be an entanglement monotone, meaning that any Gaussian operation[8] on the state ρ cannot increase its negativity [55]. Setting the negativity $\mathcal{N}$ equal to the sum of the negative eigenvalues of the partially transposed state in eq. (2.118) gives the upper bound for the negativity, equal to applying the ideal negativity-maximizing Gaussian operation on the state. The negativity is a convex measure, which cannot be said about the logarithmic negativity. It has, on the other hand, the comfortable quality of being additive for tensor products, meaning that increasing our system to more than a bipartite state is easily calculable. Moreover, the logarithmic negativity $E_{\mathcal{N}}$ gives a *upper bound* of the distillable entanglement [55]. Entanglement distillation [56] takes several weakly entangled copies and performs measurements that distill one highly entangled state out of those copies. A state is distillable if its entanglement is increased via this process of distillation and by definition all PPT-negative states are distillable [54]. There are many entanglement measures for distillable states, but given that logarithmic negativity already gives an upper bound, we will only present two more measures, that are interesting for us. One can also base an entanglement criterion on the fidelity with a maximally entangled state, which has to be above 50% [57]. Another measure of entanglement is the famous Bell-inequality-violation [58]. There the correlation is tested against local and real hidden variables, which form a general class of classical models of physics. We will further discuss the Bell basis and the

[8] Sometimes called LOCC for local operations and classical communication.

Bell inequality in chapter 4. A complete table of possible distillable entanglement measures can be found in the paper by H. Jeng et al. [59].

Bound entanglement cannot be used to distill, therefore its fidelity with a maximally entangled state is below 50%. Nonetheless, it is not fully separable. Proper definitions of bound entanglement are plentiful and are thoroughly discussed by M. Gaida et al. [60]. Interestingly we do not generally know how many bound entangled states there are [61], even though they have been under intense study. We note, however, that a two-mode Gaussian entangled state cannot have bound entanglement [62]. Importantly, bound states can violate locality [63] if their modes are not two-level systems, showing their usefulness for many device-independent quantum applications. Entanglement plays an important role in our experiments. We will quantify the entanglement of an experimentally generated state in chapter 4 and its quality plays a key role in the working principle of chapter 5. More generally we will discuss in those two chapters, that the choice of entanglement in the context of networks depends on the specific application. However, in most cases, distillable entanglement is favored.

2.1.2.4 The Wigner function: a quantum phase-space representation

As elaborated in subsubsection 2.1.1.3, the phase-space representation of the quadrature eigenvalues belonging to the quadrature operators $\hat{x}$ and $\hat{p}$ can be written as

$$\mathcal{W}(x_c, p_c) = \frac{1}{2\pi} \int d\lambda_{pc} \, \langle x_c - \frac{\hbar\lambda_{pc}}{2} | \, \hat{\rho} \, | x_c + \frac{\hbar\lambda_{pc}}{2} \rangle \, e^{ip_c\lambda_{pc}}, \tag{2.120}$$

where we interpreted x_c as the mean value of the position and λ_{pc} as a position shift. The standard expression of the Wigner functions can be obtained by substituting $y = \hbar\lambda_{pc}/2$ and dropping the subscript "c", such that we can write

$$\mathcal{W}_\rho(x, p) = \frac{1}{\pi\hbar} \int dy \; e^{2ipy/\hbar} \, \langle x - y | \hat{\rho} | x + y \rangle \, . \tag{2.121}$$

The derivation in subsubsection 2.1.1.3 can be straightforwardly applied to mixed density matrices too, such that eq. (2.121) is a general phase-space description. Note that if the state is not living in one single mode and therefore has to be described by multiple phase spaces, the normalization for k modes changes to $(\pi\hbar)^{-k}$. For pure states, the Wigner function simplifies to

$$\mathcal{W}_{\rho_{pure}}(x, p) = \frac{1}{\pi\hbar} \int dy \; e^{2ipy/\hbar} \psi^*(x - y)\psi(x + y), \tag{2.122}$$

where ψ is the wave function in the position representation $\psi(x) = \langle x|\psi\rangle$. The Wigner function has the following properties [64]

$$\mathcal{W}(x,p) \in \mathbb{R}^{(2k)} \qquad \text{Real-valued function} \tag{2.123}$$

$$\int dx \mathcal{W}_\rho(x,p) = \langle p|\hat{\rho}|p\rangle$$

$$\int dp \mathcal{W}_\rho(x,p) = \langle x|\hat{\rho}|x\rangle \qquad \text{Marginal distributions} \tag{2.124}$$

$$\int dp \int dx \mathcal{W}_\rho(x,p) = \mathrm{Tr}[\hat{\rho}] = 1 \qquad \text{Normalization} \tag{2.125}$$

$$\text{if} \quad \psi(x) \to \psi(x+a) \quad \text{then} \quad \mathcal{W}(x,p) \to \mathcal{W}(x+a,p) \qquad \text{Galilei invariant} \tag{2.126}$$

$$\text{if} \quad \psi(x) \to \psi(-x) \quad \text{then} \quad \mathcal{W}(x,p) \to \mathcal{W}(-x,-p) \qquad \text{Space symmetric} \tag{2.127}$$

$$\text{if} \quad \psi(x) \to \psi^*(x) \quad \text{then} \quad \mathcal{W}(x,p) \to \mathcal{W}(x,-p) \qquad \text{Time symmetric} \tag{2.128}$$

We can define fidelity and purity in this formalism too. An overlap between two operators $\hat{A}$ and $\hat{B}$ can be calculated with their Wigner functions as

$$\mathrm{Tr}[\hat{A},\hat{B}] = 2\pi\hbar \int dx \int dp \mathcal{W}_A(x,p)\mathcal{W}_B(x,p), \tag{2.129}$$

which is called the *inner product rule*. The fidelity of two pure states can be calculated straightforwardly with this equation[9]. Moreover, it follows, that the purity of a state can be calculated as

$$\mathcal{P}(\hat{\rho}) = 2\pi\hbar \int dx \int dp \mathcal{W}_\rho(x,p)^2. \tag{2.130}$$

The limits of the Wigner function remind us again why it is not a properly defined probability distribution: The Wigner function is bound to be between

$$-\frac{1}{\pi\hbar} \leq \mathcal{W}(x,p) \leq \frac{1}{\pi\hbar} \tag{2.131}$$

and therefore has negative values. It will become visible in section 2.2 that pure non-Gaussian states have negative Wigner function values.

2.1.2.5 The Wigner function for composite systems

The Wigner function is not as well suited for an easy formulation of composite systems in comparison to the density matrix. Instead, one uses the same tensor product formalism as in subsubsection 2.1.2.2 to write the composite system as a weighted sum of pure states and then translates this into the Wigner function. As the Wigner function is *linear convex*

$$\mathcal{W}_{\sum_i p_i \rho_i}(x,p) = \sum_i p_i \mathcal{W}_{\rho_i}(x,p) \tag{2.132}$$

[9] The fidelity for mixed states is more elaborate and will be omitted here.

any mixture of pure states can be calculated analytically with the formulas presented in the next subsubsection.

2.1.2.6 The Wigner function and the Fock basis

Let us now consider how to write the Wigner function conveniently for the Fock basis, in which we formulated the density matrix. For each element of the density matrix, one can write

$$\begin{aligned} \mathcal{W}_{|k\rangle\langle n|}(x,p) &= \frac{(-1)^k}{\pi\hbar}\sqrt{\frac{k!}{n!}}e^{i(n-k)\theta}z^{(n-k)/2}e^{-z/2}L_k^{n-k}(z), \\ \text{with} \quad z &= \frac{2}{\hbar}(x^2+p^2) \quad \text{and} \quad \theta = \arctan(p/x), \end{aligned} \tag{2.133}$$

with L_k^{n-k} being the Laguerre polynomial for $n \geq k$. Here we can view z and θ as the radial and angular variables of the quantum Hamiltonian of eq. (2.82) with $\omega = 1$. We already know the eigenvectors of this Hamiltonian to be the Fock state $|n\rangle$. We can now project those Fock states onto the position eigenstate $|x\rangle$ of phase-space. This gives a normalized, real-valued eigenfunction, called the wavefunctions of the corresponding Fock state

$$\langle x|n\rangle = \Psi_n(x) = (\sqrt{\pi\hbar}\ 2^n\ n!)^{(-1/2)}e^{-x^2/(2\hbar)}H_n(\frac{x}{\sqrt{\hbar}}), \tag{2.134}$$

where $H_n(x)$ are the Hermite polynomials as defined the appendix, section 8.1 [65]. The marginal distribution of the Fock state $|n\rangle$ can be easily calculated as $\langle x|\hat{\rho}_n|x\rangle = |\Psi_n(x)|^2$. Now we combine that the Wigner function is linear convex, with our eq. (2.133). For a density matrix $\hat{\rho}$ of dimension N the Wigner function now reads

$$\mathcal{W}(x,p) = \sum_{k=0}^{N}\sum_{n=k}^{N}\hat{\rho}_{kn}\mathcal{W}_{|k\rangle\langle n|}(x,p) + \text{c.t.}, \tag{2.135}$$

where c.t. stands for conjugate transpose, which can be calculated easily by utilizing the time symmetry in eq. (2.128). Moreover, the expression (2.133) produces complex values but due to the hermitian conjugate, the resulting value of the Wigner function is real.

At the origin of phase-space $x = 0, p = 0$ the Wigner function values only depend on the diagonal elements of the density matrix, such that

$$\mathcal{W}_\rho(0,0)) = \frac{1}{\pi\hbar}\sum_n(-1)^n\hat{\rho}_{nn}. \tag{2.136}$$

This shows that the maximal and minimal Wigner function values can be obtained by pure Fock states, where even Fock states maximize, while odd Fock states minimize the Wigner function.

The operation to go from the density operator to the Wigner function has now been extensively studied. Let us now consider the opposite direction, i.e. how to retrieve the density matrix from the Wigner function. Mathematically, we can define *phase-point operators* $\hat{A}(x,p)$, which are hermitian operators that act on the Hilbert space of the system. There is one operator per phase point (x,p), making it an infinite set of operators, such that

$$\hat{\rho} = \int dx \int dp \mathcal{W}_\rho(x,p)\hat{A}(x,p) \tag{2.137}$$

holds [66]. Practically it is hard to numerically construct such a phase-point operator. Luckily we can use the tools to compute the Wigner function of density matrices in the Fock basis and invert them. One can use the overlap formula of eq. (2.129) together with eq. (2.133) to find the density matrix of the Wigner function $\mathcal{W}_?$ as

$$\hat{\rho} = \sum_{k=0}^{N}\sum_{n=k}^{N} c_{nm}\hat{\rho}_{kn} + \text{c.t.} \qquad c_{nm} = 2\pi\hbar \int dx \int dp \mathcal{W}_{|k\rangle\langle n|}(x,p)\mathcal{W}_?. \tag{2.138}$$

We can see that the Wigner function and the density matrix contain the same information about the state of the system. In the laboratory, we always reconstruct the density matrix of the system and use the Wigner function for state analysis, as explained in subsection 3.3.4.

2.1.2.7 On the uniqueness of the Wigner function

Until here we only have presented the Wigner function as a possible phase-space distribution. In fact, there is a large class of possible phase-space distributions that can be connected with the Wigner function. If we consider the phase-space function $e^{-\frac{i}{\hbar}(\lambda_x x+\lambda_p p)}$ then this function can be associated with the characteristic operator

$$\hat{M}(\lambda_x,\lambda_p) = \mathrm{e}^{-\frac{\mathrm{i}}{\hbar}(\lambda_x\hat{x}+\lambda_p\hat{p})}, \tag{2.139}$$

called the *Weyl association*. Due to the Baker-Campbell-Hausdorff expansion we can write $e^{-\frac{i}{\hbar}(\lambda_x\hat{x}+\lambda_p\hat{p})} = e^{-i\lambda_p\hat{p}/(2\hbar)}e^{-i\lambda_x\hat{x}/(\hbar)}e^{-i\lambda_p\hat{p}/(2\hbar)}$ such that we can write the characteristic function belonging to the operator $\hat{M}$ of an arbitrary state ρ as

$$\begin{aligned} M(\lambda_x,\lambda_p) &= \mathrm{Tr}[e^{-i\lambda_p\hat{p}/(2\hbar)}e^{-i\lambda_x\hat{x}/(\hbar)}e^{-i\lambda_p\hat{p}/(2\hbar)}\rho] && (2.140)\\ &= \int_{-\infty}^{\infty} dx e^{-i\lambda_x\hat{x}/(\hbar)} \langle x|e^{-i\lambda_p\hat{p}/(2\hbar)}\rho e^{-i\lambda_p\hat{p}/(2\hbar)}|x\rangle && (2.141)\\ &= \int_{-\infty}^{\infty} dx e^{-i\lambda_x\hat{x}/(\hbar)} \langle x-\lambda_p/2|\rho|x+\lambda_p/2\rangle\,, && (2.142) \end{aligned}$$

which has the form of an inverse Fourier transform. If we invert it we find

$$\langle x - \lambda_p/2|\rho|x + \lambda_p/2\rangle = \frac{1}{2\pi\hbar}\int_{-\infty}^{\infty} d\lambda_x M(\lambda_x, \lambda_p) e^{i\lambda_x x/nq}. \tag{2.143}$$

We can rewrite in the form of our well known Wigner function as

$$W(x,p) = \frac{1}{(2\pi\hbar)^2}\int_{-\infty}^{\infty}\lambda_x \int_{-\infty}^{\infty}\lambda_p M(\lambda_x,\lambda_p) e^{\frac{i}{\hbar}(\lambda_x x+\lambda_p p)}. \tag{2.144}$$

Therefore we find that the Wigner function is the Fourier transform of the characteristic function. The choice of characteristic function itself is flexible and if we set $e^{-\frac{i}{\hbar}(\lambda_x x+\lambda_p p)}) = e^{z\alpha^* - z^*\alpha}$ we define the characteristic function as $e^{z\hat{a}^\dagger}e^{-z^*\hat{a}}$, leading to the *Glauber–Sudarshan* P-function. If we choose $e^{-\frac{i}{\hbar}(\lambda_x x+\lambda_p p)}) = e^{z\alpha^* - z^*\alpha}$ with the characteristic function $e^{-z^*\hat{a}}e^{z\hat{a}^\dagger}$ we find the *Husimi* Q-function. Here we choose to work with the Wigner function for both historical reasons in the laboratory and personal preferences and refer the reader to [67, 68] for more information.

It is important to realize that the Wigner function itself has several conventions, which all depend on how the factor $\hbar$ is defined. In literature there are three common conventions: $\hbar = 0.5, 1, 2$. They change the normalization of the Wigner function but also translate and re-scale the phase-space coordinates. The usual use in literature is $\hbar = 1$, such that the phase-space operators are expressed in their standard form with a factor $1/\sqrt{2}$. It will become clear later that for us the choice of

$$\hbar = \frac{1}{2} \tag{2.145}$$

is the most convenient, in section 2.2. We will moreover use this factor, but set to $\hbar = 1$, as a normalization to vacuum fluctuations in the reconstruction of our experimental states in subsection 3.3.4.

Now that we know how to express states in quantum optics, let us transition to operations and measurements. We remark that from now on, we will sometimes omit the hat-superscript for operators if it is clear from context that they are operators.

2.1.3 How to describe operations and measurements

Here we will first discuss the action of general operators on a system, corresponding to unitary transformation applied to the system. We then describe the general formalism of a specific operation, the measurement of a quantum system, in the density matrix and Wigner function formalism.

2.1.3.1 Unitary evolution of a quantum system

Operations generally describe the evolution of a system under the influence of a Hamiltonian $\hat{H}$. A pure state vector $|\Psi\rangle$ evolves according to Schrödinger's equation, which is equivalent to Stone's theorem of eq. (2.17) such that

$$i\hbar\frac{d}{dt}|\Psi(t)\rangle = \hat{H}|\Psi(t)\rangle\,. \tag{2.146}$$

For a general density matrix one writes

$$i\hbar\frac{d}{dt}\hat{\rho} = [\hat{H},\hat{\rho}] = \hat{H}\hat{\rho} - \hat{\rho}\hat{H}. \tag{2.147}$$

We can see from eq. (2.146), that for a time-independent Hamiltonian, the states evolve as

$$U = e^{-\frac{i}{\hbar}\hat{H}t} \tag{2.148}$$

$$|\Psi(t)\rangle = U|\Psi(0)\rangle \tag{2.149}$$

$$\hat{\rho}(t) = U\hat{\rho}(0)U^{\dagger}, \tag{2.150}$$

where the time evolution is defined by the unitary operator $\hat{U}$ of eq. (2.148). This unitary evolution of quantum systems assumes, that the quantum system is isolated and does not interact with its environment, which makes it trace-preserving. This does not have to be the case. If we introduce a second quantum system of dimension K and extend our Hilbert space such that

$$\mathcal{H} = \mathcal{H}_N \otimes \mathcal{H}_K, \tag{2.151}$$

where we can call the Hilbert space $\mathcal{H}_K$ the environment. The full state of the system can be denoted by $\hat{\rho}'$. Now any unitary U can act on the full Hilbert space such that $\hat{\rho}' \to U\hat{\rho}'U^{\dagger}$. To see the effect on the system of interest in $\mathcal{H}_N$ we can trace out the environment via the partial trace such that

$$\hat{\rho} = \mathrm{Tr}_K[\hat{\rho}']. \tag{2.152}$$

One particularly important (trace-preserving) operation is the measurement of a quantum system, which cannot in general be described as a Hamiltonian [10].

[10] Only quantum non-demolition measurements can be formulated with a Hamiltonian.

2.1.3.2 Measuring the density matrix: POVM formalism

Let us define how a general measurement acts on the density matrix of a quantum system in $\mathcal{H}_N$. A general measurement has k possible outcomes and each outcome i has one measurement operator A_i associated to it, such that the *completeness relation*

$$\sum_{i=1}^{k} A_i^\dagger A_i = \mathbb{1} \tag{2.153}$$

is satisfied. It ensures that the probabilities for each outcome i add up to one and incorporates the trace-preserving nature of measurements. A measurement on the initial state $\hat{\rho}$ giving the ith outcome with probability p_i transforms $\hat{\rho}$ into $\hat{\rho}_i$ such that

$$\hat{\rho} \to \hat{\rho}_i = \frac{A_i \hat{\rho} A_i^\dagger}{\mathrm{Tr}[A_i \hat{\rho} A_i^\dagger]}, \tag{2.154}$$

with $p_i = \mathrm{Tr}[A_i \hat{\rho} A_i^\dagger]$ such that the normalization is preserved. This measurement postulate is a direct consequence of axioms 1-4 [46]. Note here that if we do not select a certain outcome measurement i then $\hat{\rho}$ will be transformed into a convex mixture of all possible outcomes $\sum_{i=1}^{k} A_i \hat{\rho} A_i^\dagger$. This stands in contrast to classical physics, where the probability distribution of a state is not changed if no selection of measurement outcomes i is made $\sum_i P(X|Y_i)P(Y_i) = P(X)$. Equation (2.154) shows that A_i is equivalent to a Hamiltonian-type evolution if there exists only one measurement outcome $k = 1$, such that $\mathrm{Tr}[A_1 \hat{\rho} A_1^\dagger] = 1$. This shows that in general, any measurement on a quantum system will *perturb* its unitary time evolution.

The most general formulation of a measurement is via *Positive Operator Valued Measures* (POVM), which are defined by any partition of the identity operator into k positive operators E_i, called *effects* and satisfy

$$\sum_{i=1}^{k} E_i = \mathbb{1} \qquad E_i = E_i^\dagger \qquad E_i \geq 0. \tag{2.155}$$

The probability of the ith outcome can then be calculated by

$$p_i = \mathrm{Tr}[E_i \hat{\rho}]. \tag{2.156}$$

The POVM effects do not have to form a discrete set, such that the sum in eq. (2.155) can be replaced by an integral. Moreover, the operators E_i do not need to commute and can be expressed as $E_i = A_i^\dagger A_i$ to fit with the completeness relation of eq. (2.153), where in general E_i does not define A_i uniquely.

A POVM applied to a Hilbert space of size N is called *informationally complete* if it has

at least N^2 elements, which means that any input state can be reconstructed from its measurement outcomes. A POVM is called *pure* if each effect E_i fulfills eq. (2.106). As such a pure POVM has effects that are proportional to the pure density matrices $\hat{\rho}_{pure}$ and are called *projective measurements*. Note that here it seems as if the projective measurement is a special case of the general POVM formalism. This can be inverted by Naimark's theorem, which states that any pure POVM can be embedded in a larger Hilbert space as a projective measurement [68]. The POVM formalism will be used in chapter 4, where the importance of the projectivity of a measurement will become clear.

2.1.3.3 Operations on the Wigner function

The mathematical definition of the Wigner function can be applied to any Hermitian operator, not only density matrices such that we can use eq. (2.121) to write the Wigner functions for any POVM element and any unitary evolution, defined in eq. (2.148). In the case of a measurement, the probability of the outcome of a pure POVM element, applied on a Wigner function can then be calculated with eq. (2.129). Although possible, in this way we are losing the simplicity of matrix multiplications, which is why Wigner functions are rarely used in this way.

The power of the Wigner formalism lies in the fact, that we can rather easily calculate the action of any unitary $\hat{U}$ on the phase-space coordinates $\hat{x}, \hat{p}$. If we have an analytical solution of the Wigner function for a certain state, applying a unitary does not require us to recalculate this solution. We can simply calculate the action of the unitary on $\hat{x}$ and $\hat{p}$ and plug this action into the Wigner function. This approach also favors a fast understanding of the action of a unitary, which is hard to see at first glance for density matrices.
To facilitate the calculation of the action of any unitary operator $\hat{U} = e^{\hat{X}}$ on the quadrature operators we use a particularly useful variant of the Baker–Campbell–Hausdorff formula. The action of $\hat{U} = e^{\hat{X}}$ on any operator $\hat{Y}$, which in our case in either position or momentum, can be computed via

$$e^{\hat{X}}\ \hat{Y}\ e^{-\hat{X}} = \sum_{n=0}^{\infty} \frac{[(\hat{X})^n, \hat{Y}]}{n!}, \quad \text{where} \quad [(\hat{X})^0, \hat{Y}] = Y \tag{2.157}$$

and $[(\hat{X})^n, \hat{Y}]$ is the formulation of n-nested commutators. Indeed now the action of the unitary can be written as as a change of coordinates

$$\mathcal{W}_\rho(x, p) \to \mathcal{W}_\rho(x', p'). \tag{2.158}$$

We will see the usefulness of this approach in section 2.3. For completeness, we note, that one can also compute the phase-space evolution due to any operation with Moyal's equation (2.49). This equation of motion is difficult to solve and many numerical methods

are under active development [51, 69] and can lead to insights into quantum chaos and the classical-to-quantum transition [70].

2.1.4 Discrete and continuous variables

Until now we have seen two different formalisms that can describe a quantum system: a Hilbert space with excitation states called Fock states and a phase-space with quadrature operators. The former is formulated in a discrete density matrix formalism while the latter uses a continuous integral over phase-space. For this reason, the quantum optics community often makes the distinction between a *continuous variable* (CV) system which would live in infinite dimensional Hilbert spaces and therefore prefers to be expressed as a Wigner function, and *discrete variable* (DV) systems with a small excitation occupation that can be easily expressed via a density matrix.
This stems from the fact that the Hilbert space is often considered a quantum object while a phase-space is connected to the notion of classicality. But as we saw in subsubsection 2.1.1.3 a Hilbert space itself does not point to any quantumness and quantum and classical phase-space are isomorphic to their Hilbert spaces. As argued by M. Walschaers [41], a Hilbert space makes it easier to forget the underlying mode structure of light, because no direct connection to the vocabulary of classical optics is possible. Importantly, the modes are the physical system that contains the quantum system we are interested in, much like electrons are the physical systems that contain spins. The difference is, that light modes can be changed by optical elements thereby also transforming the Hilbert space or phase-space to be considered.
The experimental implications of this can be significant. For instance, in a DV approach, entanglement between two paths can be generated by directing a single photon onto a beam-splitter, a phenomenon known as path-entanglement. However, this type of entanglement is not considered inherent or "intrinsic" in a CV approach, as it doesn't remain unchanged under mode transformation [41]. In the CV approach, any quantity that remains constant is termed "intrinsic", with system purity or entropy serving as useful examples. This leads to the introduction of "intrinsic entanglement", which remains unchanged under mode basis transformation. This particular definition of entanglement excludes any Gaussian states, which we will define in the next subsection, from being considered entangled.

In this thesis, we adopt the terms CV and DV to classify systems that reside in small or large Hilbert spaces, respectively, based on historical conventions. However, it's important to note that this distinction is somewhat arbitrary from a theoretical perspective. In the context of this experiment, we combine and leverage diverse methods of state creation and measurements that have been separately developed within the distinct experimental communities of DV and CV. This integrated approach employs theoretical frameworks from both domains, reflecting a unified strategy.

2.1.5 Quantifying quantumness: Non-Gaussianity

We have already defined a quantum state to be a state of maximal purity and a classical state a state of minimal purity in the Fock basis. This is because a maximally mixed state, showing no coherences between Fock states and therefore being fully classical, has minimal purity, as in eq. (2.106). In order to approach this idea in a realistic scenario, we need to define what we say is a *quantum* system and when this system for us becomes classical.

We recall that the reason why the Wigner function is non-positive is the Heisenberg uncertainty. Let us therefore define for which kinds of states the Heisenberg limit eq. (2.98) is reached. To find this limit, we remind ourselves that we started from

$$(\Delta\hat{x})^2(\Delta\hat{p})^2 = \langle\Psi|\hat{x}^2|\Psi\rangle\,\langle\Psi|\hat{p}^2|\Psi\rangle \tag{2.159}$$

and used two inequalities to define the Heisenberg limit: The Cauchy-Schwartz inequality and the modulus square inequality of a complex number. We therefore need to find constraints on the state $|\Psi\rangle$, such that those inequalities become equalities.
The Cauchy-Schwartz inequality can generally be written as

$$|\,\langle f|g\rangle\,|^2 \leq \langle f|f\rangle\,\langle g|g\rangle \tag{2.160}$$

and only becomes an equality if f and g are linearly dependent. In our case we can define f and g to be of the form

$$|f\rangle = (\hat{x} - \langle\hat{x}\rangle)\,|\Psi\rangle\,, \tag{2.161}$$
$$|g\rangle = (\hat{p} - \langle\hat{p}\rangle)\,|\Psi\rangle\,, \tag{2.162}$$

such that we find that we have rewritten the Heisenberg uncertainty (this time without shifting to the phase-space origin). In order to make $|f\rangle$ and $|g\rangle$ linearly dependent, we require $|g\rangle = c\,|f\rangle$. The coefficien c can now be determined via the second inequality we used. The modulus square inequality of a complex number $|z|^2 \geq (\frac{z-z^*}{2i})^2$ becomes an equality if z has no real part. We therefore require c to be a complex number $c = ia$, such that

$$|g\rangle = ia\,|f\rangle\,. \tag{2.163}$$

As $|f\rangle$ and $|g\rangle$ are linearly dependent, we expect to find one type of state vector $|\Psi\rangle\,(a)$, which will generally minimize the Heisenberg uncertainty. We can now find the wavefunction of $|\Psi\rangle$ as in eq. (2.134) and write

$$(\hat{p} - \langle\hat{p}\rangle)\,|\Psi\rangle = ia(\hat{x} - \langle\hat{x}\rangle)\,|\Psi\rangle \qquad / \quad \langle x| \tag{2.164}$$
$$(-i\hbar\frac{\partial}{\partial x} - \langle\hat{p}\rangle)\psi(x) = ia(x - \langle\hat{x}\rangle)\psi(x). \tag{2.165}$$

Solving this equation we find

$$\psi(x) = Ae^{-a/(2\hbar)(x-\langle\hat{x}\rangle)^2+i\langle\hat{p}\rangle x/\hbar} \tag{2.166}$$

with $a = 1/(2c^2)$ and $A \propto (a/\pi)^{-1/4}$ for normalization. This means that minimal uncertainty states take the form of a displaced Gaussian wavefunction. Importantly, it shows that mixed states can never reach the Heisenberg uncertainty limit as our approach only works for pure states. Moreover we can calculate the Wigner function for such general Gaussian states and find

$$\mathcal{W}_G(x,p) = \frac{1}{\pi\hbar} e^{-\frac{(x-\langle\hat{x}\rangle)^2}{2(\Delta x)^2}} e^{-\frac{(p-\langle\hat{p}\rangle)^2}{2(\Delta p)^2}}, \tag{2.167}$$

where we set $\Delta x = c\sqrt{\hbar}$ and $\Delta p = \sqrt{\hbar}/(2c)$ [71]. This is just a product of a Gaussian position and momentum distribution and therefore is positive over the whole phase-space. Indeed it seems that we have found a class of states that one can consider *trivial states* as they can be described by a joint classical probability distribution of momentum and position. Interestingly, those are the states that fulfill the Heisenberg uncertainty relation. Let us now require additionally that position and momentum have a symmetric uncertainty, $\Delta x = \Delta p = \sqrt{\hbar/2}$. This leads to $|g\rangle = i\,|f\rangle$, which shows that common eigenvectors for position and momentum exist $|\Psi\rangle_{\Delta x=\Delta p=\sqrt{1/2}} = |x', p'\rangle$. Such states are approximate eigenstates of position and momentum, where the error in this approximation is given by the Heisenberg uncertainty. We can therefore write $\langle\hat{x}\rangle = x'$ and $\langle\hat{x}\rangle = p'$ such that we find a subclass of Gaussian states that we shall call *coherent states* or *classical states* with a Wigner function of

$$\mathcal{W}_C(x,p) = \frac{1}{\pi\hbar} e^{-(x-x')^2/\hbar} e^{-(p-p')^2/\hbar}, \tag{2.168}$$

Their classicality can be connected to subsubsection 2.1.1.3, where classical state are defined to have shared eigenvectors for position and momentum. We note that in phase-space those states will exactly show a marginal distribution standard deviation of $\sqrt{\hbar/2}$ as expected from the Gaussian distribution we required. This is due to those minimal uncertainty states *normalizing* the state space (compare eq. (2.75)-(2.78)) and consequently the Wigner function. We have now defined a class of pure states that we define to be non-quantum, due to convexity. Indeed any mixture of such states will also lead to non-quantum states. One usually singles out a property L of the state $\hat{\rho}$ and then compares them to the set of Gaussian and Classical states. If any mixture of Gaussian states cannot reach the value such that $L_G < L(\hat{\rho})$, then $\hat{\rho}$ is said to be **non-Gaussian**. If any mixture of classical/coherent states cannot reach the value such that $L_C < L(\hat{\rho})$, then $\hat{\rho}$ is said to be **non-Classical**, where $L_C \leq L_G$ as it is just a special case of the non-Gaussian set. What we called here L_C and L_G will be referred to as *thresholds* in the following chapters.

The underlying meaning of a state being non-Gaussian is that it cannot be efficiently sim-

ulated by a classical system, which has been extensively studied [72–76] and will be further discussed in section 2.4.

2.1.6 Take-away message

The most important concepts we have developed so far as summarized here.
About classical light:

- Light is classically described by an electromagnetic wave. This wave lives in a vector space, spanned by its modes, called the modal Hilbert space.
- We can have polarization, temporal, or spatial modes that can be used independently in the continuous wave regime we are operating in. Each mode has a complex field amplitude, whose real and imaginary parts are called quadratures. Those quadratures form the optical phase-space. Each mode has its phase-space and can be described by a harmonic oscillator.
- In the single mode approach we assume that one mode describes the electromagnetic field. This will be our experimental regime.

About the transition from classical to quantum mechanics:

- The main difference between classical and quantum mechanics is Heisenberg's uncertainty and therefore the idea that quantum measurements can interfere. An example of interfering measurements are the quantized field quadratures or position and momentum. They form a phase-space, which can be mapped to a complex Hilbert space.
- In classical mechanics pure states in this phase-space are not the basis of their Hilbert space, which prevents them from being in superpositions. In quantum mechanics, pure states are the basis of their Hilbert space, such that they can be in superpositions.
- We can develop a joint probability distribution, describing the evolution of position and momentum in phase space. The governing equation for this evolution is the Liouville equation in classical and Moyal's equation in quantum mechanics. In this way, we can define the Wigner function, which is normalized but can take negative values. It is therefore not a proper probability distribution.

About the implications of quantizing the light field:

- The complex field amplitude becomes the annihilation operator $\hat{a}$. The quadratures therefore also become operators $\hat{x}$, $\hat{p}$. The complex conjugate of the annihilation operator is the creation operator $\hat{a}^\dagger$.
- The harmonic oscillator describing the electromagnetic field of a quantized mode has discrete energy levels. Those levels depend on the number of excitations

in the system, defined by the number operator $\hat{n}$. Applying the annihilation operator to a system decreases the number of excitations by one and inversely for the creation operator. The eigenvectors of the number operators are called the Fock states.

About expressing a state as a matrix:

- Any state can be described as a superposition of Fock states and their statistical mixtures, forming the density matrix. Those density matrices $\hat{\rho}$ are Hermitian positive semi-definite. A density matrix is pure if the trace of its square is one $\mathrm{Tr}[\hat{\rho}^2] = 1$. This defines the purity of a state $\mathcal{P}(\hat{\rho})$. A state of minimal purity is called a fully mixed state. The overlap between two states is called the fidelity $\mathcal{F}(\hat{\rho}_1, \hat{\rho}_2)$.

- A pure composite system is entangled. Taking the partial trace of a fully entangled system results in fully mixed sub-states. Entanglement between two modes can be calculated by applying a partial transpose and calculating if the resulting matrix has negative eigenvalues resulting in the measure of negativity or logarithmic negativity.

About writing a state as a phase-space probability function:

- The Wigner function describes the phase-space distribution of the two quadratures and is written as $\mathcal{W}_\rho(x,p) = \frac{1}{\pi\hbar}\int dy\; e^{2ipy/\hbar}\,\langle x-y|\hat{\rho}|x+y\rangle$.

- It is a real-valued function, that is normalized to one. Its minimum and maximum value are $\pm 1/(\hbar\pi)$, where $\hbar$ is the normalization. Changing the normalization changes the proportionality factor between annihilation, creation, position, and momentum operator. The Wigner function is not the unique phase-space description.

Wigner function and density matrix are equivalent representations for the state.
About the evolution and measurement of quantum systems:

- The evolution of a state is described by Schrödinger's equation and is equivalent to a unitary operator. If this unitary acts on an isolated system, the evolution is trace-preserving. If it acts on an environment and a system, the action on the system is not trace-preserving.

- A measurement is an example of a trace-preserving operation. Measurements can be formulated as positive operator valued measures (POVMs), which are described by one matrix per possible measurement result and add up to unity. If the matrices of a POVM are pure then the measurement is projective.

- The effect of an operation on the Wigner function can be calculated by the effect this operation has on the phase-space coordinates.

From the viewpoint of the Wigner function or the density matrix two different communities developed, focusing on a continuous variable (CV) or discrete variable (DV) approach. While historically they have developed different experimental and theoretical practices, nowadays they are merging. We are using their naming convention to describe states that live in approximately two-dimensional Hilbert spaces as DV or larger Hilbert spaces as CV.
About Non-Gaussianity:

- All states that have a minimal Heisenberg uncertainty can be described in phase-space by a product of a Gaussian position and momentum distribution. Those states are called Gaussian states. Gaussian states are states that have a positive Wigner function and therefore can be described by classical mechanics. Classical states are Gaussian states that have symmetric uncertainty in position and momentum.

- Non-Gaussian states are states that cannot be described by classical mechanics and therefore capture the quantum character of states.

After having developed a notion of Gaussian and non-Gaussian states the next section will give typical examples of those states.

2.2 States in quantum optics

In this section we want to investigate states, that are typically found in quantum optical systems and investigate if they are non-Gaussian. For each state we will show the its density matrix, Wigner function, marginal distribution of the quadratures and the photon-number distribution $P_\Psi(n) = |\langle n|\Psi\rangle|^2$. The phase-space normalization $\hbar$ will be set to $\hbar = 0.5$ for plotting or left as a variable.

2.2.1 Gaussian states

In this subsection, we will introduce four types of states: the vacuum state, coherent state, thermal state, and squeezed state. It should be noted that while the thermal state does not satisfy the minimal Heisenberg uncertainty relation, the other three states do.

2.2.1.1 Vacuum

The easiest state in any optical system is the vacuum state. The vacuum state has no photon excitation such that corresponds to a Fock state $|0\rangle$. We can use eq. (2.133) to find its corresponding Wigner function

$$\mathcal{W}_{|0\rangle\langle 0|}(x,p) = \frac{1}{\pi} e^{-(x^2+p^2)/\hbar} \tag{2.169}$$

as the Laguerre polynomial is always $L_0^0(x) = 1$. For such a state the density matrix is simply

$$\hat{\rho}_0 = |0\rangle\langle 0|, \tag{2.170}$$

and its photon number distribution is only nonzero for $P_0(0) = 1$ because $\hat{n}|n\rangle = n|n\rangle$.
The properties of the vacuum state are shown in fig. 2.1, where in (d) we see that this state is completely symmetric. Indeed we will see that this is the case for all Fock states. Moreover, the Wigner function is a coherent state with its mean at the phase-space origin.

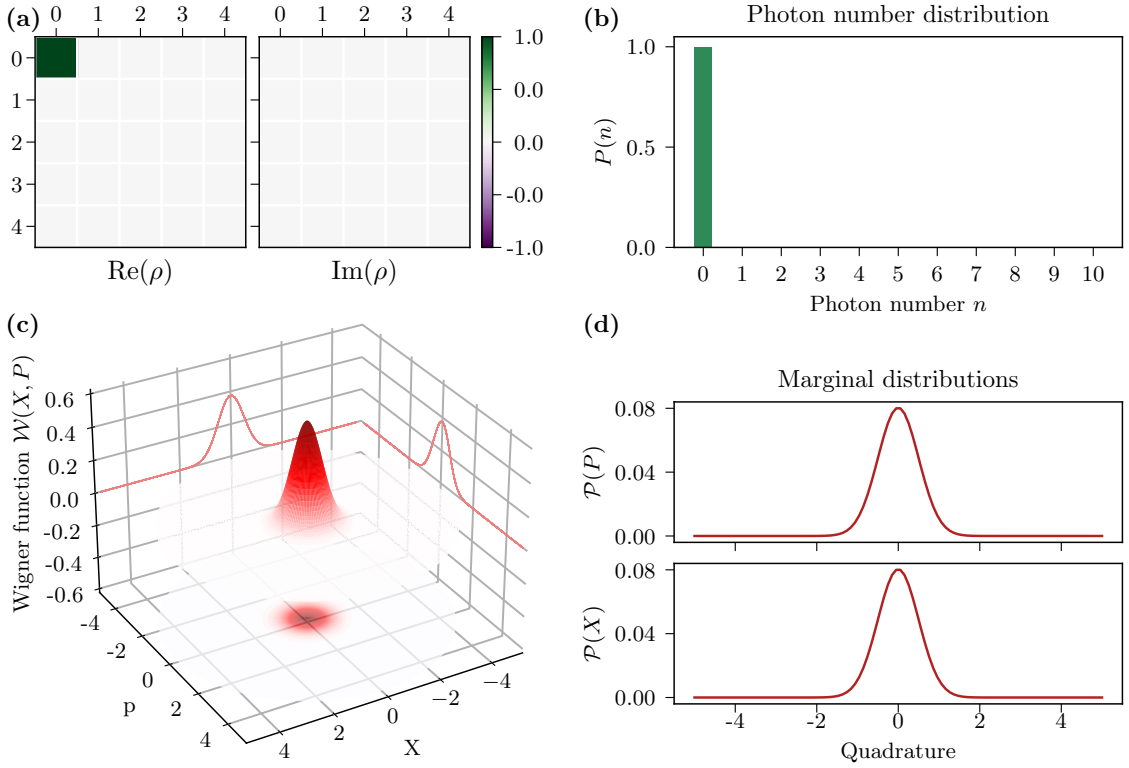

Figure 2.1: Properties of the vacuum state $|0\rangle$. In **(a)** the imaginary and real parts of the density matrix in the Fock basis of vacuum are shown. **(b)** depicts the photon number distribution of this state, equivalent to the diagonal of the density matrix. The Wigner function is visible in **(c)** with its marginal distributions in **(d)**. Note that the marginal distributions drawn in (c) are not up to scale.

2.2.1.2 Coherent states

Let us now define properly what a coherent state is. We have already stated that all classical or coherent states have shared eigenvectors $|x, p\rangle$ in subsection 2.1.5. We can define this as a complex vector $|\alpha\rangle$ and use eq. (2.165) to find its eigenvalues. Indeed we stated that the constant a for coherent states is $a = 1/(2c^2) = 1/(2(1/\sqrt{2})^2 = 1$ and can therefore write

$$\begin{aligned}
(\hat{p} - \langle\hat{p}\rangle)\,|\alpha\rangle &= i(\hat{x} - \langle\hat{x}\rangle)\,|\alpha\rangle \\
\hat{x} + i\hat{p}\,|\alpha\rangle &= \langle\hat{x} + i\hat{p}\rangle\,|\alpha\rangle \\
\sqrt{2\hbar}\,\hat{a}\,|\alpha\rangle &= \langle\hat{x} + i\hat{p}\rangle\,|\alpha\rangle \qquad (2.171) \\
\hat{a}\,|\alpha\rangle &\equiv \alpha\,|\alpha\rangle\,, \qquad (2.172)
\end{aligned}$$

where α are the eigenvalues and are usually defined as $\alpha = |\alpha|e^{i\phi}$ with the amplitude $|\alpha|$ and the phase ϕ. We can see here that $|\alpha\rangle$ are eigenstates of the annihilation operator of eq. (2.77) and as such $\hat{a}$ it is unchanged by the annihilation of a photon. Importantly we see that there is a factor $\sqrt{2\hbar}$ appearing in eq. (2.171). This means that there is a

re-scaling factor of the eigenvalues $\alpha = 1/\sqrt{2\hbar}\,\langle\hat{x} + i\hat{p}\rangle = 1/\sqrt{2\hbar}(\Re(\alpha) + i\Im(\alpha))$ in the x, p representation. If we set $\hbar = 0.5$ we find $\alpha = \Re(\alpha) + i\Im(\alpha)$ and can avoid always re-scaling the input state to the Wigner function.
If we now want to write the generating Hamiltonian of the eigenvalue equation 2.171, we first search for the corresponding equation for the eigenvectors in terms of annihilation and creation operators

$$
\begin{aligned}
\text{assume the general form} \qquad |\alpha\rangle &= \sum_{n=0}^{\infty} c_n\,|n\rangle \\
\hat{a}\,|\alpha\rangle &= \hat{a}\sum_{n=0}^{\infty} c_n\,|n\rangle \\
\alpha\,|\alpha\rangle &= \sum_{n=1}^{\infty} c_n\sqrt{n}\,|n-1\rangle \qquad /n \to n+1 \\
|\alpha\rangle &= \sum_{n=0}^{\infty} c_{n+1}\sqrt{n+1}\,|n\rangle \\
\alpha\sum_{n=0}^{\infty} c_n\,|n\rangle &= \sum_{n=0}^{\infty} c_{n+1}\sqrt{n+1}\,|n\rangle
\end{aligned}
\tag{2.173}
$$

we get the recursion relation $c_{n+1} = \alpha/\sqrt{n+1}c_n$ which leads to $c_{n+1} = \alpha^n/\sqrt{n!}c_0$ and with normalization we finally arrive at

$$
|\alpha\rangle = e^{-|\alpha|^2/2}\sum_{n=0}^{\infty}\frac{\alpha^n}{\sqrt{n!}}\,|n\rangle\,. \tag{2.174}
$$

We can now write the creating Hamiltonian of the coherent state as

$$
\begin{aligned}
|\alpha\rangle &= e^{-|\alpha|^2/2}\sum_{n=0}^{\infty}\frac{\alpha^n}{n!}(\hat{a}^\dagger)^n\,|0\rangle && (2.175)\\
&= e^{-|\alpha|^2/2}e^{\alpha\hat{a}^\dagger}\,|0\rangle && (2.176)
\end{aligned}
$$

$$
\text{due to} \quad \hat{a}\,|0\rangle = 0 \quad \text{we also find} \quad e^{\alpha^*\hat{a}}\,|0\rangle = |0\rangle
$$

$$
\begin{aligned}
\text{such that} \quad |\alpha\rangle &= e^{-|\alpha|^2/2}e^{\alpha\hat{a}^\dagger}e^{\alpha^*\hat{a}}\,|0\rangle && (2.177)\\
&= e^{\alpha\hat{a}^\dagger - \alpha^*\hat{a}}\,|0\rangle && (2.178)\\
&= D(\alpha)\,|0\rangle && (2.179)
\end{aligned}
$$

which shows indeed that the vacuum state is $|0\rangle = |\alpha = 0\rangle$ a coherent state and therefore has minimum uncertainty. The operator $D(\alpha)$ in eq. (2.178) is called *Displacement operator* and

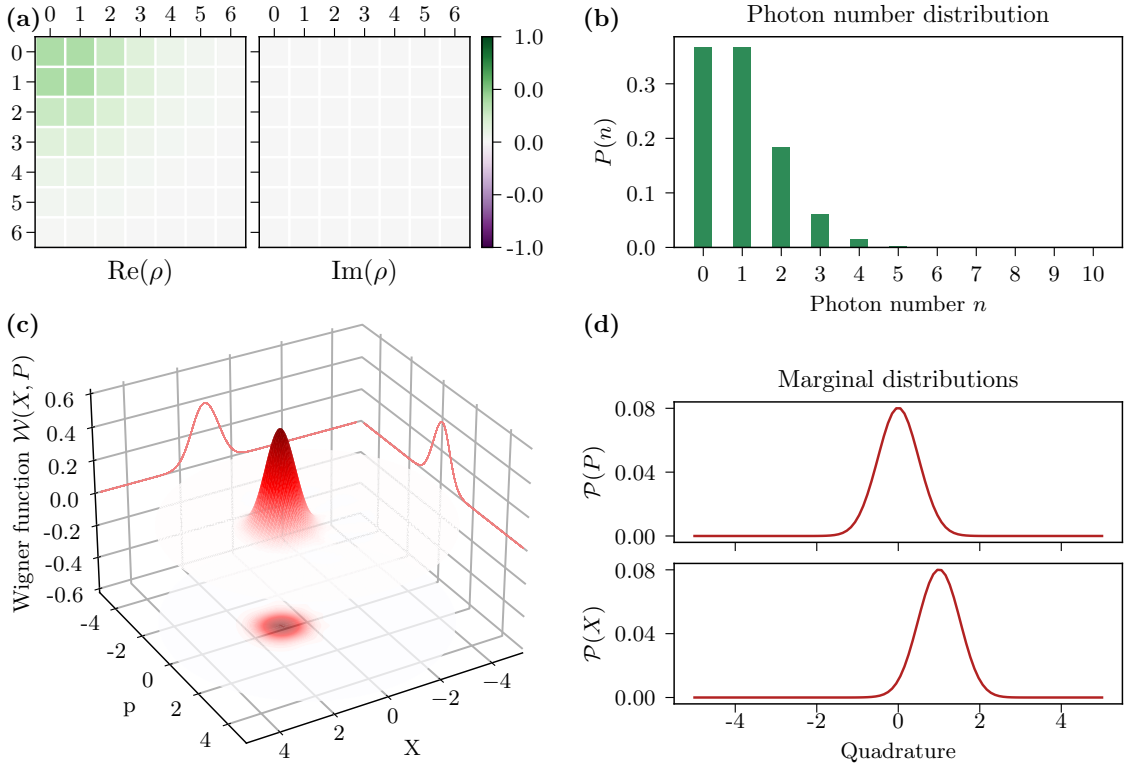

Figure 2.2: Properties of the coherent state $|\alpha = 1\rangle$. Caption as in fig. 2.1.

generates coherent states by displacing them in phase-space. If we write the displacement operator in terms of position and momentum for $\hbar = 0.5$, we find

$$D(\alpha) = e^{\alpha\hat{a}^\dagger - \alpha^*\hat{a}}, \tag{2.180}$$

$$D_\alpha(x,p) = e^{\alpha(\hat{x}-i\hat{p}) - \alpha^*(\hat{x}+i\hat{p})} \tag{2.181}$$

$$= e^{i[\Im(\alpha)\hat{x} - \Re(\alpha)\hat{p}]}. \tag{2.182}$$

The Wigner function of a displaced state is therefore

$$\mathcal{W}_\alpha(x,p) = \frac{2}{\pi} e^{-2(x-\Re(\alpha))^2} e^{-2(p-\Im(\alpha))^2} \tag{2.183}$$

and has the wavefunction

$$\psi_\alpha(x) = (2/\pi)^{-1/4} e^{-(x-\Re(\alpha))^2 + i2\Im[\alpha]x}. \tag{2.184}$$

We moreover see that a real amplitude influences x while an imaginary amplitude influences p in the displacement.

This is shown in fig. 2.2, where we plot for $\alpha = 1$. As visible in (c) this constitutes a shift of $x + 1$ in phase-space. The coherent state basis is over-complete, meaning that two coherent states are not orthogonal, but in fact overlap

$$|\langle\alpha|\beta\rangle|^2 = e^{-|\beta-\alpha|^2}. \tag{2.185}$$

Interestingly in the phase-space representation, we have to adapt the normalization to our choice of $\hbar$

$$\int dx[\Psi_\beta(x)\Psi_\alpha(x)^*]^2 = e^{-|\beta-\alpha|^2/\hbar}. \tag{2.186}$$

The photon statistics can be calculated as

$$P_\alpha(n) = |\langle n|\alpha\rangle|^2 \tag{2.187}$$

$$= |e^{-|\alpha|^2/2} \sum_{m=0}^{\infty} \frac{\alpha^m}{\sqrt{m!}} \langle n|m\rangle|^2 \tag{2.188}$$

$$= e^{-|\alpha|^2} \frac{(|\alpha|^2)^n}{n!} \tag{2.189}$$

and therefore follows a Poisson statistic. The expectation value of the number operator is

$$\langle\hat{n}\rangle_\alpha = |\alpha|^2 \tag{2.190}$$

giving a mean photon number of the squared amplitude of the coherent state.

Let us define the term *shot noise*, which describes the fluctuations of the number of photons present in a state being the standard deviation of the photon number operator $\Delta\hat{n}$, which grows with n. This is not to be confused with the Heisenberg limit, which is the same for all coherent states. Because $\langle\alpha|(\Delta\hat{n})^2|\alpha\rangle = \langle\hat{n}\rangle_\alpha$ we see that the vacuum state with $\alpha = 0$ has no shot noise because it has no photon number fluctuations. In an experimental setup, the shot noise is equivalent to the accumulation of electronic noise and the above-explained intensity fluctuations. In our experiment, we use the shot noise of the vacuum state to calibrate the whole setup, as we will see in chapter 3.

2.2.1.3 Thermal states

Thermal states are all states that have symmetric standard deviations $\Delta x = \Delta p$. Those states connect the quantum descriptions to the laws of thermodynamics such that the quantum counterpart of the canonical (Gibbs) ensemble, corresponding to the equilibrium state at the temperature T and a Hamiltonian $\hat{H}$ is described by

$$\hat{\rho}_b = \frac{1}{Z} e^{-b\hat{H}} \quad b = 1/(k_B T) \quad Z = \mathrm{Tr}[e^{-b\hat{H}}], \tag{2.191}$$

where k_B is the Boltzmann constant [77]. Let us consider the quantum harmonic oscillator of eq. (2.82) where for simplicity we set $\omega = 1$. This system is closed and as for classical systems preserves entropy. It therefore cannot describe the equilibration process for an isolated quantum system needed to achieve a state of the form $\hat{\rho}_b$. The only equilibrium state we can achieve is by imagining a kind of time averaging of the eigenstates of the quantum harmonic oscillator, leading to the loss of all coherences in the density matrix such that we can redefine a quantum optical thermal state as follows

$$\hat{\rho}_{Th} = \frac{1}{Z}\sum_{n=0}^{\infty} |n\rangle \langle n| e^{-bE_n}, \tag{2.192}$$

where $E_n = \hbar(n+1/2)$ are the energy eigenvalues of the corresponding Fock states [77, 78]. We find $Z = \sum_n e^{-bE_n} = e^{-b\hbar/2}/(1-e^{-b\hbar})$ and the mean value of the excitation in the oscillator becomes $\langle \hat{n} \rangle = 1/(e^{b\hbar} - 1)$. Let us find the Heisenberg uncertainty for thermal states. The standard deviations for the eigenstates of our Hamiltonian read

$$\langle n|(\Delta\hat{x})^2|n\rangle = \langle n|\hat{x}^2|n\rangle - (\langle n|\hat{x}|n\rangle)^2 = \hbar(n+\frac{1}{2}), \tag{2.193}$$

$$\langle n|(\Delta\hat{p})^2|n\rangle = \hbar(n+\frac{1}{2}), \tag{2.194}$$

which are their energies. If we now write the variances of the thermal state of eq. (2.192)

$$(\Delta\hat{x})^2_{Th} = \hbar(\frac{1}{2} + \langle n\rangle), \tag{2.195}$$

$$(\Delta\hat{p})^2_{Th} = \hbar(\frac{1}{2} + \langle n\rangle), \tag{2.196}$$

we find symmetric values that for $n = 0$ reduce to the Heisenberg limit. As we know that $\langle n\rangle = 1/(e^b - 1)$ we see that the Heisenberg uncertainty goes towards its minimal value as $T \to 0$ and goes towards infinity for $T \to \infty$. Following our definition in eq. (2.167), the Wigner function of a thermal state reads

$$\mathcal{W}_{Th}(x,p) = \frac{1}{\pi\hbar} e^{-\frac{(x-\langle\hat{x}\rangle)^2}{2\hbar(0.5+\langle\hat{n}\rangle)}} e^{-\frac{(p-\langle\hat{p}\rangle)^2}{2\hbar(0.5+\langle\hat{n}\rangle)}}, \tag{2.197}$$

This kind of state with a temperature of $T = 5\ 10^{-11}$K (and the Boltzmann constant expressed as $k_B = 2.083661912\ 10^{10}$ Hz/K) and $\hbar = 0.5$ is visible in fig. 2.3. The values were chosen for the clarity of the plot.

Thermal states provided an early link between thermodynamics and quantum mechanics and opened the path toward the calculation of entropy in quantum systems. Nowadays quantum thermodynamics is an active area of research where many concepts are connected with the quantum informational aspect of quantum mechanics. In experiments, thermal

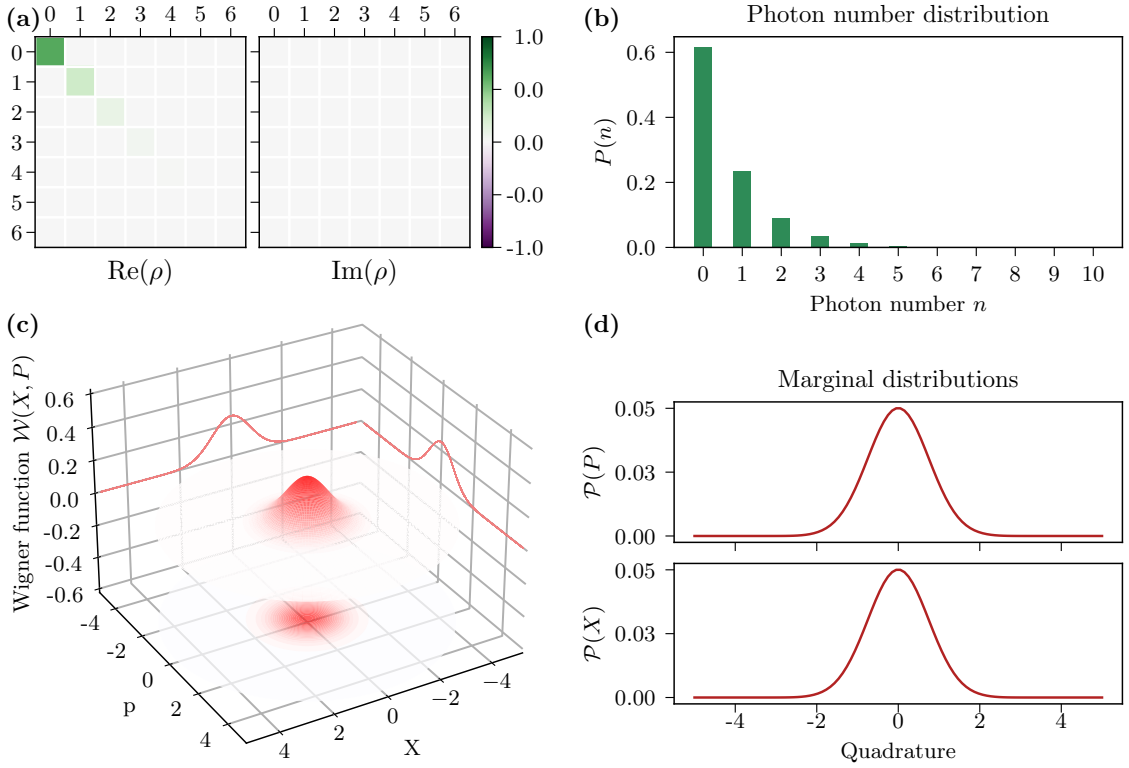

Figure 2.3: Properties of the thermal state ρ_{Th} with a temperature of 5 10^{-11} K. Caption as in fig. 2.1

states are usually unwanted, as the equilibration towards the thermal state washes out interesting quantum phenomena like superposition and entanglement.

2.2.1.4 Squeezed states

Up until now, we have only considered Gaussian states with symmetric standard deviations, let us now introduce states that also reach the Heisenberg limit, but with $\Delta\hat{x} \neq \Delta\hat{p}$. Then one quadrature will be *squeezed*, while the conjugate quadrature will be *anti-squeezed*, such that we can define a squeezing $e^{-\xi}$ with $\xi \in \mathbb{C}$ and therefore a squeezing factor $s = (e^{-\xi})^2 = e^{-2\Re(\xi)}$. We can now write

$$\Delta\hat{x} = e^{-\xi}\sqrt{\frac{\hbar}{2}}, \tag{2.198}$$

$$\Delta\hat{p} = e^{\xi}\sqrt{\frac{\hbar}{2}}, \tag{2.199}$$

where we used again the connection $a = 1/(2c^2)$ with $c = e^{-\xi}\sqrt{\frac{1}{2}}$ of subsection subsection 2.1.5. We can plug our coefficient $a = 1/(2c^2) = e^{2\Re(\xi)}$ into eq. (2.164) such that

$$(\hat{p} - \langle\hat{p}\rangle)\,|\Psi\rangle = \frac{i}{2c^2}(\hat{x} - \langle\hat{x}\rangle)\,|\Psi\rangle \tag{2.200}$$

$$(e^{2\Re\xi}\hat{x} + i\hat{p})\,|\Psi\rangle = \langle e^{2\Re\xi}x + ip\rangle\,|\Psi\rangle \tag{2.201}$$

$$(\sqrt{2\hbar}\sinh(\xi)\hat{a}^\dagger + \sqrt{2\hbar}\cosh(\xi)\hat{a})\,|\Psi\rangle = \langle e^{2\Re\xi}x + ip\rangle\,|\Psi\rangle\,, \tag{2.202}$$

where in eq. (2.202) we have written the left-hand side in terms of annihilation and creation operators instead of the quadrature operators. We have defined the squeezed state as a deviation from the coherent state, such that we expect eq. (2.202) to reduce to eq. (2.171) for $\xi = 0$. We can now define an operator $\hat{O}$, capturing the left-hand side of eq. (2.202) and rewrite it, such that we see the coherent state solution

$$\begin{aligned}\hat{O} &= \sqrt{2\hbar}\sinh(\xi)\hat{a}^\dagger + \sqrt{2\hbar}\cosh(\xi)\hat{a} = \sqrt{2\hbar}\sinh(r)\hat{a}^\dagger + \sqrt{2\hbar}e^{i\phi}\cosh(r)\hat{a} \\ &= \sqrt{2\hbar}U\hat{a}U^\dagger,\end{aligned} \tag{2.203}$$

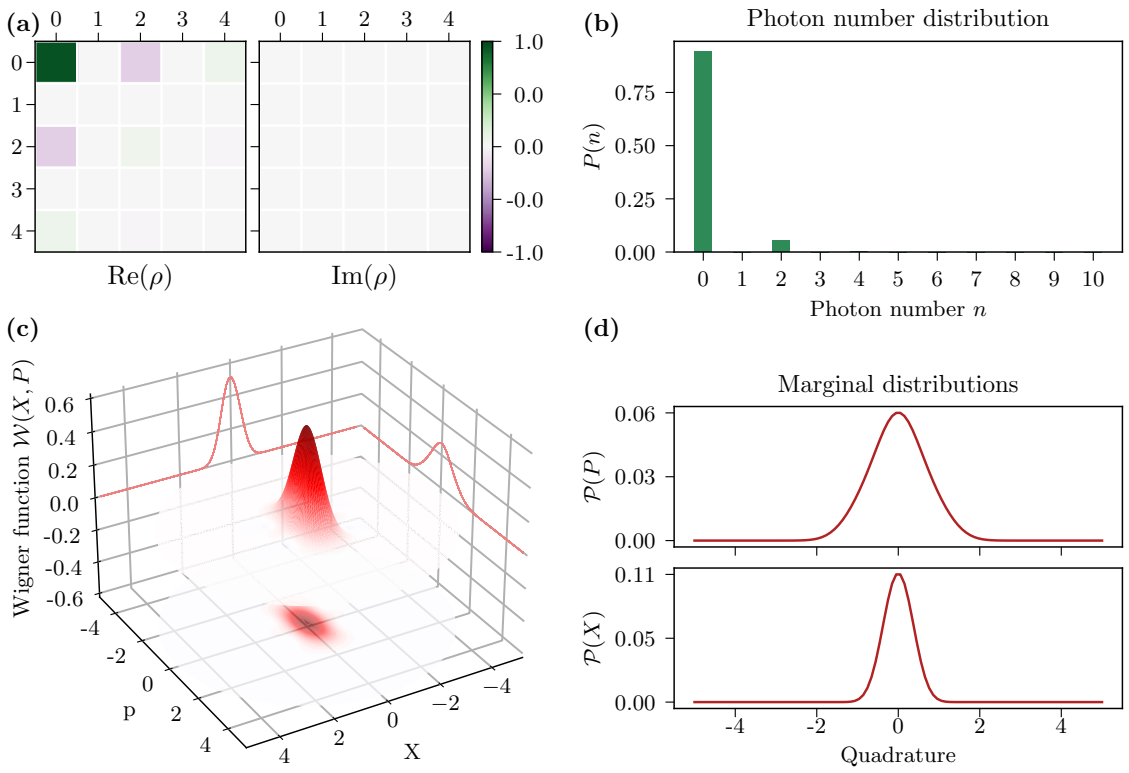

Figure 2.4: Properties of the squeezed vacuum state $|\xi\rangle$ with a squeezing of 4 dB, i.e. $r = 0.46$ or $\lambda = 0.43$. Caption as in fig. 2.1.

with U being a unitary transformation and $\xi = re^{i\phi}$. Therefore, a squeezed state is a coherent state up to this unitary transformation, that is defined as the *squeezing operator*

$$U = S(\xi) = e^{\frac{1}{2}(\xi^* \hat{a}^2 - \xi(\hat{a}^\dagger)^2)}. \tag{2.204}$$

We often use the squeezed vacuum state, defined as

$$S(\xi)\,|0\rangle = |\xi\rangle\,. \tag{2.205}$$

The fact that eq. (2.204) shows that $\hat{O}$ is a linear transformation of the annihilation operator, such that for $\xi = 0$ we retrieve our eigenvalue equation of the coherent state shows, that both coherent $|\alpha\rangle$ and squeezed vacuum states $|\xi\rangle$ are general eigenstates of $\hat{O}$ such that we can write the general eigenvalue equation

$$\hat{O}\,|\Psi\rangle = \left(\sqrt{2\hbar}\sinh(r)\hat{a}^\dagger + \sqrt{2\hbar}e^{i\phi}\cosh(r)\hat{a}\right)|\alpha,\xi\rangle = (\alpha\cosh(r) + \alpha^*\sinh r)\,|\alpha,\xi\rangle\,. \tag{2.206}$$

In this way we found the most general states that are Gaussian as the eigenstates of $\hat{O}$, being squeezed and displaced vacuum:

$$D(\alpha)S(\xi)\,|0\rangle = |\alpha,\xi\rangle\,. \tag{2.207}$$

We can write the *squeezed vacuum state* of eq. (2.205) in the Fock basis as

$$|\xi\rangle = \frac{1}{\sqrt{\cosh(r)}}\sum_{n=0}^{\infty}(-1)^n\frac{\sqrt{(2n)!}}{2^n n!}e^{in\phi}\tanh(r)^n\,|2n\rangle \tag{2.208}$$

which can be simplified by setting $\lambda = \tanh(r)$ and explicitly written in subsection 3.2.3. The squeezing is then often given in decibels

$$s_{dB} = -10\log_{10}(\frac{1-\lambda}{1+\lambda}) = \frac{20}{\ln(10)}r. \tag{2.209}$$

We see in eq. (2.208), that squeezed vacuum is a superposition of even numbers of Fock states. The probability of a $2n$-photon detection is

$$P_\xi(2n) = \frac{(2n)!}{2^{2n}(n!)^2}\frac{\tanh(r)^{2n}}{\cosh(r)}. \tag{2.210}$$

Its marginal distribution in position can be written as

$$P_\xi(x) = \frac{e^\xi}{\sqrt{\pi\hbar}}e^{-\frac{x^2}{\hbar e^{-2\xi}}}\,. \tag{2.211}$$

The Wigner function of a squeezed state is

$$\mathcal{W}_G(x,p) = \frac{1}{\pi\hbar} e^{-\frac{(x-\langle\hat{x}\rangle)^2}{\hbar e^{-2r}}} e^{-\frac{(p-\langle\hat{p}\rangle)^2}{\hbar e^{2r}}}. \tag{2.212}$$

Such a state can be seen in fig. 2.4, where we applied a squeezing of 4 dB, i.e. $r = 0.46$ or $\lambda = 0.43$. We notice that the x-quadrature is squeezed while the p-quadrature is anti-squeezed, as defined above. The squeezing operator of eq. (2.204) can also be rewritten, such that the squeezing is applied to two modes. This is nothing else than a mode change of the classical modal light basis and we will encounter it in subsection 3.2.4. For completeness, the displaced squeezed state in the Fock basis can be written as [79]

$$\begin{aligned} |\alpha,\xi\rangle &= \frac{e^{-|z|^2/2\sinh(2r)+(z^*)^2\sinh^2(r)}}{\sqrt{\cosh(r)}} \sum_n \frac{1}{\sqrt{n!}} (e^{i\phi}\frac{\tanh(r)}{2})^{n/2} H_n(z^*)\,|n\rangle\,, \\ \text{with} \quad z &= \frac{1}{\sqrt{2\tanh(r)}}\alpha^* e^{i\phi/2} + \sqrt{\frac{\tanh(r)}{2}}\alpha e^{-i\phi/2}. \end{aligned} \tag{2.213}$$

2.2.2 Non-Gaussian states

Now we explore all states, that cannot be described by a Gaussian distribution in phase-space. The most common states of those non-Gaussian states are the so-called Fock states, equivalent to the excitations in the quantum harmonic oscillator. Other famous non-Gaussian states are superpositions of Gaussian states. We refer to those states as "qubit" states and will explain qubits before presenting two examples: cat- and GKP-qubits.

2.2.2.1 Fock states

In the previous subsection, we have already explored the vacuum state. We can write an arbitrary Fock state as

$$|n\rangle = \frac{(a^\dagger)^n}{\sqrt{(n+1)!}}\,|0\rangle \tag{2.214}$$

and have previously defined its wavefunction in eq. (2.134) and Wigner function in eq. (2.133). In fig. (2.5) we can see that the single photon has the maximal Wigner negativity of $-2/\pi$ at the phase-space origin.

All Fock states are symmetric around the origin, which is why both marginal distributions are identical. The photon number distribution is trivial in this ideal case. In experiments both marginal and photon number distribution are good indicators of the system quality. We see that the higher the Fock number, the more x-p-zero-crossings are present, as visible in fig. 2.6. Those crossings are circular around the origin. We can moreover see that each odd Fock state tends to $-2/\pi$ and each even Fock state towards $2/\pi$ at the phase-space origin. This is expected due to eq. (2.136).

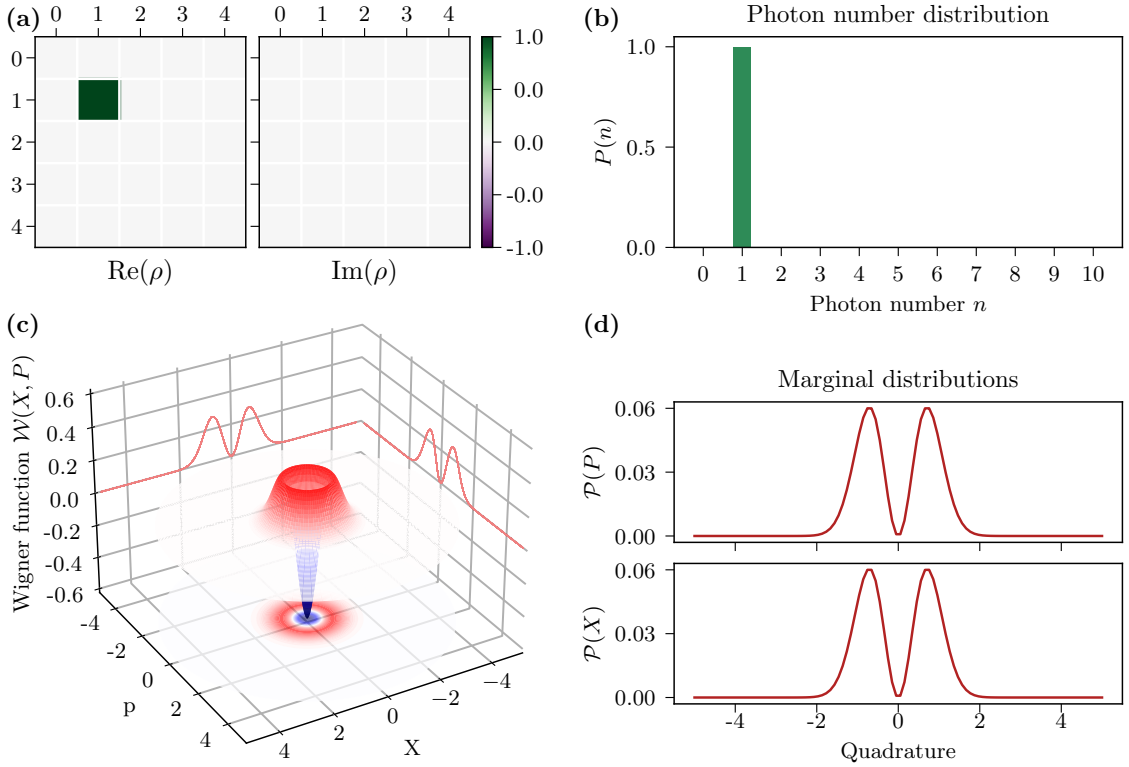

Figure 2.5: Properties of single photon state $|1\rangle$. Caption as in fig. 2.1.

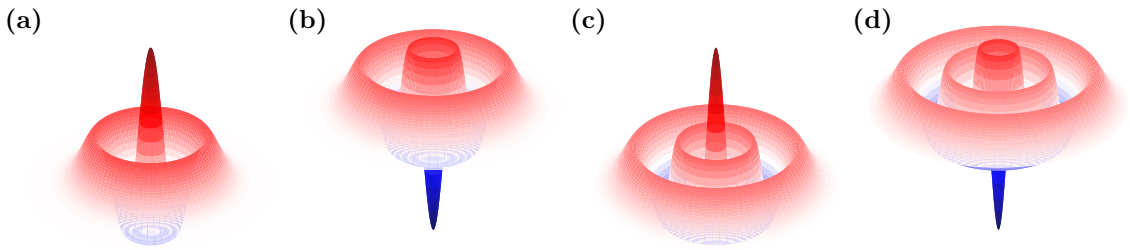

Figure 2.6: Wigner functions of the Fock states **(a)** for a two photon state, **(b)** a three photon state, **(c)** a four-photon state and **(d)** a five-photon state.

2.2.2.2 The qubit

Any of the Gaussian states we defined in subsection subsection 2.2.1, can be used to create non-Gaussian states by creating a superposition of two (quasi-) orthogonal Gaussian states. The weights of each and the phase between the superposition-components can vary, forming a two-dimensional parameter space. Any possible state in this parameter space is called

a *pure qubit*. In order to have a general description, the *logical states* $|0\rangle_L$ and $|1\rangle_L$ are defined. Those states are orthogonal and a qubit can thus be written as

$$|\text{qubit}\rangle = c_0 |0\rangle_L + e^{i\phi} c_1 |1\rangle_L \quad \text{and} \quad c_0^2 + c_1^2 = 1 \tag{2.215}$$

for normalization. A realistic qubit does not have to be a pure state and can be written in the basis of any 2x2 Hermitian matrices, which are the logical *Pauli matrices* X_L, Y_L, Z_L together with the identity $\mathbb{1}$ such that the qubit density matrix is

$$\hat{\rho}_Q = \frac{1}{2}[\mathbb{1} + \vec{r}\,\vec{\sigma}], \tag{2.216}$$

$$\text{with} \quad \vec{r} = (r_x, r_y, r_z)^T \quad \text{and} \quad \vec{\sigma} = (X_L, Y_L, Z_L)^T \tag{2.217}$$

$$X_L = \begin{bmatrix} 0 & 1 \\ 1 & 0 \end{bmatrix} \quad Y_L = \begin{bmatrix} 0 & -i \\ i & 0 \end{bmatrix} \quad Z_L = \begin{bmatrix} 1 & 0 \\ 0 & -1 \end{bmatrix}. \tag{2.218}$$

The eigenvectors of the Pauli matrices with eigenvalues $1, -1$ are the qubits

$$|0\rangle_L \qquad\qquad |1\rangle_L \qquad \text{for} \quad Z_L \tag{2.219}$$

$$|+\rangle_L = \frac{1}{\sqrt{2}}(|0\rangle_L + |1\rangle_L) \qquad |-\rangle_L = \frac{1}{\sqrt{2}}(|0\rangle_L - |1\rangle_L) \qquad \text{for} \quad X_L \tag{2.220}$$

$$|+i\rangle_L = \frac{1}{\sqrt{2}}(|0\rangle_L + i\,|1\rangle_L) \qquad |-i\rangle_L = \frac{1}{\sqrt{2}}(|0\rangle_L - i\,|1\rangle_L) \qquad \text{for} \quad Y_L, \tag{2.221}$$

where $Y = iXZ$. The state is pure if $|\vec{r}| = 1$.
We can now represent this state in spherical coordinates by using the transformation

$$\vec{r} = (\sin(\theta)\cos(\phi)), \sin(\theta)\sin(\phi), \cos(\theta), \tag{2.222}$$

where θ is the colatitute with respect to the $z-$axis and ϕ is the longitude with respect to the $x-$axis. In those coordinates a qubit is a sphere, where all pure states lie on its surface and a fully mixed state at its center.

The logical Pauli matrices of eq. (2.218) have to be adapted to the physical system, that represents the qubit. In principle, any decomposition of the density matrix into a set of linearly independent operators is sufficient to represent a qubit as a Bloch vector. Those operators have to be generators of the special unitary group $SU(N)$ to represent quantum systems, which are always based on Lie-algebra. As long as the matrices of those operators are unitary, they can be chosen as Pauli matrices, depending on the application.

2.2.2.3 Cat states

The cat states, or Schrödinger cat states, in optics, are defined as the superposition of two orthogonal coherent states

$$|\text{cat}\rangle_\phi = \frac{1}{N_\phi}(|\alpha\rangle + e^{i\phi}|-\alpha\rangle),$$
$$\text{where} \quad N_\phi = \sqrt{2(1+\cos(\phi)e^{-2|\alpha|^2})} \tag{2.223}$$

is the normalization factor.

The naming convention goes back to the famous *Gedankenexperiment* of Schrödinger, where he imagined two massive systems in a superposition, an alive and a dead cat. In the original idea, the superposition was rather an entanglement of this massive system with a quantum particle. This is why sometimes the state of eq. (2.223) is rather called *coherent-state superposition*. We will stick with the name *cat state*, as it is the more common naming convention.

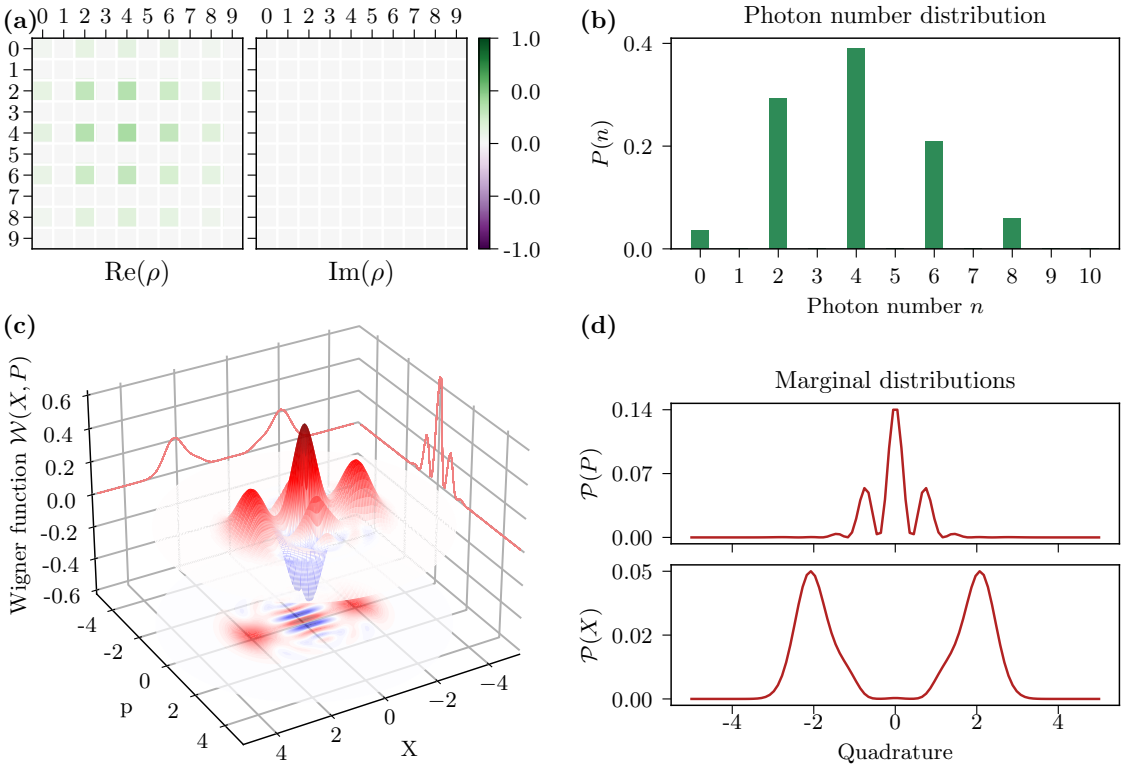

Figure 2.7: Properties of an even cat state $|\text{cat}\rangle_+$ with an amplitude of $\alpha = 2$. Caption as in fig. 2.1.

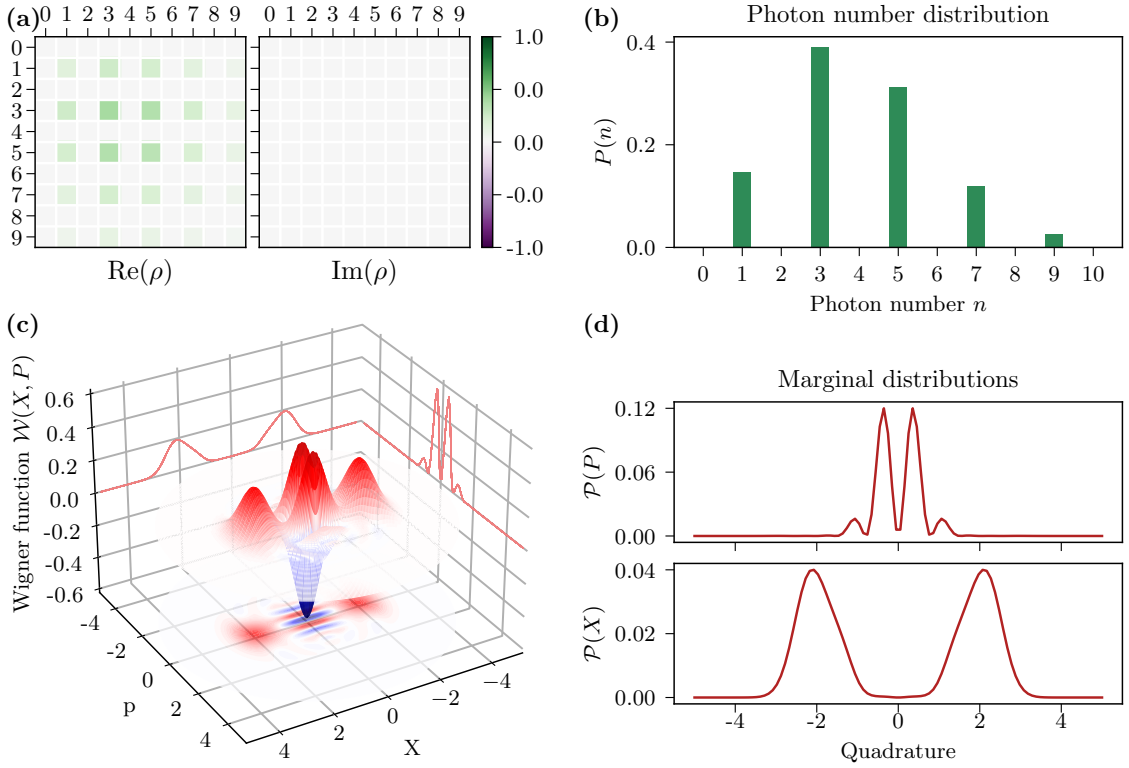

Figure 2.8: Properties of an odd cat state $|\text{cat}\rangle_-$ with an amplitude of $\alpha = 2$. Caption as in fig. 2.1.

Note, that if the phase $\phi = 0$, this superposition consists of only even Fock states and for $\phi = \pi$ of only odd Fock states. Consequently, they are called *even* and *odd cat states* and can be written as

$$|\text{cat}\rangle_+ = \frac{1}{N_0}(|\alpha\rangle + |-\alpha\rangle) \tag{2.224}$$

$$= \frac{2}{N_0} e^{-|\alpha|^2/2} \sum_n \frac{\alpha^{2n}}{\sqrt{(2n)!}} |2n\rangle\,, \tag{2.225}$$

$$|\text{cat}\rangle_- = \frac{1}{N_\pi}(|\alpha\rangle - |-\alpha\rangle) \tag{2.226}$$

$$= \frac{2}{N_\pi} e^{-|\alpha|^2/2} \sum_n \frac{\alpha^{2n+1}}{\sqrt{(2n+1)!}} |2n+1\rangle\,. \tag{2.227}$$

If we want to write those states in a phase-space description, we have to adapt the normalization dependent on $\hbar$. This stems from the fact that the overlap between coherent states

changes depending on the chosen $\hbar$, as visible in eq. (2.186). With this re-normalization change in phase-space $N_\phi \to N_\phi^{x,p}$ we can express the wavefunction of a cat state as

$$\psi_{\text{cat},\alpha,\phi} = \frac{1}{N_\phi^{x,p}}(\psi_\alpha(x) + e^{i\phi}\psi_{-\alpha}(x)),$$
$$\text{where} \quad N_\phi^{x,p} = \sqrt{2(1+\cos(\phi)e^{-|\alpha|^2/\hbar})}. \tag{2.228}$$

If we assume $\alpha \in \mathbb{R}$, we find a simplified expression for the Wigner function

$$\mathcal{W}_{\text{cat},\alpha,\phi} = \frac{1}{(N_\phi^{x,p})^2}[\mathcal{W}_\alpha(x,p) + \mathcal{W}_{-\alpha}(x,p) + \hbar^2\mathcal{W}_0(x,p)\cos(\frac{p}{2\hbar x}\alpha - \phi)]. \tag{2.229}$$

We can see an even and odd cat state with an amplitude of $\alpha = 2$ in figures 2.7 and 2.8. We clearly see the two coherent states, that form those cats, appearing in the marginal position distribution, respectively sub-figures (d). The interference fringes between the coherent states shift with the phase-change of the cat state.

2.2.2.4 Gottesman-Kitaev-Preskill (GKP) states

Gottesman Kitaev and Preskill proposed the so-called GKP states in 2001 as a *qubit encoded in an oscillator* [80]. It therefore describes the use of an infinitely large system to encode a finite-size object in it. The infinitely large system they chose is the phase-space of bosonic modes, which in our case is the light mode and therefore the optical phase-space. Here, we focus on the case where one single bosonic mode is used to encode a n dimensional state space in it, with n eigenvectors that are defined as superpositions of position eigenvectors. Those position eigenvectors are spaced in regular multiples of $n\,\gamma$, where γ can be connected to a displacement amplitude, as we will see later. In this way, the ideal ("id") GKP basis states in position and momentum representation can be written as

$$|\text{GKP}_x^{id}\rangle = \sum_{s\in\mathbb{Z}} |x = \gamma(ns+k)\rangle\,, \tag{2.230}$$

$$|\text{GKP}_p^{id}\rangle = \sum_{s\in\mathbb{Z}} |p = \frac{2\pi\hbar}{n\gamma}(ns+k)\rangle\,, \tag{2.231}$$

where $k \in [0, n-1]$ switches between the n eigenvectors and $n \in \mathbb{N}^+$. For the most common case of $n = 2$, this system forms a qubit. For $n > 2$, a *qudit* is formed, where the "d" in qudit stands for the dimension n of the system.

Due to their regular spacing in both quadratures, those states therefore form a grid in phase-space such that their Wigner function can be written as a sum of two-dimensional Dirac peaks

$$\mathcal{W}_{GKP}^k(x,p) = \sum_{s,t=-\infty}^{\infty} (-1)^{st}\delta(p - \frac{\pi\hbar}{n\gamma}t)\delta(x - \frac{n\gamma}{2}s - \gamma k). \tag{2.232}$$

In eq. (2.230) and eq. (2.234) we clearly see, that the amplitude γ is connected to the displacement operator of eq. (2.178). If we calculate the effect of the displacement operator on $\hat{x}$ (and similarly for $\hat{p}$), we find

$$D^\dagger(\alpha)\hat{x}D(\alpha) = \hat{x} - \sqrt{2\hbar}\Re(\alpha) \tag{2.233}$$

such that we can rewrite equations (2.230) and (2.231) as

$$|\mathrm{GKP}_x^{id}\rangle = \sum_{s\in\mathbb{Z}} D((ns+k)\frac{\gamma}{\sqrt{2\hbar}})\,|x=0\rangle = \sum_{k\in\mathbb{Z}} D(\alpha(ns+k))\,|x=0\rangle\,, \tag{2.234}$$

$$|\mathrm{GKP}_p^{id}\rangle = \sum_{k\in\mathbb{Z}} D((ns+k)\frac{i2\hbar\pi}{n\gamma\sqrt{2\hbar}})\,|p=0\rangle = \sum_{k\in\mathbb{Z}} D(\beta(ns+k))\,|p=0\rangle\,, \tag{2.235}$$

such that $\alpha = \gamma/\sqrt{2\hbar}$ and $\beta = i2\hbar\pi/(n\gamma\sqrt{2\hbar})$. We learned that ideal GKP states are displaced position or momentum eigenstates. The displacement operator is most commonly used to define GKP states, which will become clear in section section 2.4.
The above-defined states have infinite energy and are thus un-normalizable and unphysical. In order to make the states physical, Gottesman Kitaev and Preskill proposed to approxi-

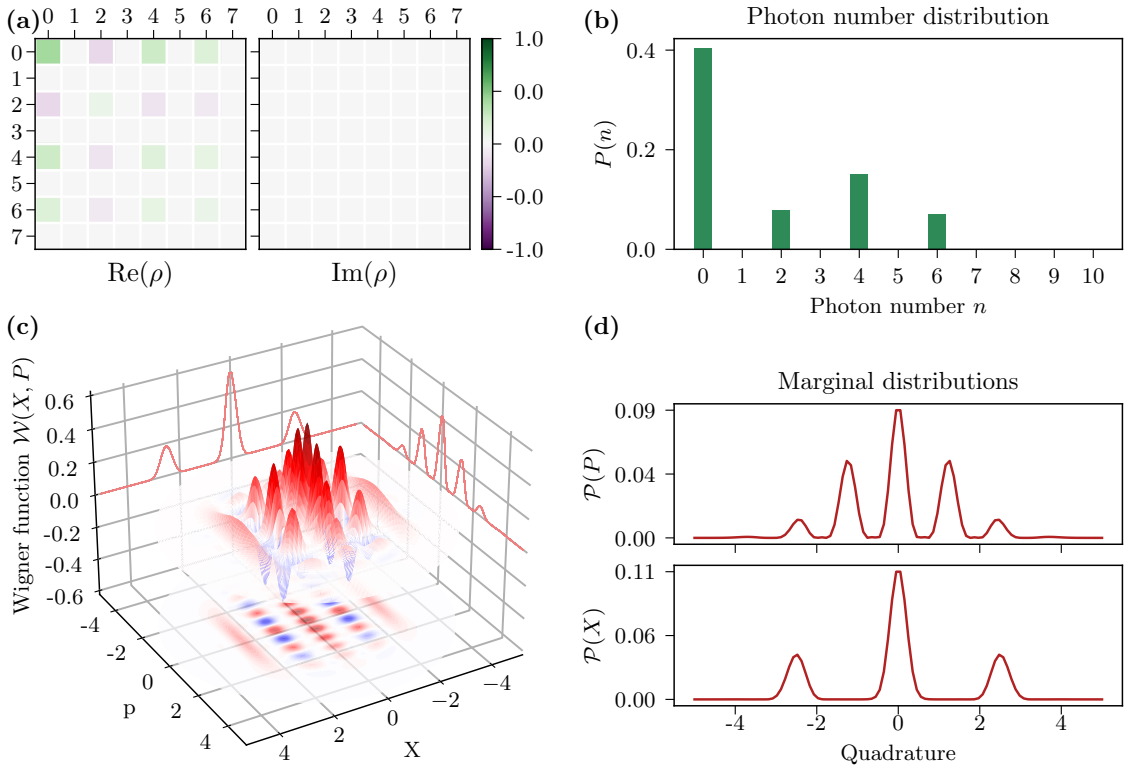

Figure 2.9: Properties of a logical 0 GKP state with with $\Delta = \kappa = 0.4$, $n = 2$ and $\gamma = \frac{2\pi\hbar}{n}$. Caption as in fig. 2.1.

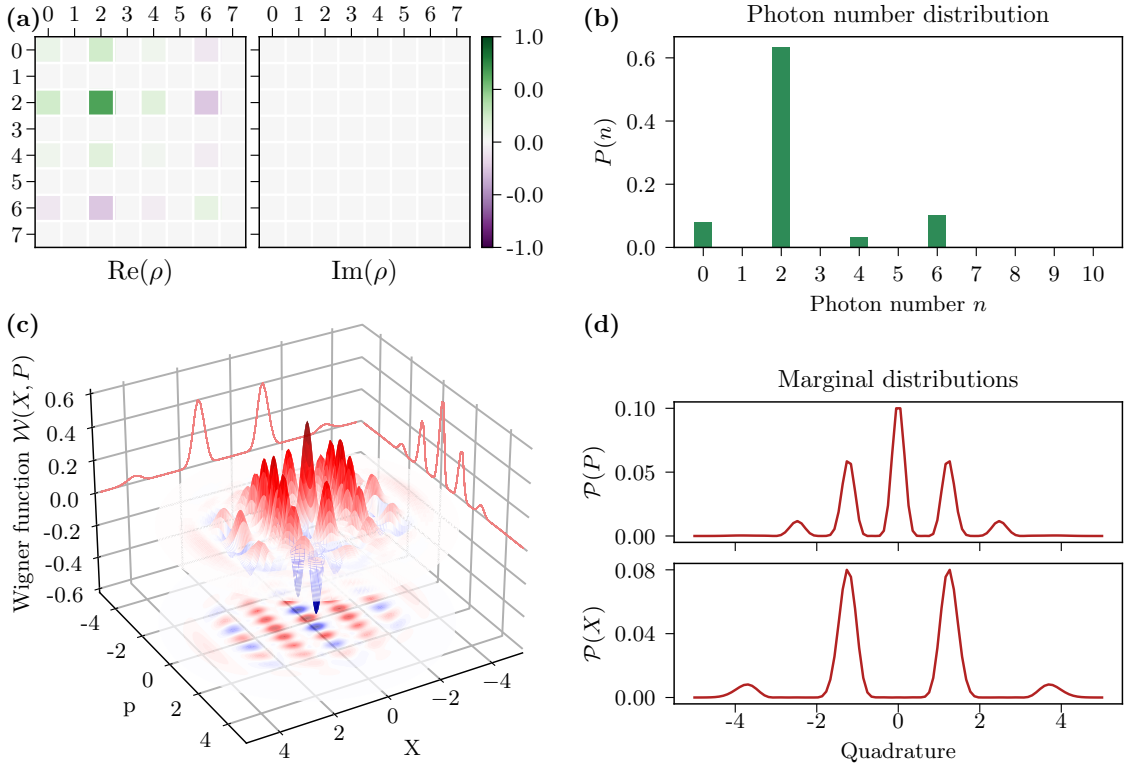

Figure 2.10: Properties of a logical 1 GKP state with with $\Delta = \kappa = 0.4$, $n = 2$ and $\gamma = \frac{2\pi\hbar}{n}$. Caption as in fig. 2.1.

mate the ideal GKP state as a sum of displaced squeezed states[11] with a Gaussian envelope of width κ^{-1} to truncate the summation, such that we arrive at the physical GKP states (here only written in the position representation)

$$|\text{GKP}^{\kappa}\rangle = N_k \sum_{s\in\mathbb{Z}} e^{-0.5(ns+k)^2\kappa^2\alpha^2} D(\alpha(ns+k))S(\xi)\,|0\rangle \tag{2.236}$$

where N_k is the normalization constant. We see that in the limit $(\xi, \kappa) \to (\infty, 0)$ the ideal GKP states are recovered. The definition of eq. (2.236) can also be written in terms of the position wavefunction [81, 82] as in

$$\psi^{\kappa,\Delta}_{GKP,k} = \frac{1}{\widetilde{N}_k} \int dx \sum_{s\in\mathbb{Z}} e^{-0.5(ns+k)^2\kappa^2\alpha^2} e^{-(x-\alpha(ns+k))^2/(n\hbar\Delta^2)} \psi(x), \tag{2.237}$$

where $\widetilde{N}_k$ is the normalization constant, κ the same as in eq. (2.236) and Δ^2 is connected to the squeezed variance of the position $\Delta^2 = e^{-2\Re(\xi)}\frac{\hbar}{2}$. GKP states are promising states for quantum error correction, which we will sketch in subsection section 2.4. For the choice

[11] Here, squeezing should approximate a Dirac peak in the quadrature the state is formulated in, corresponding to infinite squeezing.

of $\gamma = \frac{2\pi\hbar}{n}$ such that $\alpha = \sqrt{\pi/n} = i\beta$ we can observe a grid structure where the momentum has half the spacing of the position quadrature, which enables equal correctability of errors in position and momentum. Those states are called *square GKP states* and are depicted in fig. 2.9 and fig. 2.10 for $\kappa = \Delta = 0.2$ and $n = 2$.
The analytical Wigner function and marginal distribution of the GKP states was calculated by L. García-Álvarez for any superposition of the two ideal GKP basis states [83]. For approximate GKP states the analytical Wigner function is rather complicated and does not provide more insight than the ideal GKP Wigner function, such that we omit it here.

2.2.3 Take-away message

Here we have presented the usual states used in quantum optics.
For Gaussian states:

- Vacuum has symmetric and minimal uncertainty. Shot noise theoretically is the photon-number fluctuation of a state and practically also includes electrical noise. Vacuum has minimal shot noise and is used to calibrate our setup.
- Coherent states have symmetric and minimal uncertainty and an amplitude α. They are vacuum states, which have been displaced by the amplitude α. The displacement can be cast into an operator, the displacement operator.
- Two coherent states are not necessarily orthogonal to each other.
- Thermal states have symmetric but not minimal uncertainty.
- Squeezed states have minimal uncertainty but are not symmetric. In this way, one quadrature can be measured more precisely than the other. Any coherent state can be squeezed but we use squeezed vacuum in our setup. The squeezing can be quantified in decibels.

For non-Gaussian states

- Fock states have negative Wigner functions and are symmetric around the phase-space origin.
- Many non-Gaussian states are formed by superpositions of Gaussian states. Allowing for any phase and weights between those superpositions creates a qubit.
- Qubits are defined via the Pauli matrices and can be described by a Bloch sphere.
- Cat states are superpositions of orthogonal coherent states. This superposition creates interference between the coherent states.
- Gottesmann-Kitaev-Preskill states are ideal superpositions of position (or momentum) eigenstates. Those states are unnormalizable and therefore unphysical. They are approximated by a superposition of displaced squeezed states.

Now that we've covered various properties of Gaussian and non-Gaussian states, let's delve deeper into the distinction between Gaussianity and non-Gaussianity when it comes to operations.

2.3 Operations in quantum optics

Let us now define what operations and measurements we can apply to states. We have already established, that any operation can be written as a Wigner function in the subsection subsection 2.1.3. Consequently not only states can be non-Gaussian - operators can have this property too. If an operation is Gaussian or non-Gaussian can be easily judged by their generating Hamiltonian: Gaussian operation have a Hamiltonian that is maximally *quadratic* in the position and/or momentum operator. For measurements, one can determine their (Non-)Gaussianity via a threshold (as explained in the subsection subsection 2.1.5). In practice, the non-Gaussian measurements we are presenting, are easily identifiable as non-Gaussian via their proximity to known non-Gaussian states. In the following, we will discuss Gaussian and non-Gaussian operations and measurements. While experimentally we make use of almost all Gaussian operations and measurements, the non-Gaussian operations are notoriously hard to implement. This is why we use non-Gaussian measurements only in the experiment. We choose to show the non-Gaussian operations for completeness.

2.3.1 Gaussian gates

Here we will give a list[12] of Gaussian operators, that are relevant for optics. Some operations have already been introduced in section 2.2. In fig. 2.11 (a)-(d) the action of all single-mode Gaussian operations we will discuss here on the Wigner function of an exemplary state is shown.

2.3.1.1 The displacement operator

We have already seen the displacement operator appear in eq. (2.178) as the generator of coherent states. We recall its definition:

$$D(\alpha) = e^{\alpha\hat{a}^\dagger - \alpha^*\hat{a}} \tag{2.238}$$

$$= e^{i\sqrt{\frac{2}{\hbar}}(\Im(\alpha)\hat{x} - \Re(\alpha)\hat{p})} \tag{2.239}$$

A displacement operator shifts the center of any state in phase-space by the amplitude α, which is a complex number and therefore can span the two dimensions x and p of phase-space.

[12] No claim of completeness is made here.

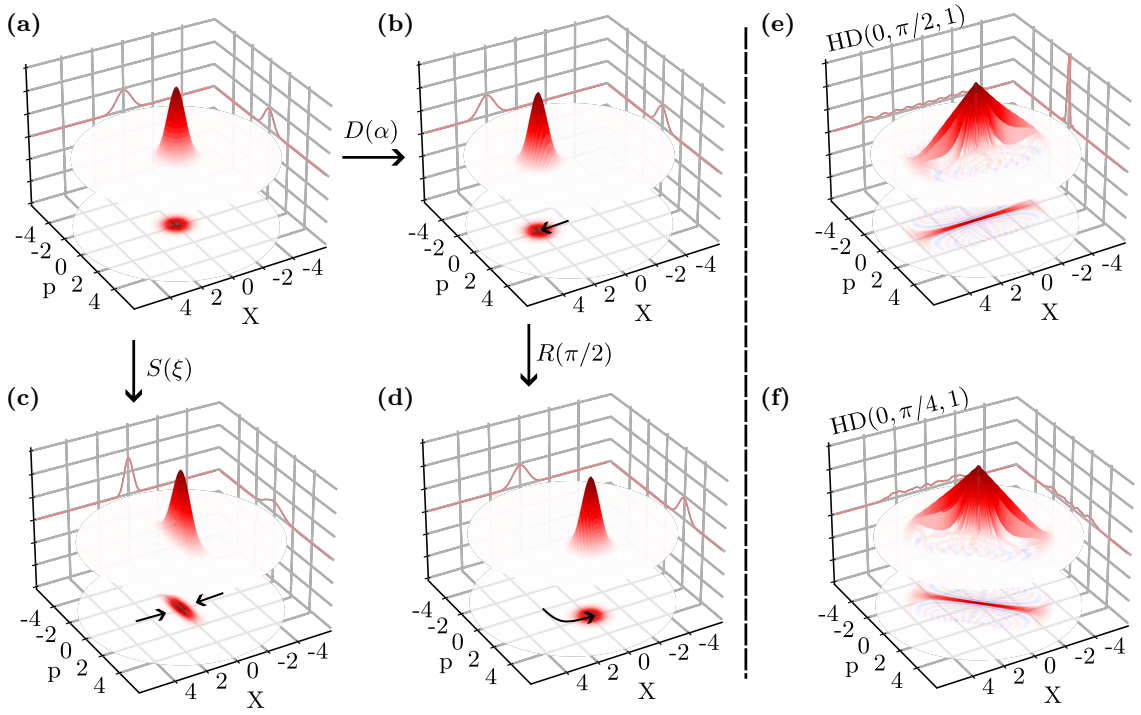

Figure 2.11: In **(a)** a vacuum state is shown. In **(b)** this vacuum state is displaced by the displacement operator $D(\alpha)$ with $\alpha = 2$. The action of a squeezing operator $S(\xi)$ on vacuum, with a squeezing of 5 dB, is shown in **(c)**. In **(d)** the rotation operator $R(\phi)$ with $\phi = \pi/2$, giving a Fourier gate, is applied to the displaced state of (b). In **(e)** and **(f)** the Wigner functions of the homodyne projectors $\mathrm{HD}(x, \phi, \eta)$ are shown for $x = 0$ and $\eta = 1$ for the two angles $\phi = \pi/2$ in (e) and $\phi = \pi/4$ in (f). We note that the slight negativities that appears in those two plots are parasitic and due to finite size effects. The homodyne measurements were normalized before plotting.

Such a shift is visible in fig. 2.11 (a) to (b) for a shift of $\alpha = 2$. This operator has the following properties:

$$D^\dagger(\alpha) = D(-\alpha), \tag{2.240}$$

$$D^\dagger(\alpha)\hat{a}D(\alpha) = \hat{a} + \alpha, \tag{2.241}$$

$$D^\dagger(\alpha)\hat{a}^\dagger D(\alpha) = \hat{a}^\dagger + \alpha^*, \tag{2.242}$$

$$D(\alpha + \beta) = D(\alpha)D(\beta)e^{-i\Im(\alpha\beta^*)}, \tag{2.243}$$

$$D(\beta)D(\alpha) = e^{\beta\alpha^* - \beta^*\alpha}D(\alpha)D(\beta). \tag{2.244}$$

The displacing property of this operator can be seen in eq. (2.241) and eq. (2.242), where its action on creation and annihilation operator corresponds to a shift in phase-space, dependent on the amplitude α. In eq. (2.243) we see that the product of two displacement operations is a new displacement operator, equivalent to their summed-up displacement amplitude $\alpha + \beta$. The global phase factor is not measurable and therefore irrelevant here. If one wants to swap the causal order of the two displacement operators in eq. (2.243), another global phase factor appears, as visible in eq. (2.244). This equation can be used to

define the commutator relation of displacement operators in section section 2.4.
The displacement operator's action in the phase-space can be calculated with the help of eq. (2.157) as

$$D^\dagger(\alpha)\hat{x}D(\alpha) = \hat{x} - \sqrt{2\hbar}\Re(\alpha) \qquad D^\dagger(\alpha)\hat{p}D(\alpha) = \hat{p} - \sqrt{2\hbar}\Im(\alpha). \tag{2.245}$$

To displace a state, whose analytical Wigner formula is known, one therefore only needs to replace each x by $x - \sqrt{2\hbar}\Re(\alpha)$ (and similarly for p). Instead of applying the operation on each individual state, this approach can be used on all states, whose Wigner function is known.

However, if there exists no analytical Wigner function, then the displacement operator is often used on density matrices. For this we need to write $D(\alpha)$ in the Fock basis, the question is therefore how to write this operator as a matrix. For this, we remark that the annihilation and creation operators can be written as matrices

$$\hat{a} = \begin{bmatrix} 0 & \sqrt{(0+1)} & 0 & 0 & ... \\ 0 & 0 & \sqrt{(1+1)} & 0 & ... \\ 0 & 0 & 0 & \sqrt{(2+1)} & ... \\ 0 & 0 & 0 & 0 & ... \\ ... & ... & ... & ... & ... \end{bmatrix}. \tag{2.246}$$

This means that the displacement operator can be written as an exponential, whose argument is a matrix. To write this as a matrix, we can either perform a Taylor expansion of the exponential or (more conveniently) use the fact, that the exponential of any diagonal matrix can be obtained by exponentiating each entry on the main diagonal. Because this principle will be used many times it is quickly drafted here.

Let e^X be the operator you want to write as a matrix and let X be a diagonalizable matrix [13]. Then you can first diagonalize X via its eigen-decomposition such that $X = UDU^{-1}$ where U is the unitary matrix incorporating the basis change and D is the diagonalized version of the original matrix. We can then proceed to write $e^X = Ue^DU^{-1}$. Luckily, the coding language *python* with its in-build functions, makes this computation very easy and fast.

We have already discussed in subsubsection 2.1.2.1, that the dimension of the density matrix has to be adapted to the maximal Fock excitation in the system. This argument carries over to the Fock representation of operations, where here the maximal excitations are determined

[13] All matrices X such that $X^*X = XX^*$ (normal matrices) are diagonalizable, thereby including hermitian matrices.

by α. Note that a displacement (seen as a POVM) is not pure and as such is not a projective measurement. If we view the displacement as a POVM, then each α corresponds to a different POVM element. We know that two amplitudes α and α' can create states, that are not orthogonal (eq. (2.185)). Consequently, there are more than N^2 POVM element displacement operators than orthogonal states in a system of size N.

2.3.1.2 The squeezing operator

Another operator we have already seen is the squeezing operator defined in eq. (2.204) where we set $\xi = re^{i\phi}$. It squeezes the standard deviation of the quadratures while preserving the Heisenberg uncertainty, the state had before the squeezing operation. In fig. 2.11 (a) to (c) we can see such a squeezing applied to a vacuum state. This squeezing of 5 dB decreased the uncertainty of the momentum quadrature, at the cost of increasing the uncertainty of position. The squeezing operator has the following properties

$$S(\xi)S^\dagger(\xi) = S^\dagger(\xi)S(\xi) = \mathbb{1}, \tag{2.247}$$

$$S^\dagger(\xi)\hat{a}S(\xi) = \cosh(r)\hat{a} - e^{i\phi}\sinh(r)\hat{a}^\dagger, \tag{2.248}$$

$$S^\dagger(\xi)\hat{a}^\dagger S(\xi) = \cosh(r)\hat{a}^\dagger - e^{-i\phi}\sinh(r)\hat{a}. \tag{2.249}$$

As for the displacement, its matrix is unitary, visible in eq. (2.247). The action of the squeezing operator on the annihilation and creation operator is visible in eq. (2.248) and (2.249). The action of the squeezing operator is most intuitive in its transformation of the phase-space coordinates

$$S^\dagger(\xi)\hat{x}S(\xi) = \cosh(r)\hat{x} - \sinh(r)[\cos(\phi)\hat{x} + \sin(\phi)\hat{p}], \tag{2.250}$$

$$S^\dagger(\xi)\hat{p}S(\xi) = \cosh(r)\hat{p} + \sinh(r)[\cos(\phi)\hat{p} - \sin(\phi)\hat{x}], \tag{2.251}$$

such that we can also write the squeezing operator in terms of position and momentum:

$$S_\xi(x,p) = \exp[\frac{1}{2\hbar}[ir\sin(\phi)\hat{x}^2 - r\cos(\phi)\hat{p}^2 - r\cos(\phi)(\hbar - 2i\hat{x}\hat{p})]. \tag{2.252}$$

If one wants to write the squeezing as a matrix in the Fock basis, the matrix diagonalization method that we already explained in the last subsubsection, can be used. As for the displacement, we do not write this matrix explicitly because its dimension cut-off depends on ξ.

2.3.1.3 The Fourier and rotation gate

The rotation gate is defined as

$$R(\phi) = e^{i\phi\hat{n}} = e^{\frac{i}{2\hbar}\phi(\hat{x}^2+\hat{p}^2-\hbar\mathbb{1})}, \tag{2.253}$$

such that it rotates the quadrature operators anticlockwise in phase-space:

$$R^\dagger(\phi)\hat{x}R(\phi) = \cos(\phi)\hat{x} - \sin(\phi)\hat{p}, \tag{2.254}$$

$$R^\dagger(\phi)\hat{p}R(\phi) = \cos(\phi)\hat{p} + \sin(\phi)\hat{x}. \tag{2.255}$$

For $\phi = \pi/2$ this gate is called *Fourier gate*. Its action on a displaced state is visible in fig. 2.11 (b) to (d), where the displaced state is rotated. If one wants to write the Fourier (or rotation) gate as a matrix in the Fock basis, the matrix diagonalization method that we already explained in the last subsubsection, can be used. In fact its transformation on the state $|\phi\rangle$ of dimension N can be written as

$$|\phi\rangle = \sum_k^{N-1} c_k |k\rangle \xrightarrow{R(\pi/2)} \sum_k^{N-1} \left[\frac{1}{\sqrt{N}} \sum_j^{N-1} c_j \omega_N^{k\,j} \right] |k\rangle\,, \qquad \omega_N = e^{i2\pi/N}. \tag{2.256}$$

We see that this gate performs a discrete Fourier transform on the coefficients c_k [84].

2.3.1.4 Beamsplitter operation

The beamsplitter acts on the physical mode of the state, splitting it into two different paths for which we use two different creation and annihilation operators $\hat{a}, \hat{a}^\dagger$ and $\hat{b}, \hat{b}^\dagger$. Its operator is

$$\mathrm{BS}(\theta,\phi) = \exp[\theta e^{i\phi}\hat{a}\hat{b}^\dagger - \theta e^{-i\phi}\hat{a}^\dagger\hat{b}], \tag{2.257}$$

$$\text{with} \quad t = \cos(\theta) \quad \text{and} \quad r = e^{i\phi}\sin(\theta) \quad |r|^2 + |t|^2 = 1. \tag{2.258}$$

Here r and t are the reflective and transmittive amplitude of the beamsplitter: if $R = |r|^2 = 1$ then the beamsplitter is a mirror if $T = |t|^2 = 1$ it does nothing to the input mode. The phase ϕ corresponds to the phase of the reflective coating of the beamsplitter. We can now formulate the effect on the two modes

$$\mathrm{BS}(\theta,\phi)^\dagger\hat{a}\mathrm{BS}(\theta,\phi) = t\hat{a} - r^*\hat{b}, \tag{2.259}$$

$$\mathrm{BS}(\theta,\phi)^\dagger\hat{b}\mathrm{BS}(\theta,\phi) = t\hat{b} + r\hat{a}. \tag{2.260}$$

For the quadratures we find

$$\mathrm{BS}(\theta,\phi)^\dagger \hat{x}_a \mathrm{BS}(\theta,\phi) = \cos(\theta)\hat{x}_a - \sin(\theta)[\cos(\phi)\hat{x}_b + \sin(\phi)\hat{p}_b], \tag{2.261}$$

$$\mathrm{BS}(\theta,\phi)^\dagger \hat{p}_a \mathrm{BS}(\theta,\phi) = \cos(\theta)\hat{p}_a - \sin(\theta)[\cos(\phi)\hat{p}_b - \sin(\phi)\hat{x}_b], \tag{2.262}$$

$$\mathrm{BS}(\theta,\phi)^\dagger \hat{x}_b \mathrm{BS}(\theta,\phi) = \cos(\theta)\hat{x}_b + \sin(\theta)[\cos(\phi)\hat{x}_a - \sin(\phi)\hat{p}_a], \tag{2.263}$$

$$\mathrm{BS}(\theta,\phi)^\dagger \hat{p}_b \mathrm{BS}(\theta,\phi) = \cos(\theta)\hat{p}_b + \sin(\theta)[\cos(\phi)\hat{p}_a + \sin(\phi)\hat{x}_a]. \tag{2.264}$$

The beamsplitter is very useful to model losses, which are then equivalently expressed as the efficiency of a path η, with $1-\eta = R$. The phase ϕ is dependent on the coating on the reflective port of the beamsplitter and is usually set to π or $\pi/2$ for energy conservation.

2.3.1.5 Controlled gates

Controlled gates [85] refer to gates that act on two modes, where one mode is unchanged and functions as a "control" mode that determines if a gate is applied to the second mode. The most common controlled gates are the controlled X-gate and controlled phase-gate. The controlled X-gate is also called the sum gate as it acts in the position basis as follows

$$\mathrm{CX}(s)\left|x_a, x_b\right\rangle = \left|x_a, x_b + s x_a\right\rangle. \tag{2.265}$$

We can see here, that mode a is left unchanged, while mode b is displaced in dependence of x_a. The controlled phase-gate acts as

$$\mathrm{CZ}(s)\left|x_a, x_b\right\rangle = e^{i s x_a x_b/\hbar}\left|x_a, x_b\right\rangle, \tag{2.266}$$

such that the global phase of the state is changed. We do not use those gates experimentally as they are very hard to implement.

2.3.2 The Gaussian measurements: Homodyning

In optics, the most commonly used Gaussian measurement is the homodyne detection. It will be discussed experimentally in chapter 3 and chapter 4. Here we will rather focus on its measurement operator, given by

$$\mathrm{HD}(x,\theta) = \left|x,\theta\right\rangle\left\langle x,\theta\right| \tag{2.267}$$

$$\left|x,\theta\right\rangle = \left\langle x_\theta | n\right\rangle = e^{in\theta}(\sqrt{\pi\hbar}\, 2^n\, n!)^{(-1/2)} e^{-x^2/(2\hbar)} H_n(\frac{x}{\sqrt{\hbar}}), \tag{2.268}$$

which is eq. (2.134) with the quadrature x_θ. We can account for an imperfect detection efficiency η, by applying a beamsplitter operation, called Bernoulli transformation B. The resulting homodyne POVM elements can be written as

$$\Pi_\eta(x,\theta) = \sum_{m,n,i} B_{m+i,m}(\eta)\, B_{n+i,n}(\eta)\, \mathrm{HD}(x,\theta)\, |n+i\rangle \langle m+i|\,, \tag{2.269}$$

$$B_{m+i,m} = \sqrt{\binom{m+i}{m}\eta^m(1-\eta)^i}. \tag{2.270}$$

We can therefore interpret this measurement as sampling from the marginal distribution along x_ϕ of the Wigner function. This is also an intuitive way of seeing why it is a Gaussian measurement: It projects the state onto a positive, classical probability distribution. The Wigner functions of two measurement settings with $\mathrm{HD}(x=0,\phi,\eta=1)$ are shown for $\phi=\pi$ in fig. 2.11 (e) and $\phi=\pi/2$ in (f). The measurement operator is un-normalized and for $\eta=1$ corresponds to a position eigenstate.

Naturally, this measurement can be used to reconstruct the Wigner function, which we will also see in chapter chapter 3 as our main technique. Being a position eigenstate, this measurement is a pure POVM, and therefore a projection.

We note that a second common measurement is called heterodyning, which we will not discuss here.

2.3.3 Non-Gaussian gates

There exist many non-Gaussian operations. What they have in common is that their generating Hamiltonian is at least *cubic in the position and/or momentum operator*. This can be intuitively understood when remembering the Gaussian Wigner function, showing at most quadratic polynomials of the position and momentum operator. Any of those gates are experimentally extremely challenging, which is why Non-Gaussianity is rather achieved through measurements, as we will see in subsection 3.2.3 and subsection 3.2.4.
In fig. 2.12 (a)-(c) the action of the two non-Gaussian operations presented here are shown.

2.3.3.1 The cubic phase gate

One of the most famous gates with cubic polynomials of the position is the cubic phase gate, which is often proposed for universal quantum computation. Its operator is

$$C(\gamma) = e^{\frac{i}{3\hbar}\gamma\hat{x}^3} \tag{2.271}$$

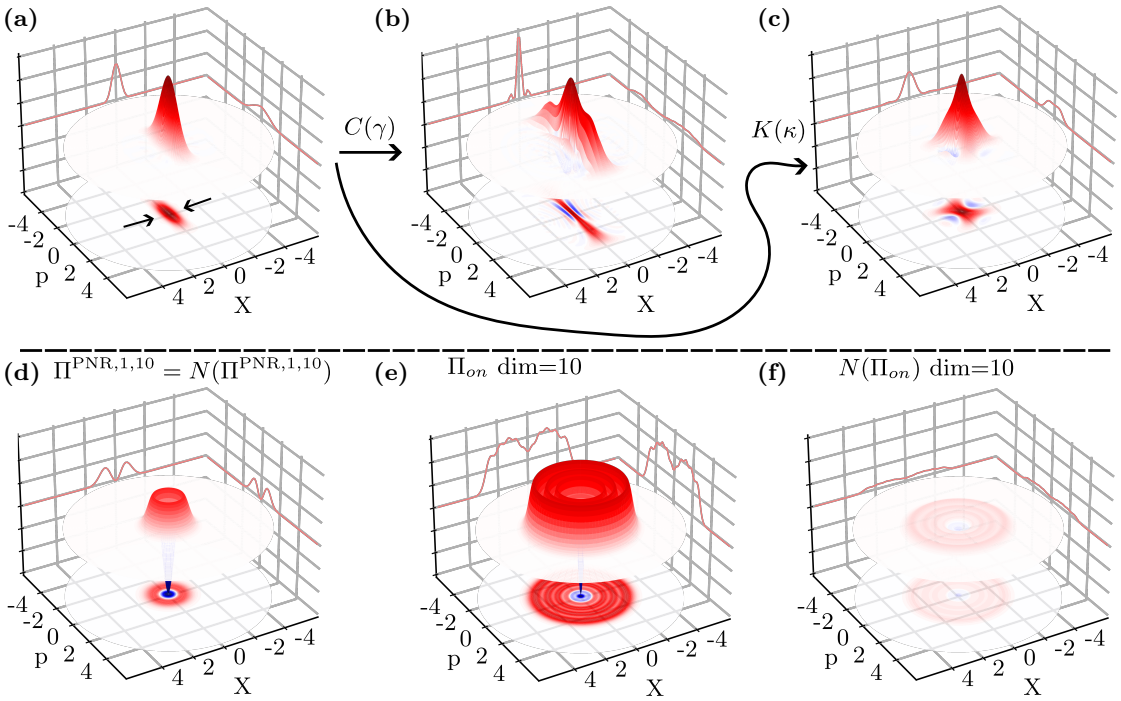

Figure 2.12: In **(a)** a squeezed state with 5 dB of squeezing is shown. In **(b)** the action of a cubic phase gate with $\gamma = 21$ on this state is shown, while in **(c)** a Kerr gate of strength $\kappa = 0.4$ is shown. The Fock dimension of all operations and states is set to 20. In **d** the photon number resolution (PNR) single click element is shown with no losses. This corresponds to the Wigner function of a single photon. In **(e)** the POVM "on" element is shown for no losses. In **(f)** we have artificially normalized $N(\Pi)$ the POVM "on" element. This shows the action of this measurement if all Fock states from $|0\rangle$ to $|10\rangle$ are present in the system to be measured. Note that this can of normalizing has no influence on (d).

and acts on annihilation, position, and momentum operators as follows

$$C(\gamma)^\dagger \hat{a} C(\gamma) = \hat{a} + \frac{\gamma}{2\sqrt{2/\hbar}}(\hat{a} + \hat{a}^\dagger)^2, \tag{2.272}$$

$$C(\gamma)^\dagger \hat{x} C(\gamma) = \hat{x}, \tag{2.273}$$

$$C(\gamma)^\dagger \hat{p} C(\gamma) = \hat{p} + \gamma \hat{x}^2. \tag{2.274}$$

It changes the momentum dependent on the quadratic position and can create coherences. Its action on a squeezed state is shown in fig. 2.12 (a) to (b) for $\gamma = 21$, where we see negativities appearing.

2.3.3.2 The Kerr gate

The Kerr gate describes the effect of a χ^3 non-linearity, which will be introduced in subsection 3.1.2. This gate changes already existing coherences but does not affect states that are diagonal in the Fock basis. Its operator is written as

$$K(\kappa) = e^{i\kappa\hat{n}^2} = e^{i\kappa(\hat{x}^2+\hat{p}^2-\hbar\mathbb{1})^2/(4\hbar^2)} \tag{2.275}$$

and changes the annihilation operator as follows

$$K^\dagger(\kappa)\hat{a}K(\kappa) = \hat{a}e^{i\kappa(2\hat{a}^\dagger\hat{a}-1)}. \tag{2.276}$$

Its action on a squeezed state is shown in fig. 2.12 (a) to (c) for $\kappa = 0.4$. We note that the cross-Kerr gate also exists, acting on two modes instead of one mode, such that $\hat{n}^2 \to \hat{n}_1\hat{n}_2$.

2.3.4 Non-Gaussian measurements

The most used non-Gaussian measurement is a projective measurement on the Fock basis. For this we can first introduce on-off detectors and then proceed to its idealized extension, the photon-number-resolving detector. Here we choose to focus on the theory and discussion their implementation in chapter 3 and section 4.2.

2.3.4.1 On-off detectors

On-off detectors are also called bucket detectors as they cannot distinguish between different excitations/Fock states. They detect the existence of photonic energy and therefore give binary outputs 0 for *no photon* and 1 for *some number of photons*. They therefore have two POVM elements, Π^{off} if the output is 0 and Π^{on} if the output is 1. The detection, corresponding to the POVM "on" element, can be written as

$$\Pi^{\text{on}} = \sum_n (1-(1-\eta)^n)\,|n\rangle\langle n|\,, \tag{2.277}$$

where η is the measurement efficiency. Here only diagonal elements exist. Depending on the efficiency, the on-off detector has a higher probability of detecting higher-order Fock states. If $\eta = 1$ we can see that the probability for this measurement to detect any Fock state is equal. This can be seen in fig. 2.12 (e) and (f). In (e) the Wigner function of the POVM "on" element up to dimension 10 is plotted. We can see the maximal negativity of this measurement. This negativity stems from the fact that POVM elements are not normalized, which means that we are plotting the sum of the Fock states $n = 1 - 9$. To see why this is problematic we can (somewhat artificially) normalize Π^{on}, which is visible in (f). We observe that this Wigner function only has faint negativities. This illustrates the problem of this measurement if an equally weighted superposition $\sum_{n=1}^{9}|n\rangle$ is measured. The state is

projected onto a full mixture of all its Fock states, losing any coherences. Moreover, this case is indistinguishable from measuring a single photon. We, therefore, need a good estimation of the states traveling in our experimental setup, to use this measurement faithfully.

2.3.4.2 Photon number resolving detectors (PNRD)

It can be beneficial to be able to distinguish photon numbers in the detection. This can be theoretically described as *multiplexing* on-off detectors [86, 87], which gives the operator

$$\Pi^{PNR,s,N} = \sum_n p(s|n,N,\eta)\,|n\rangle\langle n|\,, \tag{2.278}$$

$$p(s|n,N,\eta) = \sum_{p=0}^{s} \binom{p}{s-p} \binom{N}{p} \sum_{j=0}^{p} \binom{p}{j} (-1)^{p-j} (1-\eta-\frac{j}{N}\eta)^n, \tag{2.279}$$

where $p(s|n,N,\eta)$ is the probability to detect s photons if n photons are impinging on the detector, that is multiplexed with N on-off detectors that each have an efficiency of η. For $\eta \to 1$ and $N \to \infty$ this becomes the perfect photon number resolving detector, where each POVM element is the perfect projection onto one Fock state. Note that this POVM has $N+1$ elements, corresponding to the detector clicking s times. This detector will become important in chapter 4 and chapter 7.

2.3.5 Take-away message

Here we have discussed Gaussian and non-Gaussian operations that are typical for quantum optics.
For Gaussian gates and measurements:

- Single-mode Gaussian operations are displacement, squeezing, and rotation gates. In our experiment, we implement the first two.
- Two-mode Gaussian operations are the beamsplitter operation and controlled gates. In our experiment, we use the beamsplitter. In simulations, it can model losses.
- The typical Gaussian measurement is homodyne detection. It corresponds to the measurement of a quadrature operator. Scanning over the phase of this quadrature gives a data set that can be used to reconstruct the measured state.

For non-Gaussian gates and measurements:

- Non-Gaussian operations have to have a generating Hamiltonian that is at least cubic in the position or/and momentum operator.
- Non-Gaussian single-mode gates are the cubic phase gate and the Kerr gate. We do not implement those experimentally.
- Non-Gaussian two-mode gates are the cross-Kerr gate. We do not implement it experimentally.
- Typical non-Gaussian measurements are on-off detectors and photon number resolving detectors. We use the former experimentally. Those two detectors are not mode-selective.

We have developed the differences between Gaussian and non-Gaussian states and measurements. In the next section, we will elaborate, on why this is not only of theoretical interest but has real relevance in the application of quantum mechanics.

2.4 The benefits of Non-Gaussianity

In this section, we will finally argue, why we are interested in creating and measuring non-Gaussian states. The two main arguments lie in the computational advantage and error correctability of quantum systems. While computational advantage needs Non-Gaussianity (or Non-Clifford operations), error correction codes try to work with only Gaussian (or Clifford) operations, which are easier to implement. This sets the stage for arguing why Bosonic qubits, which are inherently non-Gaussian and, if chosen well, error correctable with Gaussian operations, are good candidates for computation and error correction. Creating bosonic qubits adapted to those tasks is challenging in any physical platform, including photonics. In chapter 3 and chapter 4, experimental states are presented that are bosonic qubits, but do not yet fulfill all requirements to be usable in the computational context. In chapter 7 we will discuss how GKP states could be created with our experimental platform, which is why we lay a large focus on their working principle here.

2.4.1 Computational advantage and Non-Gaussianity

Quantum information is envisioned to improve security for communication and to enable considerable speed-ups in calculations that can make use of parallelization. Even though there are many different ways in which one can analyze or try to establish those benefits there are a few no-go theorems that draft the broader idea. It has been shown that improving the transmission of Gaussian states in a Gaussian channel with Gaussian error correction is impossible [88]. Usually, noise in the transmission is assumed to be Gaussian too, such that either the states or the error-correction operations have to be non-Gaussian for error correction to work. In the field of quantum computation, a similar result exists: either the measurements or the input states have to be non-Gaussian to obtain a computational advantage over classical computers [89–91].

The group of all Gaussian gates is called the *Clifford group* and can be represented by the displacement gate, squeezing gate, Fourier gate, and the beamsplitter [92], which reduces to the minimal set of Clifford gates for a single mode: displacement and squeezing, which is consistent with our Wigner function analysis. If only those gates are used, the quantum computation is proven to be *efficiently simulatable on a classical computer* which is the usual definition of a computation being *not quantum*. If we add for example the cubic phase gate with only one allowed value of γ, we already reach universal quantum computation. As those gates are hard to get by, many proposals envision so-called measurement-based quantum computation, where all measurements are Gaussian and either then the input states have to be non-Gaussian [90].

We emphasize, that even though we are focusing here on bosonic encodings, the same challenges are faced by quantum computers utilizing two-level systems, or qubits. There, the Clifford group is defined as the Hadamard gate, phase gate S, and $CNOT$ gate. The Hadamard gate can be defined via the Pauli matrices as $H = \frac{1}{\sqrt{2}}(X + Z)$ and as such performs a basis change rotation on the Bloch sphere. The phase S gate can be expressed as the n-th root of the Pauli Z gate. The $CNOT$ gate carries the same idea as our two-mode gates, such that the bit flip of the second qubit is conditioned on the state the first qubit is in. To achieve universal quantum computation with qubits, a non-Clifford gate has to be added and there are many candidates like the qubit version of the controlled phase gate or a rotation gate [93]. For bosonic encodings, a promising candidate is non-linear feed-forward [94].

2.4.2 Error correctability

If one wants to use a physical system as a carrier of information, it is important to verify that the information will not be altered by the environment, i.e., that no *error* occurred. Let us quickly review concepts of "good" classical bits to generalize them to the quantum case.
For the review of classical and quantum error correction we mostly use "Quantum computation and quantum information" by M. Nielsen and I. Chuang [84], together with the article "Introduction to Quantum Error Correction and Fault Tolerance" by S. Girvin [95].

2.4.2.1 Classical error correction

Classical information is stored in bits, meaning that we only have two logical ("L") bits 0_L and 1_L but do not allow superposition between them. For bits, there are two types of errors

- Bit-flip error: $0_L \to 1_L$ or $1_L \to 0_L$
- Loss/erasure error: $0_L \to$ or $1_L \to$.

Bits are usually encoded in the physical system as two discrete voltages, where the higher voltage represents the 1 state. In classical systems, the bit-flip error is considered the main error. The loss-error will become more important in the quantum case. The error rate of the bit-flip is considered to be symmetric $\epsilon = p_{01} = p_{10}$. An error correction code means to define a logical basis, consisting of physical bits, in which a certain set of errors can be detected and corrected via operations on the physical bits.

The easiest is the repetition code, in which three physical bits are used to encode one logical bit $0_L = \{000\}$, $1_L = \{111\}$. The additional bits (2 in this case) are called *ancilla bits*. The detection of errors is done via measurement of each physical bit. If we express the bit as a density matrix this measurement is equivalent to $\mathrm{Tr}[Z\rho_{0,1}]$, where X is the Pauli Z-gate in the physical basis we choose. We therefore obtain results ± 1, define an

error detection as a majority vote, and can correct a detected error by applying a Pauli X-gate. If more than one error occurs in the system the majority is wrong and the error correction fails. We can nicely see here that adding ancillas to the system increases the error probability as we now have to write

$$\text{Probability of no error} \quad p_0 = (1-\epsilon)^3 \tag{2.280}$$

$$\text{Probability of one error} \quad p_1 = 3\epsilon(1-\epsilon)^2 \tag{2.281}$$

$$\text{Probability of two error} \quad p_2 = 3\epsilon^2(1-\epsilon) \tag{2.282}$$

$$\text{Probability of three error} \quad p_3 = \epsilon^3 \tag{2.283}$$

such that the probability of at least one error is $1-p_0 \approx 3\epsilon$ for small ϵ. Therefore by defining three physical bits as one logical bit, the logical bit error [14] probability got worse and therefore our error correction needs to be able to push the logical bit error below ϵ, otherwise there is no use for the ancillae. As we can only correct a single logical error (corresponding to the probability of one error), the logical error is $\epsilon_L = p_2 + p_3 = 3\epsilon^2 - 3\epsilon^3$. In our case, this works if we hit the physical error probability $\epsilon^* = 0.5$, where $\epsilon_L = \epsilon$, which is called the *break-even point of error correction*. If $\epsilon < \epsilon^*$, error correction decreases the errors, if $\epsilon > \epsilon^*$ it makes things worse. In this simple example, we see that the main idea in classical error correction is redundancy and this intuition will be carried over to the quantum regime.

The repetition code is very inefficient which can be seen by computing the minimal redundancy needed to correct for n errors [95]. Imagine we have M data bits that we want to protect by adding R ancillary bits. In total, there are $N = M + R$ possible single-bit errors and a total of $M + R + 1$ so-called error states (including no error). Error states are the states after any possible error occurred. Not being able to encode them would be equivalent to not being able to detect them, as they would leave the code space, i.e. would be lost. This means that there have to be enough ancillary bits R such that their state space is at least as big as the number of error states. As a bit has two possible states per ancillary bit, we can write

$$2^R \geq M + R + 1. \tag{2.284}$$

Imagine $R = 10$, then we should be able to maximally protect $M = 1013$ states against a single bit flip. Until now, we have assumed only the error of the physical bit but of course, any gates applied to those bits to measure or correct can also introduce errors. The break-even point is therefore a purely mathematical property of the code-space and needs to be paired with gates that do not add uncorrectable errors to the circuit.

[14] The logical bit error is the error accumulation due to the physical bits.

Here there are two more important observations to make. We have implicitly assumed that the probability of an error is constant in time. In physical systems, however, it mostly grows over time. The longer we store a bit, the higher should be its error probability which is incorporated by a *effective logical error rate* κ_{eff} where the probability of the logical bit being in the right bit-state after time t is $p_0(t) \approx 1 - \kappa_{eff} t$. This time is the time to be optimized between error-correction rounds in order not to introduce errors because of correcting too often.

2.4.2.2 Quantum error correction

The fundamental difference between classical and quantum error correction lies in the logical state space we use: the qubit. However, this qubit can be encoded in an infinitely large state space, as we have seen in subsection 2.2.2. Important changes to classical error correction are:

1. *No-cloning theorem.* It is impossible to clone/copy an unknown quantum state.
2. *Errors are continuous.* As we are working with qubits an error does not have to be a discrete operation but can rotate (and shrink) anywhere within the Bloch sphere.
3. *Measurements destroy quantum information.* General measurements destroy the state and therefore it cannot be error-corrected afterward.

Due to the no-cloning theorem, we cannot straightforwardly reproduce the classical repetition code, but will see a quantum version of it later. The possible errors are coherent superpositions of all four Pauli matrices, corresponding to the bit-flip X, the phase flip Z, and a combination of both $Y = iXZ$. In general, such a *trace-preserving error* is

$$U_\varepsilon = \sqrt{1-\varepsilon}\mathbb{1} - i\sqrt{\epsilon}\vec{\sigma}_m \tag{2.285}$$

where the Pauli matrices $\vec{\sigma}$ can be defined with an arbitrary axis m. Moreover, we will also consider loss (not trace-preserving) equivalent to the application of the annihilation operator as

$$\sigma^- = \frac{1}{\sqrt{2}}(X - iY). \tag{2.286}$$

Even though there are numerous errors there exist quantum codes that can correct all possible errors (with a minimum of five physical qubits) [95]. If one uses higher levels of redundancy, qubits and therefore superpositions can in principle be stable over an arbitrary long time if the errors are sufficiently unlikely and are not correlated between physical qubits [95].

Let us now consider the quantum version of the repetition code. A logical qubit will have the form

$$\alpha \left|0\right\rangle_L + \beta \left|1\right\rangle_L \rightarrow \alpha \left|000\right\rangle + \beta \left|111\right\rangle. \tag{2.287}$$

As for its classical version we expect to be able to protect one logical qubit against three errors (and identity) according to eq. (2.284), which turns out to be single physical qubit bit-flips X_1, X_2 or X_3. Note that the logical Pauli operators of the whole system change to

$$X_L = X_1X_2X_3 \quad Z_L = Z_1Z_2Z_3 \quad Y_L = iX_LZ_L = -Y_1Y_2Y_3 \tag{2.288}$$

which means that to rotate the logical qubit a physical three-qubit joint rotation has to be applied, which is a non-trivial operation. To find the measurements we have to perform to detect and correct the errors a convenient formalism called the *stabilizer formalism* exists, which we will introduce now.

2.4.2.3 The stabilizer formalism

We need to introduce the concept of stabilizers. A state is stabilized by a unitary operation if

$$g_i |\psi\rangle = |\psi\rangle , \tag{2.289}$$

meaning that g_i stabilizes $|\psi\rangle$ if it is an eigenvector of g_i with eigenvalue $+1$. Stable here means that applying g_i on the state does not change it. If g_1 and g_2 both stabilize the state, then any product of them will. The identity matrix is a trivial stabilizer for all states. All g_i that stabilize this state form a group S which is called the *stabilizer* and uniquely defines a state (up to a global phase). We can clearly see that the Pauli matrices stabilize qubits

$$|0\rangle_L \text{ is stabilized by } \{\mathbb{1}, Z\} \qquad |1\rangle_L \text{ is stabilized by } \{\mathbb{1}, -Z\} \tag{2.290}$$

$$|+\rangle_L \text{ is stabilized by } \{\mathbb{1}, X\} \qquad |-\rangle_L \text{ is stabilized by } \{\mathbb{1}, -X\} \tag{2.291}$$

$$|i\rangle_L \text{ is stabilized by } \{\mathbb{1}, Y\} \qquad |-i\rangle_L \text{ is stabilized by } \{\mathbb{1}, -Y\} \tag{2.292}$$

The stabilizer S is always a subgroup of the Pauli group G_n for n qubits, with the elements for $n = 1$ being

$$G_1 = \{\pm\mathbb{1}, \pm i\mathbb{1}, \pm X, \pm iX, \pm Y, \pm iY, \pm Z, \pm iZ\}, \tag{2.293}$$

thereby including all the Pauli matrices (with the Identity) and the multiplicative factors $\pm$ and $\pm i$. Those are included to guarantee that G_n defines a proper group, closed under multiplication. G_n then includes all possible n-fold tensor products of G_1 with the multiplicative factors $\pm$ and $\pm i$. In order to form a non-trivial stabilizer, all elements of S have to commute and $-\mathbb{1}, \pm i\mathbb{1} \notin S$.

For large n, one might want to have a compact description of S. We already stated that any product of elements of S is also in S. We can therefore try to find the minimum number of elements g_i such that via multiplication we find back S. The set of these elements $g_1, ..., g_n$ is said to *generate* the group S. A group of size k has at most $n \leq \log(k)$ generators. If we take the example of the logical states $|0\rangle_L, |1\rangle_L$ we can see that S_{0L} has the generator Z

because $Z^2 = \mathbb{1}$ and similar for S_{1L}. The choice of generators is not unique and generally one tries to find independent generator elements. Note that only a subclass of all quantum states can be described using stabilizers.

2.4.2.4 Stabilizers and error correction

Why should we use this new formalism to describe states envisioned for error correction? If we use the stabilizers, a large state space with n qubits can be described more efficiently because the action of specific unitaries U on the state can be described by a transformation of the stabilizer group as $USU^\dagger$. Indeed those are the unitaries that map elements of G_n to G_n and therefore operate within the Pauli group. Any such unitary can be composed from the Hadamard, phase, and controlled-NOT gates and are therefore part of the Clifford group. This is very practical because we plan to use the whole Clifford group in quantum computation. If one or more gates in the Clifford group would change what kind of measurements and correction-operations we have to apply for error correction, that would be rather unfortunate. Choosing a stabilizer state for computation therefore guarantees, that one can perform (in theory) universal quantum computation if the states themselves are non-Gaussian.

More importantly for us, the stabilizer formalism can be used to analyze if a quantum code-space can protect against the effect of arbitrary trace-preserving errors on its logical qubits. We will simplify this such that our code consists of one qubit and ask the question under which errors this logical qubit is stable. Those two errors can be described by the effect of a X gate for the bit-flip and a Z gate for the phase-flip. In general, an error $E \in G_n$ is defined to be an element of the Pauli group. If now a stabilizer state is corrupted by such an error, there are three cases. If E anti-commutes with one of the elements of S, then the error will push the state not to be stabilized anymore, which is detectable. If E commutes with all elements in S and is part of S, then it is not considered an error. But if E commutes with all elements in S but is not an element of S, then the error is not correctable.

Let us now go back to our example of the quantum repetition code. Our logical qubit is encoded in three physical qubits such that the basis states are $|0\rangle_L = |000\rangle$ and $|1\rangle_L = |111\rangle$. We find that the generators for those basis states are Z_1Z_2 and Z_2Z_3 [15]. Let us now consider the set of errors $E = \{\mathbb{1}, X_1, X_2, X_3\}$ and see how they can be detected. To detect an error the measurement of both generators is performed such that we see the *error syndromes* as in the following table.

[15] Where $Z_1Z_2 = Z_1Z_2\mathbb{1}_3$.

Error	syndrome on Z_1Z_2	syndrome on Z_2Z_3
X_1	-1	$+1$
X_2	-1	-1
X_3	$+1$	-1

We see that we can detect a single bit-flip error that happened in one of the physical states. This code therefore can protect against single-qubit bit flips. There are more advanced codes protecting against bit- and phase-flip errors on multiple qubits and the interested reader is referred to [84, 96].

2.4.2.5 General framework of quantum error correctability

If the logical states are not stabilizer states or the errors to consider are not part of the Pauli group, then a more general framework is needed to analyze them. We define the general set of errors $\varepsilon = \{E_i\}$ to be error correctable if they fullfill the Knill–Laflamme condition [97]

$$PE_i^\dagger E_j P = \alpha_{ij} P, \tag{2.294}$$

where P is defined to be the projection operator on the logical state space and α_{ij} the coefficients of a Hermitian matrix [84]. Clearly this requires

$$\langle 0_L|E_i^\dagger E_j|0_L\rangle = \langle 1_L|E_i^\dagger E_j|1_L\rangle\,, \tag{2.295}$$

$$\langle 0_L|E_i^\dagger E_j|1_L\rangle = \langle 1_L|E_i^\dagger E_j|0_L\rangle = 0, \tag{2.296}$$

such that the logical states should not be distinguishable under the errors. This mirrors the requirement of subsubsection 2.4.2.1, where a state has to be encoded in the state space to be correctable.

2.4.3 Bosonic qubits for error correction

We see for the example of the quantum version of the repetition code, that even for a simple example a superposition of three qubits has to be created where errors need to be localized on one of the physical qubits to be correctable.

To scale this approach up to the error correction of multiple logical qubits can be a serious engineering challenge. Moreover, interconnecting those devices can introduce non-correctable cross-talk. An alternative approach can be to search the redundancy needed in one single mode, instead of using multiple modes with a limited Hilbert space. This promising approach avoids cross-talk and reduces the resource overhead of quantum error correction. There are infinite ways in which one can decide to split the phase-space of one mode into two logical states.

There exist two leading approaches that each exploit different symmetries in the phase-space: number-phase codes and GKP codes. The former exploits rotation-symmetry while

the latter uses discrete translation-symmetry [98]. We will draft the power of those states in the framework of error correction in the following.

2.4.3.1 Bosonic rotation codes

A quantum state is said to have a N-fold rotational symmetry if it is the +1 eigenstate of the discrete rotational operator

$$R_N = e^{i(2\pi/N)\hat{n}}, \tag{2.297}$$

where $\hat{n}$ is the number operator. The logical states (full qubit space) of any N-order rotational code can be constructed from a core state $|\Theta\rangle$ such that they form the logical basis $|0\rangle_{N,\Theta}$ and $|1\rangle_{N,\Theta}$. In order to find the equivalent to the logical Z operator, we need to define a hermitian matrix from the operator of eq. (2.297) that leaves the symmetry invariant, which we find to be its square root $Z_N = e^{i(\pi/N)\hat{n}}$. We can now define the general form of the logical basis states via

$$Z_N |0\rangle_{N,\Theta} = |0\rangle_{N,\Theta} \qquad |0\rangle_{N,\Theta} \propto \sum_{m=0}^{2N-1} e^{i(m\pi/N)\hat{n}} |\Theta\rangle , \tag{2.298}$$

$$Z_N |1\rangle_{N,\Theta} = -|1\rangle_{N,\Theta} \qquad |1\rangle_{N,\Theta} \propto \sum_{m=0}^{2N-1} (-1)^m e^{i(m\pi/N)\hat{n}} |\Theta\rangle . \tag{2.299}$$

Let us now find the ideal states of rotational symmetry. We can write the logical ideal states in the Fock basis via the observation $Z_N \sum_n c_n |n\rangle = \sum_n e^{i\pi n/N} c_n |n\rangle$ such that to be ± 1 eigenstates we have to write

$$|0\rangle_N = \sum_k f_{2kN} |2kN\rangle , \tag{2.300}$$

$$|1\rangle_N = \sum_k f_{(2k+1)N} |(2k+1)N\rangle , \tag{2.301}$$

$$\text{with} \quad f_{2kN} = \frac{c_{2kN}}{\sum_k |c_{2kN}|^2} \quad \text{and} \quad f_{(2k+1)N} = \frac{c_{(2k+1)N}}{\sum_k |c_{(2k+1)N}|^2} \tag{2.302}$$

where the superposition of the two basis states $\frac{1}{\sqrt{2}}(|0\rangle_N \pm |1\rangle_L)$ show a more visually clear rotational structure

$$|+\rangle_N = \frac{1}{\sqrt{2}} \sum_k f_{kN} |kN\rangle \qquad |-\rangle_N = \frac{1}{\sqrt{2}} \sum_k (-1)^k f_{kN} |kN\rangle . \tag{2.303}$$

Those states are practical as they have the same average excitation numbers. This means that photon loss does not make the logical states distinguishable pointing to the fact that they can correct loss. Moreover, as we have defined them to be rotational invariant, they

will also be able to correct rotational errors. The set of correctable errors is therefore $E = \{\mathbb{1}, E_1, E_2\}$ such that they can detect:

$$\text{Loss error} \qquad E_1 \propto \hat{a}^k \quad \text{for} \quad k < N, \tag{2.304}$$

$$\text{Rotational error} \qquad E_2 \propto e^{i\theta\hat{n}} \quad \text{for} \quad \theta < \pi/N. \tag{2.305}$$

We note that the code is equivalently able to detect gain errors $\propto (\hat{a}^\dagger)^k$ (which is usually not an error that occurs in photonics).

Whether this code is also able to correct those errors depends on the chosen core state $|\Theta\rangle$. Most realistic states are only approximately able to correct errors. To correct for loss errors one would measure the excitation number and round up to the nearest kN. An even outcome announces a logical $|0\rangle_L$ while an odd outcome announces a logical $|1\rangle_L$. Here, the error correction was implicitly done by rounding up the result, which is only working if gain and loss errors are equally likely. This is a good example to see that even though a code can correct an error, one still needs to find an error correction strategy adapted to the realistic errors in the system. A phase error can be measured via phase estimation of the estimator ϑ. This estimator is to be determined in $e^{i\vartheta\hat{n}}$ such that if $\vartheta \mod (2\pi/N) = 0$ if the state is $|+\rangle_N$ and $\vartheta \mod (2\pi/N) = \pi/N$ if the state is $|-\rangle_N$. With continuous errors, the outcome will be between $[0, \pi/N]$ such that we have to define the uncertainty on this measurement, which will tell us if we can know in which logical state the measured system should have been. The phase uncertainty is defined as $\Delta\vartheta = 4/(\sum_k |f_{kN} f_{(k+1)N}|^2) - 1$ and depends on the rotation symmetry order N and the chosen core state. We can see that this uncertainty is minimized if $|f_{kN}| = |f_{(k+1)N}|$ for all k.
Similar to the GKP states in the next subsubsections, this leads to unnormalizable, unphysical ideal states which have the stabilizers R_N and $T_N = \sum_n |n\rangle \langle n + 2N|$ and the logical operators $X_N = \sum_n |n\rangle \langle n + N|$ [98].

One example of an approximate rotational code is the **binomial code**. It is based on the fact that the coefficients f are binomial and have a cut-off Fock number K. The lowest binomial code has the logical states

$$|0\rangle_L = \frac{1}{\sqrt{2}}(|0\rangle + |4\rangle) \qquad |1\rangle_L = |2\rangle \tag{2.306}$$

which can correct up to one photon lost because $N = 2$, as stated above. In terms of rotational correction, its uncertainty is very large with $\Delta\vartheta = 7$, with the general formula being $\Delta\vartheta_{K,N} = (0.5^K \sum_{k=0}^{K-1} \sqrt{(K-k)/(k+1)}\binom{K}{k})^{-2} - 1$. Higher-order binomial codes are needed to perform any kind of phase error correction and will also enable higher loss corrections.

Another rotational code is the **Cat code**. The cat code is based on using coherent states as the core state such that the qubits defined in eq. (2.227) and (2.226) are the easiest examples of cat states. In general, cat codes are based on a superposition of $2N$ coherent states, being spaced equidistantly on a circle around the phase-space origin [99]. For our simple case of $N = 1$ which we will see in subsection 3.2.3, error correction is not possible, but for $N = 4$ the cat code is promising. We will discuss a possible implementation of such a state in chapter 7.

2.4.3.2 The GKP-code

The GKP states we defined in eq. (2.234) and (2.235) form a qubit basis, that is invariant under discrete translation. We can define the Pauli matrices of those states as displacement operators, that have to fulfill the displacement operators commutator relation of eq. (2.244) to ensure they anti-commute [80]

$$Z = D(\beta) = e^{-i\gamma\hat{p}/\hbar} \quad X = D(\alpha) = e^{2i\pi\hat{x}/(n\gamma)} \quad Y = iXZ, \\ \text{with} \quad \beta\alpha^* - \beta^*\alpha = 2i\pi/n. \tag{2.307}$$

The stabilizers of those GKP states are then

$$S_{GKP} = \{S_Z = Z^n = D(n\beta), S_X = X^n = D(n\alpha)\}, \tag{2.308}$$

where there are infinite choices of α and β as long as they obey the anti-commutator relation of eq. (2.244), such that we find $\beta = i\pi/(n\alpha)$. The most common choices in literature are

Square GKP	$\alpha = \sqrt{\frac{\pi}{n}}$	$\beta = i\sqrt{\frac{\pi}{n}}$,	(2.309)
Rectangular GKP	$\alpha = \lambda\sqrt{\frac{\pi}{n}}$	$\beta = \frac{i}{\lambda}\sqrt{\frac{\pi}{n}} \quad \lambda > 0,$	(2.310)
Hexagonal GKP	$\alpha = \sqrt{\frac{\pi}{n\sqrt{3}}}$	$\beta = i\sqrt{\frac{\pi\sqrt{3}}{n}}.$	(2.311)

Since S_X and S_Z are stabilizers of the GKP states, bit-flip and phase-flip errors can both be corrected. If a Pauli gate is applied, a full bit- or phase-flip occurs. We should be able to calculate less than half a bit-flip and phase-flip. If the error exceeds this range one does

not know if the state has to be corrected towards the logical zero or one. We can calculate the correctable magnitude with

$$Z^\dagger \hat{x} Z = \hat{x} - \gamma, \tag{2.312}$$

$$X^\dagger \hat{p} X = \hat{p} - \frac{2\pi\hbar}{n\gamma} \tag{2.313}$$

such that the correctable errors are $|\Delta x| < \frac{\gamma}{2}$ and $|\Delta p| < \frac{\pi\hbar}{n\gamma}$ obeying $\Delta x \Delta p < \frac{\pi\hbar}{2n}$, where we can see that increasing n decreases the maximal correctable error. Now we can understand the naming of the square GKP state $\gamma = \sqrt{2\pi\hbar/n}$, as we see that it is the only configuration that enables the same error correction in position and momentum $\Delta x = \Delta p$. This is not the case in the rectangular or hexagonal code [80, 100, 101].

In the realistic physical GKP state case of eq. (2.236), the quality of a GKP state can be measured either via the stabilizers or via its error-correctability. First, we can define how close a GKP approximation is to its real state via the modular squeezing parameters

$$\Delta_x = \frac{1}{2|\alpha|}\sqrt{-\ln(|\mathrm{Tr}[S_x\hat{\rho}]|^2)}, \tag{2.314}$$

$$\Delta_z = \Delta_p = \frac{1}{2|\beta|}\sqrt{-\ln(|\mathrm{Tr}[S_z\hat{\rho}]|^2)}, \tag{2.315}$$

which in dB is $s_{x,z} = -10\log_{10}(\Delta^2_{x,Z})$. For $\Delta_{x,Z} = 0$ we recover the ideal state. It is important to note though that this modular squeezing is not sufficient as an indicator for quantum error correction. Indeed many error correction thresholds depend strongly on the error correction code one wants to use [102, 103]. Another possibility is to calculate the expectation value of its stabilizers. We will further investigate those approaches in chapter 7.

2.4.4 Take-away message

Here we have shown the power of non-Gaussian states in the context of error correction. We first developed an idea of classical error correction:

- The two main errors are: bit-flip error and erasure error.
- If more than one physical bit is used to define a logical bit, the overhead is called ancillae.
- If more than one physical bit is defined as a logical bit, the error probability is raised. The break-even point is defined as the moment when the error correction code can push the error probability of the logical qubit below the error probability of a single physical qubit.
- The state after an error can only be corrected, if we can encode it in our system.

In quantum error correction, we saw:

- The main errors are: bit-flip errors, phase-flip errors, and erasure errors.
- We cannot clone states, errors are continuous and measurements destroy quantum information.
- To ensure that all errors can be corrected, we also need to be able to encode all states after an error in the system. This is ensured by using the stabilizer formalism.
- Stabilizers are operators that do not change a state. They also uniquely define a state. Those operators are part of the Pauli group.
- As the Pauli group can be efficiently simulated by classical computers we need to add Non-Gaussianity to the system to gain a quantum advantage.
- This can be done by choosing non-Gaussian stabilizer states, which are bosonic qubits. Dependent on their symmetries in phase-space they can correct either phase-flip or phase-flip and bit-flip errors. The former are binomial or cat codes and the latter are GKP codes. In chapter 7 we will discuss how GKP codes and binomial states could be created in our system.

Chapter 3

Experimental toolbox

Contents

This chapter presents the operational framework for our experiment, which aims to generate high-purity non-Gaussian states and entangle them. The chapter proceeds by describing how both the generated non-Gaussian states and their entanglement are utilized in various protocols. The **first section** emphasizes the key components of the experiment: three optical parametric oscillators (OPOs) that generate either two-mode or single-mode cavity-enhanced squeezing. To achieve these states, stable locks and filtering stages are required, along with two detection methodologies: homodyne detection using high-efficiency conventional balanced photodiodes and single photon detection using superconducting nanowire

single-photon detectors. In the **second section** we focus on quantum state engineering. We discuss how such created Gaussian two- or single-mode squeezed states are then projected onto non-Gaussian states via heralding. The operation mode of our experiment, alternating between measuring and lock stabilization, is presented. This section ends with the analysis of our experimentally generated single-mode non-Gaussian output states, created with the three OPOs. The **third section** concludes with an explanation of the data processing, enabling us to infer the measured state from our measurement data. The current optical table setup is shown in fig. 3.1

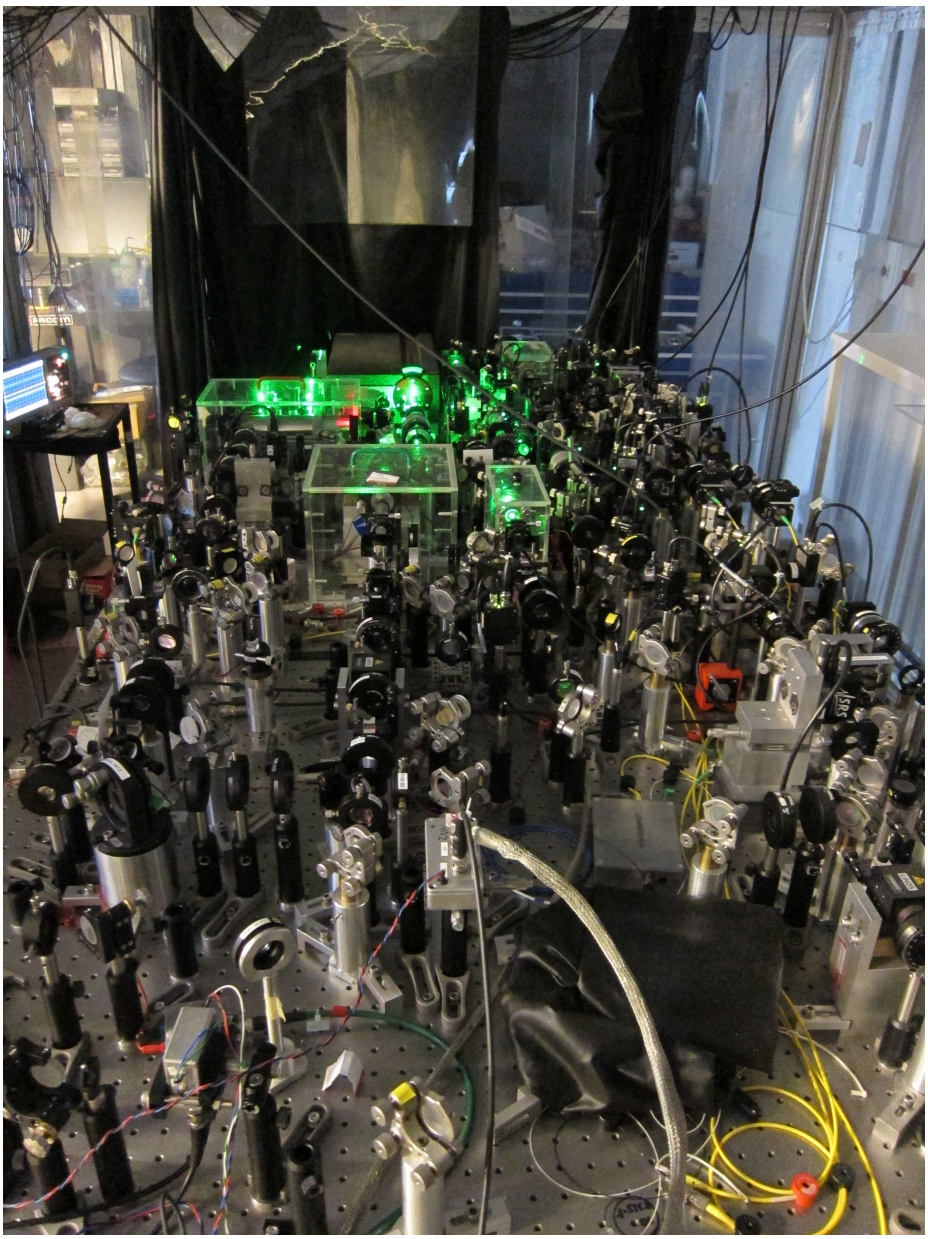

Figure 3.1: The optical table in early 2024.

3.1 Lab Gear Description

This section is dedicated to introducing the main optical table components and measurement devices we use throughout this thesis. First, the laser, providing us with infrared and green light, is presented. The green output of this laser is used to pump nonlinear crystals inside cavities, called optical parametric oscillators. Their theoretical description and experimental implementation are discussed. As we are using many cavities in our setup, filtering and locking methods will be presented. Finally, our two types of detectors are introduced.

3.1.1 The Laser

We are working in the lab with the commercial laser *Diabolo* from *Innolight*. It consists of two outputs. The first comes from a continuous Nd:YAG solid-state laser that is optically pumped using two laser diodes. Its output wavelength is centered at 1064nm and can be slightly tuned by changing the set temperature of the temperature PID of the Nd:YAG crystal. Half of the power, around 250 mW, is used in various stages of our experiment while the rest is sent to a doubling cavity that is inside of the laser housing. This doubling cavity is semi-monolithic with a Lithium Niobate crystal. Here the laser light is doubled via second-harmonic generation. The cavity is locked with a Pound-Drever-Hall generated error signal, which will be explained in subsection 3.1.3. We have access to the doubling crystal's temperature and the overall gain and offset of the error signal for the PID of the cavity lock. The output power is in the 500-600 mW range at a wavelength of 532 nm. In table 3.1 we summarize what the two laser outputs are used for in our experiment, which will be discussed in detail in this section. This laser has been in the group since the thesis of Julien Laurat in 2004 [104].

During this thesis, the doubling cavity of the laser stopped emitting light due to photorefractive damage. We will describe the problem and its solution in the following. During the production period of this laser, many commercial doubling cavities were built as a two-mirror Fabry-Perot cavity, which is also our case. In this setting, the powerful standing wave building up in the cavity can damage the crystal via the *photorefractive* effect, which was first reported (to our knowledge) in 1966 [105] and is nicely explained in the PhD thesis of A. Hellwig [106]. The observed effect can be a change in the output mode or, as in our case, a slow (at the scale of seconds) power and spatial shape modulation. This effect is sometimes also called gray tracking or optical damage. The photorefractive damage can be

Table 3.1: Full use of the two laser outputs in this experiment.

wavelength	used in/for
1064 nm	Mode cleaner, OPO seed, lock micro cavities, local oscillator
532 nm	pump OPO and lock OPO cavity length

explained in a nutshell by charges in the crystal moving away from the illuminated area. This leads to a charge field building up, which locally changes the refractive index of the crystal due to the electro-optic effect. This local change stays even after the illumination has seized. The most common solution is to heat the crystal for several weeks, suggesting that some self-re-ordering occurs. In our case, we solved the issue by heating the crystal to 104°C for 3.5 weeks, which is only one degree above its working temperature. The ideal heat load, to make this effect disappear depends heavily on the crystal specification, which we do not have. Most likely we could have sped up the repair process by increasing the temperature even more. Given our working temperature, we think that our Lithium Niobate crystal has been annealed in nitrogen to produce oxygen deficiencies. Those crystals are also more prone to show photorefractive damage [105].

3.1.2 Optical Parametric Oscillators - theory and design

An optical parametric oscillator (OPO) consists of a second-order nonlinear crystal being placed inside a cavity. The crystal exhibits spontaneous parametric down-conversion (SPDC), which is a broadband nonlinear optical process in which a high-frequency *pump* photon impinges on the crystal and spontaneously splits into two lower-frequency photons that are called *signal* and *idler*. Placing the crystal inside a cavity can enhance the efficiency of the down-conversion and will define the bandwidth of the down-converted photons. In the following, we will consider the physical requirements for this process and introduce its Hamiltonian in free space, before analyzing the effect of the cavity. For this analysis, we closely follow G. Shafiee et al. [107].

3.1.2.1 SPDC phase-matching

Here we investigate the physical constraints for spontaneous parametric down-conversion. The subscripts p, s, i henceforth stand for the pump, signal, and idler photons. SPDC is described as a closed system and as such obeys energy conservation, which implies

$$\omega_p = \omega_s + \omega_i, \tag{3.1}$$

where the process is called *degenerate in frequency* if $\omega_s = \omega_i$. Momentum conservation is ensured via the pump, signal, and idler wavevectors $\vec{k}$ if

$$\vec{k}_p = \vec{k}_s + \vec{k}_i. \tag{3.2}$$

If the momentum conservation is fulfilled, a crystal is said to be phase-matched such that $\Delta\vec{k} = \vec{k}_p - \vec{k}_s - \vec{k}_i = 0$. Phase-matching prevents the three waves from interfering destructively inside the crystal and needs to be achieved via the crystal design. The wave vector in a medium $\vec{k} = \frac{2\pi}{\lambda}\vec{n}$ depends on the index of refraction, which in turn depends on the wavelength, polarization, and propagation direction of the incoming light. The non-linear

property of the crystal arises from the polarization density $\vec{P}$ of the medium reacting to an electrical field $\vec{E}$ non-linearly, such that

$$P_i = \varepsilon_0 \chi_{ij}^{(1)} E_j + \varepsilon_0 \chi_{ijk}^{(2)} E_j E_k + \varepsilon_0 \chi_{ijkl}^{(3)} E_j E_k E_l + ... \tag{3.3}$$

The polarization density $\vec{P}$ describes the formation of microscopic electrical dipoles that form in dielectric materials if an electrical field is applied. The polarization density then translates to the dipole moment per volume. Here we are interested in the second-order non-linearity, governed by the second-order susceptibility $\chi_{ijk}^{(2)}$ which is a tensor that generally describes non-linear processes involving three frequencies and depends on the wavelengths involved. Each tensor $\chi_{ijk}^{(2)}(\omega_1, \omega_2, \omega_3)$ has 18 elements which usually can be reduced due to symmetries and properties of the crystal. One can then calculate the effective non-linearity of a material for the given polarization $\chi_{eff}^{(2)}$ [108], which corresponds to the non-linearity given the pump input angle and polarization. In the case of KTP crystals for example, the effective non-linearity can change from 1.3 pm/V to 14.3 pm/V dependent on the input polarization [109].

As all non-linear crystals inherit their non-linearity from being non-isotropic, one often uses birefringence to achieve phase-matching. In our case, uni-axial birefringent materials are used, which means that one crystal axis governs the non-isotropic behavior of the medium, and rotating around this *optical axis* does not change the optical properties of the crystal. The index of refraction will depend on the direction of the electrical field vector which is governed by the polarization of this field (eq. (2.5)). If the electrical field direction is parallel to the optical axis it will experience the extraordinary refractive index n_e. This means that the wavevector is perpendicular to the optical axis. If the electrical field direction is perpendicular to the optical axis, then the light will experience the ordinary refractive index n_o and propagate along the optical axis. An arbitrary direction of propagation to the optical axis will therefore lead to a difference in refractive index dependent on the polarization. With this, the birefringence can compensate for the difference in refractive index due to its wavelength dependency (dispersion) and lead to *birefringent phase-matching*. This practically means that the angle and polarization, at which the incoming pump beam impinges on the crystal is adapted such that $\Delta\vec{k}_p = 0$. If both angle and polarization have to be tuned, the phase matching is said to be "critical", while it is "non-critical" if the polarization tuning is sufficient. The two main configurations are

Type-I phase-matching	Type-II phase-matching
$o \rightarrow e + e$	$o \rightarrow e + o$
$e \rightarrow o + o$	$e \rightarrow o + e$,

where o and e stand for a beam polarized along the ordinary or extraordinary axis of the crystal. A crystal that uses type-I phase-matching is said to output photons that are *degenerate in polarization*.

If birefringent phase matching is not possible, the second most used method at hand is called *quasi phase-matching* where the crystal has a periodic switching of the sign of its non-linearity. This can either be done by cutting the crystal and rotating each second piece by π or (more commonly) by ferroelectric domain engineering [110]. The domain linearity direction is then switched with a periodicity of $\Lambda = 2\pi m/\Delta\vec{k}$, where $\Delta\vec{k}$ is the phase mismatch in one domain and m called the order of this quasi-phase-matching. The poling is chosen such that the effective non-linearity $\chi^{(2)}_{eff}$ is growing over the crystal length. Only if phase-matching is fulfilled we can observe any SPDC output.

3.1.2.2 SPDC Hamiltonian

The Hamiltonian of SPDC can be divided into a linear and non-linear Hamiltonian. The linear Hamiltonian is our known quantum harmonic oscillator of eq. (2.82) for each field, while the non-linear part H_{nl2} can be guessed by the physical process: One photon of the pump is annihilated to create two signal and idler photons such that [107]

$$H_{nl2} = \hbar\kappa(\hat{a}_p\hat{a}_s^\dagger\hat{a}_i^\dagger + h.c.) \quad \text{with} \quad \kappa = \chi^{(2)}_{eff} O \frac{\sqrt{(2\pi)^3\hbar\omega_p\omega_s\omega_i}}{n_p n_i n_s}, \tag{3.4}$$

where κ is the parametric coupling which is connected to the effective non-linearity $\chi^{(2)}_{eff}$, the overlap between signal, pump, and idler modes O[1] and the frequencies and refractive indices of the fields. We see that here the hermitian conjugate ($h.c.$) creates one high-frequency photon out of two lower-frequency photons, which is exactly the second-harmonic generation process used to create our second laser output (see subsection 3.1.1).
If we now assume the pump to be a bright field, then its operators can be approximated by an amplitude α_p such that $\hbar\kappa(\alpha_p\hat{a}_s^\dagger\hat{a}_i^\dagger + \alpha_p^*\hat{a}_i\hat{a}_s)$. If we now compare this to the squeezing operator of eq. (2.204), we find that in the degenerate case of $\omega_i = \omega_s$ the Hamiltonian of spontaneous parametric down conversion produces squeezing. In this case the time evolution of the annihilation operator $\hat{a} = \hat{a}_s = \hat{a}_i$ [2] (and creation operator $\hat{a}^\dagger$) can be written as

$$i\hbar\frac{d}{dt}\hat{a} = [H^{\alpha_p}_{nl2}, \hat{a}] \qquad i\hbar\frac{d}{dt}\hat{a}^\dagger = [H^{\alpha_p}_{nl2}, \hat{a}^\dagger], \tag{3.5}$$

$$\frac{d}{dt}\hat{a} = 2i\kappa\alpha\hat{a}^\dagger \qquad \frac{d}{dt}\hat{a}^\dagger = -2i\kappa\alpha\hat{a}, \tag{3.6}$$

[1] Here the temporal and spatial mode overlap is considered.
[2] Here, signal and idler are assumed to have the same polarization

such that we find the solutions

$$\hat{a}(t) = \hat{a}(0)\cosh(2\alpha\kappa t) + i\hat{a}^\dagger(0)\sinh(2\alpha\kappa t), \tag{3.7}$$
$$\hat{a}^\dagger(t) = \hat{a}^\dagger(0)\cosh(2\alpha\kappa t) - i\hat{a}(0)\sinh(2\alpha\kappa t). \tag{3.8}$$

The position quadrature is transformed as

$$\hat{x}(t) = \hat{x}(0)\cosh(2\alpha\kappa t) + \hat{p}(0)\sinh(2\alpha\kappa t), \tag{3.9}$$

which is equivalent to the action of a squeezing operator with $r = 2\alpha\kappa t$ and phase $\phi = -\pi/2$ in eq. (2.250). The time t here can be seen as the interaction time with the non-linear crystal.
If we now choose to analyse the non-degenerate case of $\omega_i \neq \omega_s$ or signal and idler having orthogonal polarization, then we find

$$\begin{aligned}
\hat{a}_i(t) &= \hat{a}_i(0)\cosh(2\alpha\kappa t) + i\hat{a}_s^\dagger(0)\sinh(2\alpha\kappa t),\\
\hat{a}_i^\dagger(t) &= \hat{a}_i^\dagger(0)\cosh(2\alpha\kappa t) - i\hat{a}_s(0)\sinh(2\alpha\kappa t), \qquad (3.10)\\
\hat{a}_s(t) &= \hat{a}_s(0)\cosh(2\alpha\kappa t) + i\hat{a}_i^\dagger(0)\sinh(2\alpha\kappa t),\\
\hat{a}_s^\dagger(t) &= \hat{a}_s^\dagger(0)\cosh(2\alpha\kappa t) - i\hat{a}_i(0)\sinh(2\alpha\kappa t), \qquad (3.11)\\
\hat{x}_i(t) &= \hat{x}_i(0)\cosh(2\alpha\kappa t) + \hat{p}_s(0)\sinh(2\alpha\kappa t),\\
\hat{x}_s(t) &= \hat{x}_s(0)\cosh(2\alpha\kappa t) + \hat{p}_i(0)\sinh(2\alpha\kappa t), \qquad (3.12)
\end{aligned}$$

which looks like squeezing between the signal and idler mode leading to its name, *two-mode squeezing*, which can be described via the operator

$$S_2(\xi) = e^{\frac{1}{2}(\xi^*\hat{a}_i\hat{a}_i - \xi\hat{a}_i^\dagger\hat{a}_s^\dagger)}. \tag{3.13}$$

We have already stated in chapter 2 that this can be interpreted as squeezing with an imperfect choice of mode basis. Indeed if we perform a beamsplitter operation with $R = 0.5$, we find

$$\hat{x}_{i/s}(t) \xrightarrow{\text{BS}(0.5)} \frac{1}{\sqrt{2}}(\hat{x}_i(t) + \hat{x}_s(t)) \tag{3.14}$$

such that two-mode squeezing corresponds to two squeezing operations with half the squeezing

$$S_2(\xi) \xrightarrow{\text{BS}(0.5)} S_i(\frac{\xi}{2})S_s(-\frac{\xi}{2}). \tag{3.15}$$

Here we implicitly choose to simplify the Hamiltonian by disregarding that SPDC is a broadband process and focusing on its central frequency, which is motivated by our experi-

mental setup. A more complete model can be found in [111, 112], where the full-width half maximum (FWHM) of the SPDC process is approximated as

$$\mathrm{FWHM}_{\mathrm{SPDC}} \approx 5.56 \frac{c}{2\pi L} \frac{1}{|n_{gs} - n_{gi}|}, \tag{3.16}$$

where L is the crystal length and $n_{gi/s} = n_{s/i} + \omega_{s/i} \frac{\partial n}{\partial \omega_{s/i}}$ the group index of signal and idler. In our case the FWHM_{SPDC} is wider than the cavity bandwidth the crystal is placed in, and thus can be ignored, as the cavity will fully determine the spectral properties of the emitted light.

3.1.2.3 SPDC in a cavity

Placing a nonlinear crystal inside a cavity forms a system of gain and loss [107]. This can be compared to a laser but instead of the gain through stimulated emission, the optical gain is coming from parametric amplification. The gain is competing against the loss inside the cavity. Increasing the pump power will bring the system to a point where loss and gain are the same, called the *OPO threshold*. This can lead to two distinct regimes, above and below threshold. While above threshold the vacuum-fluctuations can be ignored, leading to a semi-classical treatment of the physical system, below threshold a quantum treatment is necessary. All our experiments are performed below threshold, such that we will discuss the field evolution in a quantum framework.

We also need to specify the fields, with which the OPO cavity resonates. If the cavity is resonant on the pump, it extends the effective length of the nonlinear crystal by making the pump light interact with the crystal for many round-trips. If the resonator is resonant with the created signal and idler fields, it also acts as a filter by cutting the output's spectral width to the cavity transmission. In our case the cavity is built such that it is resonant with all circulating light fields inside of it, making it *triply resonant* for a type-II crystal and *doubly resonant* for a type-I crystal.

We will now investigate the time evolution of the creation operators of signal and idler. For this, we will take inspiration from the paper of M. Collett and C. Gardiner, serving as the foundational cornerstone of the analysis of squeezing in cavities [113]. In order to express the time evolution of the annihilation operator $\hat{a}$ in a cavity system, the quantum Langevin equations can be used

$$\frac{d}{dt}\hat{a} = -\frac{i}{\hbar}[\hat{a}, H_s] - \frac{\gamma_1 + \gamma_2}{2}\hat{a} + \sqrt{\gamma_1}\hat{a}_{in} + \sqrt{\gamma_2}\hat{b}_{in}, \tag{3.17}$$

where γ_i are defined to be unit-less cavity damping constants[3], $\hat{a}_{in}$ is the input field towards the cavity and $\hat{b}_{in}$ the loss mode of the cavity. With the system Hamiltonian H_s defined

[3] Originally a coupling constant $\kappa(\omega)$ between a bath (either the input/out modes or the loss mode) and the cavity mode is considered. The damping constant appears if we assume that the coupling is frequency independent such that $\kappa(\omega) = \sqrt{\gamma/(2\pi)}$ [114]

in eq. (3.4) we therefore find a system of three intracavity operators $\hat{a}_s, \hat{a}_i$ and $\hat{a}_p$. As previously, we assume the pump field to be classical $\hat{a}_p \to \alpha_p$, such that for signal and idler we write

$$\frac{d}{dt}\hat{a}_s = -i\kappa\alpha_p\hat{a}_i^\dagger - \frac{T+L}{2}\hat{a}_s + \sqrt{T}\hat{a}_{in,s} + \sqrt{L}\hat{b}_{in,s}, \tag{3.18}$$

$$\frac{d}{dt}\hat{a}_i = -i\kappa\alpha_p\hat{a}_s^\dagger - \frac{T+L}{2}\hat{a}_i + \sqrt{T}\hat{a}_{in,i} + \sqrt{L}\hat{b}_{in,i}. \tag{3.19}$$

We can see that the main damping factors are set to be the transmission of the output coupler T and the loss inside the cavity L, which is set to be the same for signal and idler. A sketch of the relevant parameters of this system can be found in fig. 3.2 (a).
We can decouple those two differential equations in the same way we did for the two-mode squeezing in the previous subsubsection, by defining new operators $\hat{a}_1 = (\hat{a}_s + \hat{a}_i)/\sqrt{2}$ and $\hat{a}_2 = (\hat{a}_s - \hat{a}_i)/\sqrt{2}$, leading to the uncoupled equation

$$\frac{d}{dt}\hat{a}_n = (-1)^n i\kappa\alpha_p\hat{a}_n^\dagger - \frac{T+L}{2}\hat{a}_n + \sqrt{T}\hat{a}_{in,n} + \sqrt{L}\hat{b}_{in,n} \quad \text{for} \quad n \in 1,2, \tag{3.20}$$

where we note that the sign of the non-linear interaction changes from one mode to the other, such that we expect the squeezing to be in orthogonal quadratures. In eq. (3.20) we can see the previously mentioned threshold, which is exactly when the losses equal the gain

$$|i\kappa\alpha_p^{th}| = \frac{T+L}{2} \to |\alpha_p^{th}| = \frac{T+L}{2\kappa}. \tag{3.21}$$

In order to connect this intracavity power to a measurable input power we use the formula of Wagner et al. [115]

$$P_{in} = P_c(1-g)^2 \quad \text{with} \quad g = \frac{2F^2 + \pi^2 - \pi\sqrt{4F^2+\pi^2}}{2F^2} \tag{3.22}$$

with the round trip cavity gain g that can be defined from the cavity pump finesse $F_p = \pi\sqrt{g}/(1-g)$, and the circulating power $P_c = |\alpha_p|^2$. This leads to the threshold

$$P_{in}^{th} = (T_{s/i} + L_{s/i})^2\frac{(1-g)^2}{4\kappa^2} = \frac{\pi\left(\sqrt{4F_p^2+\pi^2} - \pi\right)(T_{s/i}+L_{s/i})^2}{8F_p^2\kappa^2} \tag{3.23}$$

$$\propto \frac{(T_{s/i}+L_{s/i})^2}{F_p^2} \propto \frac{(T_{s/i}+L_{s/i})^2}{\sqrt{1-T_p}}. \tag{3.24}$$

We can therefore see that we can decrease the threshold by either increasing the finesse of the cavity for the pump or decreasing the transmission for the signal and idler fields, which in turn increases the signal and idler finesse. It would also be lowered by decreasing the signal and idler losses. As those are mainly attributed to the losses inside the non-linear crystal, they are harder to change than the finesse or transmission.

Let us now return to the uncoupled intra-cavity field operator of signal and idler and solve equations (3.20). For this, we move into the rotating frame $\hat{a}(t) \rightarrow \hat{a}(t)e^{i\omega_s}$ and assume the signal and idler frequencies to be degenerate $\omega_s = \omega_i$. This means that for now, we are interested in the frequency response of a single-mode squeezer inside a cavity around the central frequency ω_s. Furthermore, we define the threshold parameter $\varepsilon = i\kappa\alpha_p$ and drop the subscript n. The solution to the problem can be obtained by moving into the frequency domain, such that

$$\widetilde{a}(\omega+\omega_s) = \frac{1}{\sqrt{2\pi}}\int d\omega e^{-i\omega t}e^{i\omega_s}\hat{a}(t) \qquad \widetilde{a}^\dagger(\omega-\omega_s) = \frac{1}{\sqrt{2\pi}}\int d\omega e^{-i\omega t}e^{-i\omega_s}\hat{a}^\dagger(t). \tag{3.25}$$

Solving eq. (3.20) now for the annihilation and creation operator gives

$$\begin{aligned}\widetilde{a}(\omega+\omega_s) =& \frac{(\frac{T+L}{2}-i\omega)\Big[\sqrt{T}\widetilde{a}_{in}(\omega+\omega_s)+\sqrt{L}\widetilde{b}_{in}(\omega+\omega_s)\Big]}{(\frac{T+L}{2}-i\omega)^2-|\varepsilon|^2} \\ &+ \frac{\varepsilon\Big[\sqrt{T}\widetilde{a}^\dagger_{in}(\omega-\omega_s)+\sqrt{L}\widetilde{b}^\dagger_{in}(\omega-\omega_s)\Big]}{(\frac{T+L}{2}-i\omega)^2-|\varepsilon|^2},\end{aligned} \tag{3.26}$$

and similar for the creation operator. This is the solution for the intra-cavity field, which we can translate into the cavity output field with

$$\widetilde{a}_{out}(\omega+\omega_s) = \sqrt{T}\widetilde{a}(\omega+\omega_s) - \widetilde{a}_{in}(\omega+\omega_s). \tag{3.27}$$

We expect the output state to be squeezed in quadratures, which is why we want to now write the output quadratures

$$\widetilde{x}_{out}(\omega+\omega_s) = \sqrt{\frac{\hbar}{2}}\Big(\widetilde{a}^\dagger_{out}(\omega-\omega_s)+\widetilde{a}_{out}(\omega+\omega_s)\Big), \tag{3.28}$$

$$\widetilde{p}_{out}(\omega+\omega_s) = i\sqrt{\frac{\hbar}{2}}\Big(\widetilde{a}^\dagger_{out}(\omega-\omega_s)-\widetilde{a}_{out}(\omega+\omega_s)\Big). \tag{3.29}$$

To analyze squeezing we need to compute the variance of the quadratures (see chapter 2)

$$(\Delta\widetilde{x}_{out}(\omega+\omega_s))^2 \quad \text{and} \quad (\Delta\widetilde{p}_{out}(\omega+\omega_s))^2. \tag{3.30}$$

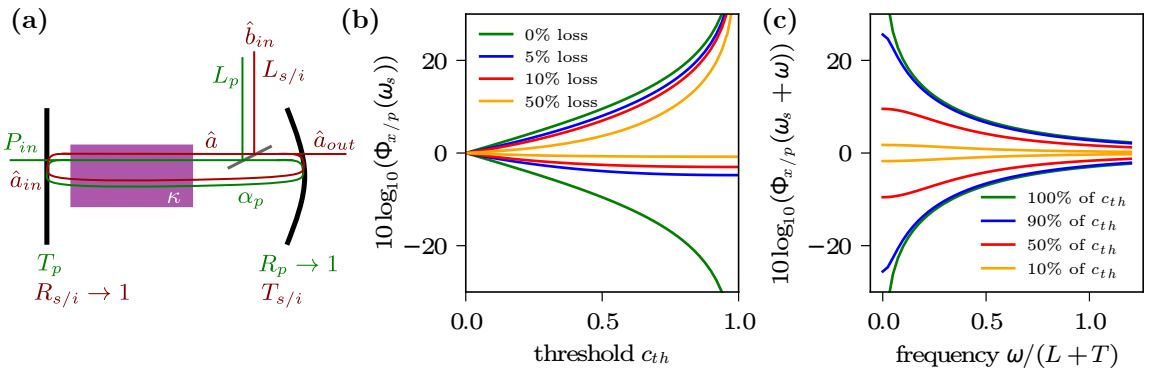

Figure 3.2: In **(a)** the schematics of the optical parametric oscillator are shown. The crystal with the non-linear coefficient κ is placed inside a Fabry-Perot cavity. The fields circulating inside the cavity are the pump field (green) and the signal and idler fields (red), which are created by the nonlinear process. Here signal and idler share the description for simplicity. The input power of the pump field P_{in} becomes the intracavity field α_p, both are classical. The cavity is designed such that the flat mirror has a transmittivity $T_p \neq 1$ while the output mirror (output coupler) reflects the maximum of the pump field $R_p \to 1$. The losses in the cavity are modeled by a beamsplitter with the reflectivity equal to the loss L_p for the pump field. The signal and idler fields are connected to the vacuum fluctuation of their mode via $\hat{a}_{in}$ and hence are described as quantum fields. Their losses can be modeled by the same beamsplitter that is now connecting the cavity to a vacuum fluctuation bath of the loss mode $\hat{b}_{in}$. The flat input mirror has high reflectivity $R_{s/i} \to 1$ while the output coupler has some transmission $T_{s,i}$ such that the intracavity field $\hat{a}$ can be converted to the output field $\hat{a}_{out}$ to be analyzed. In **(b)** we see the analysis of this output field in terms of squeezing, following eq. (3.35). Here the frequency to analyze is set to $\omega = 0$, meaning that we are at the center frequency of the down-conversion process. The transmission of the output coupler is set to $T_{s/i} = 0.1$ and losses are varied from 0% to 50%. In **(c)** the frequency ω is a detuning from ω_s, to scan the cavity bandwidth of signal and idler $L+T$. We see the development of the squeezing spectrum as is approaches the threshold c_{th}.

We find [113] that the variances are

$$\begin{aligned}(\Delta\widetilde{x}_{out}(\omega+\omega_s))^2 &= \langle \widetilde{x}_{out}(\omega+\omega_s), \widetilde{x}_{out}(\omega'+\omega_s)\rangle \\ &= \frac{\hbar}{2}\frac{4|\varepsilon|T/2}{(\frac{T+L}{2}-|\epsilon|)^2+\omega^2}\delta(\omega+\omega'), \qquad (3.31)\\ (\Delta\widetilde{p}_{out}(\omega+\omega_s))^2 &= -\frac{\hbar}{2}\frac{4|\varepsilon|T/2}{(\frac{T+L}{2}+|\epsilon|)^2+\omega^2}\delta(\omega+\omega'). \qquad (3.32)\end{aligned}$$

Integration over ω yields the spectrum $S_{x/p}$ of the OPO output. Now we write ε in terms of the OPO threshold c_{th} (eq. 3.21) such that $\frac{\varepsilon}{(T+L)/2} = c_{th}$ and normalize the spectrum by the vacuum variance $\Delta_0^2 = \frac{\hbar}{2}$ such that

$$S_{x/p}(\omega+\omega_s) = \pm\eta\frac{4c_{th}}{(1\mp c_{th})^2+4(\omega/(T+L))^2} \qquad (3.33)$$

$$\eta = T/(T+L), \qquad (3.34)$$

where η is called the *escape efficiency*, which describes the probability of the output mode exiting via the output coupler.
The frequency $\omega/(T+L)$ can be connected to the decay rate of the cavity [116] such that we can interpret $(T+L)$ as the dimensionless bandwidth BW_c of the cavity for signal and idler. We see that if the threshold is reached $c_{th} = 1, \eta = 1, \omega \to 0$, anti-squeezing at the central frequency reaches infinity $S_x \to 1/(\omega^2) \to \infty$ while squeezing approaches $S_p \to -1/(1+\omega^2) \to -1$, consistent with literature [30, 116, 117]. On a measurement device, like homodyne detection or a spectrum analyzer, the spectral density is measured, which is related to the spectrum via the equation [118]

$$\Phi_{x/p}(\omega + \omega_s) = 1 + \eta_{meas} S_{x/p}(\omega + \omega_s), . \tag{3.35}$$

It tells us, that the spectral density shows the spectrum with an offset, due to the vacuum variance (or shot noise in general), and a re-scaling factor, due to imperfect detection. We are now profiting from the fact that we have normalized the spectrum to the vacuum quadrature variance (otherwise the addition factor "1" would be the vacuum variance). The factor η_{meas} includes path losses after the OPO, detector efficiency, and other loss factors that will be discussed more in detail in subsection 3.1.4. We can now realize that we could have added the losses inside the cavity to η_{meas}, therefore showing that an imperfect escape efficiency is equivalent to adding losses after a perfect OPO. In fig. 3.2 (b) and (c) we can see how the squeezing develops with losses, threshold values, and in the frequency domain. We can see in (b) that the symmetry of squeezing and anti-squeezing is destroyed by losses, which act harsher on squeezing. In (c) we can see (for no losses) that the squeezing and anti-squeezing rapidly reduce within the cavity bandwidth. We note that the sensitivity to losses in (b) can be decreased by increasing the transmission of the output coupler. This discussion showed that the controllable parameters of our non-linear cavity system are the output coupler transmission $T_{s/i}$ and the transmission of the flat input mirror for the pump T_p. Losses are hard to control as they depend mostly on the losses inside the non-linear crystal, which also fixes the non-linearity.

To gain a better understanding of how the cavity properties are affected, let's take a closer look at the influence of the two tunable parameter $T_{s/i}$ and T_p. For this, we will define the most important formulas for two-mirror optical cavities [119] in table 3.2. Usually, the approximation for the Airy finesse is used in experiments. In our case of the dominant transmission T_p or $T_{s/i}$ we can approximate (first order Taylor expansion)

$$\text{pump or signal/idler} \quad \Delta\nu \approx \frac{cT}{4\pi L} \quad \text{and} \quad F \approx \frac{2\pi}{T} - \pi - \frac{5\pi T}{24}.$$

We can see that *decreasing* T_p leads to a smaller OPO threshold, but also a smaller bandwidth and a larger finesse for the pump. If we *decrease* $T_{s/i}$ this will reduce the escape

efficiency and therefore results in a reduction of the maximal possible squeezing in the system. It will also lead to smaller bandwidth and a larger finesse for signal and idler.
It is in our interest to decrease T_p up to the point where every pump regime is easily accessible with our laser and to increase $T_{s/i}$ such that the escape efficiency and therefore the maximal squeezing become sufficiently large. Importantly there is a trade-off with the bandwidth of the electronics, which we discuss in subsection 3.1.4.

Table 3.2: Important formulas for two-mirror optical cavities. Here $T+R=1$ are transmittivity and reflectivity, and $L'=2L$ is the absolute length of the cavity (including the crystal). the bandwidth is sometimes also refereed to as linewidth. The bandwidth/linewidth here is given in [Hz] and can be converted to [m] via $\Delta\lambda = \lambda^2\,\Delta\nu/c$.

Round trip time [s]	$t_{RT} = \dfrac{2L}{c}$	(3.36)
Photon decay time [s]	$\tau_c = \dfrac{t_{RT}}{\sum_i -\ln(R_i)}$	(3.37)
Free spectral range	$\mathrm{FSR} = \dfrac{1}{t_{RT}} = \dfrac{c}{2L}$ [Hz] $\quad \mathrm{FSR} = \dfrac{\lambda^2}{2L}$ [m]	(3.38)
Lorentzian bandwidth [Hz]	$\Delta\nu_L = \dfrac{1}{2\pi\tau_c} = \dfrac{c}{4\pi L}\sum_i -\ln(R_i)$	(3.39)
Lorentzian finesse	$F_L = \dfrac{\mathrm{FSR}}{\Delta\nu_L} = \dfrac{2\pi}{\sum_i -\ln(R_i)}$	(3.40)
Airy bandwidth [Hz][4]	$\Delta\nu_A = \dfrac{c}{\pi L}\arcsin\left(\dfrac{1-\sqrt{\prod_i R_i}}{2\sqrt[4]{\prod_i R_i}}\right)$	(3.41)
Airy finesse	$F_A = \dfrac{\mathrm{FSR}}{\Delta\nu_A} = \dfrac{\pi}{2}\left[\arcsin\left(\dfrac{1-\sqrt{\prod_i R_i}}{2\sqrt[4]{\prod_i R_i}}\right)\right]^{-1}$ $\approx \dfrac{\pi\sqrt[4]{\prod_i R_i}}{1-\sqrt{\prod_i R_i}}$	(3.42)

3.1.2.4 OPOs in the lab

In the lab, we are using three OPOs, where two have a type-II phase-matched bulk KTP crystal of dimension 3x3x10 mm^3 and the other a type-I phase-matched ppKTP (periodically poled) crystal of dimension 1x2x10 mm^3. All crystals are bought from the company *Raicol* and coated by the company *Layertec GmbH*. We will now name them such that in the rest of this thesis we will speak about OPOIIa, OPOIIb, and OPOI. Photos of all three OPOs are shown in fig. 3.3.

[4] $\Pi_i R_i = R_1 * R_2 * R_3 * ...$

The laser light at 532nm is used to pump the cavities and we are phase-matching signal and idler at 1064nm (IR), degenerate in frequency. OPOIIa and OPOI are semi-monolithic cavities, such that the input mirror is coated on one facet of the non-linear crystal, while OPOIIb has a flat input mirror. All cavities must have the same bandwidth and length such that we can guarantee good interference between all output states having the same spectral and spatial properties.
All three cavities have an output coupler curvature of 38mm. The transmission of the output coupler for the IR signal and idler is chosen to be $T_{s/i} = 0.1$. The transmission of the input mirror for the green pump is $T_p = 0.05$. The cavity length is chosen to be $L = 38$ mm and locked in resonance with the laser by a piezo-electric transducer (PTZ), which is glued to the output coupler.
As we want the cavities to be fully resonant, meaning *triply resonant* in the OPOII cases and *doubly resonant* in the OPOI case we use the degrees of freedom given in table 3.3. The change of the Nd:YAG crystal temperature changes the IR and thus the green output frequency such that we are adapting the OPO pump frequency. As this parameter can only be tuned for one cavity, we now understand why OPOIIb has its own input mirror. This ensures that the crystal can be tilted without changing the cavity axis. In general, the main loss channels are absorption in the crystal and scattering from surfaces inside the cavity. Therefore it is preferable to reduce the number of interfaces inside the cavity, which is why we can expect higher losses for OPOIIb. In table 3.3 we see that we need one active lock of the OPO cavity length on the 532 nm pump frequency. This is achieved via Pound-Drever-Hall locking and explained in the next subsection. All the degrees of freedom for signal and idler frequencies are passively stable but have to be optimized every 5-7 hours. Passively stable in this case means that the tilt of the IIb-crystal and the temperature of the crystals do not drift much over time. Of course, the temperature of each crystal itself is stabilized by a PID control. For the three OPOs, we use the *Vescent SLICE-QTC Four-channel Temperature Controller* with a stability below 0.2 mK since 2023.

To be able to monitor the tuning of those parameters, we inject infrared probe beams at the signal and idler frequency 1064 nm into the cavity. Then, by scanning the cavity length, we can overlap the peaks (or dips) of the three fields.

Table 3.3: Here the degrees of freedom, used to ensure triple or double resonance of the OPOs are shown. All cavities have a output coupler curvature of 38mm, a length of 38mm, $T_{s/i} = 0.1$ and $T_p = 0.05$.

OPO	pump	signal	idler
OPOIIa	IIa-cavity length	IIa-crystal temperature	Nd:YAG crystal temperature
OPOIIb	IIb-cavity length	IIb-crystal temperature	tilt of the IIb-crystal
OPOI	I-cavity length	I-crystal temperature	not needed

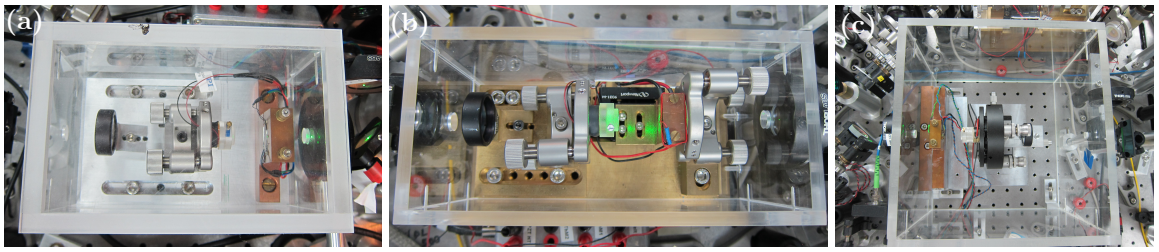

Figure 3.3: Here OPOI, OPOIIb and OPOIIa are shown in **(a)**-**(c)**. One can clearly see that only OPOIIb has an input mirror that is not coated on the crystal facet.

This procedure will be explained in subsubsection 3.1.3.2. After locking the cavity length, the power increase usually requires a slight adaptation of the signal and idler degrees of freedom due to thermal effects.

We can also measure the finesse of the pump, signal, and idler, which allows us to give a first approximation of the losses inside the cavity. Measuring the finesse consists of measuring the free spectral range and (Lorentzian) bandwidth on an oscilloscope trace while applying a large scan on the cavity PZT. Especially the bandwidth, being the FWHM of the peak, can cause resolution problems. A high sampling has to be guaranteed, such that one is sure to see the peak of the transmission faithfully. Otherwise, a fitting function can be used. A more precise way of characterizing the escape efficiency, and thereby the losses, is by analyzing the state fidelity of the OPO output states, which is given in section 3.2. The following finesses were measured and are given in table 3.4 and can give a first estimation of the losses[5]. The measured free spectral range is around 4.3 GHz, slightly above the expected theoretical value. The bandwidth of the selected TEM_{00} mode is therefore ≈ 60 MHz. The formulas to measure length, bandwidth, and FSR are given in section 8.2. The threshold input power of OPOI is estimated to be 50 mW, while the threshold power for OPOIIa and OPOIIb is estimated to be 80 mW [120].

Table 3.4: Here the measured finesse for pump and signal/idler frequencies of all three OPOs are given. From those, the losses can be estimated (est.).

OPO	pump finesse	signal/idler finesse	est. loss pump	est. loss signal/idler
OPOIIa	$F_p = 75.1$	$F_{s/i} = 68.0$	$L_p^{OPOIIa} = 0.03$	$L_{s/i}^{OPOIIa} = 0$
OPOIIb	$F_p = 50.9$	$F_{s/i} = 29.4$	$L_p^{OPOIIb} = 0.07$	$L_{s/i}^{OPOIIb} = 0.1$
OPOI	$F_p = 44.2$	$F_{s/i} = 53.5$	$L_p^{OPOI} = 0.09$	$L_{s/i}^{OPOI} = 0.01$

[5]Those values are obtained by fitting the traces on the oscilloscope to double exponential decays and should give the reader a feeling for the order of magnitude of finesse. Due to small fitting errors resulting in a big change of the Finesse, we do not expect those values to be precise.

3.1.3 Locking and Filtering

The main reasons why we need stable locks in this experiment are three-fold: Most simply we need stable locks to have stable OPO and filtering cavities. We further need a stable lock to have a stable reference power for alignment and third, we want to have a controlled phase between two paths interfering.

We will introduce the three types of locks we are using in our system and show how they are used in our setup. In table 3.5 we summarize the locking method for each locked system and specify how often we check those locks. The goal of the rest of this subsection is to explain this table. We will first elaborate on the elements to lock and then the locking methods.

Table 3.5: Here we see all locked elements in our setup, together with the locking method, if the PID is analog or digital and the continuity of the check. PDH stands for Pound-Drever-Hall locking and S&H for sample and hold.

Locked element	method	analog or digital	check
Mode cleaner	Tilt locking	digital since July 2023	continuous
Doubling laser cavity length	PDH	analog	continuous
OPO cavity lengths	PDH	digital since July 2023	S&H
OPO seed phase	side-locking	digital since July 2023	S&H
Micro cavities	side-locking	digital	S&H
Path fringes	side-locking	digital	S&H

3.1.3.1 Optical cavities as filters

Optical cavities can be used for filtering/ cleaning spatial and spectral aspects of a beam. We will use two- and three-mirror configurations, such that we choose to discuss three-mirror configurations as the more general case. In the case of cavities only containing parabolic mirrors, which is approximately our case, the cavity modes are Hermite-Gaussian TEM_{nm} modes, where n and m determine the shape of the beam profile in the x and y direction. In order for a mode to resonate (interfere constructively) the phase shift it experiences after each round trip has to be an integer i multiple of 2π. Moreover, only the two eigenpolarizations of the cavity can resonate, which are linear or degenerate without additional birefringence in the cavity [121]. The optical frequencies that can resonate within a cavity of n_M mirrors can then be defined via the resonance condition [122]

$$\text{H (p) polarization} \quad 2\pi i = \frac{4\pi L}{c}\nu_{n,m,i} + \varphi_{G(n,m)}, \tag{3.43}$$

$$\text{V (s) polarization} \quad 2\pi i = \frac{4\pi L}{c}\nu_{n,m,i} + \varphi_{G(n,m)} + \pi n_M \ (\mathrm{mod}\ 2), \tag{3.44}$$

where $\varphi_{G(n,m)} = (1+m+n)\varphi_{G(0,0)}$ is the Gouy phase shift[6], that takes into account the non-plane, Gaussian, wavefront evolution and is different for each TEM mode[7]. We see that higher-order Hermite-Gaussian modes have higher resonant frequencies than the fundamental mode ν_0. The fundamental mode here refers to $m = n = 0$, such that the beam profile is perfectly Gaussian. The fundamental modes resonate in the cavity axis, while all higher-order modes only appear as off-axis coupling, either by misaligning the cavity or the incoming beam. Therefore we note that a cavity can clean the incoming beam from higher order modes, outputting only the fundamental mode TEM_{00}. For this, the incoming light needs to be aligned onto the cavity axis, and the waist of the incoming beam ω_0 needs to be matched with the cavity waist x_0 and its position [124, 125]. A misalignment of the beam on the cavity axis creates coupling to mostly the TEM_{01} and TEM_{10} modes, while a waist size mismatch and waist positioning mismatch lead mostly to coupling to the TEM_{02} and TEM_{20} modes. The bandwidth for each TEM_{nm} is slightly different due to a change in effective cavity length L for the off-axis modes. Each cavity mode can then be expressed in the frequency domain as a Lorentzian

$$f(\nu) = \frac{1}{\sqrt{0.5\pi\Delta\nu_L^{i,m,n}}}\left(1+\left(\frac{\nu}{0.5\Delta\nu_L^{i,m,n}}\right)^2\right)^{-1} \tag{3.45}$$

and in time domain as a double exponential decay

$$f(t) = \sqrt{\pi\Delta\nu_L^{i,m,n}}e^{-\pi\Delta\nu_L^{i,m,n}|t|}. \tag{3.46}$$

The sketch of a frequency spectrum of an imperfectly coupled cavity is shown in fig. 3.4 (b).

Additionally one can use cavities as *band-pass or band-stop filters*. This can be more easily seen for triangular cavities, with distinct reflection and transmission ports as visible in fig. 3.4 (a), but can be applied as well to linear Fabry-Perot cavities. A cavity that is resonant to the frequency $\nu_0 = \nu_{0,0,0}$ adds a frequency dependent phase shift $\Phi = \Omega L/c$ to any sideband frequency $\nu = \nu_0 + \Omega$ for one round trip in the cavity. We can write the cavity amplitude transmission and reflection coefficient as

$$r(\Omega) = \sqrt{R_1} - \frac{T_1\sqrt{R_2R_3}e^{2i\Phi}}{1-\sqrt{R_1R_2R_3}e^{2i\Phi}}, \tag{3.47}$$

$$t(\Omega) = \frac{\sqrt{T_1T_2}e^{i\Phi}}{1-\sqrt{R_1R_2R_3}e^{2i\Phi}}, \tag{3.48}$$

[6] $\varphi_{G(0,0)} = -\arctan(z/z_R)$, where z_R is the Rayleigh length and $z = 0$ is the position of the beam waist

[7] Note that this degeneracy in polarization of the resonance condition is only valid if the angles of incidence on the mirrors are greater than the polarization Brewster angle [123]

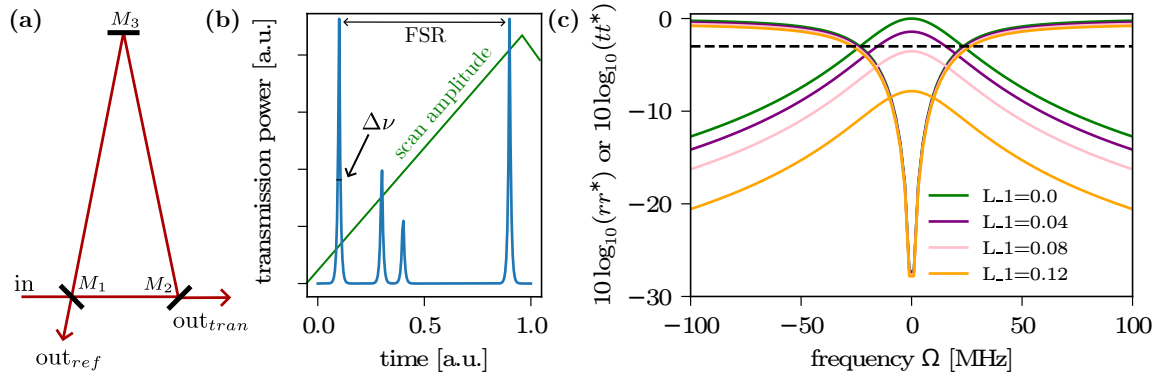

Figure 3.4: In **(a)** a sketch of a triangular cavity is shown with its two output modes, one in reflection and one in transmission. In **(b)** the sketch of a spectrum of an imperfectly matched cavity is plotted. We see the fundamental mode, accompanied by TEM_{01} mode due to imperfect alignment and TEM_{02} due to imperfect mode-matching. In **(c)** the output spectrum around the resonance frequency $\Omega = 0$ of the cavity is shown for the reflected spectrum (dip) and the transmitted spectrum (peak). Here a bandwidth of 20 MHz was chosen. The transmission heavily depends on the losses L_1 in the system. The dotted line marks -3 dB, and therefore the filter cut-off frequency.

where $r(\Omega)$ gives the reflected output port amplitude, while $t(\Omega)$ gives the transmitted output port amplitude. It is common to model all losses inside the cavity with one coefficient, where we choose the loss on M_1, such that $R_1 + T_1 + L_1 = 1$ but $R_2 + T_2 = 1$ and $R_3 + T_3 = 1$. Moreover, we will see that the cavity analysis becomes easier to read if we write the reflectivities in terms of the Lorentzian bandwidth, where we use $\Delta\nu_L \approx (1 - R_1R_2R_3)c/(4\pi L)$, which is the first order Taylor expansion of the Loretzian bandwidth of eq. (3.39). The reflectivities that are important in eq. (3.47) and (3.48) then become

$$R_1 = \sqrt{1 - \frac{4L\Delta\nu_L}{c}} \times (1 - L_1), \tag{3.49}$$

$$R_2R_3 = \sqrt{1 - \frac{4L\Delta\nu_L}{c}}/(1 - L_1). \tag{3.50}$$

Here we will additionally assume $R_3 = 1$, which is the ideal case. We can now insert the above equations (3.49) and (3.50) in eq. (3.47) and (3.48) and find

$$r(\Omega) = \frac{\sqrt{R_1}(1 - e^{2i\Phi})}{1 - \frac{R_1}{1-L_1}e^{2i\Phi}} \approx \frac{\Omega}{i\Delta\nu_L + \Omega}, \tag{3.51}$$

$$t(\Omega) = \frac{\sqrt{(1 - R_1 - L_1)(1 - \frac{R_1}{(1-L_1)^2})}e^{i\Phi}}{1 - \frac{R_1}{1-L_1}e^{2i\Phi}}. \tag{3.52}$$

The approximation in eq. (3.51) shows that the cavity acts as a band-stop filter at the reflected output and as a band-pass filter at the transmitted output. Ideally (without losses) the reflected port output filters out all frequencies within the cavity bandwidth, while the transmitted port only lets those frequencies pass. The band of the band-stop filter is mostly

dependent on the cavity bandwidth, while the band-pass filter quality[8] is strongly influenced by both loss L_1 and bandwidth. In fig. 3.4 (c) we see the effect of loss on a cavity with length $L = 1$ and bandwidth $\Delta\nu_L = 20$ MHz. Importantly the reflected port keeps its band-stop property, almost independent of the cavity loss, while the transmitted output port rapidly loses its filtering quality. The transmission port is often used to filter out laser intensity noise above the cavity frequency [126, 127].

Triangular cavities can moreover be used as *polarization filters*. Different from Fabry-Perot cavities, the round-trip phase shift is different for the two linear polarizations in a triangular cavity, as visible in eq. (3.43) and (3.44). Horizontally polarized light has a phase shift of 0 after one round trip, independent of the number of mirrors, while vertically polarized light (s-polarized) will have a phase shift of $\pi\ n_M$, where n_M is the number of mirrors in the cavity. The output is therefore non-degenerate in polarization, making it easy to reject one polarization by locking the cavity resonance on the other [122, 128]. This condition is only fulfilled for certain incident angles on the mirrors, as explained by S. Saraf et al. [123].

The first cavity in our setup that is used as a filter is the **mode cleaner**. It is a triangular cavity, placed at the output of the Nd:YAG infrared laser. At low frequencies, typically below 10 MHz, a laser has technical noise due to acoustic, thermal, or electrical disturbances as well as possible relaxation oscillation. This results in the beam showing intensity fluctuations above the standard quantum noise limit until a frequency of the order of 10 MHz. This is the case for our laser, for which a strong relaxation oscillation occurs around 1 MHz [104]. Next to using an inbuilt feedback called "noise-eater" we can also reduce the low-frequency noise by installing a triangular low bandwidth, high finesse cavity and use it as a band-pass filter in transmission, as described above. This will also ensure that we have a clean TEM_{00} mode at the output. It can be used at both linear polarizations, where it has a finesse of $F_V = 3500$ for vertically polarized light and of $F_H = 200$ for horizontally polarized light. Here we choose to work with the latter to ensure easier locking. The mode cleaner cavity is locked via tilt locking on the laser resonance.
The second important filter cavity type in our setup is called **micro cavity** and is a linear two-mirror Fabry-Perot cavity. Especially for detectors that are not mode selective, like on-off detectors or photon number resolving detectors, we have to select the output mode of the OPO cavity we want to detect. If we do not perform additional filtering that allows us to select, in our case ν_0, we would create a statistical mixture of several modes separated by the OPO FSR and could not detect high purity states. In our setup, a homemade micro cavity, in addition to an interferential filter (IF) from *Barr associates* centered at 1064 nm with a bandwidth of 125 GHz is placed before each non-mode-selective detector. The bandwidth of the homemade micro cavity is designed to be at least four times larger

[8] Quality here asks where the -3 dB cut-off frequencies are, relative to the ideal cavity bandwidth.

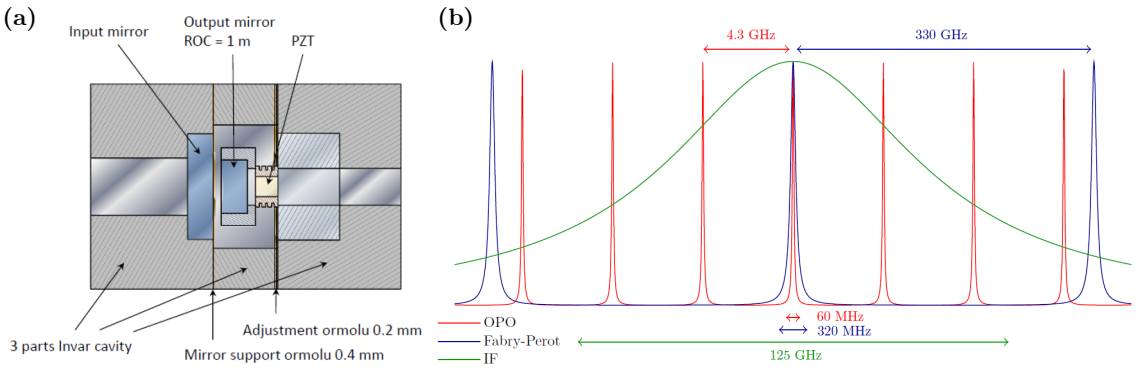

Figure 3.5: **(a)** shows the design of the homemade micro cavity, used to filter the OPO output. The cavity is composed of three invar modules that are screwed together in a bulk configuration. In **(b)** the filtering of the OPO output IR mode, at a free spectral range of 4.3 GHz and a bandwidth of 60 MHz (red), is shown. The first broad filtering is performed by an interferential filter (IF) with a bandwidth of 125 GHz. To have a clean output mode, the Fabry-Perot micro cavity with a bandwidth of 320 MHz and a free spectral range of 330 GHz is used.

than the OPO bandwidth, such that in the design considerations $\Delta\nu_{uCav} = 5\Delta\nu_{OPO} = 320$ MHz. Furthermore, the FSR should shift the non-centered resonance peaks beyond the IF bandwidth. We choose $\text{FSR}_{uCav} = 330$ GHz. If we now calculate the length of this cavity, we find $L = 0.45$ mm, hence the name micro cavity. The plano-concave cavity is built in a monolithic configuration, visible in fig. 3.5 (a). Input and output mirrors are coated by *ATFilms* and have a transmission of 0.3% each, ensuring the desired bandwidth and FSR. Its high filtering power due to the large finesse comes at the price of a lower transmission. The overall filtering scheme is shown in fig. 3.5 (b). Those cavities cannot be aligned as soon as they are closed. This is why it is very important to ensure that all the parts are assembled parallel to each other. In order to control the cavity length one can insert ormolu plates of 200-400 μm. The curved mirror has a radius of curvature (ROC) of one meter.
In total, we have three micro cavities in the setup, called μCavI, μCavII, and μCavIII. The (Lorentzian) finesse of the micro cavities has been measured to be $F_{\mu CavI} = 132.8$, $F_{\mu CavII} = 260.1$, and $F_{\mu CavIII} = 392.9$.

3.1.3.2 Cavities for up and down conversion

The other types of cavities in our systems have already been described in detail before. The doubling laser cavity is used to create a bright TEM_{00} output beam at 532 nm, see subsection 3.1.1. The three OPOs in our system generate our quantum states of interest, see subsection 3.1.2. The OPO cavity shapes the spatial and spectral output mode of the signal and idler. The interesting point to mention here is the fourth locked element in table 3.5, called **OPO seed phase**. To enable us to lock cavities and paths after the OPO with the resonance of the infrared OPO output, we need a stable reference beam. This is achieved by sending ("seeding") a few mW of the 1064 nm laser into each OPO cavity. The

cavity length is already locked onto the 532 nm green pump laser, such that the IR is by default also resonant. This configuration is called *optical parametric amplification (OPA)*. The seed power can be increased (amplified) or decreased (de-amplified) by constructive or destructive interference with the down-converted light from the pump. With the seed being polarized like the signal beam we find the phases [129]

$$\phi_s = \phi_s(0) \qquad \phi_i = \frac{\pi}{2} + \phi_p - \phi_s \qquad \phi_p = \phi_p(0) \tag{3.53}$$

of the light created in this three-wave mixing process. If (as in our case) the polarization is put at 45° between signal and idler, a stable relative phase $\phi_p - \phi_{s,i}$ between IR seed and green pump is needed in order to have a stable output power after the OPO.
We, therefore, install a piezo-electric transducer (PZT) on the IR seed path and lock it on any part of the amplification/de-amplification fringe. This does not only allow us to have a bright, stable output-power, locking light for path locks and micro cavities but could also be used to calculate the threshold power of the OPO [127].

3.1.3.3 A QUICK NOTE ON LOCKING

Here we want to give a quick overview of system control, specifically PID control. For a more in-depth discussion, we suggest the lecture notes on the control system design of K. Åström [130]. In order to lock, an error signal is needed. An error signal $e(t)$ is the direct response of the system to active or passive changes and incorporates the deviation from a desired set-point. This error signal is fed to a proportional–integral–derivative controller (PID) that sends a control signal $u(t)$ to the element of interest, mostly a piezo-electric transducer for controlling a path phase or cavity length or a Peltier element to control temperature. The error signal is modified by the PID such that the control signal is

$$u(t) = K_p e(t) + K_i \int_0^t e(\tau)d\tau + K_d \frac{d}{dt} e(t), \tag{3.54}$$

where K_p, K_i, K_d are the proportional, integral, and derivative gain. The integration adds a slow trend towards the set value, while the derivation allows for a fast reaction to changes. Often we set $K_d = 0$ to avoid unstable behaviour. Each PID has an electronic bandwidth, describing to which frequency noises it can react in dependence on its integration time and derivation precision. The limiting element is often the system itself, piezo-electric transducer, or Peltier element, which themselves have a limited bandwidth and in the case of PZT eigenresonance frequencies that limit its use.

We will now describe the three locking methods used in our setup for controlling piezo-electric transducers, where a locking method corresponds to a method to create an error signal. An ideal error signal has a linear region around the set point (not a symmetric behavior) such that we know in which direction we need to apply the correction. If we take

the simple example of taking a cavity transmission peak as an error signal we easily see that the theoretical set-point should be the peak maximum. However, any deviation from the peak is symmetric, such that the error signal gives us no indication of direction. The PID can therefore not discriminate the sign of the deviation from the set point and might drive the system away from the set point. In general, the reflected beam from the cavity is used to create an error signal. Its intensity shows the interference between two beams: one directly reflected from the cavity input mirror and another that circulated in the cavity. On resonance, those two beams are perfectly out of phase, leading to no measurable intensity. By using interference, the signal is independent of laser intensity fluctuations.
In fig. 3.6 we can see our three looking methods, which are explained in the next subsubsections.

3.1.3.4 Tilt locking

Tilt locking uses spatial mode interference between symmetric and asymmetric modes to lock a cavity to a laser frequency [131, 132]. As spatial modes are orthogonal to each other, no interference can be measured if the whole beams are detected. This is why this method necessitates split photodiodes, where the active area is divided into two or four elements and the beams centered between them. Here we use two elements of the four-split photodiode (until 2023: *EG&G C30843E*, now: *Thorlabs (PDQ80A)*) to lock the triangular mode cleaner cavity. We want to misalign the input beam such that a few percent of the beam power circulate in the TEM_{01} (or TEM_{10}) mode. As analyzed above, the cavity is not resonant on both TEM modes for the same length. If we scan the cavity around the TEM_{00} resonance, the TEM_{01} mode is fully rejected into the reflected port and as such has a phase that is independent of the cavity length. The TEM_{00} mode on the contrary does accumulate a phase in dependence on the cavity length deviating from resonance. Using TEM_{01} as a reference we can now measure the interference between the two beams on each split photodiode and subtract the two photodiode outputs, which gives zero on resonance. This can be seen in fig. 3.6 (a) on the right, where the electrical field vectors are shown in green for the TEM_{01} and in red for the TEM_{00} mode. The output of each photodiode is proportional to the squared vector summation (in black). The three examples in (a) show three points of a cavity length scan, where only the middle example is on resonance. Here we can see that the length of the vector summation (in black) is equal, such that a subtraction of the two photodiode outputs results in zero. The left and right examples are out of resonance, resulting in a non-zero subtraction with opposite signs.

3.1.3.5 Pound Drever Hall (PDH) locking

We follow closely the methodology outlined by E. Black [133] on PDH locking, with a particular focus on our use case. The PDH scheme is based on frequency(or phase)-modulated light, which generates the error signal via a beat note between the back-reflection of reso-

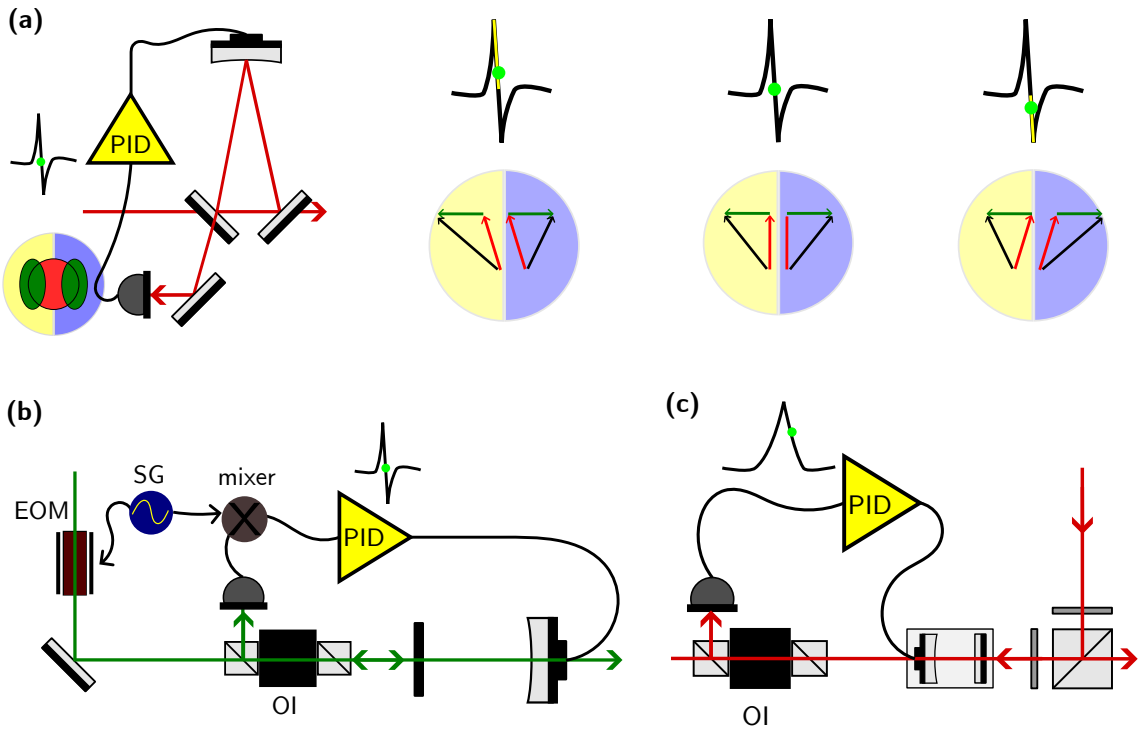

Figure 3.6: In **(a)** tilt locking on the mode cleaner is shown. We see that the reflection port of a triangular cavity is monitored by an effective two-quadrant photodiode. The intensity distribution of the detected TEM_{00} (red) and TEM_{01} (green) mode on the lower left. The output of each sub-photodiode is proportional to the vector summation (in black) of the electric field vectors (red and green) of the two modes, visible on the right side of the (a) from one side of the resonance to the other. The difference signal of the two photodiodes is the error signal, fed into the PID that controls the piezo-electric transducer, which determines the cavity length. In **(b)** the Pound-Drever-Hall method is depicted. This method requires sidebands on the incoming laser beam, created via an electro-optical modulator (EOM) that is driven by the signal generator (SG) at 12 MHz. The beat signal between the reflected sidebands and the resonant cavity mode exiting on the reflection port is separated from the main beam via an optical isolator. The output of the photodiode, which has to be faster than the modulation frequency, is mixed with the modulation from the signal generator. The demodulated signal is sent to the PID and can control the cavity length via the piezo-electric transducer of the output coupler. In **(c)** side-locking is shown, in the example of a micro-cavity. An additional beam ("alignment beam") is inserted as a counter-propagating beam into the cavity and its transmission is separated from the main beam via an optical isolator (OI). The recorded transmission is used to control the cavity length via the piezo-electric transducer of the input coupler.

nant and off-resonant frequencies impinging on the cavity. A beat-note is an output signal at the frequency difference between two optical frequencies, that impinges on a photodiode and is created if the two beams are indistinguishable in all degrees of freedom except for the frequency. The off-resonant frequencies, called sidebands, do not accumulate a phase as a function of the cavity length and can therefore act as a reference. Inside the laser-head the 1064 nm laser beam is phase-modulated via an electro-optical modulator (EOM) at

12 MHz, creating sidebands at integer multiples of ±12 MHz. The electrical field can be written as

$$E_{in} = E_0 e^{i(\omega t + \beta sin(\Omega t))} \approx E_0(J_0(\beta)e^{i\omega t} + J_1(\beta)e^{i(\omega+\Omega)t} - J_1(\beta)e^{i(\omega-\Omega)t}, \tag{3.55}$$

where β is the modulation depth (strength), which is assumed to be small enough to only create first-order sidebands. We use the Bessel functions to expand the first expression. In the case used for the PDH technique we only want one pair of sidebands to appear, meaning that we want low modulation depth, such that the total power of the beam splits as

$$P_0 = P_c + 2P_s = J_0^2(\beta)|E_0|^2 + 2J_1^2(\beta)|E_0|^2, \tag{3.56}$$

where P_0 is the power impinging on the cavity, P_c is the power in the carrier frequency, and P_s is the power in each sideband. The reflected power P_r after the beam impinged on the cavity is then measured on a fast photodiode that has at least enough bandwidth to resolve the beat pattern, as visible in fig. 3.6 (b). The reflected power can be written with the help of eq. (3.51) where we assume the cavity to be resonant on ω'

$$E_r = E_0\Big(r(\omega)J_0(\beta)e^{i\omega t} + r(\omega+\Omega)J_1(\beta)e^{i(\omega+\Omega)t} - r(\omega-\Omega)J_1(\beta)e^{i(\omega-\Omega)t}\Big), \tag{3.57}$$

$$\begin{aligned} P_r = |E_r|^2 &= P_c|r(\omega)|^2 + P_s(|r(\omega+\Omega)|^2 + |r(\omega-\Omega)|^2) \\ &+ 2\sqrt{P_c P_s}\Re[r(\omega)r^*(\omega+\Omega) - r^*(\omega)r(\omega-\Omega)]\cos(\Omega t) \\ &+ 2\sqrt{P_c P_s}\Im[r(\omega)r^*(\omega+\Omega) - r^*(\omega)r(\omega-\Omega)]\sin(\Omega t) + \mathcal{O}(2\Omega), \end{aligned} \tag{3.58}$$

where we omitted terms that are oscillating at $\geq 2\Omega$. To create an error signal we now have to find a way to extract the deviation δ of the carrier frequency from the cavity resonance frequency ω' inside of r, where we need to see the phase of this deviation. This is only possible in the terms oscillating at Ωt, as all other terms lose the phase information by being squared. Until now we have made no assumption on the relationship between the sidebands and the bandwidth of the cavity. We can use the relationship between the Lorentzian bandwidth and the FSR of the cavity. By using the first-order Taylor expansion of the Lorentzian bandwidth $\Delta\nu_L \approx (1 - R_1R_2)c/(4\pi L)$ and the FSR $\mathrm{FSR} = c/(2L)$ we find $\Delta\nu_L \approx \mathrm{FSR}(1 - R_1)/(2\pi)$, where we assume R_2 to be high. If we think about the case of the OPOs, where the PDH is used on the green pump beam, then this is indeed the case as the output coupler has high reflectivity ($R_2 \to 1$). We can now write the sideband frequency in terms of the Lorentzian bandwidth divided by the finesse, multiplied by a proportionality factor k, such that $\Omega = k\Delta\nu_L/F_L = k(\Delta\nu_L)^2/\mathrm{FSR} = k\ \mathrm{FSR}(1-R)^2/(4\pi^2)$, where we rename $R_1 = R$. Moreover, we can write r, given by eq. (3.51) in dependency of $\phi = \Omega L/c = \Omega/(2\mathrm{FSR}) = k(1-R)^2/(8\pi)$. We can now write the terms of eq. (3.58)

that oscillated with Ω with this proportionality factor and find after a first-order Taylor expansion around $\omega + \delta$, assuming a small deviation from the cavity resonance $\omega' = \omega + \delta$

$$r(\delta)r^*(\delta+\Omega) - r^*(\delta)r(\delta-\Omega) \propto \delta\left(i - i\cos\left(\frac{k}{4\pi^2}(R-1)^2\right) + \sin\left(\frac{k}{4\pi^2}(R-1)^2\right)\right) \left((L-R-1)R + (L-1)^2\left[\cos(\frac{k}{4\pi^2}(R-1)^2) + i\sin(\frac{k}{4\pi^2}(R-1)^2)\right]\right) \tag{3.59}$$

$$\text{for} \quad k \gg 1 \qquad \propto i\delta \tag{3.60}$$

$$\text{for} \quad k \leq 1 \qquad \propto \delta \tag{3.61}$$

showing that if the sidebands are larger than the bandwidth divided by the finesse, this term becomes imaginary such that we want to isolate the $\sin(\Omega t)$-term in eq. (3.58), while if the sidebands are transmitted by the cavity we want to isolate the $\cos(\Omega t)$-term in eq. (3.58) in order to get a signal that is proportional to the deviation from resonance δ.
To isolate the cos or sin terms, we are mixing the output signal of our photodiode $\propto P_r$ with the modulation signal $\sin(\Omega' t)$ that was sent to the EOM. Here we are trying to isolate the $\cos(\Omega t)$-term such that after mixing

$$\sin(\Omega t)\cos(\Omega' t) = \frac{1}{2}\big(\sin([\Omega - \Omega']t) - \sin([\Omega + \Omega']t)\big) \tag{3.62}$$

we want a DC signal. We therefore need to apply a $\pi/2$ phase shift one of the two electrical inputs into our mixer (by simply adding BNC cables) such that $\Omega' t = \Omega\, t + \pi/2$, giving us a DC term $\sin(\pi/2) = 1$ and a fast oscillating term $\sin(2\Omega\, t + \pi/2) = \cos(2\Omega\, t)$. After the mixer, our electrical signal power P_{mix} will be proportional to

$$P_{mix} \propto \sin(\Omega\, t)\big(P_c|r(\omega)|^2 + P_s(|r(\omega+\Omega)|^2 + |r(\omega-\Omega)|^2)\big) + 2\sqrt{P_c P_s}\delta + \mathcal{O}(2\Omega), \tag{3.63}$$

from which the error signal can be extracted by applying a low-pass filter, suppressing all the oscillating terms at Ω or higher, such that the power of the error signal P_e becomes proportional to the deviation from the cavity resonance

$$P_e \propto 2\sqrt{P_c P_s}\delta, \tag{3.64}$$

which can be fed into the PID and now used for locking.
We note that the first time PDH is used in our setup is for the doubling cavity. As this cavity does not reject the sidebands, they carry over to the green 532 nm output and are subsequently used for locking all OPO cavities. At the output of those cavities, the signal and idler will also carry those sidebands, which will be visible in their squeezing spectrum.

The error signal is then created via analog mixing. The PDH locking of the OPO cavities was changed from an analog custom-made PID to a digital PID lock in 2023 by using a low noise Red Pitaya *STEMlab 125-14 Low Noise* together with the python package *PyRPL* [134], which is used for both PDH and side-locking.

3.1.3.6 Side locking

Side locking uses the cavity transmission as the error signal. As we have already stated, the peak of the transmission should not be used for locking, as a slight detuning of the cavity length gives no indication in which direction we need to correct. Locking at the top will therefore lead to an increase in locking noise. If the locking point we are aiming for is not the peak, we regain the power of knowing the direction and can use the transmission as an error signal for the price of losing power as the maximal output power will be at the peak. This is why this technique is called "side" locking and not "peak" locking. Optimal locking is achieved in the steepest slope of the cavity transmission. This method is extremely easy and used in our setup for locks that do not require high power outputs, like the micro-cavities, OPO seed-to-pump phase, and relative phases of path interferences. Side locking in this experiment is always performed via an electronic PID, programmed on the micro-controller *ADUC7020*. The corresponding code can be found in the thesis of H. Le Jeannic [135].

3.1.4 Homodyne detection

We have already briefly mentioned homodyne detection in subsection 2.3.2, as our preferred method for state analysis. Homodyne detection aims at recording the quadratures of the signal field at different angles by interfering it with a bright coherent beam, the *local oscillator*, on a 50:50 beamsplitter. Here we follow the analysis of Ling-An Wu, Min Xiao, and H. J. Kimble [118]. Each beamsplitter output is detected on a photodiode, creating the photocurrents $i_1(t)$ and $i_2(t)$, whose subtraction results in the current $i(t) = i_1(t) - i_2(t)$. We can now analyze the homodyne output in time and frequency, where we will add the effect of losses in the frequency domain.

3.1.4.1 Homodyning in the time domain

The basic idea (without losses) is sketched as follows. Let us define the signal mode $\hat{a}_s$ and the bright local oscillator $\alpha = E_0 e^{i\theta}$. After impinging on a 50:50 beamsplitter the output modes are

$$\hat{a}_1 = \frac{1}{\sqrt{2}}\left(E_0 e^{i\theta} + \hat{a}_s\right) \qquad \hat{a}_2 = \frac{1}{\sqrt{2}}\left(E_0 e^{i\theta} - \hat{a}_s\right), \tag{3.65}$$

$$i_{1,2} \propto \hat{n}_{1,2} = \hat{a}_{1,2}^\dagger \hat{a}_{1,2} = \frac{1}{2}\left(E_0^2 + \hat{n}_s \pm E_0(\hat{a}_s e^{-i\theta} \mp \hat{a}_s^\dagger e^{i\theta})\right), \tag{3.66}$$

$$i = i_1 - i_2 \propto E_0(\cos(\theta)\hat{x}_s + \sin(\theta)\hat{p}_s) = E_0 \hat{x}_s^\theta, \tag{3.67}$$

where we can see that after subtraction the current $i(t)$ is proportional to the quadrature of the signal field, rotated by the relative phase θ between the signal and local oscillator. Importantly here we assume that the time to take a measurement t is smaller than the time needed for a phase change. Experimentally we guarantee this by adding a slow active phase scan with a piezo-electrical transducer. In the above calculation, we implicitly assumed that the measured current i at one time is equivalent to the whole mode of our state in the time domain. While this is true for the pulsed regime, in our case we have a continuous trace of current values, transformed to voltage $v(t)$, that we need to integrate over the temporal mode $f(t)$ of the signal mode of eq. (3.46), such that the real quadrature is calculated as

$$x^{\theta} = \int v(t) f(t) dt, \tag{3.68}$$

where the integration limits have to be adapted to the temporal mode. Any time trace with the values $v(t)$ is recorded in a mixture of all possible temporal modes and by the above integration we are performing a projection onto the temporal mode of the cavity. This is equivalent to an eigenanalysis, as we will see in section 3.3.

3.1.4.2 Homodyning in the frequency domain

Instead of recording a time trace on an oscilloscope, we can think about the output of the homodyne detection in the frequency domain, plugged into a spectrum analyzer. We mainly follow the analysis of Wu et al. [118]. In this case, we expect that the spectral density $\Phi(\nu)$ as in eq. (3.35) of the current $i(t)$ is recorded and can write

$$\Phi(\omega) = \int \langle \Delta i(t)\ \Delta i(t+\tau) e^{-i\omega\tau} d\tau \rangle \quad \text{where} \quad \Delta i(t) = i(t) - \langle i \rangle\,, \tag{3.69}$$

where τ is the response time of the detector. For the simplest case of both photodiodes having a delta function response, one can write

$$\begin{aligned} \langle \Delta i(t)\ \Delta i(t+\tau) e^{-i\nu\tau} d\tau \rangle =& (R_1 Q_1^2 + R_2 Q_2^2)\delta(\tau) + R_1^2 Q_1^2 \lambda_{11}(\tau) + R_2^2 Q_2^2 \lambda_{22}(\tau) \\ & - R_1 R_2 Q_1 \lambda_{12}(\tau) - R_1 R_2 Q_1 Q_2 \lambda_{21}(\tau), \end{aligned} \tag{3.70}$$

where R_i is the count rate of each photodiode, $Q_i = eG_i$ the charge per photopulse, where G_i is the gain of the detector and λ_{ij} is a fourth-order correlation function. In the limit of a strong local oscillator $E_{LO} = E_0 e^{i\theta}$, the count rates depend on the beamsplitter coefficients $R_{BS} + T_{BS} = 1$ and the quantum efficiency of each detector η_{PDi}, such that the count rates of the photodiodes are $R_1 = \eta_{PD1} R_{BS} E_0^2$ and $R_2 = \eta_{PD2} T_{BS} E_0^2$. With those assumptions, we find the spectral density

$$\Phi(\omega, \theta) = \langle Q_1 i_1 + Q_2 i_2 \rangle\, (1 + \eta_{meas} S_{\theta}(\omega_s + \omega)), \tag{3.71}$$

where ω_s here is set by the local oscillator frequency, η_{meas} the measurement efficiency and $S_\theta(\omega_s+\omega)$ the spectrum of the signal. If the signal input is vacuum we measure $\Phi(\omega,\theta)_0 = \langle Q_1 i_1 + Q_2 i_2\rangle$ (compare to eq. (3.33)), such that as in eq. (3.35) we can normalize the homodyne output by the vacuum noise experimentally, such that after normalization we have the normalized spectral density $\Phi'(\omega,\theta) = 1 + \eta_{meas} S_\theta(\omega_s+\omega)$. Importantly this spectral density can only be measured within the bandwidth of the homodyne detector. This requires the bandwidth of the homodyne detector to be adapted to the bandwidth of the OPO cavity, as otherwise, we would lower the overall detector efficiency.

3.1.4.3 Homodyne measurement efficiency

Let us now focus on the overall detector efficiency η_{meas}. It is comprised of the loss on the signal path L_s, the mode overlap $O = V^2$, connected to the visibility V of the signal beam and local oscillator, the photodiode quantum efficiency η_{PD} (which are assumed to be equal) and the efficiency reduction due to electronic noise of the detector η_{noise}, such that

$$\eta_{meas} = (1 - L_s)V^2 \eta_{PD} \eta_{noise}. \tag{3.72}$$

Electronic noise adds random values to each quadrature measurement. As we are calibrating each quadrature element by a vacuum measurement, we are effectively re-scaling the quadratures due to those random values, which can be shown to be equivalent to loss [136]. While path losses L_s can be reduced by choosing better optical components and the mode overlap O can, in continuous wave experiments, almost be increased to unity, a smart choice has to be made for the photodiodes and electronic components of the homodyne to combine the targeted bandwidth with low noise. The electrical noise can be measured via the clearance C, which shows the signal-to-noise ratio in decibel [dB], and therefore corresponds to the difference between the spectral density of the homodyne electronics without any input light and the spectral density with input light. It depends on the local oscillator power and can be used to calculate the electronic noise efficiency [137] as

$$\eta_{noise} = \frac{C-1}{C}. \tag{3.73}$$

Note that increasing the local oscillator power only increases the clearance in the linear region of the homodyne detector. Linear here means that the response of the photodiodes and amplifiers, and therefore the response of the detector increases linearly with the power. This poses a power limit on the local oscillator.

3.1.4.4 Homodyne circuit considerations

The most widely used circuit design for homodyne detection is the *current subtracting design*, visible in fig. 3.7 (a). Here the two currents are subtracted before undergoing any electronic gain. Each photodiode PDi has a junction capacitance C_{PDi} and shunt resistance

R_i, where ideally the capacitance should be as small as possible and the resistance as high as possible. This can be understood when writing down the photodiode bandwidth [138]

$$f_{PD} = \left(\frac{1}{f_t^2} + \frac{1}{f_{RC}^2} \right)^{-1/2}, \tag{3.74}$$

where $f_{RC} = 1/(2\pi RC)$ is the known cut-off frequency for a simple RC low pass filter and f_t is the transit limit bandwidth of the device. We can easily see that f_{RC} grows inversely proportional to C. The shunt resistance R_i leads to the resistance of the zero-biased photodiode junction, which ideally is infinite. Of course, photodiodes have to be chosen that have a good quantum efficiency at our target wavelength of 1064 nm. We choose *Fermionics FD500N-1064* with a bandwidth of several GHz and a quantum efficiency of $\eta_{PD} = 0.98$. The two photodiodes have opposite biasing, such that Kirchhoff's law dictates that the merged current is a subtraction $i(t) = i_1(t) - i_2(t)$. The following description of the circuit is highly simplified and should give a feeling about what the components in the circuit are for. A more in-depth analysis can be found in the PhD thesis of O. Morin [30]. The subtracted current $i(t) = i_1(t) - i_2(t)$ is converted to voltage via a transimpedance amplifier (TIA), where the clearance can be improved by selecting an appropriate capacitance C_3 and resistance R_3. The resistance R_3 converts the current to a voltage via Ohm's law but it also forms a low pass filter with the capacitance of the photodiodes. This is why C_3 is introduced in parallel to R_3 to counteract by decoupling the circuit before and after the amplifier. R_3 and C_3 also form a low-pass filter. Typically the clearance increases with increased resistance R_3 at the price of a decreased bandwidth. We can see that a capacitor C_4 and resistance R_4 form a high pass filter. On this output, there is no DC-offset. This *high-frequency output* is used to record the measurement traces. The *low-frequency output* part undergoes a high gain amplifier with variable offset. With our current parameters, we expect a bandwidth of 50 MHz, visible in the power spectral density of fig. 3.7 (b) and the homodyne clearance, plotted in (c). There are two identical homodyne detectors in our setup.

We can now perform a *detector efficiency analysis* of our two homodyne detection stages. For this, we analyze the electronic noise at the local oscillator measurement power of around 6 mW and the effect it has on the cavity spectrum $S_C(\nu) = |f(\nu)|^2$, where the cavity mode $f(\nu)$ is defined in eq. (3.45). The electronic noise efficiency is shown in fig. 3.7 (d) in the frequency domain and is multiplied in (e) with the cavity spectrum.

The *integration* of the difference between the lossy cavity spectrum and the lossless cavity spectrum is defined as the *electronic noise inefficiency*. Importantly we can see in (e) that for a homodyne detection, the low-frequency noise is dominant for the degradation of the cavity spectrum. We calculate that with the measured clearance, the losses would increase by only 1% if the cavity bandwidth is increased from 60 MHz to 100 MHz. All homodyne noise contributions are given in table 3.6.

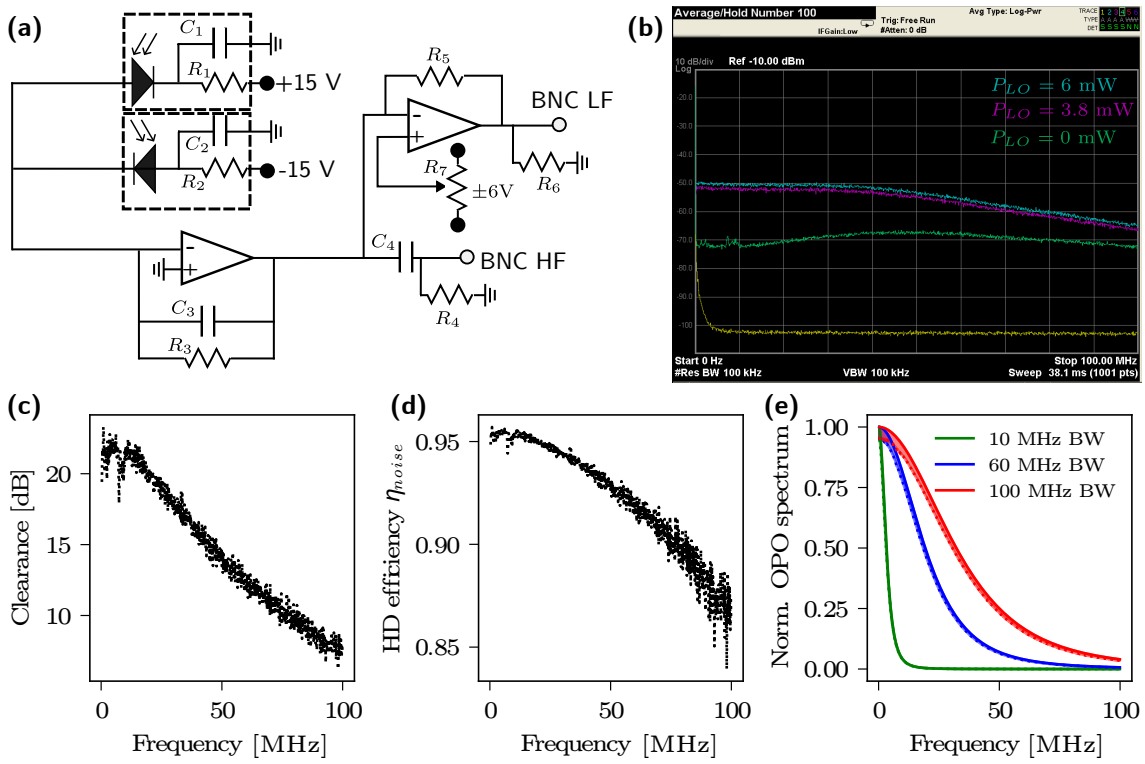

Figure 3.7: In **(a)** our simplified homodyne detection circuit is shown. The light is impinging on two photodiodes, with their junction capacitance and shunt resistance C_1, R_1 and C_2, R_2. Their subtracted current is amplified and converted to a voltage by the transimpedance amplifier. The homodyne has a high-frequency output (HF) and a low-frequency output (LF). In **(b)** the power spectral density of the homodyne for different power levels of the local oscillator is depicted. The corresponding clearance for a local oscillator power of 6 mW is shown in **(c)**. The homodyne noise efficiency in the frequency domain is shown in **(d)** and its effect on the cavity bandwidth spectrum for different cavity bandwidths can be seen in **(e)**. The solid lines show the cavity spectrum for no noise, while the dotted lines show the cavity spectrum for the measured HD efficiency of (d). The integrated difference between those two curves is defined as the loss due to the homodyne electronics.

Table 3.6: Here the overall HD efficiency is shown for all three OPOs. OPOIIa and OPOIIb use the same homodyne but are different in mode matching, while OPOI uses its own homodyne. Transmission, Visibility, and noise efficiency are experimentally measured, while the PD efficiency was given by the manufacturer.

path	transmission T_s	Visibility V	PD efficiency η_{PD}	noise efficiency η_{noise}	η_{meas}
OPOI	0.92	0.996	0.98	0.95	0.85
OPOIIa	0.90	0.993	0.98	0.95	0.83
OPOIIb	0.90	0.990	0.98	0.95	0.82

We will see later, that one can correct for all losses given in table 3.6 before reconstructing the state from homodyne measurement. This process will be explained in the section 3.3.

3.1.5 On-off detectors: SNSPDs inside a cryostat

In our setup, we want to perform non-Gaussian operations and on-off detectors as described in eq. (2.277) are the most used detectors to induce non-Gaussianity. We have four superconducting nanowire single-photon detectors (SNSPD) in a custom-made cryostat from *MyCryoFirm*. We will first describe the cooling stages of the cryostat and the working principle of SNSPDs. We will then discuss further improvements and current limitations of the system. In the last subsubsection, we will discuss two problems we encountered after the repair of our cryostat and how we could solve them.

3.1.5.1 Cooling principle of the cryostat

The cryostat reaches a stable temperature of 1.3 K for on average five days, such that we can cool it down remotely on Sunday and leave it to warm up over the weekend. It has two cooling mechanisms: a commercial cooling stage reaching 4K and a custom-made saturation-based cooling stage to reach 1.3 K. The first one cools the cryostat from room temperature to 50 K and then to 4 K via a *two-stage Gifford McMahon* (GM) cooling cycle. This closed-cycle cryostat therefore needs an expander (usually called cold-head), compressor, vacuum shroud, and radiation shield. We use the commercial cold head *Sumitomo RDK101-D* and water-cooled helium compressor *Sumitomo HC-4E2*. Cold-head and compressor are connected by two gas lines and an electrical power cable. One of the gas lines supplies high-pressure helium gas to the cold-head, and the other gas line returns low-pressure helium gas from the cold-head, which is sketched in fig. 3.8 (a) and photographed in (c). The cooling capacity of the cold-head is dependent on the Helium gas flow rate at both pressures. The vacuum shroud is the vacuum created at the cold end of the cold-head, isolating the created cold from the room temperature. The radiation shield is cooled via the first stage such that no room temperature thermal radiation from the vacuum shroud disturbs the second cooling stage.

The MG cooling cycle has four stages. First, the high-pressure valve is opened. Due to its high pressure, the gas passes through the regenerating material[9] into the expansion space. In the second stage, the pressure differential forces the displacer upwards such that the gas can expand and cool at the bottom. In the third stage, the low-pressure output is opened, which now makes the cold gas flow through the regenerating material and into the output. While passing through the regenerating material the gas removes heat from the system. In the fourth step, the displacer returns to its original position due to the pressure differential, and the cycle can start anew. In a two-stage MG cycle, the above-described stages happen for both cycles at the same time.

[9] It stores heat from a warm gas passing through it and supplies heat when cold gas is passed through it.

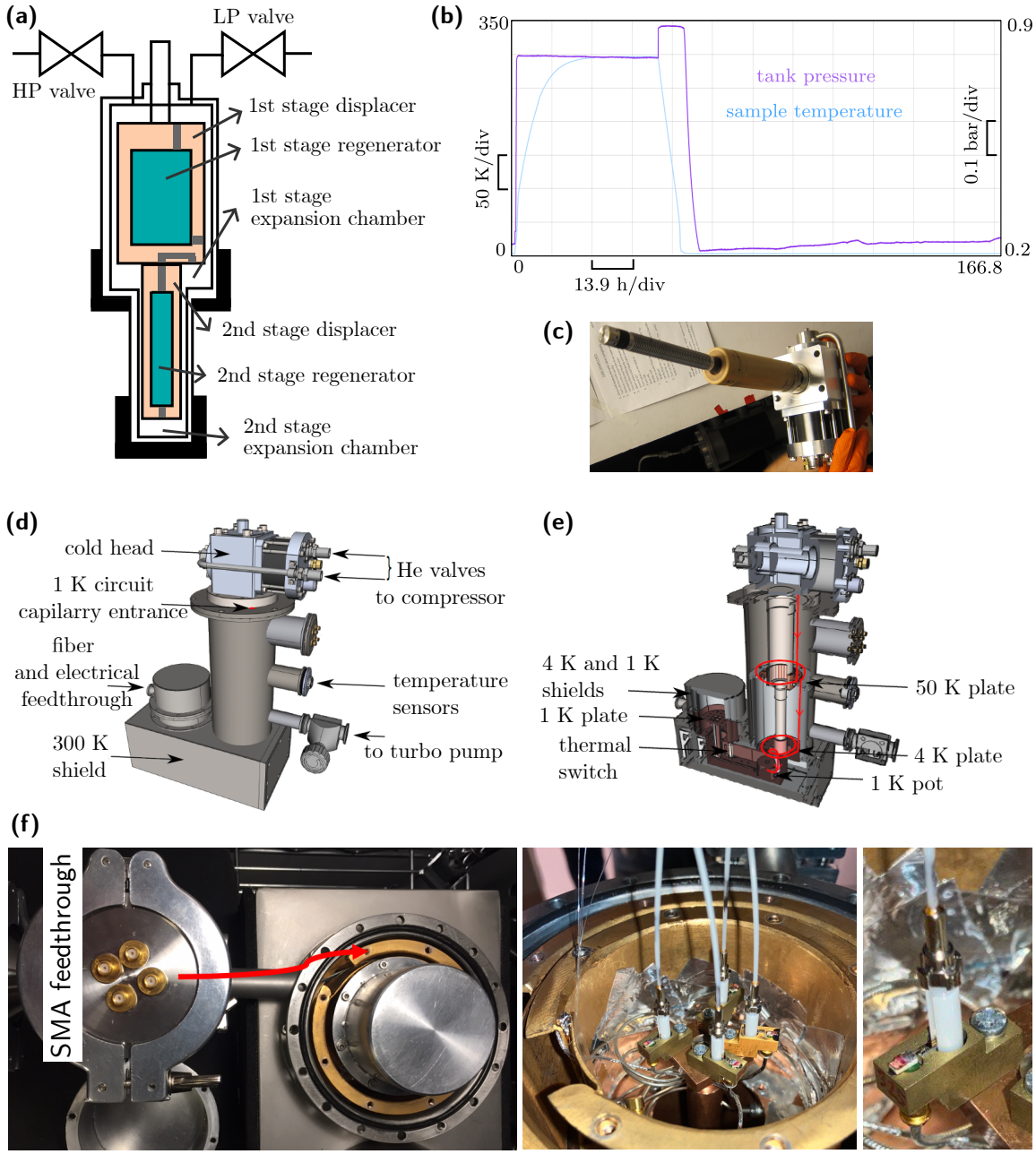

Figure 3.8: In **(a)** the coldhead for a two-stage Gifford McMahon cooling cycle is shown. The 1st and 2nd stage displacer are moving together, such that temperatures around 4 K can be reached within half a day. A photo of the coldhead in our system is shown in **(c)**. In **(b)** the screenshot of a typical cooling cycle of one week is shown from Sunday to Friday. The technical drawing of the whole cryostat system is shown from the outside in **(d)** and from the inside in **(e)**. The SNSPDs installed in the cryostat are shown in **(f)**, where they are screwed onto the cold-plate that is connected to the 1 K-pot. Fibers and electrical feed-through are homemade.

After 4 K has been reached, the second cooling mechanism comes into play, which is completely independent.

It uses the fact that condensation cools down a system. The gas that we use for the condensation is again He^4, which is stored in a tank beneath the cryostat at a pressure of 800-1000 mbar. This tank is connected to capillaries that circulate through the coldhead, first passing the 50 K stage for thermalization and then passing through the 4 K stage, being driven by a dry scroll pump *Edwards nXDS 15i*. When the Helium thermalizes with the 4K stage at this pressure, it condenses. For the condensation temperature under certain pressure, we can use the approximation of the Clausius–Clapeyron equation, to get an approximate saturation/condensation temperature

$$T_{sat} = \left(\frac{1}{T} - \frac{R}{H}\ln\left(\frac{P}{P_{sat}}\right)\right)^{-1}, \tag{3.75}$$

where T $[K]$ is the temperature of the gas, R $[J/(\text{mol } K)]$ is the specific gas constant, H $[J/\text{mol}]$ is the specific latent heat, P [mbar] is the actual pressure of the gas and P_{sat} [mbar] is the saturation pressure. For He^4 we have $R = 8.313$ $J/\text{mol } K$, $H = 84.5$ J/mol, $P_{sat} = 1013.25$ mbar such that for a temperature of $T = 4.2$ K and a pressure of $P = 800-1000$ mbar we find a saturation temperature of $T_{sat} = 4.1-3.8$ K, which can be provided by our commercial cooling stage. The lower the pressure, the lower the temperature needs to be for the saturation to occur. The saturation itself is happening in a *flow impedance*, favoring condensation, that is placed right before the 1 K pot, which stores the condensed Helium. A flow impedance is a porous disordered material placed within the capillary. The material exerts an attractive potential on the fluid, such that a liquid film can form on its surface. This creates a liquid-gas interface, inducing a pressure difference between the two phases such that the unconfined Helium saturation pressure is lowered in the medium [139]. The 1 K pot is then thermally connected to the sample region via a cold-plate. In fig. 3.8 (b) we can see a screenshot of the cooling cycle of our cryostat. Here it was turned on on Sunday and kept cold until Friday.

3.1.5.2 Electrical and optical feed-through

The SNSPDs have an electrical feed-through via vacuum-compatible SMA-to-SMA connectors. From 2020-2023 we have been using homemade SMA-to-SMP stainless steel coaxial cables to connect the SNSPD (SMP) to the feed-through (SMA). Stainless steel has a low thermal conductivity, which enabled us to not thermalize those cables. Unfortunately, they also exhibit low electrical conductivity, such that we chose to exchange them with commercial SMA-to-SMP cupronickel coaxial cables from *Intelliconnect C-SPSMPJ-CNCN047-1M* with a length of one meter. Those cables now need to be thermalized via aluminium tape at the 4 K stage.

The optical feedthrough is ensured by a homemade fiber feed-through. The fibers *Oz Optics SMJ-32.5F-1064/125-0.25-1.1-AR2* have an FC/PC connector for outside the cryostat and a fiber ferrule end face that is AR coated and can be plugged directly to the SNSPD (as

visible in fig. 3.8 (f)). The fibers are passed through a homemade QF16 centering ring and are then sealed applying vacuum epoxy *Varian Torr Seal*. The fiber ends hanging out of the QF16 centering ring are passed through a QF16 to QF50 reducing nipple to protect the sensitive parts around the epoxy. The fiber ends are then fixed on a QF50 flange with four FC/PC to FC/PC mating sleeves *Thorlabs ADAFC2*. This structure can easily break at any point of the fiber, when not handled with care. In total, we have four optical fibers leading to the four detectors. The transmission from the mating sleeve to the ferrule was measured to be above 80% for each fiber feed-through at room temperature.

3.1.5.3 Working principle of SNSPDs

Superconducting nanowire single-photon detectors (SNSPDs) are high-speed, high detection efficiency, and low noise on-off detectors that are based on superconductivity and thus need a cryostat to operate. Our WSi SNSPDs are provided by *NIST* and are starting to be superconducting around 1.5 K. The working principle is given with the electrical equivalence scheme in fig. 3.9 (a). The model description of the SNSPDs follows mostly Kerman et al. [140]. The SNSPD is modeled with a variable resistance R_n, which is zero in the superconducting state, and has a kinetic inductance L, which is proportional to the device area and depends on the substrate. The current I_d is the current flowing through the SNSPD, which is biased at I_0. Each nanowire has a critical current I_c above which it loses its superconductivity. The nanowire response is read out via the load impedance R_L, which is typically the transmission line resistance of 50 Ω and has a current I_L flowing through it. Usually, one wants to operate the device as close to I_c as possible, to obtain the highest sensitivity to photons, translating directly to the quantum efficiency. We note, that R_n and R_L form a current divider.

As long as the nanowire is superconducting, such that $R_n = 0$ Ω all current is flowing through the nanowire, such that $I_L = 0$ A. As soon as a photon hits the nanowire, hundreds of Cooper-pairs are broken by the photon energy being up to three orders of magnitude larger than the Cooper-pair binding energy. The such created quasi-particles form a hotspot in the nanowire and the current now flows around this hotspot, where the device is still superconducting. Now, because the effective area of the SNSPD changed (excluding the hot spot) the critical current is lowered in the region around the hot spot, leading to the biasing current exceeding the critical current. The resistive area can therefore grow around the hot-spot until it exceeds the width of the nanowire, by which time it has a resistance of several hundred ohms. Due to Joule heating it expands along a large section of the nanowire [141]. As soon as the nanowire has some resistance, part of the current is divided towards I_L. The nanowire resistance R_n grows exponentially after the detection of a photon but could be completely counter-balanced by a perfect voltage divider between I_L and I_d. Fortunately for us, the inductive time constant of the SNSPD is long enough, such that before I_L becomes large, Joule heating is already taking place. In this way, $R_n \gg R_L$ and

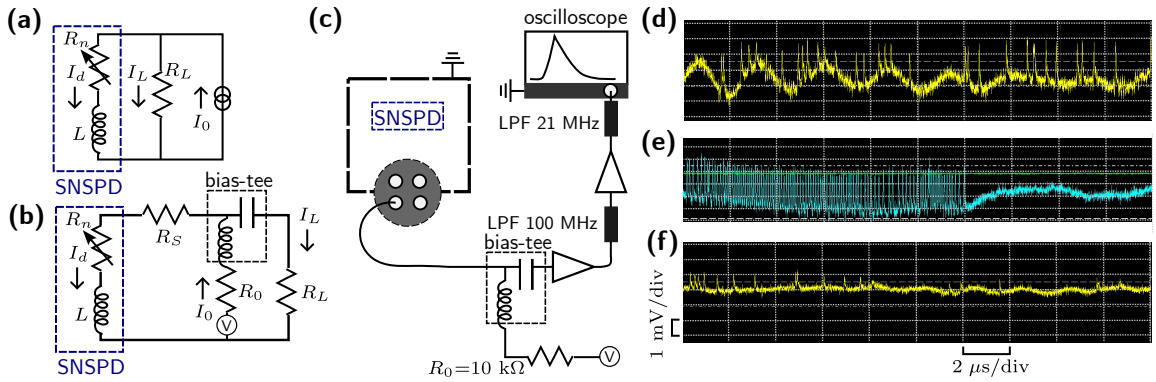

Figure 3.9: In **(a)** the equivalent electrical circuit of an SNSPD is shown. The SNSPD can be modeled as a variable resistance R_n and inductance L. The biasing current I_0 is divided between the detector current I_d and load current I_L, which can be read out by the load resistance R_L. The experimental circuit is shown in **(b)**, where a series resistor R_s can be used to increase the signal amplitude. A bias-tee is used to supply the SNSPD with the bias current I_0, created by a stable voltage source in series with the resistor R_0. The RF output of the bias-tee enables read-out of the load current I_L on the load resistance R_L. This readout is amplified and filtered, as shown in **c**. The traces are then recorded by a high-bandwidth oscilloscope. In **d** and **(e)** the two main detection problems of SNSPDs are shown: ground loops and after-ringing. A clean detection trace is shown in **(f)**. (d)-(f) are shown on the x-axis with 2 μs per division and on the y-axis 1 mV per division. For those traces, only one amplifier was used and all filters were removed.

the current I_d reduces to nearly zero. We detect this sharp rise of current I_L as a voltage peak through R_L. As now there is no current flowing through the SNSPD it can recover to its superconducting state, where the recovery time is $\tau_{\text{rec}} = L/R_L$. As the rise time of an SPSND is very fast, this recovery time usually limits the maximal detection rate of the device. Decreasing L or/and increasing R_L can help to make the SNSPD faster, but can also render the device unusable, by preventing Joule heating.

This will cause the resistance R_n to stabilize around a fixed value and never go back to the superconducting state, which is called *latching* and is associated with a latching current I_{latch}. One should choose a device where $I_{\text{latch}} > I_c$, such that the device can operate also at high rates. We remark that $L \propto I_{\text{latch}}$, such that if the inductance L is decreased too much, the device will have $I_{\text{latch}} < I_c$ and as such cannot be used close to the critical current, reducing its quantum efficiency. Of course, those design considerations are fixed once the SNSPDs are produced, and we experience low latching at count rates of $200 - 900$ MHz. If an SNSPD has latched, it can be automatically reset by turning the bias on and off.

3.1.5.4 SNSPD READOUT AND BIASING IN THE LABORATORY

Now that we understand the general principle of SNSPDs, let us explain the experimental setup, shown in fig. 3.9 (b). The SNSPD is shown in series with a resistor R_s. Here a large resistance can be used to increase the readout voltage pulse but has to be impedance-matched to the 50 Ω readout circuit [142]. In our case $R_s = R_L = 50\ \Omega$. Read-out resistance R_L, SNSPD, and bias source are connected via a bias-tee (*Minicircuits ZFBT-6G+*). The

bias source consists of an ultra-stable voltage source *SRS SIM928* in series with a resistance $R_0 = 10$ kΩ, such that the SNSPD are biased around 15-30 μA. The readout is only possible with at least one amplifier, as the voltage peak into 50 Ω is below 1 mV. We usually employ two low noise amplifiers (*Minicircuits ZFL 1000LN+*) in series and record the output on a fast oscilloscope (*Lecroy Teledyne WaveRunner 6 Zi*). A low-pass filter at 100 MHz (*Crystek Corp. CLPFL-0100-BNC*) is used between the two amplifiers, and a 21 MHz low-pass filter before the input to the oscilloscope (*Crystek Corp. CLPFL-0021-BNC*). On the oscilloscope, we use a voltage trigger to trigger on the rising edge of each pulse. The whole setup is sketched in fig. 3.9 (c).
The main figures of merit for SNSPDs are the quantum efficiency at maximal possible bias before latching, the dark count rate, and the timing jitter. Experimentally we have access to the overall system detection efficiency, including the optical fibers and electronic readout. We measure an overall detection efficiency to be $\eta_{on-off} = 0.8 - 0.85$. The dark count rate, false clicks induced by charge-discharge in the SNSPD or stray photons, should be low and is measured to be around 10 Hz in our setup. The dark count rate not only depends on the SNSPD characteristics but also on the cryostat temperature. A notable discussion on this topic can be found in the work of Shehata et al. [143]. Moreover, the timing jitter, defined as the FWHM of the normalized detection event distribution, is of the order of tens of picoseconds. In general, the maximal possible count rate should be adapted to the maximal capability of the setup, which is our case with a measured count rate of up to 2 MHz.

3.1.5.5 Possible error sources

The main sources of error in the setup of fig. 3.9 (c) are ground loops and after-ringing of the SNSPDs. *Ground-loops* can occur if a system has several grounds. If each ground has a slightly different potential, a closed circuit between the grounds is created, leading to slow (in comparison with the SNSPD pulses) oscillations over the whole signal. Ideally one would avoid multiple grounds, but our setup needs at least two grounds, one ground for the high voltage compressor, grounding thereby also the cryostat, and another ground for the oscilloscope. If multiple grounds cannot be avoided a *preferred ground* can be defined, meaning that a low-resistance grounding cable can be installed on the cryostat. We used the ground of a power line and connected all electrical equipment, except for the inherently noisy compressor, on this power line. In fig. 3.9 (d) we can see 0.5 MHz ground-loop oscillations, on top of which we can see detection peaks of the SNSPD. For the study of this problem, we removed all low-pass filters and left only one amplifier in the setup of fig. 3.9 (c). We were able to suppress the ground loops by the above-described grounding procedure and by using the same power line for all electronic equipment. Moreover, we also decided to try increasing the detection amplitude by changing from a stainless-steel to a cupronickel read-out coaxial cables for the electronic feed-through, as already written before.

After-ringing, often also called after-pulsing is observed as a train of pulses after a detection event. This increases significantly the dark count rate, visible in fig. 3.9 (e). Explanations of this phenomenon are rare, but most often it is explained by either unwanted trapping of charge carriers that are released after a single photon detection event or back-reflections in the detection circuit, causing a ringing effect [144]. In our case, we observed this effect for the first time around 2023, after a repair on the cryostat. We could reduce it substantially by removing a capacitance after R_0, which is intended to form a low-pass filter to suppress any possible voltage fluctuations from the voltage source. A further reason for the effect to persist could be small vacuum leaks, leading to depositions on the SNSPD detection area.

3.1.6 Take-away message

In this section, we have presented the tools available in our laboratory. Our laser is a continuous Nd:YAG solid-state laser that emits light at 1064 nm. It includes a doubling cavity that emits light at 532 nm. This second output is used to pump three optical parametric oscillators (OPOs):

- An OPO consists of a second-order nonlinear crystal placed inside a cavity. The cavity enhances the pump and the non-linear process. The non-linear process is spontaneous parametric down-conversion, where one pump photon is spontaneously split into signal and idler.
- All three OPOs in our lab are degenerate in frequency. Two OPOs emit signal and idler at orthogonal polarizations (OPOIIa and OPOIIb) while the third (OPOI) is fully degenerate. The former create two-mode squeezing, while the latter creates single-mode squeezing.
- The OPO cavities are resonant on pump, signal, and idler fields. For this, we control cavity length, crystal temperature, and the Nd:YAG output frequency (OPOIIa) or crystal tilt (OPOIIb). The cavity enhances the pump power. It furthermore introduces a threshold, marking the pump power at which the gain in the signal and idler creation overcomes the losses inside the cavity. We always operate below this threshold.
- The probability of the output mode exiting via the output coupler and not being lost is captured by the escape efficiency $\eta = T/(T + L)$. This parameter limits the squeezing of the output and is therefore a measure of state quality. There is a trade-off between having a high finesse or a high escape efficiency. In our experiment we chose $T_p = 0.05$ and $T_{s/i} = 0.1$, leading to a finesse between 30 and 68, depending on the intracavity losses. The cavities are linear Fabry-Perot cavities with a bandwidth of 65 MHz. The threshold is estimated to be 50 mW for OPOI and 80 mW for OPOIIa and OPOIIb.

We have furthermore discussed which locking techniques and cavities we use in our experiment:

- We use a mode cleaner with tilt locking to have a pure TEM00 mode at 1064 nm.
- The OPO cavities are locked via the Pound-Drever-Hall locking. Additionally, we ensure that they are resonant on the signal and idler fields by injecting a seed at 1064 nm and conditioning the Pound-Drever-Hall lock on the seed resonance.

- Before detection on on-off detectors, we filter the OPO output mode via an interferential filter and a homemade microcavity, locked with a side lock. This combination allows only the central OPO cavity mode to pass.

We detect the OPO output signal via homodyne detection

- Homodyne detection samples the field quadrature x^θ at different phases θ. For this, a local oscillator is interfering with the signal path on a 50:50 beamsplitter. Each beamsplitter output is detected on a photodiode and their subtracted photo-current is recorded. The phase of the quadrature is the relative phase between the local oscillator and the signal.

- Integrating the recorded photo-current over the temporal mode of the signal gives a value proportional to the quadrature x^θ. This requires the bandwidth of the homodyne detector the be adapted to the temporal mode, for us the homodyne bandwidth is 60 MHz. This measurement is mode-selective as it can only measure a signal in the same mode as the local oscillator.

- Losses in this detection accumulate from path losses, visibility, photodiode efficiency, and electronic noise. In total, we have an efficiency of 85% when measuring OPOI, 83% when measuring OPOIIa, and 82% when measuring OPOIIb.

Another detection method available to us are four superconducting nanowire single-photon detectors (SNSPDs), operating in a cryostat:

- The cryostat uses a two-stage Gifford McMahon cooling cycle to cool to 4 K. We then use He condensation to cool the cryostat further to 1.3 K. For this, helium is circulating in capillaries at room pressure through the coldhead and condensates into a cold pot. This cold pot is thermally connected to the samples. The cryostat can stay at 1.3 K for five days.

- Electrical and optical feed-through are homemade and lead to a SNSPD overall detection efficiency of 80% to 85% with a dark count rate below 10 Hz and a timing jitter of the order of tens of picoseconds. The maximal count rate before latching is around 2 MHz.

Next, we will explain the process of generating non-Gaussian states using the available laboratory resources. This process, along with the locking mechanisms, represents the routine tasks performed in this experiment on a daily basis.

3.2 Non-Gaussian state creation and data acquisition

So far, we have discussed which kind of states we can create in our setup: single- and two-mode squeezed states, which are Gaussian. Furthermore, we have presented our detection methods, which we now use in two different ways. The Gaussian homodyne detection will be used for state analysis, while the on-off SNSPD detection makes our states non-Gaussian via an essential process, the heralding. To achieve efficient heralding we need to periodically check all locks in our system, as explained in the Sample & Hold subsection. Finally, the output states of all three OPOs are presented and analyzed, followed by a discussion about possible improvements. We remark that those states are the most common ones we produce but that our catalog of states will be extended in the next chapters.

3.2.1 Heralding

Since spontaneous parametric down-conversion is a probabilistic process, we require a signal to indicate when a state can be measured using homodyne detection. This is why we tap part of the output of each OPO and use it to *herald* a signal arriving on homodyne detection. Each OPO therefore has two output paths, one for heralding and one for signal analysis. What part of the output it sent to the heralding depends on the envisioned signal state and will be discussed in subsection 3.2.3 and subsection 3.2.4.
The heralding path filters the light via an interferential filter and a micro-cavity, as described in subsubsection 3.1.3.1 and shown in fig. 3.5. This filtered heralding mode is then detected on a SNSPD, thereby projecting the signal mode onto this filtered mode. The filtering can as such be seen as a mode selection, allowing us to take the *single mode approximation* (see subsubsection 2.1.1.2) for the signal path. The filtering therefore justifies the full state-characterization via the homodyne detection, which can only resolve one single mode: the mode of the local oscillator.

As we have three micro-cavities in our setup we can have three simultaneous heralding events. Heralding can also be performed between two paths. This means that two heralding paths are mixed on a polarizing beam splitter (PBS) and projected onto the same polarization. The rejected polarization can then be used to lock the relative path difference between the two paths. A detection click of the new merged heralding path can not be back-tracked to either of the two original heralding paths, such that this process can induce entanglement or superpositions. A general experimental sketch of an heralding path is shown in fig. 3.10 (a) and heralding between two paths is visible in (b). Here we can see the two possibilities of where to place the merging of heralding paths, either before the cavity or after the cavity.
In our experiment, uCavII has merged heralding paths before the uCav, uCavI after the cavity and uCavIII has simply one heralding path. The heralding detection event, being

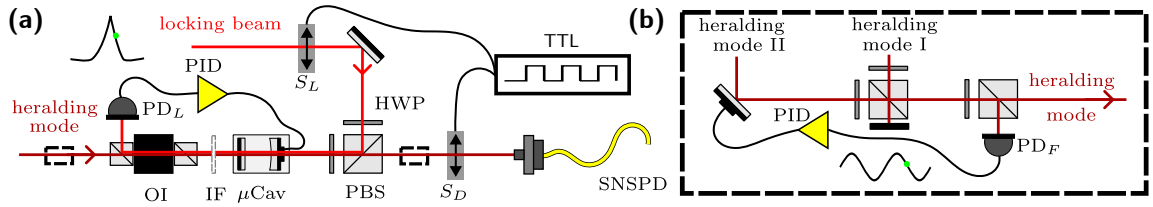

Figure 3.10: In **(a)** a general heralding scheme is shown. The heralding mode is filtered by an interferential filter (IF) and a micro-cavity (μCav). It is then transmitted towards a fiber coupler, leading towards the SNSPD detection if the detection shutter S_D is open. The shutter is controlled via a TTL signal and opens when the TTL voltage is low. To lock the cavity, a locking beam is injected into the cavity if the locking shutter S_L is open, such that after the optical isolator (OI) the reflected transmission signal on the photodiode PD_L can be used to lock the cavity length. The locking shutter is controlled by the same TTL signal as the detection shutter but closes when the TTL voltage is low. **(b)** is an inset of (a), showing the merging of two heralding modes either before or after the filtering. Here part of the heralding mode II is scanned via a piezo-electric transducer and can be locked on any point in the resulting fringe, recorded on the photodiode PD_F. The locking is only possible while the OPOs are seeded, which is controlled by yet another shutter (not visible in the figure) that opens when the TTL voltage is high.

the SNSPD detection pulse, is then used as a trigger on a fast oscilloscope (*Lecroy Teledyne WaveRunner 6 Zi*). This trigger indicates when a homodyne detection trace should be recorded. It is therefore essential to take into account the time delay between a SNSPD heralding click and the homodyne trace showing the corresponding signal. The time delay can be adapted with additional BNC cables.

3.2.2 Sample & Hold - keeping the experiment locked

To lock the OPOs, micro-cavities, and the relative lengths of paths that are interfering as they are merged, a bright IR light is needed. This bright light cannot be present during quantum state generation and detection as it would saturate and therefore dominate the detection. This is why we need two phases in our experiment that alternate in 50 ms: a non-measurement "sample" phase where bright light is allowed and all locks are checked, followed by a "hold" phase, where the bright IR light is blocked and the locks unchanged such that quantum states can be measured. Here we will discuss the experimental setup for this procedure in a single-mode measurement.

3.2.2.1 Experimental setup of a single-mode measurement

The experimental setup of a single-mode measurement is similar for all three OPOs. It is depicted in fig. 3.11 (a) for the example of OPOI. Each OPO lock consists of three stages. First, a side lock on the transmission seed signal is implemented, locking the cavity length. For this, a small part of the heralding path is tapped towards a photodiode PD_{SL}. After the side lock has been established, the PDH error signal, created at the mixer with the pump reflection signal on PD_{PDH} and the EOM driving signal, is used as the final lock of the cavity length. Now the piezo-electric transducer on the IR seed path is scanned, creating

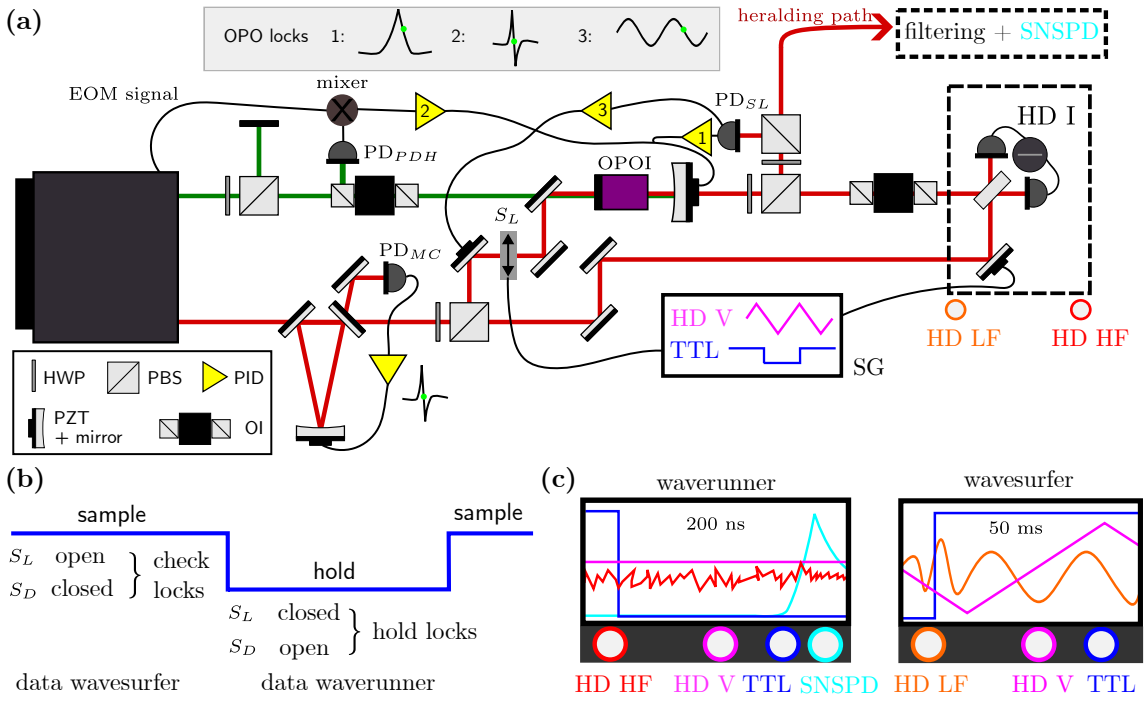

Figure 3.11: In **(a)** the whole experimental setup for any single-mode measurement on either OPOI, OPOIIa, or OPOIIb is shown. For more details, we refer the reader to the main text. The data-taking is executed as a Sample & Hold scheme, which is shown explicitly in **(b)**. During "sample", bright IR light is used to check/relock all locks, while the SNSPDs are protected by closing S_D. During this phase the oscilloscope wavesurfer takes data. The "hold" phase is the waverunner measurement phase, where we allow for no bright IR light and open the detection shutter S_D. In **(c)** the inputs to our two main oscilloscopes are shown, together with their time-settings.

fringes on the photodiode PD$_{SL}$ due to parametric amplification and de-amplification (see subsubsection 3.1.3.2), and locked close to the maximum of the fringe. Thanks to this lock we have a stable IR output of the cavity, that enables us to lock other path interference fringes down the line, as shown in fig. 3.10 (b) on PD$_F$. The signal path ends in the homodyne detection stage HDI. The phase of the local oscillator is continuously scanned via a signal generator (SG). Some of the bright locking light cannot be present during the measurement of the quantum states, as it would dominate the signal by orders of magnitude. To ensure that the OPOs, micro-cavities, and path lengths are nonetheless locked during the measurement, we implement a Sample & Hold procedure, as visible in fig. 3.11 (b).

3.2.2.2 Data acquisition

The Sample & Hold procedure is controlled by a 10 Hz TTL signal, such that we sample for 50 ms and then hold for 50 ms.

During the *sample phase*, the OPO lock is checked and the seed is transmitted via the open shutter S_L. The only shutter that is closed is S_D, leading to the SNSPDs. We use mechanical shutter heads *SRS 475 and SRS 470* that are controlled by the four-channel shutter

driver *SRS 474*. The locks of OPO, micro-cavities, and relative phases are checked during this period. Moreover, the seed is used to record interference fringes between the local oscillator beam and the signal on a slow 350 MHz digital oscilloscope *Lecroy WaveSurfer 434*, visible on the low-frequency output of the homodyne $HD\ LF$. The triangular voltage signal $HD\ V$, scanning the piezo-electric transducer, is recorded as well. During the data processing, those traces can be used to fit the phase of the fringe to the voltage applied on the piezo-electric transducer, such that we can know the phase of the quadrature that was measured on the homodyne. As this calibration can shift, we re-measure this fringe-voltage pair during each sampling phase and use it to calibrate the HD phase for the proceeding hold phase.
During the *hold phase* all shutters are closed, except for the shutters leading to the SNSPDs S_D. A fast oscilloscope *Lecroy WaveRunner 6Zi* is used to record the high-frequency homodyne output $HD\ HF$ and the homodyne voltage signal $HD\ V$. The recording of the traces of those two channels is conditioned on an AND trigger, combining a low TTL voltage with a SNSPD click. After each 1000 traces the data is sent to our laboratory PC and processed, as explained in section 3.3.

3.2.2.3 A note on the oscilloscopes

Both oscilloscopes have the possibility of employing the remote access protocol TCP/IP, with which we fetch the data and send it to our laboratory PC. While the wavesurfer is a standard oscilloscope, the waverunner has specific requirements. First, we require a reasonable *bandwidth*. The highest frequency signal might be the SNSPD detection signal, whose bandwidth is determined by the rising edge of this signal, being around 33 MHz. As we employ a 21 MHz low-pass filter before the SNSPD input to the waverunner (see subsubsection 3.1.5.4) we consider its maximal bandwidth to be 21 MHz. Therefore the homodyne detection, with its bandwidth of 60 MHz, sets the minimal bandwidth of the waverunner, which is easy to achieve. The number of samples per minute we require is more challenging. The *sample rate* determines the maximal horizontal resolution (timing resolution) of the oscilloscope, which should be as low (in s) as possible as it smears out the arrival time of the SNSPD detection and therefore the data of the quadratures. In our case, the maximal timing resolution is 50-100 ps with a timing jitter of maximally 3.5 ps and a sampling rate of 20 GigaSamples/s (2 channels) or 10 GigaSamples/s (4 channels).

Next, the *voltage resolution* or vertical resolution determines how precise the homodyne quadrature trace data is. In our case the available 8-bit resolution with a possibility of 1 mV - 1 V per division on display is sufficient. In general, higher resolution would allow us to avoid signal amplification after the HD output. Currently, we are using a low noise amplifier *Minicircuits ZFL 1000LN+* before the oscilloscope. As we see no degradation of the signal quality, we do not push for a higher resolution. The final important consideration is

the *trigger sensitivity*, which describes the smallest voltage signal that can generate a stable trigger. In our case, the trigger sensitivity is 0.9 div. Meaning that 90% of one voltage division has to be reached. Moreover, we need the possibility to employ the AND-trigger, which takes as a condition the low TTL signal and the arrival of a SNSPD signal. Last we can ask how many homodyne signals we want to record, meaning how many modes we want to measure. Currently, we have the possibility of measuring two modes, such that two channels can be used to input homodyne data, channel 3 is the homodyne voltage scan, channel 4 is the SNSPD signal and the external input is the Sample & Hold TTL signal. With this, we have maxed out the possible channels and would have to invest in a new oscilloscope to measure additional traces.
We will now discuss the single-mode states we can measure with our three OPOs.

3.2.3 Output of OPOI: The Cat state

The OPOI is used to produce odd cat states, see eq. (2.227). If we set the losses inside the cavity to $L = 0$, we can use equations (3.26) and (3.27) and connect it to the squeezing parameter of eq. (2.208) and the creation operator after squeezing of eq. (2.249). To compare those two expressions, we have to set $\omega = 0$ in eq. (3.26), corresponding to the degenerate down-conversion frequency. In this way we can write how squeezing $\xi = re^{i\phi}$ is altered by a (lossless) cavity

$$\lambda = \tanh(r) = \frac{2c_{th}}{1 + c_{th}^2} \quad \text{and} \quad \phi = \pi \quad \text{such that} \tag{3.76}$$

$$|\xi\rangle = \left(1 - \lambda^2\right)^{(1/4)} \sum_{n=0}^{\infty} \frac{\sqrt{(2n)!}}{2^n n!} \lambda^n \, |2n\rangle \,, \tag{3.77}$$

with a squeezing axis of $\phi = \pi$ in eq. (2.249) and the cavity (OPO) threshold $c_{th} = 1$. To include losses, one can now either apply a beamsplitter or use eq. (3.26). In both cases, the partial trace is used to trace out the loss mode. We can analyze the squeezing produced by OPOI, to get a better loss estimation. The measured squeezing is shown in the paper by O. Morin et al. [145] and can be compared with eq. (3.35). It suggests an intra-cavity OPOI loss of $L_{IR} = 0.01$, which indeed is lower than what we estimated with the finesse measurement (see subsubsection 3.1.2.4).

Now we want to take this squeezing and build a basis of even and odd cat states with it. Interestingly, a squeezed vacuum can have a high fidelity with an even cat state, and subtracting one photon from this squeezed vacuum can have in turn a high fidelity with

an odd cat state. This is why we usually refer to the output from OPOI as cat states, as defined in eq. (2.227) and (2.226). If $\alpha \leq 1$, we can approximate

$$|\text{cat}(\alpha)\rangle_+ \approx S\,|0\rangle\,, \tag{3.78}$$

$$|\text{cat}(\alpha)\rangle_- \approx \hat{a}S\,|0\rangle = SS^\dagger \hat{a}S\,|0\rangle = -e^{i\phi}\sinh(r)S(re^{i\phi})\,|1\rangle \tag{3.79}$$

$$= \sinh(r)S(-r)\,|1\rangle\,. \tag{3.80}$$

Intuitively we can see that both squeezing and even cat states are a superposition of even Fock numbers, while photon-subtracted squeezing transforms this into a superposition of odd Fock numbers, similar to an odd cat state. The reason why the amplitude α is rather small is the weights of the superpositions of squeezing and cat states, which are similar only in those regimes. In this regime, the odd cat state can be expressed as a squeezed single photon. Those cat states, having a small amplitude α, are sometimes called *Schrödinger's kitten*, although we will call them cat states. In fig. 3.12 the state overlaps (fidelities) between squeezed states and cat states are shown. Importantly we remark that for each cat amplitude α, a different squeezing is ideal.
Moreover, we can see that for the same targeted cat amplitude, the ideal squeezing value differs from even to odd cat. This motivates choosing a fixed cat amplitude α (not optimizing over alpha) and then computing the fidelity with even and odd cat states, to judge how good of a computational basis, or how orthogonal, the experimentally generated states are. To create a proper Bloch sphere, bigger cat amplitude values are envisioned (see coherent state overlap in eq. (2.185)).

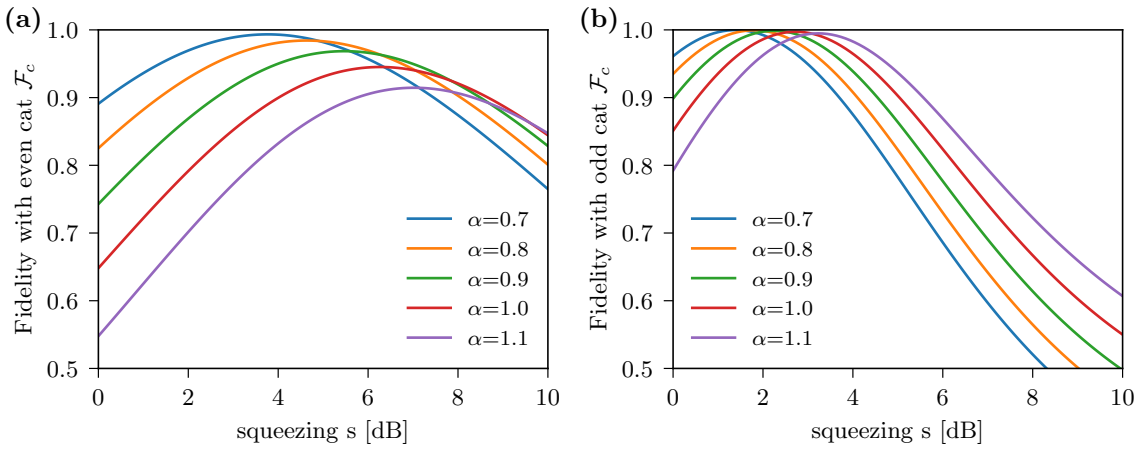

Figure 3.12: In **(a)** the fidelity $\mathcal{F}_c$ between ideal squeezing and an ideal even cat state is shown for different cat amplitudes. **(b)** shows the corresponding values for an odd cat state. For each cat amplitude, there is a different ideal squeezing to achieve maximal fidelity. The squeezing phase is set to $\phi = \pi$.

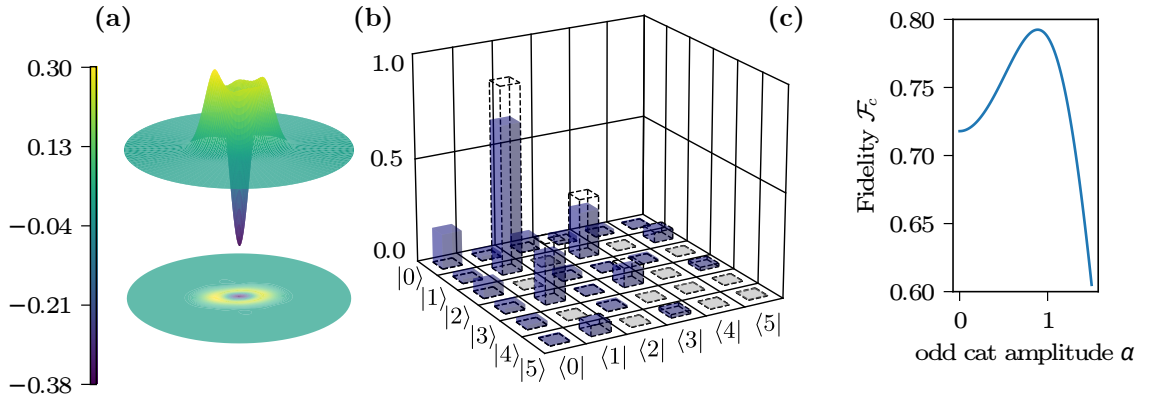

Figure 3.13: In **(a)** the Wigner function of the experimental data for an odd cat state is shown. **(b)** shows the corresponding density matrix with the ideal odd cat of $\alpha = 0.89$ in dashed lines. The fidelity with an ideal odd cat is shown in **(c)**.

The generation of odd cat states is especially interesting, as they show Non-Gaussianity also at low cat amplitudes. The experimental setup is given in fig. 3.11 (a), where we tap 3% of the OPOI output by tuning the HWP before the first PBS accordingly. The created output state is shown in fig. 3.13, where we plot the Wigner function[10] in (a) and its density matrix in (b).

If we optimize its fidelity with a lossy photon subtracted squeezed state, then we find 97% fidelity with a squeezing of $s_{dB} = 2.4$ dB. The best achievable fidelity with a cat state is around 80% for an amplitude of $\alpha = 0.89$, where the corresponding plot is shown in fig. 3.13 (c). The state is corrected for the measurement efficiency $\eta_{\text{meas}} = 0.85$, leaving only the losses inside the OPOI.

With the results of OPOI now laid out, let's move forward and discuss OPOII.

3.2.4 Output of OPOII: The single Photon

The OPOIIa and OPOIIb can produce Fock states and are mainly used to produce *single photon states*. From eq. (3.15) we can deduct how to write the output state of OPOII if no losses are present. For this, we use our results of OPOI and write

$$\xi = re^{i\phi} \qquad \lambda = \tanh(r) = \frac{2c_{th}}{1+c_{th}^2} \quad \text{and} \quad \phi = \pi, \tag{3.81}$$

$$S_2(\xi)\,|0\rangle = (1-\lambda^2)^{(1/2)} \sum_{n=0}^{\infty} \lambda^n\, |n\rangle_1\, |n\rangle_2 \tag{3.82}$$

$$\xrightarrow{\text{BS}(0.5)} |\frac{\xi}{2}\rangle_1\, |\frac{\xi}{2}\rangle_2, \tag{3.83}$$

where the subscripts 1 and 2 stand for the two orthogonal polarizations that can either be mixed in two-photon correlations (eq. (3.82)) or can be separated by a 50:50 beamsplitter

[10] with the normalization taken to be $\hbar = 0.5$

(eq. (3.83)). A very elegant derivation of this result is given by Lvovsky [146].

The photon number correlations between the two orthogonal polarization modes are often called *EPR-entanglement*, which refers to a *Gedankenexperiment* of Einstein, Podolsky, and Rosen about locality in quantum mechanics [4]. Importantly all the information in this system is stored in the correlation, such that if we trace out one mode, a thermal state is created in the other. If a beamsplitter is applied the modes are separated and thereby decorrelated, transferring the information to the separate modes. Tracing out one mode in this setting will therefore not affect the other mode. In which of those cases we are operating, depends on the HWP angle right after the OPO in fig. 3.11 (a). A complete study of the HWP setting is given in chapter five of the thesis of H. Le Jeannic [147].

To create a single photon, modes 1 and 2 have to be perfectly separated, such that one polarization component is sent to the heralding mode. If this splitting is perfect, the detection of n photons in the heralding mode will project the state onto a Fock state $|n\rangle$ in the signal mode. The single photon output of OPOIIa is shown in fig. 3.14. The fidelity with a single photon is $\mathcal{F} = 0.85$ and the state purity is $\mathcal{P} = 0.74$. The state purity and fidelity can be improved by lowering the pump rate, which was kept rather high here as those states were used in subsequent protocols, described in chapter 5.
Here, the optical isolator in fig. 3.1 before the homodyne measurement is especially important. It avoids back-reflections from the homodyne, which induce false clicks on the heralding path. Those clicks act as a displacement on the signal and are in phase with the homodyne measurement, producing a kind of qubit. A full discussion about this effect can be found in chapter 4.4.3 of the thesis of O. Morin [30].

In fig. 3.15 the single photon output of OPOIIb is shown.

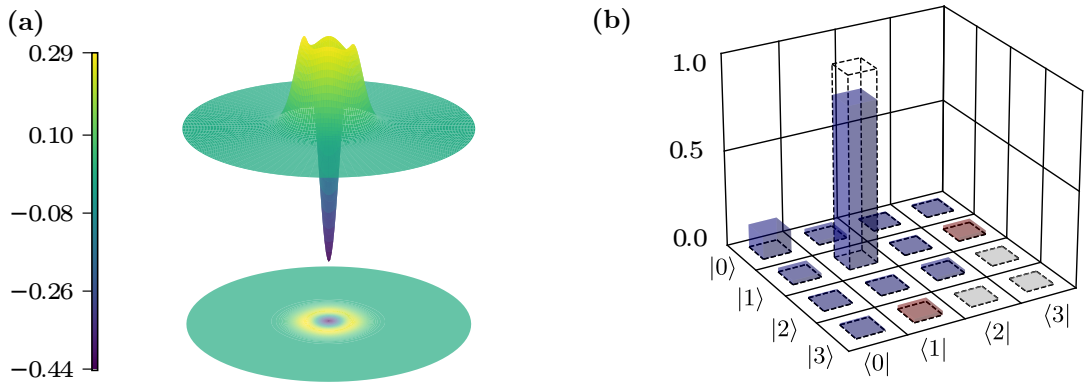

Figure 3.14: The single photon of OPOIIa is shown, where **(a)** shows the Wigner function and **(b)** the real density matrix.

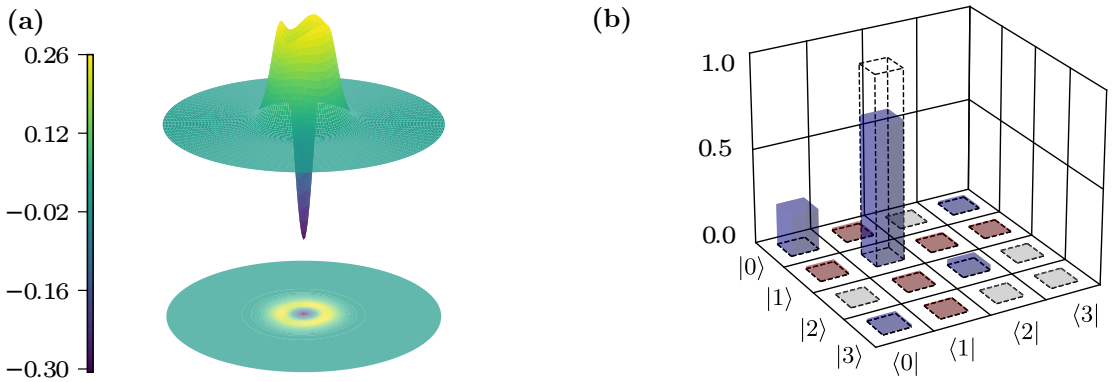

Figure 3.15: The single photon of OPOIIb is shown, where **(a)** shows the Wigner function and **(b)** the real density matrix.

The single photon fidelity $\mathcal{F} = 0.74$ and purity $\mathcal{P} = 0.6$ shows that the additional input mirror on OPOIIb increases the losses, such that this state has a lower state quality than the OPOIIa single photon. Both states have been corrected for all losses between the measurement and the OPO output, such that the single photon fidelity is equivalent here with the OPO escape efficiency $\eta = T/(T+L)$, where T is the output coupler transmission, which in our system is 10%.
With the escape efficiency, we can re-evaluate the losses in both OPOs as $L_{IR}^{\text{OPOIIa}} = 0.018$ and $L_{IR}^{\text{OPOIIb}} = 0.035$. As already remarked for OPOI, this measurement of the losses is more reliable and also shows smaller values than the measurement via the finesse (see subsubsection 3.1.2.4).
Single photons are not the only possible output states of such OPOs. We will discuss other OPOII output states in chapters chapter 6 and chapter 7.

3.2.5 Discussion

The typical single-mode state capabilities of our setup have been discussed in this section, with a large focus on the single-mode approach via state filtering and data acquisition.
We first note that the equations for single and two-mode squeezing, given in eq. (3.82) and (3.77) show the dependency of the squeezing on the OPO pump and how close it is to OPO threshold, i.e. how close it is to $c_{th} = 1$. This is directly related to the count rate, such that if we want almost no $|2\rangle\,|2\rangle$ photon component in the two-mode squeezing, we need to pump far below threshold, leading to a lower count rate. This trade-off between count rate and state fidelity will also be discussed in the next chapters. Here we explicitly optimized the state fidelity with no regard to the count rate.

To obtain a high purity state, the pump of the photon-subtracted squeezed vacuum was optimized. In this way near-unity fidelity with a (lossy) squeezing of $s_{dB} = 2.4$ was shown, which corresponds to an 80% fidelity with an ideal cat of the amplitude of $\alpha = 0.89$. In

the case of OPOIIa and OPOIIb, we achieve high single photon purity and fidelity of maximally $\mathcal{F} = 0.85$. This differs by 5% from previously reported values [30], which hints at an increase in the losses inside the OPO cavity. To counteract this, strategies will be presented in chapter 7.

In terms of Non-Gaussianity we can get an indication of the quality of our states via their negativity[11]. With the normalization $\hbar = 0.5$ we can expect the minimal value of the Wigner function to be $-2/\pi \approx -0.64$ and find especially that OPOIIa to be very close to this value with a negativity of -0.44. All three experimental states presented here show clear Wigner negativity. Moreover, the fidelity with pure states exhibiting Wigner negativities can serve as a witness for Non-Gaussianity. To show that a state is non-Gaussian one needs to exceed a threshold, which in our case is the fidelity with a single photon above 50% [148]. We compute the lowest fidelity to be that of the odd cat of OPOI, with $\mathcal{F}_1 = 0.72$, which is somehow logical as this state is not "trying" to be a single photon. All our states are therefore highly non-Gaussian.

[11] We note that negativity is only a non-Gaussian criterion for pure states.

3.2.6 Take-away message

In this section, we have seen, that

- Heralding allows us to introduce Non-Gaussianity into our two-mode or single-mode squeezed output states of the OPOs. It involves tapping part of the OPO output state, filtering it, and detecting it on SNSPDs. This detection is then used as a trigger to measure the remaining OPO signal via homodyne detection.
- To be able to measure data in a stable experiment, we need to implement a sample and hold feature. During 50 ms the experiment is sampled, meaning that all locks are relocked. The next 50 ms are for quantum state creation and their data acquisition, and all the locks are set on "hold".
- In terms of data acquisition we use two oscilloscopes: a waverunner and a wavesurfer. During the hold phase the fast waverunner records the high-frequency homodyne output, triggered by a detection click on the SNSPD. During the sample phase, the fringe between the seed and local oscillator is recorded on the wavesurfer, enabling the calibration of the homodyne phase.
- For OPOI, we tap a small fraction of the output state and use it as heralding. This corresponds to a single-photon subtraction of the squeezed vacuum and can be approximated by an odd cat state of amplitude $\alpha \leq 1$. We achieve a fidelity of 80% with an odd cat state of amplitude $\alpha = 0.89$. We estimate the intra-cavity loss to be $L_{IR}^{\mathrm{OPOI}} = 0.01$.
- For both OPOIIa and OPOIIb we split signal and idler perfectly, and use their photon-number correlation to project the state onto a single photon with fidelities of 85% and 74%. We estimate their intra-cavity losses to be $L_{IR}^{\mathrm{OPOIIa}} = 0.018$ and $L_{IR}^{\mathrm{OPOIIb}} = 0.035$.
- All three OPOs can create highly non-Gaussian states.

In this section, the density matrices and Wigner functions of the measured states have already been displayed. In the next section, we will detail the method for reconstructing them from the measured homodyne data.

3.3 Data processing

In the previous section, we have discussed data acquisition and have shown typical states that can be measured in our setup. We now present how the homodyne data is processed such that we can find the output state density matrix. In our setup, we recall that we have two distinct steps: a sample phase and a hold phase.
During the sample phase, we record the data from a relatively slow oscilloscope, the *wavesurfer*. This data is used to calibrate the voltage ramp applied to the piezo-electric transducer, attaching a phase value to each homodyne measurement with a known ramp value.
In the hold phase a high sample-rate oscilloscope, the *waverunner*, is used to record measurement traces of the homodyne detection, together with the ramp voltage. For more detail, we refer the reader to subsection 3.2.2.

Here we will focus in the **first three subsections** on how to compute the quadrature phase and value from the raw data. In the **fourth subsection**, the maximum Likelihood reconstruction algorithm is presented, followed by the **fifth subsection** about uncertainties in this reconstruction. We finally describe the transition from pure C code to a more user-friendly Python code in the **sixth subsection** and end this section with a discussion in the **seventh subsection**. The take-away messages are given in the **last subsection**.

3.3.1 Code and raw files

Historically, C has been used as the programming language for communicating with oscilloscopes, saving the data, and processing it. The communication is based on the VICP (Versatile Instrument Control Protocol) Client Library, which is developed by *Teledyne Lecroy* and is publicly available.
First, the vacuum noise or shot noise is recorded with 40000 raw traces. This data will be used as a normalization. During this measurement the signal path is manually blocked, such that only vacuum and measurement noise contribute.
Now the actual quantum signal is measured and the signal path is unblocked. We record between 20000 and 40000 traces to reconstruct the measured state. Each time the hold sequence is initiated, the oscilloscope gathers 1000 traces before sending them to the laboratory PC, as the communication time between the PC and oscilloscope is the slowest process in data taking for us.
With our usual count rate of 200 KHz to 1 MHz, single-mode data acquisition takes below five minutes. The data is saved in the form of .bin files because the VICP client library is optimized for this file format. We will now discuss how the data is processed such that quadrature values can be extracted from the raw traces.

3.3.2 Computing the quadrature values

We recall from subsubsection 3.1.4.1, that the homodyne trace $v(t)$ needs to be integrated over the temporal mode of the state. This temporal mode corresponds to the OPO cavity mode and is set to a bandwidth of $\Delta\nu = 60$ MHz for all analyzed data. Note that before taking data, the time delay between the SNSPD detection event and the homodyne trace recording has to be calibrated, such that we are sure to have the temporal mode in each raw trace. The temporal mode itself cannot be seen in the individual traces but in the variance of all recorded traces, which is equivalent to the variance of phase-averaged quadratures. For this, we calculate the point-wise variance of all recorded signal traces. Each trace has usually 2002 points, which corresponds to 10 Gigasamples per second for the recorded length of 200 ns.

If one wants to verify the single-mode approach, a temporal mode analysis can be done. For this, the autocorrelation matrix of all traces is computed. If we then perform an eigenanalysis, we find that the eigenvectors are temporal modes. Given that each eigenvector is a temporal mode, we ideally want only one eigenvalue to be non-zero. The eigenvalues mark consequently how "single-mode" our signal state is or how much it can be defined with one single temporal mode. An analysis of the single photon of OPOIIa, as shown in fig. 3.14, can be seen in fig. 3.16. In (a) we can see the dominant eigenvalue which should correspond to the cavity mode, visible in (b). The discrepancy between the measured output mode and the ideal cavity mode is mainly a broadening of the curve. This can probably be attributed to the bandwidth of the homodyne detection.

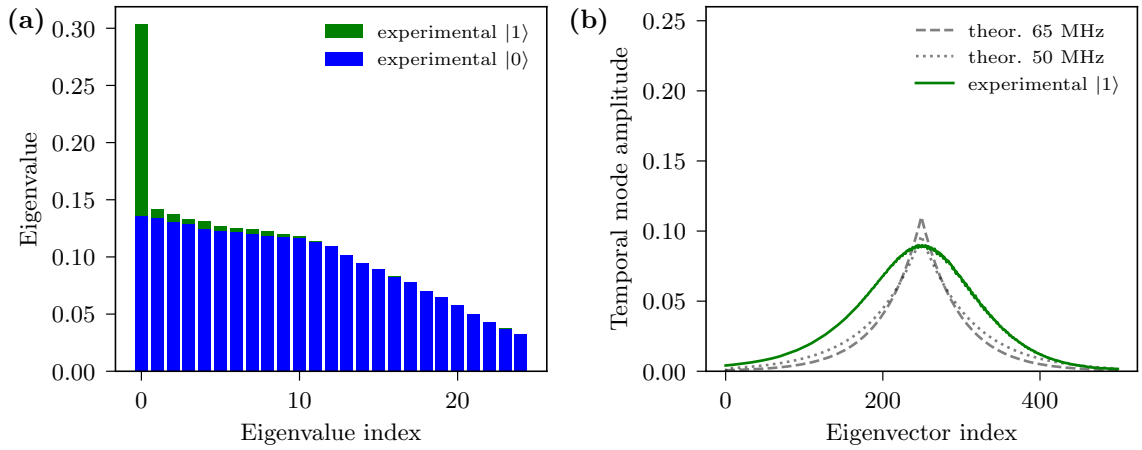

Figure 3.16: Here the temporal mode analysis of a typical state of OPOIIa is shown. In **(a)** the first 25 eigenvalues are shown, each eigenvalue corresponding to another temporal mode. In comparison to the temporal mode of vacuum, we can clearly see that the first eigenvalue dominates in the OPOIIa case. The corresponding eigenvector to the first eigenvalue is plotted in **(b)**, in comparison with the ideal cavity mode.

By performing the integration over the temporal mode we can therefore compute a value $x_\theta^{'}$, proportional to the quadrature value of each trace. Here we have the choice to integrate the computed temporal mode or the theoretical temporal mode of fig. 3.16 (b). We find that the reconstructed state is barely influenced by this choice, such that we always reconstruct with the theoretical mode. The quadrature values of the shot noise $v_0(t)$ are computed in the same way, and we can compute its standard deviation and mean and use it to find the final quadrature value

$$x_\theta^{'} = \int v(t) f(t) dt, \tag{3.84}$$

$$x_\theta^{0} = \int v_0(t) f(t) dt, \tag{3.85}$$

$$x_\theta = \Big(x_\theta^{'} - \text{mean}(x_\theta^0) \Big) / \text{std}(x_\theta^0), \tag{3.86}$$

where $v(t)$ is the recorded trace and $f(t)$ the temporal mode. Next, we need to find the phase θ of each quadrature value.

3.3.3 Finding the quadrature phases

The quadrature phase is recorded as a voltage value on the waverunner for each trace. To connect each voltage value to a phase, we need the fringes between the seed and local oscillator, recorded on the wavesurfer. A simple squared sinus fit of the fitting function

$$f(A, B, a, b, c, t)_{\text{fit}} = A \sin^2(at^2 + bt + c) + B, \tag{3.87}$$

then reveals the phase, which can now be associated with each trace. Practically we only take the rising slope of the voltage scan, such that a fit typically looks as in fig. 3.17. Here the recorded interference fringe between the seed and local oscillator is shown in orange, while the scan voltage is shown in pink. The fit is applied on the positive slope of this can voltage, colored in light green. The fit itself is shown in dashed black lines. To translate the voltage in the phase of the fitting function, we can first write the trace index vector t in terms of the voltage

$$t = \frac{\max(t) - \min(t)}{\max(V) - \min(V)} (V - V[0]), \tag{3.88}$$

where $V[0]$ is the first voltage value measured and therefore gives the offset. The phase for any voltage v' can then be translated into an index t', which can be used to calculate the phase θ' with

$$\theta' = 2\big(a\ (t')^2 + b\ t' + c\big). \tag{3.89}$$

In this way, we can fit any voltage to any phase and have now a complete set of quadratures and corresponding phases.

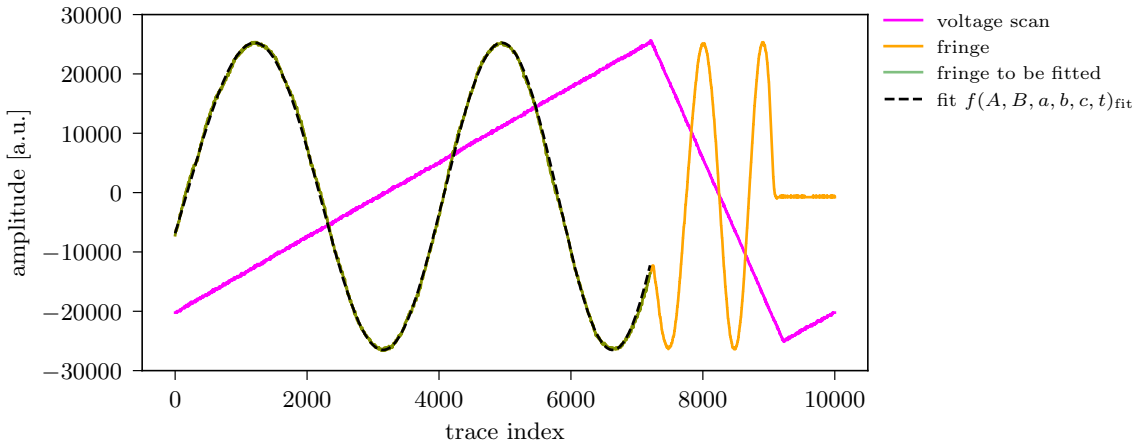

Figure 3.17: Here the phase fit of voltage to fringe-phase is shown. The interference between the local oscillator and signal (in orange) is cropped to the rising slope of the voltage scan of the local oscillator (in pink). This cropped part is fitted with the function $f(A, B, a, b, c, t)$, which is plotted in dashed lines with the found fitting parameters.

3.3.4 Maximum Likelihood reconstruction (MaxLik)

The raw homodyne data is now available as N pairs of quadratures and phases $\{x_\theta, \theta\}$. This is equivalent to sampling the marginal distribution P_θ of the state, being the integration of the Wigner function over the orthogonal quadrature. The homodyne data is therefore not a direct measurement but needs processing to reveal the state it has measured. Here a statistical approach is used, called the maximum likelihood estimation [149]. It computes the most likely state that can produce those measurement results.

3.3.4.1 General working principle

Assume we have N measurements with outcomes $x_i \quad i \in [0, N-1]$. A measurement frequency f_j is now associated with this set of outcomes, such that $f_j = n_j/N$. We see that this is the relative frequency of the outcome x_j, which occurs n_j times in the data set. The likelihood $\mathcal{L}$ of this new dataset f_j, x_j is then defined as

$$\mathcal{L} = \prod_j [\mathrm{Tr}[\Pi_j \hat{\rho}]]^{f_j}, \tag{3.90}$$

where Π_j denotes the measured POVM element, f_j the previously explained relative frequency and $\hat{\rho}$ the density matrix. This density matrix is what we are trying to compute, such that it maximizes the likelihood. For this, an operator $\hat{R}$ is introduced, which will be used iteratively to update the density matrix

$$\hat{R}(\hat{\rho}) = \sum_j \frac{f_j}{\mathrm{Tr}[\Pi_j \hat{\rho}]} \Pi_j. \tag{3.91}$$

For the exact measured state ρ_0 we should find $f_j = \mathrm{Tr}[\Pi_j \hat{\rho}_0]$. As we know from eq. (2.155), the POVM elements Π_j sum to the identity, we can find that for the ideal state $\hat{R}(\hat{\rho}_0) \approx \mathbb{1}$. The algorithm to find this perfect state starts with the initial matrix $\hat{\rho} = \mathbb{1}$ and converges towards $\hat{\rho}_0$ in K iterative steps

$$\hat{\rho}^{k+1} = \hat{R}(\hat{\rho}^k)\hat{\rho}^k\hat{R}(\hat{\rho}^k), \tag{3.92}$$

$$\hat{\rho}^{k+1} = \frac{1}{\mathrm{Tr}[\hat{\rho}^{k+1}]}\hat{\rho}^{k+1}, \tag{3.93}$$

where the second step ensures the normalization of the density matrix. In each step, the density matrix is projected onto the state it would be in if it would have been measured in a weighted superposition of all measured quadratures, represented by $\hat{R}$, such that each iteration further pushes the density matrix closer to convergence, which is when the state does not change anymore $\hat{R}(\hat{\rho}_0)\hat{\rho}_0\hat{R}(\hat{\rho}_0) \propto \hat{\rho}_0$. This algorithm assumes $\hat{\rho}$ to be a quantum state, such that after each iterative step it is a normalized, hermitian matrix. To run this algorithm one has to choose the *number of iterative steps* K and the dimension of the density matrix $\dim_\rho$.

3.3.4.2 MaxLik in practise

In our case we start from N sets of measurement data $\{x_i^\theta, \theta_i\}$ and use the set $\{f_i, x_i^\theta, \theta_i\}$ for the reconstruction. Indeed in our case $j = i$, as each measurement occurs only once. To speed up the reconstruction one could bin the homodyne data, leading to a faster but less precise algorithm. As we care for precision, we do not bin. Therefore the relative frequency of each measurement is equal $f_i = f = 1/N$. The ideal measurement POVM element in our case is the homodyne projector, as defined in eq. (2.269), where we can find a projector $\mathrm{HD}(x, \theta, \eta_{meas})$ for a certain detection efficiency η_{meas}, phase θ and quadrature outcome x^θ. This approach can be extended to several modes by using a super-POVM-element, which is the tensor product of the POVM elements that were measured on the individual systems. In our reconstructions, we set the number of iterations to $K = 200$, which shows good convergence of the algorithm. The density matrix size is chosen to be $\dim_{rho} = 5$ for OPOIIa and OPOIIb and $\dim_{rho} = 10$ for OPOI. One can verify that the correct dimension was chosen by running the algorithm with a higher dimension. If the higher-density matrix elements are not populated we can come back to the faster, smaller dimensions. The loss corrections implemented via η are given in table 3.6.

3.3.5 Uncertainties

One of the drawbacks of the MaxLik reconstructions (or any statistical reconstruction of quantum states) is, that it is very hard to define error bars. Firstly we need to define what the error bars should capture: experimental fluctuations or reconstruction uncertainty. Experimental fluctuations beyond the measured data fluctuations are only reasonable if one

measured state should represent the system over several hours. This approach is taken in chapter 5. For a single measured state, the experimental fluctuation is incorporated in the data and is therefore indistinguishable from the reconstruction uncertainty. Our preferred approach is defined by P. Faist and R. Renner [150], where a quantum error region can be calculated. This is only applicable to a measure (like fidelity) of the density matrix and cannot be applied to get the uncertainty of off-diagonal elements of the density matrix. We therefore choose the widely used bootstrapping approach. There, new homodyne data is simulated from the calculated density matrix, leading to a newly reconstructed density matrix. If this process is repeated many times, the standard deviation of the matrices from their mean can be used as error bars on each density matrix element. We note, however, that defining an uncertainty for each density matrix element is somehow artificial in an algorithm where after each iteration a fully new density matrix is calculated.
The uncertainty could be better defined as an uncertainty of the whole density matrix, approaching the definition of P. Faist and R. Renner [150]. In general, we expect and find the error bars on each density matrix element to be very small due to our high number of measurements.

3.3.6 From C to Python

The code is very fast in C, but learning to read and navigate in C is commonly challenging for any new PhD arriving. We therefore decided to transfer part of this code to Python. Since the beginning of 2024, a Python script calls a C .dll file to keep fast communication with the oscilloscopes in its native language. The quadrature calculation, phase calibration, and MaxLik are then done via Python. To speed up the MaxLik computation in Python, one can make use of parallelization. All data analysis on the density matrices was also transferred from Mathematica to Python during this PhD. Except for calling a C .ddl file and the occasional use of the programming language Julia, which serves as a fast language for programs that are not already written in C and can be used via the .dll file, all data processing is now in Python.

3.3.7 Discussion

We have presented the maximum likelihood algorithm, used to reconstruct the signal state from homodyne data. Loss correction and N-mode reconstructions were discussed and are commonly used for our setups. The discussion of uncertainties in that kind of reconstruction is closely connected to the bias introduced by the maximum likelihood algorithm. A bias in a statistical estimation incorporates the prior knowledge about the system, which in our case, is the state dimension. Moreover, the algorithm itself has a bias towards physical states, as we enforce the output to be a properly defined density matrix. There are several analytical approaches, like the Radon transform, which can output unphysical density matrices (for a more complete discussion we refer the reader to [30]). With our size of measurement data,

we can be quite confident that our reconstruction is faithful, but remark that for small data samples, the MaxLik algorithm is known to deviate from the true state [151]. New approaches use machine learning [152, 153] for a speed-up in reconstruction and to avoid a bias setting. While it can be very useful to employ machine learning for a faster data analysis, the implicit bias coming from the model or the training data set of any machine learning algorithm is hard to quantify and an active field of research [154]. Given this unknown implicit bias, we prefer the MaxLik approach, where we have full knowledge of the chosen bias.

3.3.8 Take-away message

In this section, we have discussed that:

- We record first 40000 traces of vacuum shot noise, which are used for normalization. For the data, we take between 20000 and 40000 traces. Single-mode data acquisition takes below 5 minutes.
- The center of the temporal mode in each trace is visible by computing the point-wise variance of all recorded traces. Each trace is then integrated over the temporal mode and normalized by the vacuum data. The single-mode approach can be verified by computing the eigenanalysis on the corresponding covariance matrix.
- The phase of each quadrature value is recorded as a voltage level. To connect each voltage to a phase, the fringes between the seed and local oscillator, recorded on the wavesurfer, are used. They are fitted to a squared sinus function, allowing us to extract a phase for each voltage.
- The 20000-40000 quadrature-phase tuples are then used to reconstruct the measured state. For this, we use the maximum likelihood reconstruction algorithm. With this algorithm, we can correct for the losses on the homodyne detection.
- The challenge of defining error bars in this statistical approach to reconstruction is addressed by using bootstrapping.
- To increase the ease of navigation, part of the reconstruction code was transferred from C to Python during this thesis. All data analysis was written and/or transferred to Python and Julia.

Chapter 4

Towards hybrid quantum networks

Contents

This chapter briefly introduces the idea of future quantum networks with a special focus on heterogeneity. The **first section** builds up the tools needed to use quantum networks and argues for entanglement between different non-Gaussian states to be a good testbed for quantum networks, called hybrid entanglement. Such a *hybrid entanglement* is experimentally created and analyzed towards the end of this section. The **second section** discusses an improved Bell-state measurement in the Fock basis. This Bell-state measurement improves the output fidelity of swapping and teleportation protocols. It has been fully characterized during this thesis and a paper about the results is in preparation. Moreover, it is an essential cornerstone of the protocol presented in chapter 5. Here we show this characterization and compare it with state-of-the-art photon number-resolving detectors. The **third section** concludes this chapter and the **fourth section** gives the key results.

4.1 Heterogeneous quantum networks

In this section, we want to introduce quantum networks and motivate why hybrid entanglement, which we can create in the laboratory, is interesting in this context. In the **first subsection** a general quantum network is described and current quantum networks are analyzed. In the **second subsection** the two most important protocols for networks: entanglement swapping and quantum teleportation are introduced in the framework of the Bell-state measurement. The **third subsection** aims at analyzing the most general

encoding choices for quantum networks. It furthermore discusses post-selection and non-deterministic sources. The **fourth subsection** presents and analyses our experimentally generated hybrid entanglement, between cat states and Fock states. Its network compatibility is discussed and possible improvements are suggested.

4.1.1 The idea of quantum networks

Inspired by the success of today's internet, a common goal in quantum research is the creation of a *quantum network* [155] to connect different quantum devices and enable communication between them. In the last years, we have already seen examples of small quantum networks in the context of quantum key distribution (QKD), that can enable mathematically secure information transfer, superior to the classical computational security. This technology is commercially available and is employed in Japan, China, and the European Union [156, 157]. In their current form, those QKD quantum networks use quantum channels to transmit classical information stored in quantum states in point-to-point protocols, for example with the famous BB84 protocol [158].
The quantum states are always encoded in light, being the only "flying" quantum system, and as such have to battle fiber losses of 0.2 dB/km at the standard telecommunication wavelength of 1550 nm.

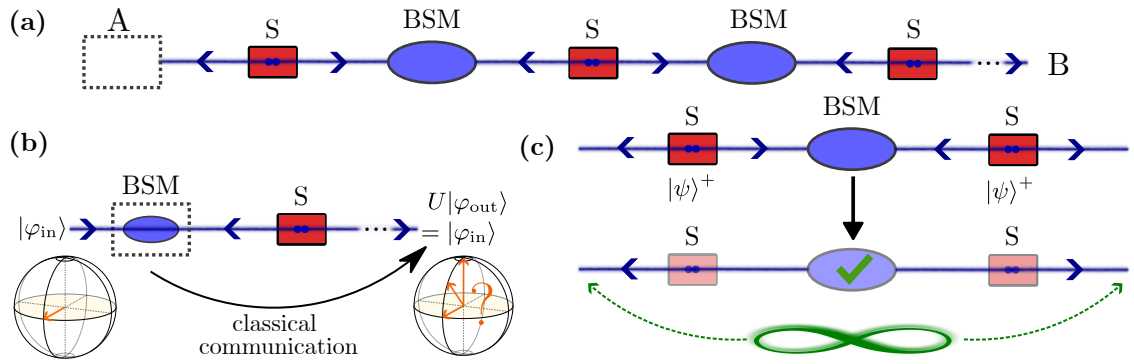

Figure 4.1: In **(a)** the structure of a linear quantum network is visible. In this simple form, the network connects user A with user B via N (in this case two) Bell-state-measurement (BSM) stations. An entangled state source S emits two photonic modes, traveling in opposite directions. One mode of each source is used for the BSM. The communication idea - quantum teleportation - is shown in **(b)**, where information is sent from left to right by projecting the input state, which we wish to send, together with one mode of the source onto a Bell state via the BSM. After the measurement, the output state is equal to the input state up to a local unitary U, which is adjusted according to the BSM outcome, communicated via a classical channel. Over a long distance, the direct entanglement link needed to perform teleportation is achieved by subsequent BSMs between the entangled state of neighboring sources. This process is shown in **(c)**, where a successful BSM between two modes of two sources entangles the remaining modes traveling in opposite directions, which is called entanglement swapping.

Even though low loss fibers are under development[1], the losses will pose a hard limit to the maximal length of a direct quantum link between two parties to several hundreds of kilometers. This is why current quantum networks define *trusted nodes*, at which the quantum signal is measured and recreated in an amplifier fashion. Those nodes pose an important security issue, as they require the trusted notes to know what they will measure.

For a quantum network to be fully usable for any quantum task and to be secure, trusted nodes have to be avoided. This requires two additional ingredients in the quantum networks of today: quantum memories and entanglement. We already know from subsubsection 2.4.2.2, that quantum information cannot be cloned. Therefore, unlike in classical networks, quantum signals can not be amplified to account for losses in the transmission channels (hence the measurement interception in the before-mentioned excising QKD networks). To still be able to build large quantum networks, we envision connecting two users via entanglement, which is stored in several *untrusted nodes* between the users with the help of quantum memories. Once all those untrusted nodes have received a signal, the *entanglement swapping protocol* creates entanglement between the two end-users, who can now perform *quantum teleportation* to exchange information in a loss-reduced fashion [157], as shown in fig. 4.1.
In the following subsection, we will explain the teleportation and swapping protocol in the context of quantum networks.

4.1.2 Swapping and teleportation with the BSM

4.1.2.1 Quantum entanglement and the Bell basis

To understand entanglement-based protocols, we remember our definition of *entanglement* in subsubsection 2.1.2.2, where a bipartite system is defined to be maximally entangled if the partial trace on one mode yields a fully mixed state on the other. For two-mode systems, the maximally entangled states are the so-called *Bell states*, which form a computational basis and are thus pure. They can be written in the logical basis $|0\rangle_L, |1\rangle_L$, where for simplicity we drop the subscripts, such that

$$|\phi\rangle^{\pm} = \frac{1}{\sqrt{2}}(|00\rangle \pm |11\rangle), \tag{4.1}$$

$$|\psi\rangle^{\pm} = \frac{1}{\sqrt{2}}(|01\rangle \pm |10\rangle). \tag{4.2}$$

The naming of those states stems from the famous *Bell theorem* of 1964 [5]. It states, that the physical principles of locality and reality are incompatible with quantum mechanics. Locality here refers to the idea that a system can only be influenced by its surroundings,

[1] For example by the company *Corning*.

defined by its light cone[2] while reality describes the assumption, that a system has properties that are independent of measurements. Any theory that fulfills reality and locality is classical and can be formulated as a so-called hidden variable mode, where those variables are assumed to describe the underlying physics of a model. Bell showed, that quantum mechanics cannot be described by such a hidden variable model and the states that maximally violate the measurement predictions of such a model are the Bell states. This theorem is based on reasoning on probability theories and can be translated into the expectation values of observables, forming an inequality such that it can be measured and verified in the lab. The most famous inequality used to measure a Bell violation is called the CHSH inequality and was formulated in 1996 [159]. It has been experimentally verified against loopholes[3] many times since 2015 [160–165]. Let us now show the ideal cases of quantum teleportation and swapping, utilizing those pure maximally entangled non-local states.

4.1.2.2 Quantum teleportation before measurement

Quantum teleportation was first proposed in 1993 by Bennet et al. [166] and experimentally implemented in 1997 by Bouwmeester et al. [167]. Since then, this protocol has known remarkable progress and lies at the heart of quantum network protocols [168, 169]. The idea is depicted in fig. 4.1 (b) and shows that the quantum state to be teleported $|\varphi\rangle_{\text{in}} = \sqrt{c_0}\,|0\rangle + \sqrt{c_1}\,|1\rangle$ is measured in a two-mode measurement with one part of a Bell-pair $|\psi\rangle^{+}$[4]. If we write the tensor product of the system with modes a, b, c before measurement we find

$$\begin{aligned} |\varphi_a\rangle_{\text{in}} \otimes |\psi_{b,c}\rangle^{+} \propto \quad & |\psi_{a,b}\rangle^{+} \otimes |\varphi_c\rangle_{\text{in}} + |\psi_{a,b}\rangle^{-} \otimes Z\,|\varphi_c\rangle_{\text{in}} + \\ & |\phi_{a,b}\rangle^{+} \otimes X\,|\varphi_c\rangle_{\text{in}} + |\phi_{a,b}\rangle^{-} \otimes ZX\,|\varphi_c\rangle_{\text{in}}\,. \end{aligned} \tag{4.3}$$

We realize that we can write the tensor product as a sum of all Bell states in the product with either the perfect input state or the input state up to Pauli Gate operations X, Z.

4.1.2.3 Entanglement swapping before measurement

Let us now transition to the case of entanglement swapping, which was first proposed in 1993 by M. Zukowski et al. [170] and experimentally implemented in 1998 by J. Pan et al. [171]. Here, any two Bell states are created and one mode of each is measured together, creating remote entanglement as shown in fig. 4.1 (c). For the example of two $|\psi\rangle^{+}$ Bell

[2] The light cone is the path light takes through space-time. This essentially requires any interaction to be at maximum at the speed of light.

[3] Loopholes in Bell tests refer to possible ways in which we could describe this system as a hidden-variable model after all. Famous loopholes are the detection loophole, the free-choice loophole, the memory loophole, and super-determinism, where the latter is usually ignored in experiments.

[4] The results is equivalent for all Bell states.

states in modes a, b, c, d, where the inner modes b, c are supposed to be measured together, we can rewrite their tensor product as

$$\begin{aligned}|\psi_{a,b}\rangle^+ \otimes |\psi_{c,d}\rangle^+ \propto |\psi_{a,d}\rangle^+ \otimes |\psi_{b,c}\rangle^+ - |\psi_{a,d}\rangle^- \otimes |\psi_{b,c}\rangle^- \\ + |\phi_{a,d}\rangle^+ \otimes |\phi_{b,c}\rangle^+ - |\phi_{a,d}\rangle^- \otimes |\phi_{b,c}\rangle^- .\end{aligned} \tag{4.4}$$

Here we can see that the input states can be rewritten as four tensor products of Bell states. This works for all combinations of input states and chosen measured-mode combinations [5].

4.1.2.4 Let's measure: The Bell state measurement

When rewriting the input states for quantum teleportation and entanglement swapping, we find a superposition of tensor products with Bell states. The *Bell state measurement* (BSM) is a two-mode projective measurement, projecting on one of the four Bell states each time a measurement is taken. Its POVM has four elements, corresponding to a pure projection on one of the four Bell states (see definition of POVM (2.155))

$$\Pi_1 = |\psi\rangle^+ \langle\psi^+| \qquad \Pi_2 = |\psi\rangle^- \langle\psi^-|$$
$$\Pi_3 = |\phi\rangle^+ \langle\phi^+| \qquad \Pi_4 = |\phi\rangle^- \langle\phi^-| \tag{4.5}$$
$$\mathbb{1} = \Pi_1 + \Pi_2 + \Pi_3 + \Pi_4. \tag{4.6}$$

Each projection occurs with an equal probability of 25%, such that the measured modes are projected in one of the four Bell states with equal probability. In the case of teleportation we can see, that such a projection recreates the input state of mode a in mode c (up to a local unitary). This is why one says that information, not matter, was "teleported". To communicate if a local unitary has to be applied, a classical channel between mode a and c is needed in addition. In the swapping protocol a projection onto one of the four Bell states in modes b, c will entangle the two modes a, d. As in the case of teleportation, this is astonishing, as those two modes have never interacted. The Bell-state measurement can therefore be seen as information preserving, where the information of a system or between systems can be imprinted onto another system. If we now consider a network, we can imagine several BSM stages between a communication line. If entanglement swapping is performed between all of them at the same time or asynchronously using quantum memories, the two user nodes can be entangled, independent of the distance between them. Using quantum teleportation then allows user A to send information to user B.

4.1.2.5 The physical BSM

Now that we have discussed the ideal BSM, let us see how we can implement it in physical systems. Our wish list for a perfect BSM should include deterministic operation, high

[5] Albeit with variations in how the different Bell states are combined in the tensor product

detection probability, and easy implementation. As our Bell-state-sources are emitting photonic states, all-optical BSMs are preferable and often used in state-of-the-art network demonstrations [157, 172–175]. Here, the basic scheme always relies on a 50:50 beamsplitter between the two modes to measure. Depending on the encoding, additional optical elements are added, where most often time-bin, polarization, and Fock basis are discussed. Here we will focus on the Fock basis, and this choice will be motivated in subsection 4.1.3. If we assume the physical basis to be vacuum for $|0\rangle_L$ and a single photon for $|1\rangle_L$, we can write the action of a beamsplitter on each Bell state in the tensor product of eq. (4.3) or (4.4) as

$$\begin{aligned} \mathrm{BS}(0.5)\,|\psi\rangle^+ &\propto |10\rangle\,, \\ \mathrm{BS}(0.5)\,|\psi\rangle^- &\propto |01\rangle\,, \\ \mathrm{BS}(0.5)\,|\phi\rangle^\pm &\propto |00\rangle \mp \frac{1}{\sqrt{2}}(|02\rangle - |20\rangle\,. \end{aligned} \tag{4.7}$$

Only the states $|\psi\rangle^\pm$ can be detected with this scheme and this detection relies on the fact that one can indeed detect exactly a single photon. Consequently, a BSM with linear optics is probabilistic and inherently limited to a success probability of 50%, if no additional resources are added [176].

This kind of measurement can be made complete (detecting all four Bell states) and deterministic, by adding a source of non-linearity in the measurement. Optically this can be achieved by using fast feed-forward in combination with homodyne detection instead of single-photon-detectors, but its usefulness is limited by a high loss-sensitivity and limited fidelity [177, 178]. Another approach consists in adding a light-matter interface in the form of (artificial) atoms to the measurement. Several complete BSM experiments have been performed in this paradigm [179–182], but suffer from very low success rates and highly involved setups, making them challenging to scale up. As all of the complete BSM nowadays have a low success probability, we can consider any state-of-the-art Bell-state measurement to be probabilistic. The two main bottle-necks to improve those existing BSM are either by improving the success rate or by improving the fidelity of the BSM. In section 4.2 we will present and analyse an improvement made to the second bottle-neck in an all-photonics setup.

4.1.3 Which quantum states to use in quantum networks?

Until now we have discussed quantum networks in a rather general manner and made no choice regarding the optical states which propagate in the system. We did however argue for the use of entangled states, such that longer distances can be overcome via entanglement swapping. Moreover, highly multi-mode entangled states are predicted to facilitate routing and network structure optimization, making those processes independent of the underlying physical network design [183]. Here, however, we will limit our discussion to bipartite

entanglement. Bipartite entanglement is experimentally accessible to us, forms a convenient test-bed for quantum networks, and has well-defined entanglement measures [61]. When choosing the kind of entangled-state sources S to be used in fig. 4.1 (a), one has to consider the quality of entanglement and the compatibility of the information encoding of each mode with the network. In the next subsubsections, we will discuss encoding considerations and present the implications of post-selection and non-deterministic sources.

4.1.3.1 Encoding considerations in a network

There is a vast choice of optical systems that can create entanglement but differ in the encoding of the individual states. One example we have already discussed is the two-mode squeezing of eq. (3.15) or the single-photon entanglement of subsubsection 4.1.2.5. Those two examples capture perfectly a choice that has to be made: Independent of the quality of entanglement, which can be high in both cases, one needs to choose if the entangled states should be non-Gaussian or Gaussian. This question is highly related to the kind of network one envisions. If we assume the network connects quantum sensing devices or/and quantum computers, then it is reasonable to assume that non-Gaussian states are the information carriers (see discussion in section 2.4). This means that node A in fig. 4.1 will input a non-Gaussian state to be teleported. To our knowledge, no BSM between two different encodings has been demonstrated so far, leading to the requirement that the mode in A of the final entangled state after swapping should be non-Gaussian. In the simplest network, with only one BSM between A and B, we therefore require the mode sent to A to be non-Gaussian.

Let us now investigate if the modes sent to the BSM have any constraints. For this, we motivate the use of quantum memories with a simple example. Let us assume a network with one BSM, where A and B create an entangled pair each, keep one mode, and send the other to the BSM station at half the distance between A and B, $l = L/2$. We can now define the probability that both states arrive at the BSM station without being absorbed due to loss in the fiber as the survival probability

$$p_s(l) = \frac{1}{2} e^{-l/L_{att}}, \tag{4.8}$$

where l is the length between A (B) and the BSM station and L_{att} is the attenuation length, defined as the length at which the signal amplitude drops to $1/e$ of its initial value, which translates to a drop of ≈ 4.34 dB. With a standard fiber at 1550 nm, we find an attenuation length of 21.7 km. Moreover, we are assuming to use a linear Bell-state measurement, succeeding with probability $p_{BSM} = 0.5$. Because of fiber losses and the probabilistic nature of the BSM, this swapping protocol will have to be performed $T_{tot}(l)$ times, before

the protocol succeeds. We find that the total average number of tries needed to successfully perform entanglement swapping is

$$\langle T_{tot}(l)\rangle = \frac{1}{p_s(l)}\frac{1}{p_{BSM}} = 2^2 e^{L/(2L_{att})}, \tag{4.9}$$

growing exponentially with the network length L. Let us now imagine that we add more BSM stations. Now if we use $N_M = 2^n - 1$ BSM stations, we can decrease the number of total tries to

$$\langle T_{tot}(l, N_M)\rangle = 2^{1+\log_2(N_m+1)} e^{\frac{L}{L_{att}(N_m+1)}}, \tag{4.10}$$

showing an exponential improvement in the number of trials. For details on this calculation, see [157, 184]. Of course, this requires all states to arrive at all BSM stations at the same time. This is why the BSM stations are replaced with *repeater stations*.

A repeater station is a BSM, equipped with one quantum memory per mode, which can store the quantum state until each memory has a quantum state stored. Quantum memories are therefore crucial for network synchronization, without which large networks cannot be built. In the above calculation, we have omitted all realistic errors except for loss, but note that there exist error correction protocols for errors in quantum memories [157]. Now that we have discussed the importance of quantum memories, we realize that the main requirement for our states arriving at the repeater stations is compatibility with quantum memories. Quantum memory technology is dominated by cold atomic clouds [185] and atomic ensembles embedded in crystalline structures [186]. Those quantum memories mostly work in the Fock basis [185, 187, 188], and are often used with weak coherent states to approximate single photons. Although weak coherent states, and cat states, have been considered [189] for quantum memories, the envisioned input state mostly stays the single photon. Moreover, quantum memories also impose a requirement on the wavelength of this single photon.

We conclude, that for a general quantum network, the entangled states are preferred to have a non-Gaussian end-point at A and should have an encoding in the low-excitation Fock basis for any state arriving at repeater stations. This still leaves open whether one wants to choose path encoding, where a qubit is encoded in the presence of a single photon in one of two paths, time-bin encoding, where a qubit is encoded in the arrival time of a single photon, which can be late or early, or Fock state encoding, where a qubit is encoded in two Fock states. One can very well envision choosing one kind of encoding flying towards the network, and another for the local use of teleportation. Moreover, those *hybrid entangled states* can be used as high dimensional qubits for a more loss-tolerant quantum computation [190]. We will present such a hybrid entangled state in subsection 4.1.4 and will proceed to discuss post-selection and non-deterministic sources in quantum networks.

4.1.3.2 Post-selection in quantum networks

Many entangled states are created via post-selection, referring to a process where only a subset of the measurement outcomes are considered. This technique, therefore, takes a (semi) classical state and creates the quantum properties afterward, by only selecting measurement results that fit quantum behavior. This prohibits any form of entanglement distillation [191] and is only possible in prepare-and-measure schemes [192], including some QKD settings or metrology protocols [193]. In a general network, post-selection has to be avoided, as it can only be performed once in the system and therefore hinders complicated protocols where entanglement is needed in subsequent processes.

4.1.3.3 Non-deterministic sources in quantum networks

Currently, sources of single-mode non-Gaussian quantum states or entangled quantum states are non-deterministic. They either are based on heralding, as in our case, which gives random state creation events, or on quasi-deterministic sources. Quasi-deterministic sources like quantum dots or other (artificial) atoms can output photons at specific times and are therefore easy to synchronize, but have non-ideal output probabilities. Those are limited by the coupling efficiencies of the emitter to free space or fiber and can be compared to the escape efficiency of an OPO. As with the OPO escape efficiency, imperfect coupling leads to a mixed output state in the Fock basis. Those coupling efficiencies are improved continuously but, up to our knowledge, do not yet reach the Fock-state purity reachable with OPOs [194]. Furthermore, interference between photonic states of quasi-deterministic sources is constrained by their distinguishability, and compared to OPOs, achieving indistinguishable states in those systems is challenging. As soon as coupling efficiencies and indistinguishability comparable to an OPO can be reached, those quasi-deterministic sources will probably be preferable due to the easier clock synchronization and very high count rates that can be achieved.

4.1.4 Hybrid entanglement in the lab

Here we present the hybrid entangled state we can create in our laboratory [145]. Using the non-Gaussian resource states presented in subsection 3.2.3 and subsection 3.2.4, we can create a hybrid entangled state of the form

$$|\psi\rangle_H = c_0 |0\rangle |\text{cat}\rangle_- + e^{i\theta} c_1 |1\rangle |\text{cat}\rangle_+ , \tag{4.11}$$

where we have full control over the weights c_0, c_1 and the phase θ. Entanglement in our case is created by erasing the "which path" information of the heralding modes of OPOI and OPOIIa, as shown in fig. 3.10 (b).
For convenience, the whole experimental setup is shown in fig. 4.2. The pump light at 532 nm, seed light at 1064 nm, and local oscillator light are shared between both OPOs. For

details about the locking, the function of the seed, of the heralding, the Sample & Hold, or of the homodyne detection we refer to chapter 3.

The important element is in the heralding mode, where the heralding path of OPOIIa and OPOI are mixed with the help of a first polarizing beamsplitter (PBS), where c_1 and c_0 of eq. (4.11) can be controlled via the half-wave plates on each path. The second PBS then projects those two modes onto the same polarization, making them indistinguishable. This is only true because of our efforts to match the OPO cavities of OPOIIa and OPOI, giving the output modes the same spectral and spatial shape. The merged heralding path then undergoes filtering and can be detected on one of our SNSPDs.

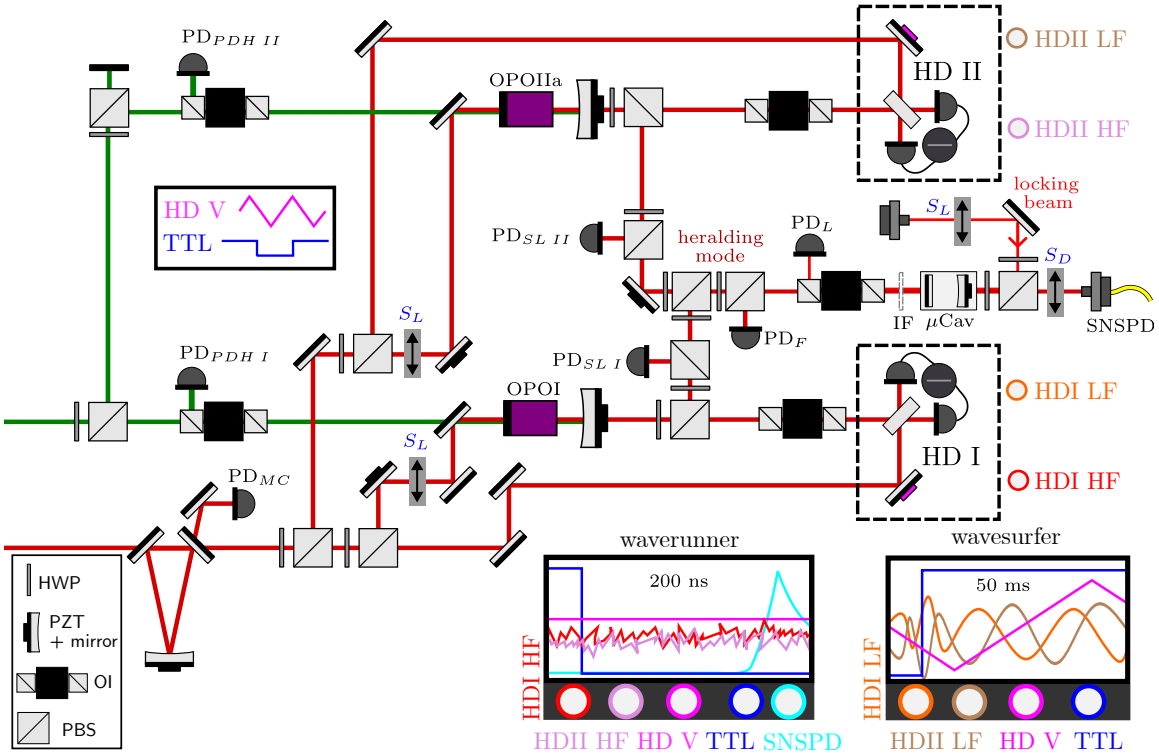

Figure 4.2: The setup for hybrid entanglement creation is shown. From the left the laser (not visible) is emitting green (532 nm) and IR (1064 nm) light. The green light is used as a pump and split towards OPOIIa (top) and OPOI (bottom). The IR light passes the mode cleaner and is then used as a seed for both OPOs and as a local oscillator for the homodynes HDI and HDII. Each homodyne analyses the signal path of its OPO. The heralding path of OPOIIa and OPOI are merged and their phase is locked. For this the heralding path phase of OPOIIa is scanned via a piezo-electric transducer (PZT) and the phase of the interference fringe of the two heralding paths is locked with the signal of PD$_F$. After this locking stage, the heralding path is filtered via an interferential filter (IR) and a homemade micro-cavity μCav, leading towards the SNSPD. A detection click on the SNSPD (conditioned on a low TTL voltage) leads to the trace of the high frequency (HF) outputs of the two homodynes being recorded on the waverunner, together with the voltage applied to the local oscillator (LO) PZT (in pink). When the TTL voltage is high, a full scan of this homodyne PZT voltage together with the fringes of the seed-LO of OPOI and OPOIIb are recorded on the wavesurfer. The measurement is taken in a Sample & Hold configuration. HWP stands for Half-wave-plate, OI for optical isolator, and PBS for polarizing beamsplitter.

To create entanglement, and not a statistical mixture, the relative phase between the heralding paths of OPOIIa and OPOI needs to be stable. For this, the phase of the OPOIIa heralding path is scanned and the resulting fringe is recorded on the photodiode PD_F. With the help of a side lock, we can now lock the fringe and thereby the phase θ of eq. (4.11) wherever we want. The data recording is shown at the bottom left of fig. 4.2, where one more trace is added on each oscilloscope to be able to calculate the quadrature value of OPOI and OPOIIa with the high-frequency output of HDII and HDI and know the corresponding phase thanks to the voltage-to-phase data on the wavesurfer, recording the low frequency (LF) output of both homodynes.

It is not trivial how to plot such a state and we follow the tradition of this laboratory, first explained in the PhD thesis of O. Morin [30].
For this, we use the fact that eq. (4.11) is a tensor product and plot the Wigner functions of the tensor elements as shown in fig. 4.3 (a). Odd and even cat states are ideally on the diagonal, while the off-diagonal terms form their bracket combinations. The off-diagonal terms are therefore not hermitian, but conjugate, such that we plot only the real elements of their Wigner function. We find that our experimental state has a fidelity of 64% with an ideal hybrid state with a cat amplitude of $\alpha = 0.82$, $c_0 = 0.4$, and a phase $\theta = 0.35\pi$. This ideal state is plotted in fig. 4.3 (b) for comparison with the experimentally measured state, shown in (c). Here both homodyne data sets were corrected for the losses given in table 3.6.

4.1.4.1 Network compatibility

We present here an experimentally generated state that fulfills many of the criteria explained in subsubsection 4.1.3.1. Each mode in this entanglement is non-Gaussian, as discussed in chapter 3 and represents two different ways of encoding: cat states and single photons. Both modes can be used locally or sent to network repeater stations, thanks to experimental strategies to counteract losses on cat states [33].
The entanglement negativity of this state is calculated to be $\mathcal{N} = 0.296$ and its logarithmic negativity is $E_{\mathcal{N}} = 0.671$, showing very strong distillable quantum correlations (see subsubsection 2.1.2.3). To test those correlations against classical local variable models, quantum steering was performed [35], which is a one-sided Bell test, formulated as one party comparing the measured output values with the other party, to decide whether or not they share entanglement.

A recent publication in collaboration with the group of Professor Magdalena Stobińska [195] discusses possible experimental Bell-test settings. There it is shown, that the specific type of hybrid entanglement is maximal non-local in its pure form, making it a different

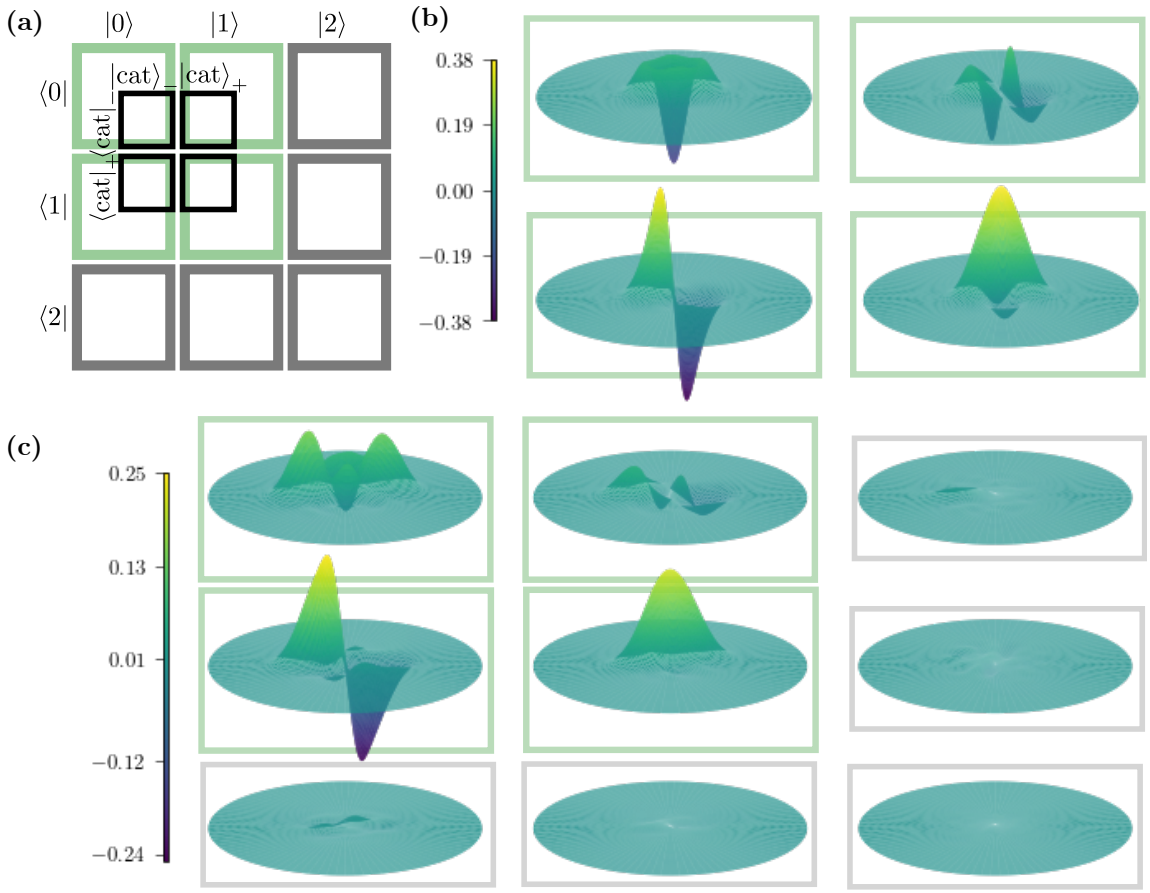

Figure 4.3: In **(a)** the visualization of the hybrid entanglement ρ_H is depicted. The tensor structure is used, where only the indices containing the cat-state combinations are plotted. The discrete mode up to the Fock state $n = 2$ therefore can be used to show 3x3 Wigner states of the continuous mode.The diagonal terms are $\langle 0|\rho_H|0\rangle$,$\langle 1|\rho_H|1\rangle$ and $\langle 2|\rho_H|2\rangle$. All terms are plotted as Wigner functions. Note that in this notation only the diagonal terms are properly defined states, while the off-diagonal terms are only conjugate and not hermitian matrices. We plot only the real part of their Wigner function. In **(b)** the corresponding plot of an ideal hybrid entanglement with $\alpha = 0.82$, $c_0 = 0.4$, and a phase $\theta = 0.35\pi$ is shown. **(c)** shows the experimental hybrid entanglement.

form of Bell-state. Moreover, the hybrid entanglement has been used for entanglement swapping [36] in 2020 and quantum teleportation in 2022 [37] during this PhD work, which will be presented in chapter 5.

4.1.4.2 Possible improvements

The quality of the above-shown entanglement depends heavily on the quality of the resource states, and therefore on the OPO output quality. To improve the single photon purity of OPOIIa, its escape efficiency can be increased, which will be discussed in chapter 7. For OPOI our main parameter to tune is the escape efficiency as well, rendering the squeezed vacuum state purer. The usability of that kind of state in quantum networks is limited by their low count rate of 30-100 kHz, which stems from the need to avoid erroneous clicks,

due to multi-photon components in the heralding paths. Those are directly connected to an increased heralding tapping on OPOI or/and an increased pump rate of OPOIIa. This trade-off can be circumvented by exchanging our SNSPD on/off detectors with photon-number resolving detectors (PNR). Currently, PNR detection is mostly performed with transition-edge sensors, which show high quantum efficiency but have a considerably slower recovery time than SNSPDs [196], which finally limits the maximal rates of those detectors. Moreover, we note, that using an encoding solemnly based on the Fock basis is very sensitive to errors. Especially losses, translating into errors due to vacuum being part of our qubit sub-spaces, hider the usability of this hybrid entanglement in long-range networks. This can be circumvented by using time-bin encoding as suggested by Gouzien et al. [197].

Now that we have discussed entanglement in quantum networks, we will shift our focus to another crucial network-enabling technology: Bell state measurements.

4.2 The hybrid Bell state measurement

Here we present an all-optical Bell state measurement (BSM), that has a boosted fidelity with the ideal optical BSM. Bell-state measurements rely on the interference of two optical modes and subsequent photon detection [198]. Central to this operation is the capability to detect a single-photon state, visible in eq. (4.7). However, the two-photon component is present in most photon creation processes including OPOs, and inherently in the BSM as more than one photon can interfere on the beamsplitter. The most common detectors used for BSMs are on-off detectors, which cannot distinguish photon numbers, and are thus unable to discriminate one- from two-photon contributions [199]. This two-photon error is a strong limitation for high-fidelity Bell-state measurements. A potential alternative to on-off detectors are superconducting photon-number resolving detectors [200], which are still under intense development and of limited availability, or a large number of multiplexed on-off detectors that would require extremely high efficiencies.

Here we investigate a method to mitigate the effect of multi-photon components: the *hybrid Bell-state measurement* (HBSM). It combines on-off single-photon detection with homodyne conditioning, as sketched in fig. 4.4. The addition of the homodyne conditioning enables a more faithful discrimination between single- and two-photon states, reducing the potential errors and thereby boosting the measurement projectivity.

Figure 4.4: Sketch of the hybrid Bell-state measurement (HBSM) consisting of an on-off single-photon detection (SPD) and a quadrature conditioning via homodyne detection (HD) in a network configuration. At a network node, two optical modes are mixed on a balanced beamsplitter. One of the output modes is tapped via a beamsplitter with reflectivity R and this part is sent to a SPD. The transmitted mode is directed to an HD, which is used for conditioning on quadrature values in a window Δ around $q = 0$. The HBSM success is heralded by both detection events.

This hybrid approach has been used in recent experimental realizations of entanglement swapping and quantum teleportation, based on the hybrid entanglement presented in subsection 4.1.4 [36, 37, 145]. It turned out to be instrumental in these successful demonstrations. We will now provide a formal description of the HBSM and analyze it in function of the different tunable experimental parameters. We then apply this approach to the key examples of quantum teleportation and entanglement swapping protocols. We finally compare the performances with demanding photon-number resolving detection.

4.2.1 Hybrid BSM: formalism and error mitigation

The hybrid Bell-state measurement is depicted in fig. 4.4. It combines an on-off single-photon detection (SPD) and quadrature conditioning via homodyne detection (HD). The incoming mode impinges on a beamsplitter with a reflectivity R and the reflected path leads to the SPD. The transmitted mode is sent to a homodyne detection, where we define a conditioning window Δ around the quadrature value $q = 0$. The success of the HBSM is heralded by both detection events. The HBSM has therefore two tunable parameters, the reflectivity R and the conditioning window Δ, and also depends on the detection efficiencies. As explained in chapter 3, Δ is normalized to the standard deviation of the vacuum shot noise.

The general principle of the HBSM can be first understood in the limit of small R. In this case, the first detection is equivalent to a photon subtraction. A two-photon state then results in a single-photon state, while a single-photon state reduces to vacuum. A subsequent homodyne detection can discriminate the parity as the states have different probabilities of returning a given quadrature value. In particular, the probability of a value close to zero is large for vacuum and negligible for a single photon, as can be seen in the conditioning box of fig. 4.4, where the associated white and black marginal distributions are shown. In the following, we provide the full theoretical analysis and benchmarking of the HBSM.

4.2.1.1 POVM of the hybrid Bell-state measurement

The overall detector can be described by its positive operator valued measure (POVM) [201], see subsubsection 2.1.3.2. In the case of the HBSM, there are two possible measurement outcomes, corresponding to a successful and an unsuccessful event. Here we are interested in the successful POVM element Π^{on}. The description of this POVM element relies on the matrices of the beamsplitter operation BS(R) that depends on its reflectivity, the single-photon detection POVM element $\Pi^{\text{on}}_{\text{SPD}}$, which corresponds here to an on-off detection [202],

and the homodyne detection POVM elements [203], integrated over the detection window Δ and independent of the detection phase θ, i.e.,

$$\Pi^{\text{on}}_{\text{HD}(\Delta)} = \int_{-\Delta/2}^{\Delta/2} dq \int_{0}^{2\pi} d\theta \, \Pi^{q,\theta}_{\text{HD}}. \tag{4.12}$$

The Π^{on} HBSM matrix in the Fock basis can then be written as

$$\Pi^{\text{on}} = \text{BS}(R)^{\dagger}\Big[\Pi^{\text{on}}_{\text{HD}(\Delta)} \otimes \Pi^{\text{on}}_{\text{SPD}}\Big]\text{BS}(R). \tag{4.13}$$

As this measurement is phase-independent, the POVM element has only diagonal terms that are non-zero. As mentioned in the introduction we mostly assume Fock states up to $|2\rangle$. The diagonal elements are given by

$$\begin{aligned}
\Pi^{\text{on}}_{[0,0]} &= 0, \\
\Pi^{\text{on}}_{[1,1]} &= R\,\eta_{\text{SPD}}\,\text{erf}\left(\frac{\Delta}{2}\right), \\
\Pi^{\text{on}}_{[2,2]} &= R\,\eta_{\text{SPD}}\Big[\text{erf}\left(\frac{\Delta}{2}\right)(2 - R\,\eta_{\text{SPD}}) \\
&\quad + \frac{2\Delta}{\sqrt{\pi}}\eta_{\text{HD}}(R-1)e^{-\Delta^2/4}\Big],
\end{aligned} \tag{4.14}$$

where η_{SPD} is the detection efficiency of the single-photon detector and η_{HD} the efficiency of the homodyne detection. Many implementations require a filtering stage before the single-photon detection, and its efficiency can be integrated into an overall η_{SPD}. In the asymptotic limit of small R and Δ, the POVM elements reduce to

$$\begin{aligned}
\Pi^{\text{on}}_{[0,0]} &= 0, \\
\Pi^{\text{on}}_{[1,1]} &\sim \frac{R\,\Delta\,\eta_{\text{SPD}}}{\sqrt{\pi}}, \\
\Pi^{\text{on}}_{[2,2]} &\sim \frac{2\,R\,\Delta\,\eta_{\text{SPD}}}{\sqrt{\pi}}(1 - \eta_{\text{HD}}).
\end{aligned} \tag{4.15}$$

As the ideal HBSM shall project on the single-photon state, we aim at reducing $\Pi^{\text{on}}_{[2,2]}$ while increasing $\Pi^{\text{on}}_{[1,1]}$ with the experimentally tunable parameters R and Δ. As shown in fig. 4.5 (a)-(d), for a fixed reflectivity R, this is obtained by decreasing the conditioning window Δ. From a certain value of Δ, typically 0.25, decreasing it further has a limited effect as can be seen in fig. 4.5(c) and 4.5(d). Furthermore, we note that we are achieving a measurement that detects odd Fock states with higher probability than even ones. In our case of interest for BSM, this feature reduces to a boosted single-photon versus two-photon detection.
To further explore the HBSM in this case a benchmark needs to be defined.

4.2.1.2 Benchmark: Purity of the HBSM

The ideal HBSM should act as a perfect single-photon detector, having only one non-zero element, i.e., $\Pi^{\text{on}}[1,1] = 1$. In order to benchmark the HBSM we propose the purity $\mathcal{P}(\Pi^{\text{on}})$, measuring the projectivity of the POVM. As above, the POVM element will be truncated such that we only consider the first diagonal elements defined in Eq. 4.14. The purity can then be defined as

$$\mathcal{P}(\Pi^{\text{on}}) = \frac{(\Pi^{\text{on}}_{[1,1]})^2 + (\Pi^{\text{on}}_{[2,2]})^2}{(\Pi^{\text{on}}_{[1,1]} + \Pi^{\text{on}}_{[2,2]})^2}. \tag{4.16}$$

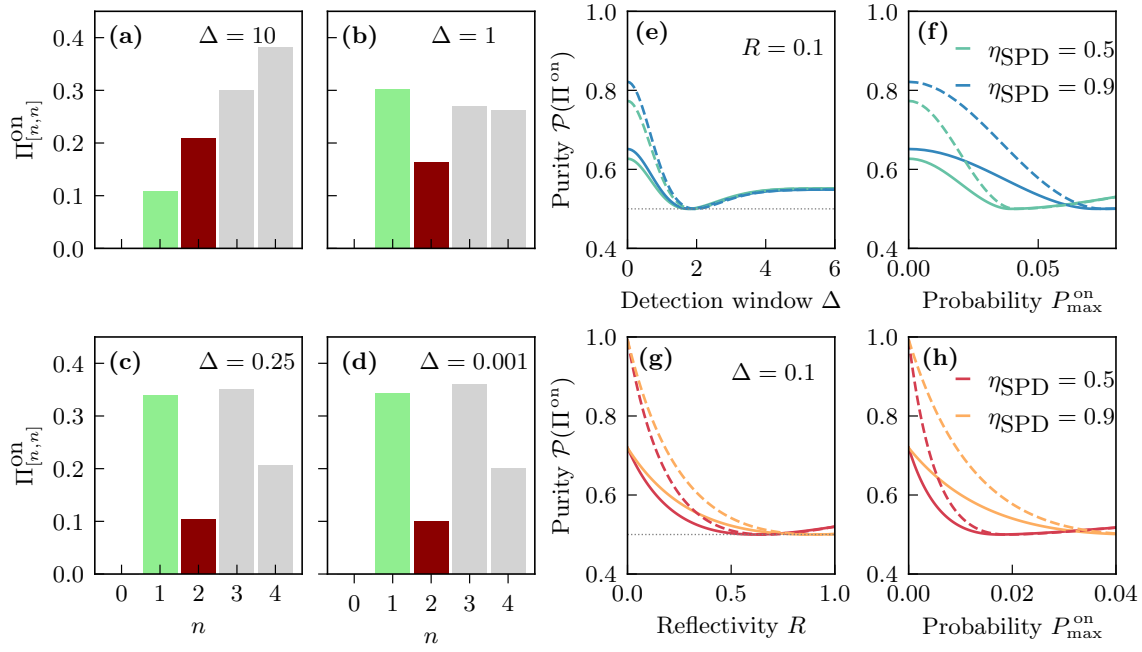

Figure 4.5: On the left, diagonal elements of the HBSM POVM Π^{on} element. They are given for a fixed reflectivity $R = 0.1$ and for different conditioning windows Δ, from a large acceptance to a very small one relative to shot noise: (a) $\Delta = 10$, (b) $\Delta = 1$, (c) $\Delta = 0.25$ and (d) $\Delta = 0.001$. The coloring indicates the wanted green $\Pi^{\text{on}}_{[1,1]}$ and unwanted red $\Pi^{\text{on}}_{[2,2]}$ elements. All matrices were normalized for comparability, with normalization factors $\mathcal{N}_a = 0.824$, $\mathcal{N}_b = 0.156$, $\mathcal{N}_c = 0.037$ and $\mathcal{N}_d = 0.00015$. The detection efficiencies are set to $\eta_{\text{HD}} = \eta_{\text{SPD}} = 0.9$. On the right the HBSM purity $\mathcal{P}(\Pi^{\text{on}})$ up to Fock state $n = 2$ is depicted. The purity is given as a function of (e) the conditioning window Δ with fixed reflectivity $R = 0.1$ and of (g) the reflectivity R with fixed window $\Delta = 0.1$. (f) and (h) provide the purity as a function of the detection probability $P^{\text{on}}_{\text{max}}$. The homodyne detection efficiency is set to $\eta_{\text{HD}} = 0.9$ ($\eta_{\text{HD}} = 1$) for the solid (dotted) line, while two values of the single-photon detector efficiency η_{SPD} are considered. The grey dotted line depicts the purity for a perfect on-off detector.

This measure takes values between 0.5 and 1, where 0.5 corresponds to $\Pi^{\text{on}}_{[2,2]} = \Pi^{\text{on}}_{[1,1]}$. In the asymptotic limit of $R \to 0$ and $\Delta \to 0$ the purity approaches

$$\mathcal{P}(\Pi^{\text{on}}) \sim \frac{1 + 4(\eta_{\text{HD}} - 1)^2}{(3 - 2\eta_{\text{HD}})^2}, \tag{4.17}$$

and only depends on the homodyne measurement efficiency η_{HD}. For $\eta_{\text{HD}} \to 1$, the HBSM becomes pure, corresponding to a projective measurement.

Given this expression, we can now evaluate how the purity depends on Δ and R. This is detailed in fig. 4.5 (e) and 4.5 (g), respectively, and for two values of SPD detection efficiency η_{SPD}. Figures 4.5 (f) and 4.5 (h) provide the maximal possible detection probability $P^{\text{on}}_{\text{max}}$. This probability is defined as the maximization of the detection probability over all states, thereby showing the detection probability for the most favorable state. This is the reason for this probability having a minimum, which corresponds to the ideal state switching from a single- to a two-photon state[6]. The reflectivity R has a larger impact on the purity while Δ shows a more favorable trade-off between purity and detection probability. Importantly we note, that a decrease in the SPD efficiency increases the importance of the two-photon component.

The purity enables to benchmark of the HBSM. With R and Δ well set, this detector can herald with high probability a single photon and with low probability two photons. In the next subsection, we now turn to the output of this hybrid measurement approach when applied to different input states and detail its use for networking protocols.

4.2.2 Application to the hybrid Bell-state Measurement

In the following, we will consider the general scenario of a two-mode input state and the HBSM applied on one of the two modes. The performance of the HBSM can be characterized by calculating the fidelity $\mathcal{F}$ of the conditioned mode with the ideal projection if a perfect single-photon measurement would be performed. We will first consider the case of an input state with single- and two-photon components, and then consider the use of the HBSM for two typical examples, namely quantum teleportation and swapping.

4.2.2.1 The HBSM as a single-photon detector

We will first investigate the effect of the HBSM on two-mode states with photon-number correlations, i.e. of the form $\sqrt{c_{11}}\,|11\rangle + \sqrt{1 - c_{11}}\,|22\rangle$ or $c_{11}\,|11\rangle\langle 11| + (1 - c_{11})\,|22\rangle\langle 22|$. These two cases are identical as the HBSM is phase-insensitive. An ideal measurement on one mode will project the other one onto a single-photon state $|1\rangle$. Specifically, we want to evaluate how the fidelity F between the conditioned mode and the target single photon

[6] This is a convex problem, thereby pure states will always maximize the detection probability

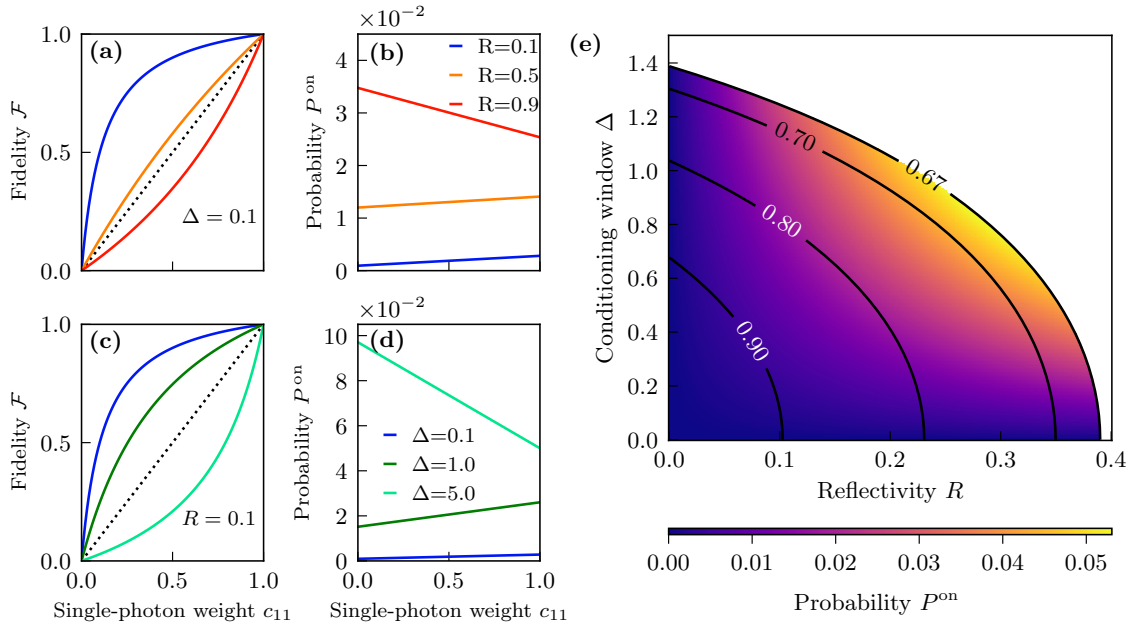

Figure 4.6: Here the effect of the HBSM applied to one mode of a two-mode state with photon-number correlations, of the form $\sqrt{c_{11}}\,|11\rangle + \sqrt{1-c_{11}}\,|22\rangle$ or $c_{11}\,|11\rangle\langle 11| + (1-c_{11})\,|22\rangle\langle 22|$ where c_{11} is the single-photon weight, is shown. The discrepancy from the ideal case, in which the HBSM projects the second mode onto $|1\rangle$, is given by the fidelity $\mathcal{F}$ as a function of the weight c_{11}. The fidelity is displayed for (a) different reflectivities R with fixed conditioning window $\Delta = 0.1$ and for (c) different conditioning windows Δ with fixed $R = 0.1$. The black dotted lines indicate the fidelity without any measurement. (b) and (d) provide the corresponding success probabilities P^{on}. In (e) a detailed map of the HBSM success probability P^{on} for the impinging two-mode state with a single-photon weight $c_{11} = 0.5$ is shown. P^{on} is given as a function of the conditioning window Δ and the reflectivity R. The detection efficiencies are set to $\eta_{\text{HD}} = 0.9$ and $\eta_{\text{SPD}} = 0.5$.

depends on the HBSM settings, i.e., Δ and R.

Figure 4.6 provides the fidelity $\mathcal{F}$ and the associated success probability P^{on} of the measurement as a function of the single-photon component c_{11}. Figures 4.6 (a) and (b) correspond to a given conditioning window and different reflectivities. A large reflectivity $R \geq 0.5$ results in a projection worse than simply tracing out the second mode without a measurement. As expected, the success probability P^{on} is increasing with the single-photon weight, except when the reflectivity is very large (here $R = 0.9$), due to SPD event corresponding more and more to a two-photon detection. In (c) and (d), the reflectivity is fixed to $R = 0.1$ while the conditioning window Δ varies. A very large conditioning window has a stronger effect than a very high reflectivity seen in (a). This leads to the conclusion that the conditioning window is the more responsive parameter, whereas the reflectivity can act as fine-tuning. This effect strongly depends on the SPD efficiency η_{SPD}, which here is set to $\eta_{\text{SPD}} = 0.5$. Decreasing both R and Δ enables to achieve a large fidelity with the target single photon but reduces the success probability P^{on}. This trade-off is shown in (e), where the success probability is given as a function of the reflectivity and the conditioning window. At the

price of a low success probability, arbitrarily high fidelities can be achieved, even if the SPD efficiency is set as here to a moderate value $\eta_{\mathrm{SPD}} = 0.5$.

As we have shown, for some sets of parameters, the HBSM can efficiently separate a two-photon contribution from a single-photon one, at the price of the success probability. For the linear BSM, the usual detection schemes do not enable this discrimination, and two-photon errors are one of the limiting factors, hindering faithful quantum teleportation and entanglement swapping. We will now focus on the performances when a HBSM is used for these two operations.

4.2.2.2 The HBSM in a teleportation protocol

Quantum teleportation as shown in fig. 4.7 (a) considers an input qubit of the form

$$|\varphi\rangle_{\mathrm{in}} = \sqrt{c_0}\,|0\rangle + \sqrt{c_1}\,|1\rangle \tag{4.18}$$

and one of the four entangled Bell state as a resource. A Bell-state measurement between one mode of the Bell state and the input state will then project the remaining mode into the input state up to a local unitary, as in eq. (4.3). With a linear BSM as in eq. (4.7), only the states $|\psi\rangle^{\pm}$ can be detected with this scheme and this detection relies on the fact that one can indeed detect exactly a single photon. For simplification, we will only consider $|\psi\rangle^{+}$.

The probability to measure a single photon is 0.25, while the probability to measure two photons is $c_1/4$. If both single- and two-photon components are detected equally, we can define the worst-case scenario for detection of the teleportation fidelity $\mathcal{F}_{\mathrm{T}}$, which decreases

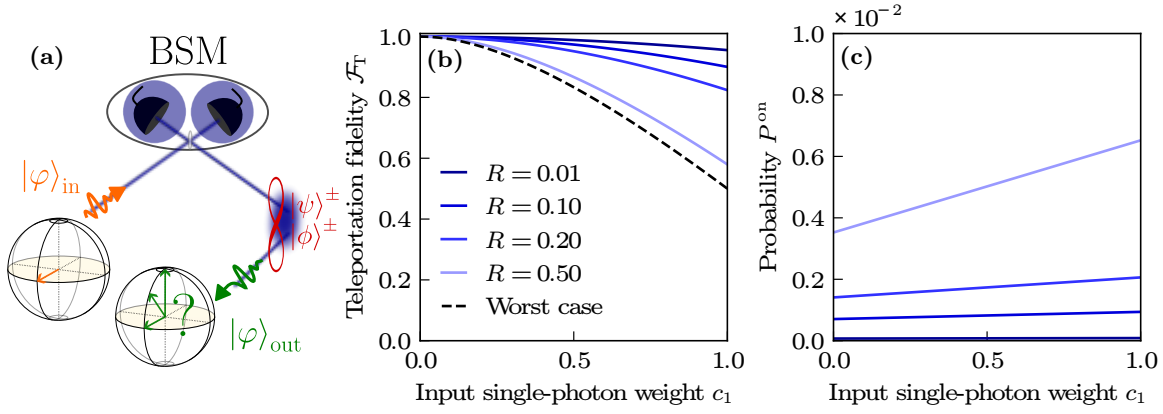

Figure 4.7: Teleportation protocol with the hybrid Bell-state measurement is shown. (a) A qubit to be teleported $|\psi\rangle_{in} = \sqrt{c_0}\,|0\rangle + \sqrt{c_1}\,|1\rangle$ undergoes a BSM with one mode of a Bell state. The remaining mode is ideally projected onto the input state upon successful detection. (b) The fidelity $\mathcal{F}_{\mathrm{T}}$ between the input and teleported states and (c) the success probability P^{on} are given as a function of the input single-photon weight c_1 for different reflectivities R of the HBSM. The conditioning window is fixed at $\Delta = 0.1$ and the detection efficiencies are set to $\eta_{\mathrm{HD}} = 0.9$ and $\eta_{\mathrm{SPD}} = 0.5$.

with the input single-photon weight. This is equivalent to the usual BSM detection, using on-off detectors.

Figures 4.7 (b) and (c) provide the teleportation fidelity $\mathcal{F}_{\mathrm{T}}$ and the probability of success when using a HBSM, for a fixed conditioning window and various values of the reflectivity R. The HBSM leads to fidelities larger than the ones obtained with the usual BSM for all possible single-photon input weights.

4.2.2.3 The HBSM in a swapping protocol

We now turn to the case of entanglement swapping, as sketched in fig. 4.8 (a). Here the input states are twice the same Bell state. A Bell state measurement between one mode of each then projects the remaining modes once again into a Bell state. We assume that the two input entangled states are of the form

$$|\psi\rangle_{\mathrm{in}}^{\sqrt{c_{10}}} \;=\; \sqrt{c_{01}}\,|01\rangle \;+\; \sqrt{c_{10}}\,|10\rangle\,, \tag{4.19}$$

such that their tensor product can be written as in eq. (4.4), where the BSM is applied between each second mode. After one mode of each interacted on a balanced beamsplitter, a projection onto a single-photon state will lead to a Bell state $|\psi\rangle^{\pm}$, dependent on the detector. We will again consider the detection on only one output port, projecting the final modes into

$$|\psi\rangle_{\mathrm{out}} = \frac{1}{\sqrt{2}}(|01\rangle + |10\rangle). \tag{4.20}$$

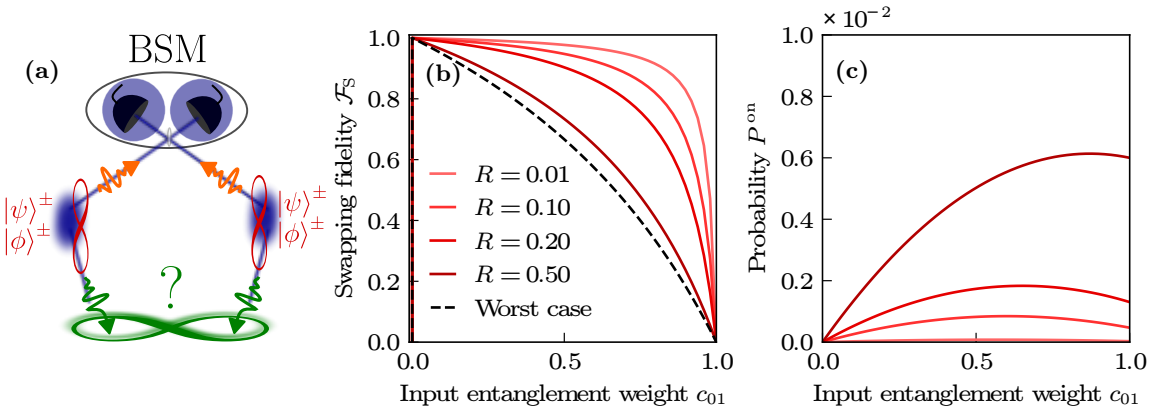

Figure 4.8: The entanglement swapping protocol used with hybrid Bell-state measurement is shown. (a) Two Bell states of the form $|\psi^{\mathrm{in}}\rangle = \sqrt{c_{01}}\,|01\rangle + \sqrt{c_{10}}\,|10\rangle$ are created and the second mode of each undergoes a BSM. This operation ideally entangles the two remaining modes onto $|\psi^{\mathrm{out}}\rangle \propto |01\rangle + |10\rangle$. (b) The fidelity $\mathcal{F}_{\mathrm{S}}$ between the ideal $|\psi^{\mathrm{out}}\rangle$ and the projected state and (c) the success probability P^{on} are given as a function of the input weight c_{10} for different reflectivities R of the HBSM. The coincidence window is fixed at $\Delta = 0.1$ and the detection efficiencies are set to $\eta_{\mathrm{HD}} = 0.9$ and $\eta_{\mathrm{SPD}} = 0.5$.

Equal detection of single photons with probability $c_{10}(1-c_{10})$ and two photons $0.5(1-c_{10})^2$ leads to the worst case of the swapping fidelity $\mathcal{F}_S$ between the ideal output state $|\psi^{out}\rangle$ and the actual output state, one again corresponding to the usual BSM.
Figure 4.8 (b) and (c) provide the swapping fidelity $\mathcal{F}_S$ and the probability of success when using a HBSM, for a fixed conditioning window and various values of the reflectivity R. Similarly to the teleportation case, the HBSM leads to fidelities larger than the worst case scenario for all possible single-photon input weights. We note that the swapping fidelity drops to zero for the extreme cases $c_{01} = 0$ and $c_{01} = 1$.
Compared to the teleportation fidelity of fig. 4.7 (b) this might seem peculiar at first glance. However, here entanglement between two remote states is verified, which cannot be created at all if the input states are not entangled, i.e., at the extreme points of c_{01}. For decreasing c_{01}, the swapping state becomes closer to the target state $|\psi\rangle^+$ as the two photon detection probability is decreasing steadily. This improvement in fidelity drops abruptly to zero for $c_{01} = 0$, corresponding to no entanglement in the system that could be swapped. This differs from the teleportation where the theoretical minimum is not zero. Depending on the reflectivity R, the two-photon event probability reduces slower or faster. Those false two-photon detection events shift the maximum of the success probability P^{on} towards lower input weights c_{10} as shown in fig. 4.8 (c).

We have seen that the HBSM enables substantially improving the output state fidelity of both swapping and teleportation operations. We will now compare the HBSM to photon-number resolving (PNR) detectors, which are another option to improve linear BSM.

4.2.3 Benchmarking the HBSM against PNR detectors

An obvious but daunting solution to two-photon errors are photon-number resolving (PNR) detectors. Those detectors are under intense development, and promising candidates are transition-edge sensors or superconducting-nanowire detectors that are multiplexed or where the number resolution is based on different dynamics [200]. There is a maximal number of Nphotons that can be distinguished in realistic detectors [200, 204].

Independent of the technology, all PNR detectors can be described via the same underlying POVM elements [86], equivalent to N multiplexed detectors.
In order to compare PNR detectors to the HBSM, as sketched in Fig. 4.9, we will only consider the POVM element of a single detection event with a photon resolution up to N,

$\Pi^{(1,N)}$. All PNR POVM elements are phase-independent such that their matrices only have diagonal elements and can be written as

$$\begin{aligned}\Pi^{(1,N)}_{[0,0]} &= 0, \\ \Pi^{(1,N)}_{[1,1]} &= \eta_{\mathrm{SPD}}, \\ \Pi^{(1,N)}_{[2,2]} &= \eta_{\mathrm{SPD}}\left[2(1-\eta_{\mathrm{SPD}}) + \frac{\eta_{\mathrm{SPD}}}{N}\right].\end{aligned} \tag{4.21}$$

We have already see this equation in subsection 2.3.4. We note that even in the limit of perfect PNR $N \to \infty$ imperfect detection efficiency $\eta_{\mathrm{SPD}} < 1$ will lead to an unavoidable two-photon error with

$$\lim_{N\to\infty} \Pi^{(1,N)}_{[2,2]} = 2\eta_{\mathrm{SPD}}(1-\eta_{\mathrm{SPD}}). \tag{4.22}$$

This trend is to be compared to the HBSM in fig. 4.10 (a), where the purity of either the HBSM POVM element Π^{on} or the PNR POVM element $\Pi^{(1,N)}$ are shown as a function of η_{SPD}. We can observe that for a PNR detector with $N = 1$ the HBSM with small Δ has a higher purity for all η_{SPD}. This is indeed also true for $N = 2$ even if here we can observe that towards larger SPD efficiency the purity recovers, still staying below the one of the HBSM.
Remarkably, even the ideal PNR ($N \to \infty$) only surpasses the HBSM purity with $\Delta = 0.1$ from $\eta_{\mathrm{SPD}} = 0.85$ onward, a very stringent condition.

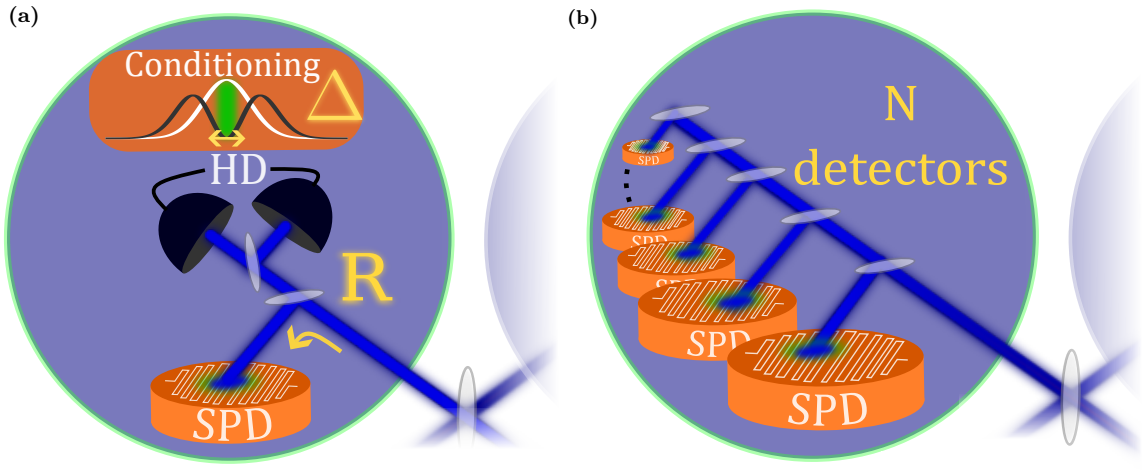

Figure 4.9: Sketch of Bell-state measurement implementations: (a) with a single-photon on/off detector in a HBSM scenario as studied before and (b) with N multiplexed single-photon on/off detectors. This multiplexed implementation leads to photon-number resolution in the limit of a large number N of detectors. We compare the two configurations.

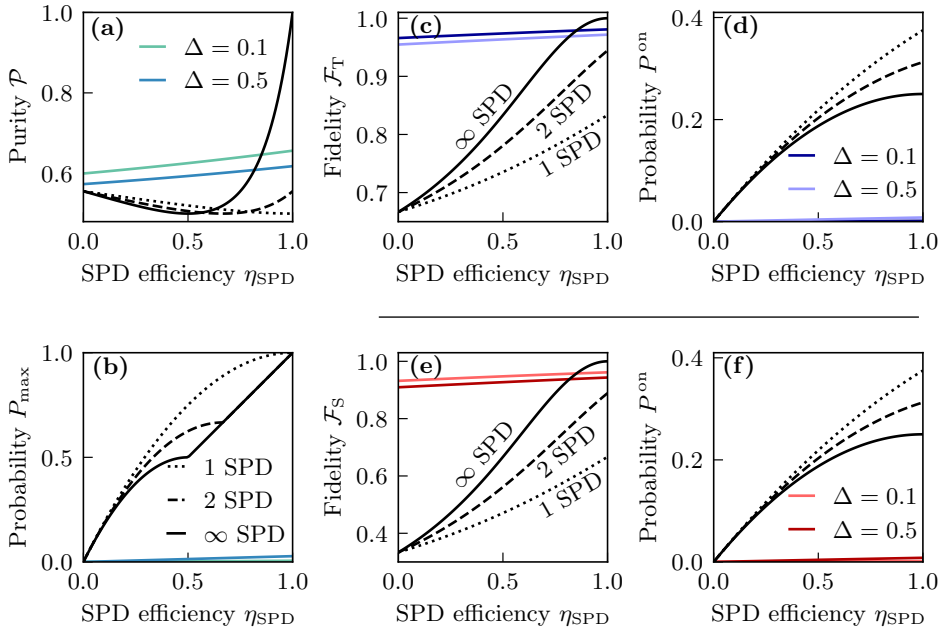

Figure 4.10: Comparison of the hybrid BSM with BSM implementations based on N-multiplexed single-photon detectors in terms of purity as well as entanglement and swapping fidelity. The POVM success element of the HBSM Π^{on} is benchmarked against the POVM elements of N-multiplexed single photon detectors $\Pi^{(1,\mathrm{N})}$. The purity $\mathcal{P}$ is given in (a) as a function of the SPD efficiency η_{SPD}. The corresponding success probability P_{max} is given in (b). Two values of conditioning window Δ are considered for HBSM, and compared to implementations with $N = 1$, $N = 2$, and $N = \infty$ that emulates perfect photon-number resolution. (c) and (d) provide the fidelity $\mathcal{F}_{\mathrm{T}}$ and success probability P^{on} for the teleportation of a balanced qubit. (e) and (f) provide the fidelity $\mathcal{F}_{\mathrm{S}}$ and success probability P^{on} for the swapping of two balanced $|\phi^+\rangle$ states. Two values of conditioning window Δ are considered for HBSM, and compared to implementations with $N = 1$, $N = 2$ and $N = \infty$ that emulates perfect photon-number resolution. All POVM elements are truncated at $n = 2$. For HBSM, the homodyne detection efficiency is set to $\eta_{\mathrm{HD}} = 0.9$ and the reflectivity is fixed at $R = 0.1$.

Indeed if we compare the limits of the HBSM purity of eq. (4.17), we can see that it is independent of the efficiency η_{SPD}, while the purity of the PNR depends on it as

$$\lim_{N\to\infty} \mathcal{P}(\Pi^{(1,\mathrm{N})}_{[1,1]}) = \frac{4\eta_{\mathrm{SPD}}^2 - 8\eta_{\mathrm{SPD}} + 5}{(3 - 2\eta_{\mathrm{SPD}})^2} < 1 \quad \text{for all } \eta_{\mathrm{SPD}}.$$

This explains the strong advantage of the HBSM in terms of purity. As stressed before, it comes at the cost of a low success probability, as shown in fig. 4.10 (b).

We further want to compare the performance of the HBSM and PNR detectors in the typical use cases of teleportation and entanglement swapping. The results are summarized in fig. 4.10 (c)-(f). Here all states are balanced, including the teleportation input state $(1/\sqrt{2})(|0\rangle + |1\rangle)$ and the swapping input states $(1/\sqrt{2})(|00\rangle + |11\rangle)$. The achieved fidelities with the HBSM with $\Delta = 0.1$ are superior to the ones obtained with the ideal PNR detector

with $N = \infty$ until an efficiency $\eta_{\text{SPD}} = 0.79$ in the case of teleportation and $\eta_{\text{SPD}} = 0.86$ in the case of swapping.
Up to typically $N = 5$, the fidelities are always larger for the HBSM whatever the efficiency. These numbers illustrate the advantage that the HBSM can provide in a variety of scenarii.

4.3 Conclusion

In summary, we have initially presented a form of hybrid entanglement that harvests the output state of both OPOI and OPOIIa. This hybrid entanglement, while not currently envisioned for direct real-world applications, provides a robust framework for investigating heterogeneous networks and the distribution of highly entangled non-Gaussian states. This exploration serves as a valuable avenue for theoretical and experimental investigations into the properties and potential applications of hybrid entanglement.
Subsequently a hybrid Bell-state measurement that relies on homodyne conditioning and single-photon detection was discussed. This original BSM implementation enables to mitigate the two-photon errors in this measurement and to thereby improve quantum teleportation or entanglement swapping fidelities. This advantage comes at the cost of a reduced success rate due to the conditioning. We have provided a detailed study of the HBSM properties as a function of the different tunable experimental parameters, namely detection efficiencies, tapping ratio and conditioning window. The effect of these parameters on protocol fidelities have been considered. Interestingly, we have also shown that this strategy beats in fidelity performances ideal photon-number resolving detectors for efficiencies up to typically 90%, a very demanding value. This study confirms the relevance of detection method combination, and calls for a broader exploration of the capabilities opened by hybrid scenario for linear-optical quantum information processing.

4.4 Key results

- The backbone of quantum networks are entanglement and Bell-state measurements. With this, the two important protocols, entanglement swapping and quantum teleportation, can be executed.
- The optical states within the network have to be compatible with quantum memories to enable synchronization. This requires an encoding in the low-excitation Fock basis. The end users will most generally use non-Gaussian states. This can lead to the need for entangled states between different encodings.
- We experimentally create entanglement between the two non-Gaussian resource states of OPOI and OPOIIa of the form $c_0 |0\rangle |\text{cat}\rangle_- + e^{i\theta} c_1 |1\rangle |\text{cat}\rangle_+$ and verify that this entanglement belongs to the class of distillable entangled states. This makes it a versatile resource in quantum networks.
- For the network to function, the Bell-state measurements have to be high-quality projections.
- We present and analyze an improved all-linear Bell-state measurement. It consists of an on-off detector, combined with homodyne conditioning, giving it the name hybrid Bell-state measurement (HBSM).
- The HBSM is shown to outperform photon-number resolving detectors up to a photon-number resolving capability of five. This comes at the price of a low count rate. It will be crucial in the experiment presented in the next chapter.

Chapter 5

The Qubit Converter

Contents

In this chapter an experiment, converting a qubit in the Fock basis to a qubit in the cat-state basis is presented. In the **first section**, the general need for information conversion in quantum networks is discussed. We expand the general idea of a quantum network, explained in the previous chapter, by focusing on the integration of each end user into the network. Specifically, different quantum machines that are implemented on a variety of physical platforms are envisioned and we argue why, next to transducers, converters play a key role in their network integration. The **second section** is dedicated to the experimental setup. The converter is based on teleportation with hybrid entanglement. As the Bell-state measurement and entanglement were already discussed in previous chapters, we focus on the input qubit creation. Moreover, coincidence detection is discussed. This experiment was carried out together with Tom Darras and is also described in his PhD thesis [120] up to this point. The **third section** explains how the success of conversion can be assessed, focusing on the process matrix formalism and a teleportation threshold, derived for this purpose. The **fourth section** discusses important steps in the analysis of the experimental

data. Specifically, we present the setting of the hybrid Bell-state measurement as well as the assessment of uncertainties of the input state. The **fifth and sixth section** present the successful quantum conversion for both the fidelity and process matrix analysis, followed by a discussion. The work presented in this chapter has been published in 2023 [37]. The chapter concludes with a summary of the key results.

5.1 Information conversion in quantum networks

In chapter 4 we have sketched how information can be transferred in future quantum networks. The simplest network has two users A and B, that are connected via entanglement swapping at repeater stations, creating two entangled modes ρ_{ab} shared between the end users. A final teleportation protocol can be used to send information from A to B (or B to A). This information is, in the most general case, a non-Gaussian state ρ_I, encoded in a chosen basis, on a physical platform. For the teleportation protocol to function, the encoding and platform have to coincide with the entangled mode a of ρ_{ab}. This is a rather stringent requirement, as there are many quantum machines and protocols, that are being developed on completely different physical systems, including photons, atoms, mechanical oscillators, solid-state or superconducting devices [29, 205]. The encoding is chosen in dependence of the favored degrees of freedom in the physical system and its practicality in the envisioned local usage. Sometimes, several routes of encoding are taken, as in the example of superconducting quantum computing, where qubits of two-level systems and Schrödinger cat states are both actively pursued [206]. Similarly, we have already seen the plurality of encodings in quantum photonics in the previous chapters [207, 208]. All of those quantum machines have to be able to connect to the network, if we want to harness the fruits of nowadays research.

This consideration adds a new dimension to our definition of heterogeneous quantum networks: the *heterogeneity of encodings* and the *heterogeneity of platforms*. The main challenge of the latter consists in transducing any non-photonic state into a photonic state close to 1550 nm for ideal fiber transmission (often called optical) via *quantum transducers*. For example, superconducting platforms need a microwave-to-optical transducer, bridging their large energy difference via nonlinear frequency mixing techniques [209, 210], which is extremely challenging and an active research area. Building high efficiency and high fidelity transducers is complicated in all physical platforms, such that another possible route to "translate" one physical system into another is by harvesting quantum teleportation. Here, microwave-optical Bell states can be created in the case of superconducting qubits [211], atom-optical Bell states in the case of atomic infrastructure [212, 213] and spin-optical Bell states in the case of solid-state qubits [214, 215]. This entanglement allows to connect a non-optical quantum device to the network. Instead of teleportation, the end user performs

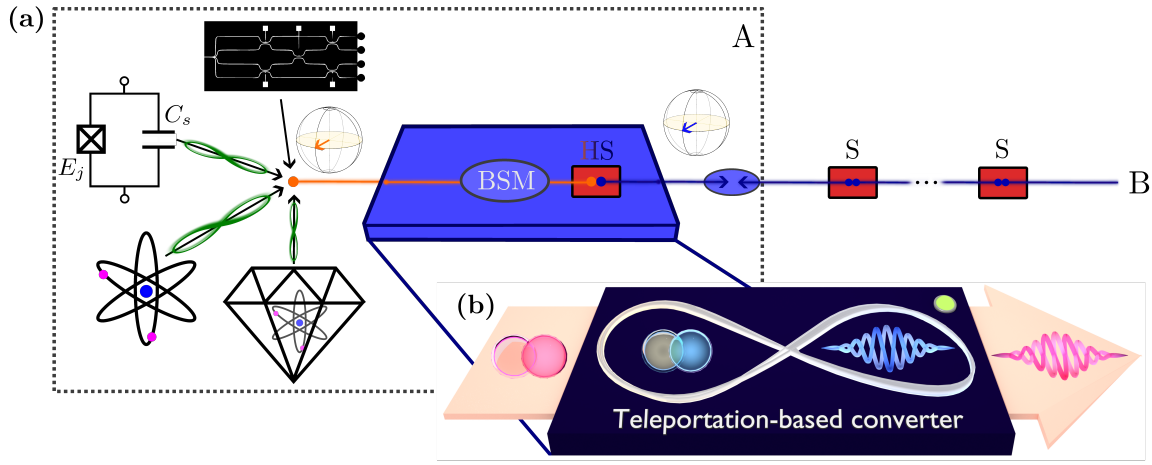

Figure 5.1: In **(a)** examples of physical platforms of quantum machines the network user A could be using in a quantum network are depicted. Those include (nano-)photonic platforms, superconducting qubits (here the transmon qubit is shown as an example), atomic processors, or solid-state artificial atoms, where here an NV center is sketched. For non-photonic platforms, entanglement between their qubit(s) and a light mode (in orange) is created, such that a BSM inside those platforms projects any information $|\psi\rangle$ onto the light mode. This light mode does not necessarily have to have the same encoding E_1 (in orange) as the network encoding E_2 (in blue). This is why a quantum converter, in marine blue, is needed. There, a hybrid source (HS) creates a hybrid entangled state between one mode encoded in E_2 and the other in E_1. A BSM between the E_1-encoded mode and $|\psi\rangle$, now projects the original quantum information onto the network-compatible optical qubit with encoding E_2. The rest of the network protocol consists of entanglement swapping and one more teleportation step, as explained in chapter 4.

entanglement swapping in the optical domain, such that any quantum teleportation can happen within the non-optical device[1].

Although all the above-mentioned platforms do exhibit the possibility of creating entanglement between their natural qubit and an optical mode, the encoding of this optical mode varies. In the references cited above, time-bin encoding, polarization encoding, and frequency encoding were used.

To guarantee that all those devices are usable in one single network, we have to be able to convert one optical encoding into another. Such *photonic quantum converters* also ensure that the encoding choice of photonic quantum machines is not dependent on the network. This conversion has to preserve fragile quantum superpositions, such that phase and amplitude are not altered during the process. Importantly, the converter has to function as a *black box*, with freely propagating input and output modes. As such, a quantum converter has to be either deterministic or heralded. As already argued for general quantum networks in subsubsection 4.1.3.2, post-selection cannot be allowed for such a process either. As for quantum transducers, we follow a teleportation-based approach for quantum encoding conversion. Although experimentally challenging, the idea of such a conversion is rather simple: a mode a, encoded in the encoding E_1 should be converted into the encoding E_2.

[1] A complete BSM is possible in non-optical platforms, [216, 217].

For this, optical hybrid entanglement between two modes b, c, one being encoded in E_1 and the other in E_2, is created. A Bell-state measurement between modes a and b, which share the same encoding, teleports the amplitude and phase information of mode a onto mode c. In this way, mode c, encoded in the target encoding E_2, incorporates the information of the former mode a. This idea requires each local node in a network to prepare hybrid entanglement, adapted to its quantum machine optical output encoding and the encoding of the network. This kind of network is shown in fig. 5.1 (a), where the different physical platforms are sketched, together with the quantum converter. We note that distillable optical hybrid entanglement is hard to experimentally produce and up to our knowledge only exists in the group of Professor M. Bellini in Florence and our group [145, 218].
A converter using post-selected hybrid entanglement between polarization-qubits and cat states has been realized in 2018 [219]. In this implementation, next to the post-selection of entanglement, the qubit itself is approximated by an attenuated coherent state, being always classical. A full analysis of this experiment can be found in the thesis of T. Darras [120]. Here, we build upon this first attempt and present a post-selection free quantum converter using hybrid entanglement of light [37]. The idea of this converter is shown in fig. 5.1 (b), where a qubit in the discrete Fock-basis encoding is converted into a qubit in the continuous cat-state encoding.

5.2 Experimental setup and input qubit creation

The complete experimental setup is shown in fig. 5.2 and can be divided into three blocks: the hybrid entanglement creation, the input qubit creation, and the hybrid Bell-state measurement (HBSM). Finally, the output qubit is analyzed to verify successful conversion. Here, we first present the hybrid entanglement and HBSM settings. For a more detailed analysis, we refer to chapter 4. Then a detailed discussion of the input qubit creation follows. Two physical qubit models are compared and the experimental input states are presented. For this experiment, three heralded events signal success: the creation of the input state, hybrid entanglement, and the HBSM. The effect of a chosen coincidence window on the temporal modes of those events is discussed in the last subsection.

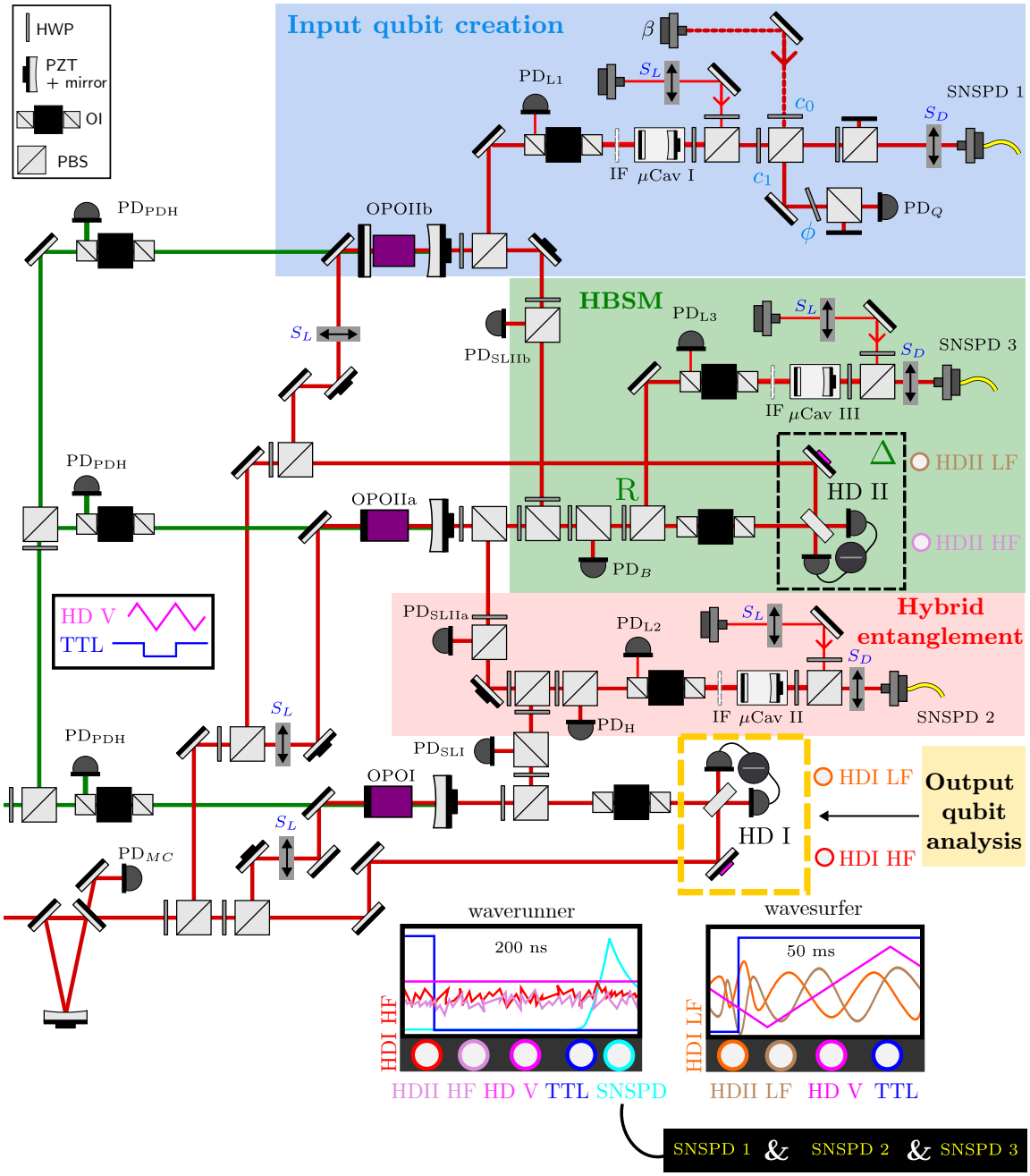

Figure 5.2: The full setup for the qubit converter experiment is shown. Here, hybrid entanglement is used to teleport phase and weights of an input qubit in the Fock basis $|\Psi\rangle_{in} = c_0 |0\rangle + e^{i\phi} c_1 |1\rangle$ onto the output qubit $|\Psi\rangle_{out} = c_0 |\text{cat}\rangle_+ + e^{i\phi} c_1 |\text{cat}\rangle_-$ in the cat basis. The protocol can be subdivided into the input qubit creation (in blue), the hybrid entanglement creation (in red), and the hybrid Bell-state measurement (in green). Qubit creation, entanglement creation, and HBSM are all heralded by probabilistic independent clicks on SNSPDs, leading to a three-fold event heralding the successful conversion of the input to the output qubit. The output qubit is then analyzed via homodyne detection on HDI (in yellow). The data is recorded via a fast oscilloscope, the waverunner, and a slow oscilloscope, the wavesurfer. The experiment is divided into sample and hold sequences, controlled by a TTL signal. During the hold sequence, the shutters S_L close and S_D open, such that data can be recorded on the waverunner. This data corresponds to the trace of the output qubit, the trace of the conditioning on HDII, and the phase-voltage of the local oscillator (LO) sweep. It is triggered by the three-fold coincidence. High TTL corresponds to the sample phase, where the wavesurfer records the interference fringes between seed and LO together with the voltage for subsequent calibration.

5.2.1 Hybrid entanglement settings

Highlighted in red in fig. 5.2 we see the merged heralding path of OPOIIa and OPOI, such that a click on SNSPD2 marks the creation of hybrid entanglement. We pump OPOI with 15 mW, corresponding to 4.5 dB of squeezing, and tap 7% of the OPOI output towards the heralding of hybrid entanglement. OPOIIa is pumped at 3.5 mW and its output is perfectly split into signal and idler polarization. The idler is merged with the heralding path of OPOI and their relative path lengths are phase-locked on the photodiode PD_H. We balance the individual count rates of OPOI and OPOIIa by tuning the HWP responsible for their mixing on the PBS and choose the phase between the two heralding paths, such that we create a hybrid entanglement of the form

$$|\psi\rangle_H \propto |0\rangle\,|\mathrm{cat}\rangle_- + |1\rangle\,|\mathrm{cat}\rangle_+ . \tag{5.1}$$

The hybrid phase is locked with a side-lock, close to the maximum of the interference fringe by using a micro-controller (*aduc7020*) and its phase-noise has been evaluated to be around 3% [220]. The heralding rate of the hybrid entanglement is 400 kHz.

5.2.2 HBSM settings

In the green box in fig. 5.2, the HBSM is performed on the two signaling paths of OPOIIa and OPOIIb, which are merged on a PBS and phase-locked via a side-lock on the signal of the photodiode PD_B with another microcontroller (*aduc7020*). A small fraction of the path is tapped and sent towards SNSPD3. The tapping ratio corresponds to the reflectivity parameter R, analyzed in section 4.2. The smaller R is, the higher the projective quality of the HBSM, but at the price of reducing the count rate on SNSPD3. Here, we choose to set $R = 0.1$, corresponding to a count rate of several kHz. The second parameter of the HBSM is the conditioning window, which is optimal towards zero. We choose a conditioning window of $\Delta = 0.5$, normalized to vacuum shot noise. This choice of parameter will reduce the effective count rate by a factor of four but ensures a high-fidelity output.

5.2.3 Input qubit creation and model

The input qubit creation is shown in blue in fig. 5.2 and will be explained now in more detail. OPOIIb's heralding path, with the photon-number correlation between signal and idler, is expected to herald a single photon, as discussed in subsection 3.2.4. However, an addition has been made to the heralding path: a second beam β is merged with the OPOIIb heralding path after its filtering. This corresponds to a scheme first used by J. Neergaard-Nielsen et al. in 2010 [221]. In their paper, the scheme is applied to single-mode squeezing, while we apply it to the heralding path of two-mode squeezing. Nonetheless, the mathematics to calculate the output state is quite similar and can also be found in the PhD thesis of T. Darras [120] and the supplementary material of the paper corresponding

to this thesis chapter [37]. Here, we discuss this simple model in the first subsubsection, add phase noise in the second, and then show the set of input qubits that we choose for the teleportation experiment, in the third subsubsection.

5.2.3.1 Qubit model with losses

For a low pump rate of 2 mW, one can approximate eq. (3.83) as

$$|\psi\rangle_{si} \propto |0\rangle_s |0\rangle_i + \lambda |1\rangle_s |1\rangle_i + \mathcal{O}(\lambda^2), \tag{5.2}$$

where λ is related to the squeezing parameter and the pump power as discussed in subsection 3.2.4. s marks the signal mode, and i the idler mode, used for heralding. We can now model the coherent state of amplitude β as a weak displacement, applied on the idler mode. Weak displacement can be approximated by a first-order Taylor expansion, such that eq. (2.178) simplifies to, $D_i(\beta) \sim \mathbb{1} + \beta \hat{a}_i^\dagger - \beta^* \hat{a}_i$. Applying this operator on the two-mode squeezed vacuum gives

$$|\psi\rangle_{si} \propto (\beta |0\rangle_s + \lambda |1\rangle_s) |1\rangle_i + \lambda\beta |1\rangle_s |2\rangle_i . \tag{5.3}$$

Now the idler path is detected by SNSPD1, which is an on-off detector. For an ideal single photon detection $|1\rangle\langle 1|$ the signal state is projected onto

$$|\psi\rangle_s \propto \beta |0\rangle_s + \lambda |1\rangle_s , \tag{5.4}$$

such that the creation of a qubit is heralded. The weights of this superposition are controlled by the displacement amplitude β. Practically, this corresponds to adjusting the heralding rate of the displacement beam N_{disp}, in relation to the heralding rate of OPOIIb N_{OPO}. The relative phase between the displacement beam and the heralding path of OPOIIb is "hidden" in this expression, in the phase of β. The full state, in dependence on the count rates, can then be written as

$$|\psi\rangle_s = \cos\left(\frac{\theta}{2}\right) |0\rangle_s + e^{i\phi} \sin\left(\frac{\theta}{2}\right) |1\rangle_s , \tag{5.5}$$

$$\text{with} \quad \cos^2\left(\frac{\theta}{2}\right) = \frac{N_{\text{disp}}}{N_{\text{disp}} + N_{\text{OPO}}} \quad \text{and} \quad \phi = \pi - \arg(\beta), \tag{5.6}$$

where the two phases θ, ϕ relate the state to the qubit Bloch sphere. The fact that a superposition, and not a mixture, is created, stems from the indistinguishability of detection clicks from the displacement or the OPOIIb heralding beam. Without a phase-lock, the phase-averaging would degrade the state to a statistical mixture too. In fig. 5.2 we see $c_0 = \cos\left(\frac{\theta}{2}\right)$ being connected to the setting of the HWP before the mixing PBS (similar for c_1). The phase ϕ is controlled by the tilt of a HWP, which will be explained in the last subsubsection of this subsection.

Let us now take into account the OPO escape efficiency η_{OPO} and the detection efficiency of realistic SNSPDs, modeled as on-off detector (see subsubsection 2.3.4.1) with efficiency η_h. This is modeled by first applying losses on the OPOIIb output via a beamsplitter, whose transmittivity corresponds to the escape efficiency. Next, a displacement, approximated to the first-order Taylor expansion is applied on the idler mode. A bucket detection then acts on the idler mode and finally, the idler mode is traced out. This calculation for a simplified model, ignoring Fock states in the OPO output above the single photon, yields the density matrix ρ_s:

$$\begin{aligned}
\rho_s[0,0] &\propto \eta_h\big(1-\lambda^2\big)\big(\beta^2\big(\lambda^2(\eta_{\mathrm{OPO}}-1)^2+1\big)-\lambda^2(\eta_{\mathrm{OPO}}-1)\eta_{\mathrm{OPO}}\big),\\
\rho_s[0,1] &\propto \beta\eta_h\lambda\big(1-\lambda^2\big)\eta_{\mathrm{OPO}}\big(2\lambda^2(\eta_{\mathrm{OPO}}-1)^2+1\big),\\
\rho_s[1,0] &= \rho_s[1,0]^*,\\
\rho_s[1,1] &\propto \eta_h\lambda^2\big(1-\lambda^2\big)\eta_{\mathrm{OPO}}\big(\beta^2(1-\eta_{\mathrm{OPO}})+4\lambda^2(\eta_{\mathrm{OPO}}-1)^2\eta_{\mathrm{OPO}}+\eta_{\mathrm{OPO}}\big),
\end{aligned} \tag{5.7}$$

where we have not normalized the state for better readability. In this simple case, it is clear, that the efficiency of the bucket detector η_h plays no role and disappears with the normalization. In the case of eq. (5.7), we have therefore effectively only added the OPO escape efficiency. If we set it to the measured value of $\eta_{\mathrm{OPOIIb}} = 0.74$ of subsection 3.2.4, and calculate $\lambda = 0.05$ for a pump of 2 mW and a threshold of 80 mW, furthermore aiming at a balanced qubit $\beta = \lambda$, we find the density matrix to be of the form

$$\rho_s = \begin{bmatrix} 0.685 & 0.425 \\ 0.425 & 0.315 \end{bmatrix}. \tag{5.8}$$

We see that the escape efficiency adds vacuum to the ideal qubit, as expected. If we now simulate the OPO output up to three-photon components and Taylor expand the displacement operator up to the third order, we can find a more complete picture of the output qubit. For this we set $\eta_h = 0.3$, taking into account the SNSPD efficiency and the losses due to filtering. We find the more realistic qubit

$$\rho_s = \begin{bmatrix} 0.684 & 0.424 & 0 & 0 \\ 0.424 & 0.315 & 0.001 & 0 \\ 0 & 0.001 & 0.001 & 0.001 \\ 0 & 0 & 0 & 0 \end{bmatrix}. \tag{5.9}$$

We can therefore see that with the experimental pump rate, the higher-order Fock components are not relevant to the qubit creation. A factor that will, however, become relevant is the stability of the phase lock of the relative phase between qubit and displacement path, on photodiode PD_Q in fig. 5.2.

5.2.3.2 Complete qubit model

We will now extend our model to capture only the signal path after heralding, with a specific focus on phase noise. We can divide the signal state ρ_s into a vacuum component, stemming from the limited OPO escape efficiency, the qubit component, showing coherences and a two-photon component, contributed to the pump rate. In this way, we ignore any non-qubit off-diagonal density matrix terms, which is justifiable, given the matrix of eq. (5.9). We can therefore formulate an input qubit as

$$\hat{\rho}_s = c_{vac} \left|0\right\rangle \left\langle 0\right| + c_{sp} \left|Q\right\rangle \left\langle Q\right| + c_{tp} \left|2\right\rangle \left\langle 2\right|, \tag{5.10}$$

where c_{vac} represents the vacuum component, c_{sp} the single-photon component and c_{tp} the two-photon component. As the qubit will be created by indistinguishable clicks on the heralding path of the OPO we choose the dominant weight c_{sp} for the qubit component. In this way, we can now model the phase noise, which will reduce the qubit coherences. To do so, we take the qubit $|Q\rangle$ of eq. (5.10) ($|Q\rangle\langle Q| = |Q(\phi)\rangle\langle Q(\phi)|$) and model it as a mixture of states with a Gaussian phase distribution, centered around the desired qubit phase ϕ,

$$\left|Q(\phi)\right\rangle \left\langle Q(\phi)\right| = \frac{1}{\sqrt{2\pi}\Delta_\phi} \int_{-\pi}^{\pi} \left|Q(\phi')\right\rangle \left\langle Q(\phi')\right| e^{\frac{-(\phi-\phi')^2}{2\Delta_\phi^2}} d\phi', \tag{5.11}$$

where Δ_ϕ is the phase standard deviation, that can be treated as a free parameter, that we can fit to the experimental states.

5.2.3.3 Experimental qubit input states

For this experiment, we create six input qubits, corresponding to the eigenstates of the Pauli Z, X, and Y operator: $|0\rangle$, $|1\rangle$, $|\pm\rangle$ and $|\pm i\rangle$. In fig. 5.3 (a) the ideal, pure qubit is plotted. The theoretical states with losses are shown in (b) for $\gamma = |\beta| = 0.05$, $\eta_h = 0.3$, and $\eta_{\text{OPO}} = 0.712$. Those values are the measured single-photon values in this data set, visible in (d), second from the left. The phase noise brings our model closer to the measured state, visible in (c). Here, the phase noise has been optimized for each qubit state. The slightly lower fidelity with the single photon measured in chapter 3 stems from the increased pump rate for this experiment. The fidelities of the experimental qubits with the ideal input states and the theoretical model of the input states are given in table 5.1. We can see that phase noise is an important parameter to model the experiment faithfully.

Experimentally, we use a side-lock on the microcontroller *aduc7020* to lock the phase. The fringe signal is very small due to the low amplitude of the displacement beam. Moreover, part of the locking beam, which is on the path with shutter S_L is back-reflected from the cavity and adds perturbations from a third interference on the PD_Q. This is why we chose to keep the locking point at its ideal value, where the fringe slope is steepest.

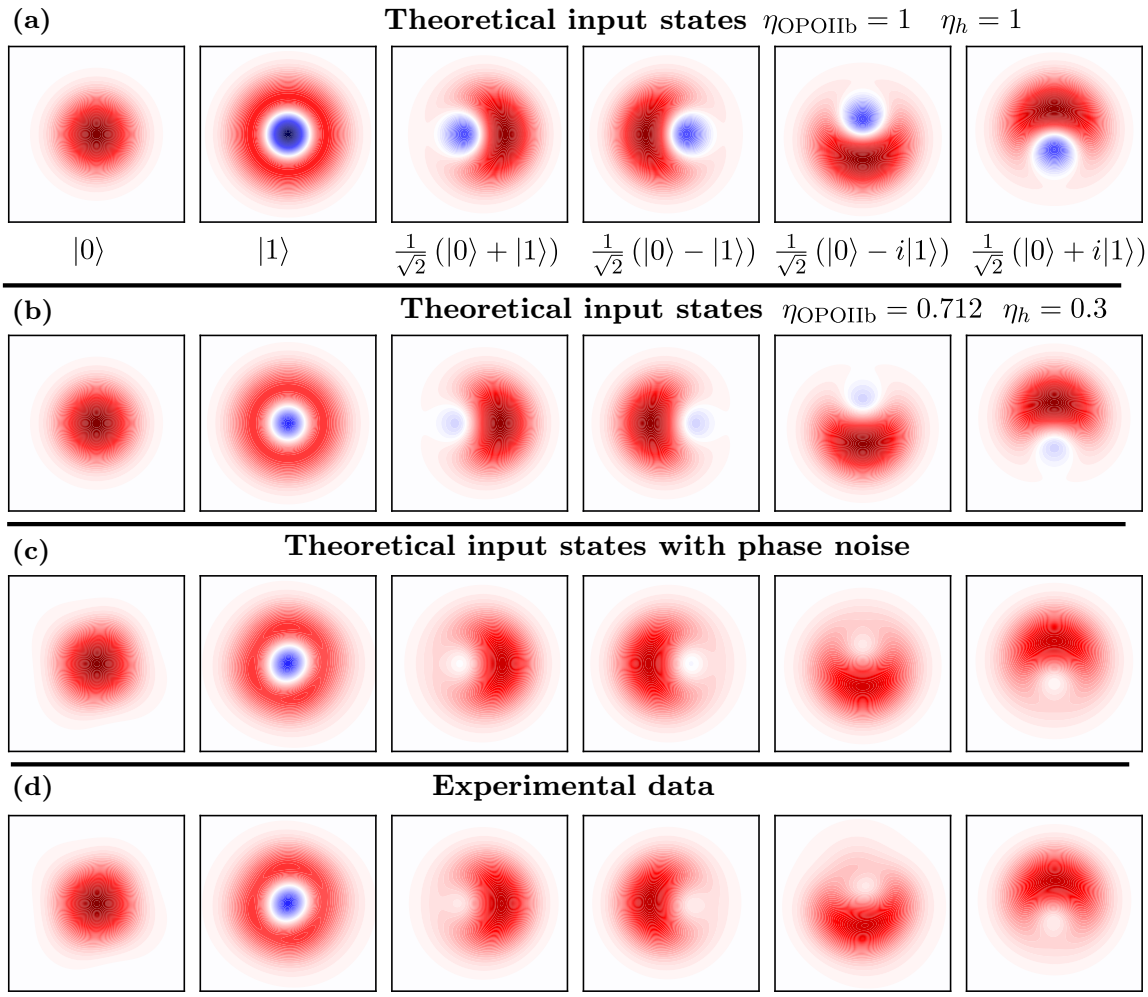

Figure 5.3: In **(a)** the ideal pure input qubit is shown. In **(b)** simulated input qubits with an escape efficiency of $\eta_{\mathrm{OPO}} = 0.712$ and a heralding efficiency of $\eta_h = 0.3$ are depicted. In **(c)** the model of eq. (5.10) is used, to include phase noise in the qubit simulation. The phase noise has been numerically optimized for each qubit and corresponds to $\Delta_\phi \in [0.56, 0.80]$. In **(d)** the experimental states are plotted. The color map is normalized to the minimal (blue) and maximal (red) Wigner function value $[-2/\pi, 2/\pi]$.

To still be able to control the phase, we tilt a HWP. The light from the displacement path has polarization V and the light from the OPO heralding path H, such that this tilt adds a different phase to each polarization component, while simultaneously applying a polarization rotation [222]. In this way, we effectively shift the phase ϕ, to which the locking point corresponds. The PBS after this tilted HWP projects both polarizations onto H, thereby cleaning the interference fringe. After the phase has been locked, a final HWP and PBS on the heralding path towards the SNSPD attenuate the coherent state further, by rejecting 99.5% of the displacement beam polarization V. All qubits are corrected for HD losses, as given in table 3.6. The heralding rate varies: For the single-photon, it is 250 kHz, for the qubits on the Bloch equator 500 kHz and 2 MHz for vacuum.

Table 5.1: Experimental input state fidelity for all six qubits. $\mathcal{F}_{id} = \mathcal{F}(\rho_{exp}, \rho_{id})$ shows the fidelity with the perfect input state, while $\mathcal{F}_{m1} = \mathcal{F}(\rho_{exp}, \rho_{id}^{loss})$ shows the fidelity to modeled input states, taking into account the escape efficiency of the OPO and imperfect on-off detection. The fidelity $\mathcal{F}_{m2} = \mathcal{F}(\rho_{exp}, \rho_{id}^{loss,noise})$ takes into account loss and phase noise.

$\|Q\rangle$	$\|0\rangle$	$\|1\rangle$	$\frac{1}{\sqrt{2}}(\|0\rangle - \|1\rangle)$	$\frac{1}{\sqrt{2}}(\|0\rangle + \|1\rangle)$	$\frac{1}{\sqrt{2}}(\|0\rangle + i\,\|1\rangle)$	$\frac{1}{\sqrt{2}}(\|0\rangle - i\,\|1\rangle)$
$\mathcal{F}_{id}$	0.975	0.710	0.783	0.797	0.785	0.753
$\mathcal{F}_{m1}$	0.975	0.956	0.924	0.933	0.922	0.893
$\mathcal{F}_{m2}$	1	1	0.965	0.966	0.968	0.967

5.2.4 Three-fold coincidences

This experiment needs three SNSPD detection events to succeed: The input qubit creation "click", the hybrid entanglement creation "click" and the HBSM "click". Ideally, those clicks should happen at the exact same moment. In this way, the input qubit and the DV part of the hybrid entanglement can interfere on the HBSM PBS, while the HBSM click corresponds to exactly those heralded resource states. The meaning of "at the same time" has to be specified: it depends on the *delay calibration* in the setup. Each SNSPD event has a slightly different delay, corresponding to the time difference between a SNSPD detection event, and the corresponding trace recording on the waverunner.

We have discussed in section 3.3, that the variance over all recorded traces shows the center of the temporal mode. We therefore plot the variance continuously and adjust the delays, such that for all three heralding events the temporal mode is visible in the chosen trace length of 500 ns on the waverunner. For this, the length of the BNC cables connecting the SNSPDs output to the waverunner, as well as the length of the BNC cables between the homodyne detectors and the waverunner, can be changed. The delays for the SNSPD BNC cables are adjusted via a coaxial delay box (*SRS DB64*) with a precision of 200 ps. The homodyne traces needed to be delayed, for which we used around 80 m of BNC cables in total. After the delay calibration, the three separate detection events of the SNSPDs have to be transformed into a three-fold-coincidence click. For this, we have to choose the maximally allowed time delay between each of those clicks, where we use the analysis about two-fold coincidences from the PhD thesis of H. Le Jeannic [135]. We can calculate the temporal mode overlap between two heralding events as

$$I_{12} = \int f_1(t) f_2(t) dt = e^{-\pi\,\Delta\nu(t_2 - t_1)}(1 + \pi\,\Delta\nu(t_2 - t_1)), \tag{5.12}$$

$$f_i(t) = \sqrt{\pi\,\Delta\nu} e^{-\pi\,\Delta\nu|t - t_i|}, \tag{5.13}$$

where we have slightly adapted the definition of the temporal mode in eq. (3.46), to be centered around the arrival time t_i and assumed $t_1 < t_2$. The graphic interpretation of this overlap integral is shown in fig. 5.4 (a). A three-mode overlap can then be modeled as a nested two-mode overlap. The first two modes build a new mode function and its overlap with the third mode is calculated.
We set $t_2 = t_1 + \delta_2$ and $t_3 = t_1 + \delta_2 + \delta_3$ and find

$$I_{123} = \int \frac{1}{2}\big(f_1(t) + f_2(t)\big) f_3(t), \tag{5.14}$$

$$I_{123} = e^{-\pi\Delta\nu(t_1+\delta_3)}\Big[e^{\Delta\nu(\pi\delta_2+2\pi t_1+2\pi\delta_3)}\left(-\frac{1}{2}\pi\Delta\nu\delta_2 - \frac{\pi\Delta\nu t_1}{2} - \frac{\pi\Delta\nu\delta_3}{2} + \frac{1}{2}\right) + \frac{\pi\Delta\nu t_1}{2} + \frac{\pi\Delta\nu\delta_3}{2} + \frac{1}{2}\Big]. \tag{5.15}$$

Note that in this formula the first click is defined at $t_1 = 0$, as we have centered all the other functions around it. This overlap is graphically shown in 5.4 (b). Modelling a three-fold event as two nested two-fold events corresponds to our experimental settings.

We use a commercial time controller (*IDQuantique ID900*), capable of coincidence detection with sub-nanosecond resolution. The resolution here is very important, as it adds time jitter to the trigger event. The time jitter should be far below the temporal mode size as it would otherwise hinder detection events to correspond to interference in the experiment. Here, we set the coincidence window to 1.5 ns for both nested two-fold events. Once the three-fold coincidence is detected, a 100 ns long TTL signal is sent to the "SNSPD" input of the waverunner in fig. 5.2. For the parameters $\delta_2 = \delta_3 = 1.5$ ns and the bandwidth of our OPOs, eq. (5.15) gives a three-mode overlap of $I_{123} = 0.865$.
This value was chosen as a trade-off between the temporal mode overlap of the three modes

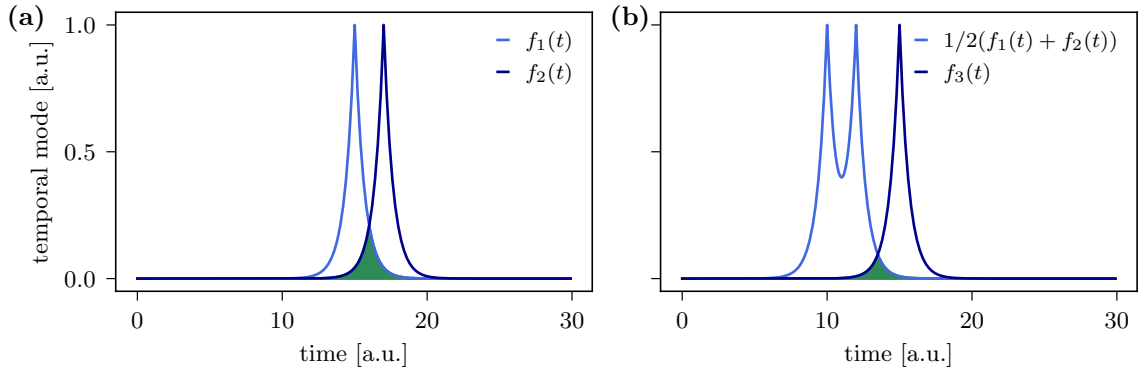

Figure 5.4: In **(a)** the temporal modes $f_1(t)$, $f_2(t)$ of two states are shown. Their overlap (in green) is dependent on their time difference $t_2 - t_1$. In **(b)** a three-mode overlap is shown. For this the first two modes form the new mode $1/2(f_1(t) + f_2(t))$ and its overlap with the third mode $f_3(t)$ is calculated (in green).

and the experimental count rate. The count rate $\mathcal{R}$ is related to the temporal mode overlap window δ as follows [120]

$$\mathcal{R}_{1,2} = \mathcal{R}_1 \mathcal{R}_2 \delta, \tag{5.16}$$

such that with the individual count rates $\mathcal{R}_1 = 250$ kHz and $\mathcal{R}_2 = 400$ kHz for the qubit and hybrid creation, the conditioning window reduces the two-fold count rate to $\mathcal{R}_{12} = 150$ Hz. The three-fold event rate, taking into account the HBSM count rate, reduces to 0.2 Hz with those settings.

5.3 Judging the "quantum" in teleportation

We present two methods here to quantify the success of quantum teleportation. For quantum teleportation to be truly "quantum", it has to perform better than classical measure-and-best-guess teleportation strategies. This leads to a threshold between the fidelity of input and output qubits, which, if surpassed, indicates true quantum teleportation. Another strategy is the evaluation of the quantumness of the process itself, called process tomography. Here we will explain both approaches and apply them in section 5.5.

5.3.1 A teleportation threshold

The usual threshold for quantum teleportation is $\mathcal{F}_c = 2/3$. This bound describes how well a qubit could be teleported without the use of a quantum channel and, therefore without the use of any quantum entanglement. This is equivalent, to calculating the optimal extraction of information from a finite quantum ensemble, derived by S. Massar and S. Popescu in 1995 [223]. They consider an experimentalist, who takes part in a game: After receiving N copies of a pure qubit, the experimentalist has to announce which qubit was sent. The catch is that only classical resources are in the experimentalist's laboratory. The game consists of several rounds and in each round the Bloch vector of the pure state will change, according to a uniform distribution.

By optimizing the measurement strategy in each run, Massar and Popescu find that with the best possible strategy, the experimentalist's guessed states have an average fidelity of $\mathcal{F} = 2/3 = \mathcal{F}_c$ with the original quantum qubit for $N = 1$, thereby giving a threshold any teleportation protocol has to beat to be quantum. This problem is equivalent to finding the threshold accuracy for the faithful cloning of a qubit [224] and connected to Maximum Confidence Quantum State Discrimination [225, 226]. Importantly, the derivation of this bound is valid only for pure input qubits because they assume pure input qubits in their theoretical model. This renders the 2/3 bound impractical unless one has a perfect experimental setup or post-selection is applied. In fact, Takeda et al. [227] argue, that any qubit that is not pure in the Fock basis cannot be treated as a pure input qubit, even if it has perfect fidelity in the chosen encoding.

Unfortunately, their approach is based on the fact that the Fock basis and the qubit-encoding are orthogonal and thus cannot be used in our case.

Here, we therefore extend the original approach of S. Massar and S. Popescu to general input qubits and find the general fidelity bound $\mathcal{F}'$. For this we closely follow Bagan et al. [228], discussing the optimal full estimation of a qubit mixed state. We formulate the qubit on the Bloch sphere and consider the input qubit as

$$\hat{\rho} = \frac{1}{2}(\mathbb{1} + \vec{r} \cdot \vec{\sigma}) \tag{5.17}$$

where $\vec{r} = (r_x, r_y, r_z)$ is the Bloch vector and $\vec{\sigma} = (\boldsymbol{X}, \boldsymbol{Y}, \boldsymbol{Z})$ a vector containing the Pauli matrices. We allow ourselves to act on this state with any POVM element Π_ε with outcomes ε such that $\sum_\varepsilon \Pi_\varepsilon = \mathbb{1}$, which corresponds to local measurement allowed in the original paper [223]. If the outcome is ε, the best classical strategy is to announce that the original state was $\hat{\rho}_\varepsilon$ with the associated Bloch vector $\vec{R}_\varepsilon$. The success of this round of the game is then evaluated with the fidelity between the actual state $\hat{\rho}$ and assumed state $\hat{\rho}_\varepsilon$

$$f(\vec{r}, \vec{R}_\varepsilon) = \left(\mathrm{Tr}(\sqrt{\sqrt{\hat{\rho}_\varepsilon}\hat{\rho}\sqrt{\hat{\rho}_\varepsilon}}) \right)^2. \tag{5.18}$$

For unit purity, this formulation reduces to the one of Massar and Popescu. Here we simply added one additional degree of freedom with the length of the Bloch vector, while they only use its angles.

The average fidelity, which will be the classical bound, is then calculated by integrating over the length of the Bloch vector and its two Bloch angles θ and ϕ. Additionally, all the possible operators Π_ε have to be taken into account, such that we can write the classical threshold in its general form

$$F = \sum_\varepsilon \int d\rho f(\vec{r}, \vec{R}_\varepsilon) p(\varepsilon|\vec{r}), \tag{5.19}$$

where the probability for the outcome ε to occur is $p(\varepsilon|\vec{r}) = \mathrm{Tr}(\Pi_\varepsilon \hat{\rho})$. We have to choose the prior probability distribution over the Bloch sphere, $d\rho$. For this, the spherical coordinates simplify the problem $\vec{r} = (r\sin(\theta)\cos(\phi), r\sin(\theta)\sin(\phi), r\cos(\theta))$, with $|\vec{r}| = r$, $\theta \in [0, \pi]$ and $\phi \in [0, 2\pi]$.
Our lack of knowledge of the direction (the two angles) implies $d\rho \propto d\Omega$ as the solid angle element $d\Omega$ represents an isotropic directional distribution on the Bloch sphere. On the contrary, the radial prior is not unique. Usually, there are two prior r-functions used in

quantum mechanics: The hard sphere prior $w(r) = 3r^3$ and the Bures prior $w(r) = \frac{4r^2}{\pi\sqrt{1-r^2}}$ [229]. We choose follow references [228, 230] and choose the Bures prior, such that

$$d\rho = w(r)d\Omega dr = \frac{\sin(\theta)r^2}{\pi^2\sqrt{1-r^2}}d\theta d\phi dr. \tag{5.20}$$

Next, we need to find the POVM Π, whose elements maximize eq. (5.19). This is simplified [228] when assuming a Bloch vector $\mathbf{R}_\varepsilon := \mathbf{V}_\varepsilon/|\mathbf{V}_\varepsilon|$ with $\mathbf{V}_\varepsilon = \int d\rho \mathbf{r} p(\varepsilon|\vec{r})$ where $\mathbf{r}$ is the four-dimensional euclidean vector $\mathbf{r} := (\sqrt{1-|\vec{r}|^2}, \vec{r})$.
In such a way, we can define the upper bound of eq. 5.19 as the general teleportation bound

$$F \xrightarrow{\text{maximize}} \mathcal{F} = 1/2(1 + \sum_\varepsilon |\mathbf{V}_\varepsilon|), \tag{5.21}$$

making it independent of the defined POVM. We will make the easy choice of the Pauli matrix $\Pi = X$, but stress that this choice is arbitrary with the above formulation. Two outcomes are possible with the X Pauli matrix: $\Pi_1 = |0\rangle\langle 0|$ and $\Pi_{-1} = |1\rangle\langle 1|$.
Let us quickly test eq. (5.21) for pure states: As expected for $|\vec{r}| = 1$ (and $d\rho = \frac{\sin(\theta)}{4\pi}d\theta d\phi$) we find $|\mathbf{V}_1| = |\mathbf{V}_{-1}| = 1/6$ such that $\mathcal{F}_{pure} = 2/3$. Equally, we find the trivial result that $\mathcal{F}^{|\vec{r}|=0} = 1$ for $|\vec{r}| = 0$, which simply states that the parameters of any fully mixed and as such classical state, can be extracted perfectly. We expect our bound to lie between those two cases, as classical teleportation becomes easier the more classical, and therefore mixed, a state is.

If no assumption whatsoever is made about the purity of the input states we find $\mathbf{V}_{\pm 1} = (\frac{2}{3\pi}, 0, 0, \pm\frac{1}{8})$ such that $|\mathbf{V}_1| = |\mathbf{V}_{-1}| \approx 0.246286$. The average fidelity for all possible states on the Bloch sphere is then $\mathcal{F}_{all} = 0.746$.
In our case, the produced input qubits will exhibit a range of different purities, depending on the weight of the single-photon component. Therefore the minimal purity or Bloch sphere radius is defined via the escape efficiency of OPOIIb used to generate the qubits, i.e., $|\vec{r}|_{min} = |1 - 2\eta_{qubit}| = 0.41$. We can therefore limit the integration space to $|\vec{r}| \in [|\vec{r}|_{min}, |\vec{r}|_{max}] = [0.41, 1]$ while renormalizing the Bures prior. This leads to the classical threshold, slightly improved from the general case, used in this work given the input qubits, $\mathcal{F}^{|\vec{r}|\in[0.41,1]} = \mathcal{F}' = 74.1\%$ and we will judge our results by this threshold.

5.3.2 The process matrix

By using a threshold, the focus is placed on the input-output relationship between experimentally teleported qubits. Alternatively, teleportation can be quantified by identifying the process that maps input qubits to output qubits. Unlike the discrete input-output approach, this method provides information about the entire Bloch sphere.

5.3.2.1 Theory of the process matrix

Quantum process tomography was first discussed in 1998 [231], where D'Ariano and Maccone proposed to reconstruct the Hamiltonian of an optical system via measurement outcomes and known input states. The general idea is nicely formulated by J. Yuen-Zhou et al. [232] and will be described briefly in the following.

Each quantum process is a quantum map $\varepsilon(\bullet)$ acting on the quantum system $\bullet$. In the process matrix representation, we choose to express this quantum map with the help of a $d^2 \times d^2$ matrix (d being the dimension of the quantum system the map acts on) and choose a full $d \times d$ basis set A_i such that the transformation is described via

$$\varepsilon(\bullet) = \sum_{n,m=1}^{d^2} \chi_{nm} A_m(\bullet) A_n^\dagger, \tag{5.22}$$

where we expect the process matrix χ to be a hermitian positive semi-definite matrix. If the process is trace preserving, the condition $\sum_{n,m} \chi_{n,m} A_m^\dagger A_n = \mathbb{1}$ is applied [233], which can be connected to the success probability $d \times d$ matrix P of the map [234]. Note, that here success is interpreted as the probability that you send any state into a black box that performs the map $\varepsilon(\bullet)$ and get an output state. The probability matrix can be reformulated in the question: Do I always have the same quality of transformation, independent on the input state? In general, our map will obey $P = \sum_{n,m} \chi_{n,m} A_m^\dagger A_n \leq \mathbb{1}$ which leaves space for two interpretations: Either the process has a state-independent success probability (in this case we expect $P \leq c\mathbb{1}$, where c is a constant factor) or a state-dependent success probability (where c changes, depending on the input state).

5.3.2.2 How to calculate the process matrix

There are many works related to the calculation of the process matrix. The easiest way is to calculate χ directly from the measured output and input states of the process. To reconstruct χ, both states and measurements must each form a basis set for the set of qubit density matrices, therefore each set holds d^2 elements. This gives the exact number of measurements on the exact number of states one has to perform to solve eq. (5.22) analytically [235]. In most cases, the experimentalist will want to measure a bigger set, thereby over-defining the problem. Ideally, one would get the exact same χ for all possible input-measurement combinations when reducing this over-complete set to the minimal set. In realistic measurement results, the success probability of the chosen set might be state-dependent and/or might be slightly altered by noise sources. This makes the outcome χ highly dependent on the initial choice of input-measurement sets. This is why, many papers in the early 2000s try to solve eq. (5.22) via a maximum-likelihood approach, where we focused mainly on the two references [236, 237]. This approach is practical, as the maximum likelihood approach guarantees a physical matrix and is well established in quantum physics.

The easiest solution to follow is the iterative approach by J. Fiurášek and Z. Hradil [236]. In this solution, the trace preservation $\sum_{n,m} \chi_{n,m} A_m^\dagger A_n = \mathbb{1}$ is assumed. To adapt it to a non-trace preserving solution, Lagrange Multipliers for inequalities can be used. Another possibility would be to perform a non-gradient maximization on the likelihood itself (we tried Nelder-Mead). Unfortunately, there seem to be many local maxima that hinder the global solution to appear[2] such that we finally chose convex programming as the most practical way to find the global solution.
We follow the suggestion of C. Baldwin et al. [233], presenting three possible formulations of a convex problem-solving eq. (5.22), where we choose the one that is equivalent to finding the constrained maximum likelihood solution under the assumption that the data is drawn from a Gaussian distribution. Conveniently, this is the only formulation where we do not need to make any prior assumptions about the process. The problem is written as follows

$$\text{minimize} \quad \sum_{jl} |f_{jl} - \mathrm{Tr}(\sum_{n,m=1}^{d^2} \chi_{nm} A_m \rho_{in}^j A_n^\dagger E^l)|^2 \tag{5.23}$$

$$\text{subject to} \quad \sum_{n,m} \chi_{n,m} A_m^\dagger A_n \leq \mathbb{1} \tag{5.24}$$

$$\chi = \chi^\dagger \tag{5.25}$$

$$\chi \geq 0. \tag{5.26}$$

One minimizes the square of the distance between the measured frequencies $f_{jl} = \mathrm{Tr}(\hat{\rho}_{out}^j E^l)$ and the computed ones from the χ of each iteration. In this way, we can use the complete measured data set and allow for non-trace preserving processes. The results for our experiment are given in subsection 5.5.1.

Now that we are familiar with the experimental procedure and have developed the necessary tools for data analysis, let's examine the results.

5.4 Converter data analysis

Here we will present two important steps in the analysis of the converter protocol. First, the homodyne conditioning window Δ of the HBSM has to be set. Next, error bars on the input states have to be established. While the conditioning window constitutes a choice, the error bars on the input states are important to give confident results for the fidelity bound. For each of the six measured qubits, 10 000 three-fold unconditioned events are detected, leading to a data acquisition time of 10 and 16 hours per qubit. The homodyne

[2] One solution here could be, to add a probabilistic noise term to the maximization, which can drive the system away from local maxima. We did not explore this possibility as we finally chose to use convex programming, naturally finding the global maxima by definition.

conditioning is applied in a post-processing step with a conditioning window of $\Delta = 0.5$, normalized to vacuum shot noise. The conditioning reduces the data per qubit to around 2500 four-fold events.

5.4.1 Homodyne conditioning window

After having measured and processed (see section 3.3) six teleported output qubits we have the following data sets

- Quadrature and phase values of each teleported state x_θ^I (HDI in fig. 5.2)
- Quadratue and phase value of the HBSM x_θ^{II}(HDII in fig. 5.2).

The conditioning step of the HBSM has not been applied yet. We remark, that it is technically possible to implement this kind of conditioning electronically via a non-linear fast feed-forward that would practically create a fourth detection event. Keeping a low time jitter on this kind of electronics is extremely challenging, which is why we choose not to investigate it further. Instead, we post-process the recorded data.

Post-processing means that we only keep a quadrature value x_θ^I of the teleported output state if the quadrature value of HDII, which was recorded simultaneously, fulfills $\Delta/2 \leq x^{II} \leq \Delta/2$, where we omit the phase as it is not relevant for this analysis. This is equivalent to a controlled gate on the data. In contrast, post-selection would mean that we try to optimize the data x_θ^I to keep the best output state, iterating over different quadratures and deciding if we keep them, based on their effect on the output state. Any subsequent operation that changes the state would therefore make post-selection impossible, rendering this method problematic, as discussed in subsubsection 4.1.3.2. Unlike post-selection, post-processing is not problematic in quantum networks, as the data selection choice is independent of subsequent operations on the output state.
Practically, the post-processing is done with the help of simple for-loops in Python. A smaller conditioning window Δ is always beneficial. In practice, we want to have enough data to faithfully reconstruct our teleported state density matrices via the maximum likelihood algorithm. Here we decide for $\Delta = 0.5$, which corresponds to around 2500 quadrature values per teleported output state. In section 5.5 we will show the effect of different conditioning windows on the fidelity of the single photon state $|1\rangle$.

5.4.2 Input state uncertainty - Fidelity uncertainty

The success of quantum teleportation is most commonly measured in terms of fidelity - the comparison between output and input state. In general, the input state that was teleported cannot be measured together with the output state as it has been destroyed during the teleportation. Here, we measured many input states over the duration of two weeks, which

Table 5.2: Average input density matrix elements and standard deviations.

$\|Q\rangle$	$\|0\rangle\langle 0\|$	$\|1\rangle\langle 1\|$	$\|0\rangle\langle 1\|$	$\|2\rangle\langle 2\|$
$\|0\rangle$	0.980 ± 0.007	0.015 ± 0.007	0.000 ± 0.000	0.005 ± 0.00
$\|1\rangle$	0.250 ± 0.020	0.710 ± 0.020	0.000 ± 0.000	0.025 ± 0.020
$\frac{1}{\sqrt{2}}(\|0\rangle + e^{i\phi}\|1\rangle)$	0.615 ± 0.021	0.355 ± 0.019	$(0.276 \pm 0.039 \pm 0.012e^{i\pi/2})e^{i\phi}$	0.014 ± 0.005

should represent possible long-term deviations in the qubit creation. We estimate those long-term deviations to be our dominant source of teleportation fidelity uncertainty. This can be intuitively understood by the time frames: Each input state is measured for one minute, while we collect the output teleported data during one day.

We therefore want to find error bars on the input qubit, accounting for experimental variations during one day. This will enable us to faithfully give fidelity error bars. The uncertainty on the input states is calculated as the standard deviation on the density matrix elements of the two weeks' worth of experimentally generated input states. The average value and standard deviation for each relevant density matrix element for the data set of all qubits are given in table 5.2. It is obtained in two steps: For the diagonal density matrix elements eq. (5.10) is optimized onto each input state. The mean and standard variance of the such acquired data set is given in table 5.2. For the off-diagonal elements, the phase noise is modeled with eq. (5.11), reducing the coherences of the qubit. With this technique, we can estimate the average phase noise to be $\Delta_\phi = 0.707$ corresponding to a relative phase noise of 11%. This rather large value is owed to the long measurement time - two weeks - in which the qubit can be measured in different experimental conditions. We are confident that with this input qubit data set, we will not underestimate the error bars on the input qubits used in this experiment.

In the next section, we will estimate the minimal and maximal fidelities for each of our six experimental output states, dependent on the minimal and maximal value of each density matrix element, given in table 5.2. Those values will give the minimal and maximal point of each qubit's error bar. We will then choose an experimental input state for the fidelity calculation. This state is chosen to represent the average input state our experiment provides and has already been shown in fig. 5.3 (d). Due to the experimental input state not perfectly representing the mean value, we will have asymmetric error bars. With this rather stringent uncertainty analysis, we want to give realistic and fair error bars to our experimental data.

5.5 Results of the qubit converter

We can now present the results of the converter experiment, as given in fig. 5.5. The input qubits (as presented in subsection 5.2.3) are plotted in the top row, while the teleported states are shown in the lower row. After conditioning, the output states are reconstructed

from respectively 3691, 2185, 2802, 2657, 3641, and 2839 homodyne measurements. The input qubits are reconstructed from 40000 homodyne measurements.

The measurement data was taken over the course of one week, with 10-16 hours of data taking per qubit, while actively stabilizing 14 locks.
After five hours, the triple-resonance condition of the OPOs was adjusted.

5.5.0.1 Qualitative assessment of the data

A first discussion of the teleportation protocol is based on how the output states "look" in the Wigner representation. The logical basis $|0\rangle_L$ was converted from vacuum to squeezed vacuum, approximated for us by an even cat. The squeezing is clearly visible in fig. 5.5. The $|1\rangle_L$ has been transformed from a single photon Fock state towards a photon-subtracted squeezed vacuum, or approximate odd cat-state. Although we can see the "ears" of the cat,

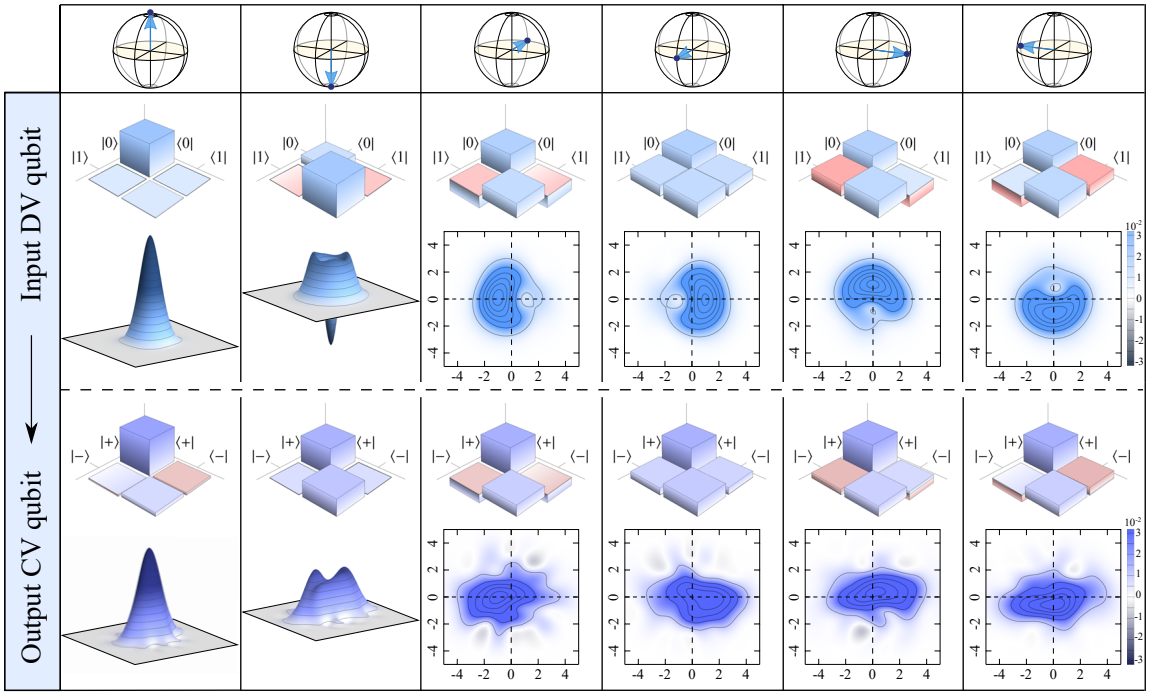

Figure 5.5: Converted qubit characterization before and after conversion. A set of six qubits, corresponding to the Bloch poles and equator qubits are converted from discrete Fock encoding (top row) to continuous cat-state encodings (bottom row). The density matrices of the input DV qubits are each reconstructed from 40000 quadrature measurements and projected onto the $\{|0\rangle, |1\rangle\}$ Fock-state basis, and their Wigner functions plotted ($\hbar = 1$). The converted output qubits are reconstructed from 3691, 2185, 2802, 2657, 3641, and 2839 quadrature measurements respectively. The density matrices are projected onto the $\{|\text{cat}\rangle_+, |\text{cat}\rangle_-\}$ cat-state basis, which is labeled $\{|+\rangle, |-\rangle\}$ here. The real parts of the density matrices are shown in blue while the imaginary parts are shown in red. The Wigner functions are shown in 3D for the Bloch poles, and in 2D top-view for the equator qubits to provide a better visualization of the phase of the qubits located along the Bloch sphere equator. This figure was published as is in [37]

which correspond to the coherent state amplitudes, we cannot see the interference fringes between them. Those fringes are extremely sensitive to losses.

The main loss in our experiment is attributed to the transmission losses of the HDII for the HBSM, estimated to be 17%, and the finite coincidence window Δ, leading to an overall vacuum admixture of 30% to the teleported state. Reducing those losses would require longer measurements per qubit (to be able to reduce the coincidence window further). Reducing the losses on the path is challenging: They mainly come from the optical isolator, ensuring that no back-reflection on the homodyne photodiodes induces false heralding clicks.

When looking at the Wigner function of the Bloch equator qubits, we see that the phase of each qubit is preserved. This can be verified by comparing where the center of the Wigner function of input and output qubits lie in phase-space. Our first assessment indicates qualitatively good teleportation, which will be analyzed in the two ways discussed in section 5.3. Before this step, an important choice has to be made.

5.5.0.2 The output basis choice

To quantitatively judge the measurement results via the teleportation fidelity and the process matrix, we have to decide what should have been the perfect output qubit. We know that the basis choice for our input qubits is the Fock basis, such that the perfect input state is parameterized as

$$|\Psi\rangle_{in} = c_0 |0\rangle + e^{i\phi} c_1 |1\rangle . \tag{5.27}$$

This basis choice for our output qubit basis is an odd and even cat state

$$|\Psi\rangle_{out} = c_0 |\text{cat}\rangle_+ + e^{i\phi} c_1 |\text{cat}\rangle_- , \tag{5.28}$$

but the size of those cat states has to be defined. In this analysis, we choose $|\alpha| = 0.9$. Any projective basis could have been chosen for the output states, including their native squeezed and single-photon subtracted squeezed vacuum basis. By enforcing cat states as the basis, with a rather high amplitude for our setup, we want to show that this teleportation is doable in the context of bosonic qubit bases, as discussed in section 2.4.

The chosen basis makes teleportation more challenging for us. In fact, when projecting the measured output states onto the cat basis, the normalization of the state is lost. This *trace-loss* corresponds to part of the measured state not belonging to the chosen cat-basis. The trace-loss for all measured output states ranges between 8% - 18%. We stress, that the output *states are not re-normalized*. This would correspond to an artificial raise of overlap between the measured output state and the chosen qubit basis. This in turn means, that even with perfect teleportation a fidelity of one is not achievable due to the non-normalized

output states. Additionally, the input states, projected onto the Fock basis of vacuum and single-photon lose maximally 2% of their trace and are not re-normalized as well. The analysis of the process matrix, as well as the fidelity overlap, uses those non-normalized input and output states, projected on their relative computational basis.

5.5.1 The qubit converter process matrix

5.5.1.1 Optimization implementation

As explained in subsection 5.3.2, we use convex optimization to find the optimal process matrix corresponding to our data. First, we have to choose the operator basis A_i of the process matrix. Given that we work with qubit input and output states, we need four basis matrices, for which we choose the Pauli basis $\mathbb{1}, X, Y, Z$. Conveniently it gives an easy physical interpretation: the diagonal elements of the process matrix correspond to the fidelity of the process, bit flip, bit-phase flip, and phase flip errors (see Quantum error correction). The off-diagonal elements are interpreted as cross-talk between the diagonal elements. We can rewrite the trace condition $\sum_{n,m} \chi_{n,m} A_m^\dagger A_n \leq \mathbb{1}$ for the Pauli basis as

$$\chi[0,0] + \chi[1,1] - \chi[2,2] + \chi[3,3] \leq 1. \tag{5.29}$$

Furthermore, we need to define how to calculate the ideal frequencies f_{jl} of eq. (5.23). In our case, each measurement POVM element E^l corresponds to a homodyne projection operator (see eq. (2.269)) such that we can compute the probability of an outcome as $f_{jl} = \mathrm{Tr}[\rho_{out}^j E^l]$. Here ρ_{out} is projected onto the cat basis, but written as a 10×10 matrix in the Fock basis. Here, it is important to take the same number of POVM elements per state, as otherwise, not all states have equal importance in the convex algorithm.

To solve the convex problem fast and efficiently, we make use of the coding language *Julia*, which is a marriage between Python and C++. In Julia, we use the package "Convex.jl" to translate our problem of eq. (5.23) to a convex problem, solvable by the solver "COSMO". Cosmo stands for "Conic operator splitting method" [238] and was developed by Garstka et al. in Oxford[3].

[3] We strongly discourage the reader to use the solver "SCS", which solve both primal and dual cone of the convex problem and gives ill-defined outcomes in our case.

5.5.1.2 Converter process matrix resuls

We calculated our process matrix to be

$$\chi = \begin{bmatrix} 0.578 + 0.000i & 0.011 - 0.021i & 0.006 - 0.027i & 0.069 - 0.065i \\ 0.011 + 0.021i & 0.165 - 0.000i & 0.001 - 0.105i & 0.002 - 0.015i \\ 0.006 + 0.027i & 0.001 + 0.105i & 0.136 - 0.000i & -0.010 + 0.006i \\ 0.069 + 0.065i & 0.002 + 0.015i & -0.010 - 0.006i & 0.026 - 0.000i \end{bmatrix}. \tag{5.30}$$

The process matrix is plotted in fig. 5.7 (a). We chose to take 2000 quadrature values (and therefore homodyne POVM elements) per state, to ensure zero state bias. The working principle of the algorithm was verified, by using the input-input data (instead of input-output) for 2000 quadrature values. As expected it gave a process matrix that is identical to no process that has occurred, with only one non-zero matrix element $\chi[0,0] = 1$. Our program needs 2-3 minutes to reach a solution.

5.5.1.3 Uncertainty of the process matrix

Now we are interested in how to calculate error bars for the matrix in eq. (5.30). The approach taken for density matrices, bootstrapping, usually takes the output state and samples new quadratures from it, which are then used to in turn reconstruct the output matrix. Here, as our output is not a state but dynamics generating this state, bootstrapping seemed impractical.

Instead, we decided to follow the approach of the supplementary information of Guccione et al. [36]: we divide the output-state data set into non-overlapping partitions of size $N = 100, 200, 300, 400, 500$ and repeat the process of partitioning the data 30 times for each data set. This ensures that the partitions of each size N are as independent as possible. We are interested in the standard deviation for $N = 2000$. This means that after having calculated the standard deviation for each partition, we need a fitting function to extrapolate the desired value.
To this end, we are only aware of one typical relation between the size of the data set and the behavior of the standard deviation, described by

$$\mathrm{std}_N \propto \frac{1}{\sqrt{N}}. \tag{5.31}$$

We use the module "LsqFit.jl" to fit the standard deviation of the partitioned data to the function $g(N, p1, p2) = p1/\sqrt{N + p2}$ thereby allowing for an offset and a re-scaling factor. Overfitting by allowing more free parameters will lead to negative standard deviation values. The corresponding plots are visible in fig. 5.6. In (a) and (b) the standard deviations for all ten independent process matrix elements are shown, where (a) corresponds to the real and (b) to the imaginary values of the matrix. The dominant uncertainty can be found in the

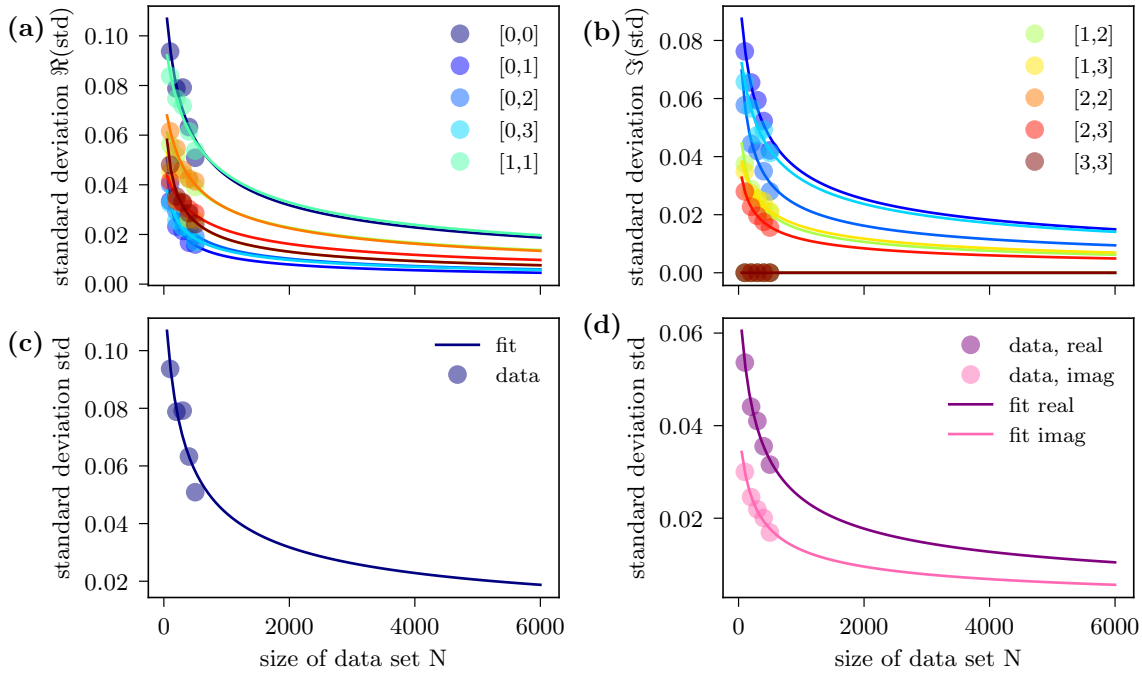

Figure 5.6: The uncertainties (standard deviations) of the process matrix for different non-overlapping partitions of size N of the full data are shown, together with a fitting function. In **(a)** and **(b)** the real (imaginary) independent process matrix element standard deviations are plotted. In **(c)** we focus on the largest standard deviation, which occurs for $\chi[0,0]$. In **(d)** the mean uncertainty on the whole process matrix is shown.

$\chi[0,0]$ value, which can be extrapolated to $\chi[0,0] = 0.578 \pm 0.032$. To get the uncertainty of the whole matrix, we take the mean of all matrix element standard deviations, visible in fig. 5.6 (d).
With this fit, we get the overall uncertainty $\chi \pm 0.0178 \pm 0.0100i$.

5.5.1.4 Visualization and discussion

Comparing this process matrix to the ideal teleportation, we find a process fidelity, meaning a fidelity between the ideal and experimental map, of $\mathcal{F}_{process} \simeq 0.58$ - corresponding to $\chi[0,0]$. This value can usually be connected to the average teleportation fidelity but assuming pure input states and trace preservation [4] [239, 240]. To adapt this analysis to our case, we can perform a test on our process matrix: we can apply the reconstructed process matrix in a simulation to pure input states and then calculate their average teleportation fidelity. We find, that we would still beat the teleportation threshold for pure states with an average teleportation fidelity of $0.687 > 2/3$. This value is expected to be lower than our actual fidelity result, as expected in a non-trace-preserving process.

[4] The formula is $\bar{\mathcal{F}} = \frac{2\mathcal{F}_{process}+1}{3} = 0.72$ but given that we meet none of the assumptions for this calculation we disregard this result.

We can now also visualize both the process matrix and its effect on pure states, which is visible in fig. 5.7. We see that the output Bloch sphere is shifted towards the logical zero in (b). This can be explained by the bit flip error $\propto \chi[1,1]$ and the bit/phase flip mixture $\propto \chi[2,2]$. Those are related to loss being part of our computational basis. Moreover, the process matrix has rather high imaginary X-Y-Pauli correlations $\propto \chi[1,3]$. The overall shrinking of the output Bloch sphere is also due to the process matrix not being trace-preserving such that the output state normalization in (b) and (c) do not correspond to one. The threshold for a process matrix to be quantum (in the Pauli basis) is given by $\chi[0,0] > 1/2$ [232]. With a value of $\chi[0,0] = 0.58 \pm 0.03 > 1/2$ we can confirm that our process matrix corresponds to quantum teleportation.

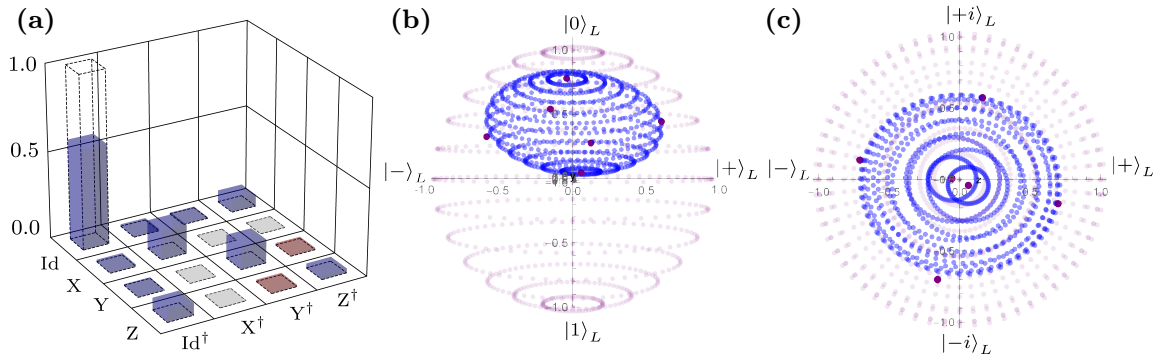

Figure 5.7: In **(a)** the process matrix of the experimental data is shown, together with the ideal process matrix for teleportation (in dashed bars). In **(b)** and **(c)** its simulated effect on pure input states is shown. The larger Bloch sphere belongs to the input states, while the inner, smaller, Bloch sphere belongs to the output states, which are highlighted in purple. Here we can see that the purity of the output states reduces, especially for the logical $|1\rangle_L$ state. Moreover, the bit- and phase-flip errors are not symmetric, such that the output Bloch sphere is distorted. Note, that the output states have not been re-normalized. As this process is not trace-preserving the inner Bloch sphere does not have the same norm as the outer Bloch sphere.

5.5.2 The converter fidelity

The final test for any teleportation protocol is the fidelity between input and output states. In order to give uncertainties, table 5.2 is used to compute the absolute maximal and minimal fidelity, which are given in table 5.3.

Table 5.3: Experimental maximal and minimal converter fidelity, providing the error estimation on the fidelity with a chosen experimental input state.

$\|Q\rangle$	$\|0\rangle$	$\|1\rangle$	$\frac{1}{\sqrt{2}}(\|0\rangle-\|1\rangle)$	$\frac{1}{\sqrt{2}}(\|0\rangle+\|1\rangle)$	$\frac{1}{\sqrt{2}}(\|0\rangle+i\,\|1\rangle)$	$\frac{1}{\sqrt{2}}(\|0\rangle-i\,\|1\rangle)$
$\mathcal{F}_{min}$	0.815	0.750	0.772	0.795	0.775	0.750
$\mathcal{F}_{max}$	0.836	0.769	0.811	0.848	0.828	0.792
$\mathcal{F}_{exp}$	$0.823^{+0.013}_{-0.008}$	$0.756^{+0.013}_{-0.006}$	$0.798^{+0.013}_{-0.026}$	$0.824^{+0.024}_{-0.030}$	$0.812^{+0.016}_{-0.037}$	$0.770^{+0.022}_{-0.020}$

The experimental fidelity has to be compared to the classical fidelity threshold for mixed states, as derived in subsection 5.3.1 to be $\mathcal{F}' = 0.741$. Figure 5.8 (a) shows this teleportation threshold for our six input qubits. It is exceeded over the full Bloch sphere, with an average fidelity of $\overline{\mathcal{F}}_{exp} = 79.7^{+0.7}_{-1.0}\,\%$. We can thereby confirm the success of the encoding conversion. In fig. 5.8 (b) we can see the effect of the conditioning window Δ, which for (a) is set to $\Delta = 0.5$. Here we can see the importance of the HBSM, as without conditioning, the teleportation threshold would not be surpassed. (c) and (d) show a fidelity sphere, where the length of the Bloch vector does not indicate purity, but fidelity.
We can see that the output qubit is shrunken in comparison to the input qubit due to the non-trace preserving process. This egg-shaped output fidelity sphere however does not show the same distortion as the analysis of the process matrix, indicating that bit- and phase-flip

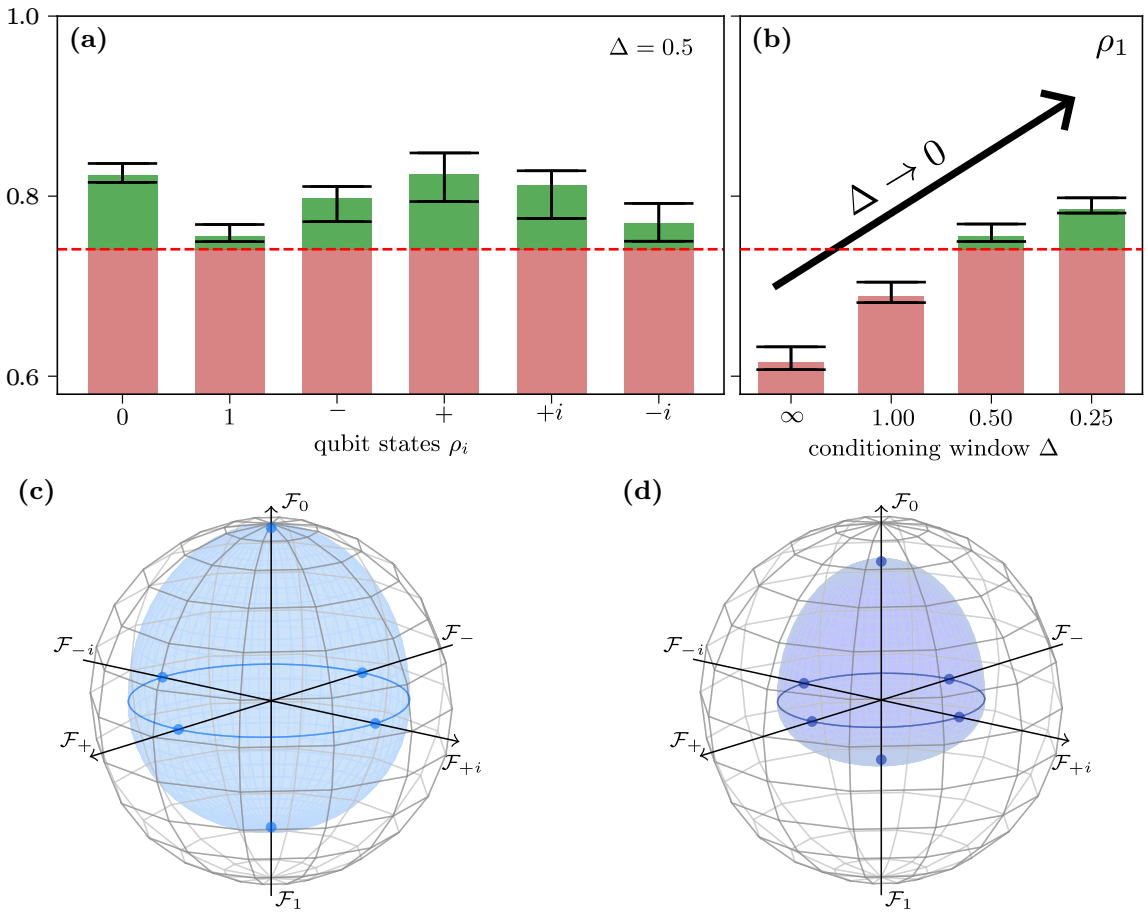

Figure 5.8: In **(a)** the six teleported qubits ρ_i with their respective fidelities are shown for the conditioning window $\Delta = 0.5$. The red dashed line marks the classical teleportation threshold $\mathcal{F}' = 0.741$. **(b)** assesses the effect of homodyne conditioning on the single photon qubit, with the conditioning window decreasing. **(c)** shows a fidelity sphere for the input qubit. Here the radius is equivalent to the fidelity between the experimental input state with an ideal input state. In **(d)** the same plot is shown for the output qubits.

errors have a larger effect on purity than on fidelity in our chosen input and output qubit bases.

5.6 Discussion

In this section we presented a post-selection-free, successful quantum teleportation, converting a discrete qubit into a continuous cat basis encoding. This was possible due to high-purity and indistinguishable sources, active phase stabilization of multiple paths, a low-loss implementation, and the use of highly efficient single-photon and homodyne detectors. Due to several heralding events having to occur in a very short time window, the rate of the protocol is reduced to three events per minute. This is a problem for distributed quantum computing or long-distance quantum communication, where resources have to be combined. Luckily several routes can tackle the slow rate. Firstly quantum memories can be used to synchronize those stochastic events, making the overall success rate decrease only polynomial with the number of modes. Secondly, we also emphasize that our input-output circuit is compatible with quasi-deterministic sources based on solid-state emitters that have also recently been used in teleportation protocols [241, 242]. They could substantially increase the rates in the future. Finally, the bit flip error on the DV mode encoded in the Fock-state basis naturally occurs upon propagation of the states in lossy quantum channels. Changing the DV mode can also be a practical route to follow. Several non-postselected schemes have been proposed either with polarization [243] or time-bin qubits [197].

Now follows a short analysis to judge if our OPOIIb output state can be used in those schemes. For this we can use the analysis of Takeda et al. [227] that we already discussed in subsection 5.3.1. In this way, we can judge the performance of our implementation with other discrete encodings, such as time-bin or polarization. We will quickly recall the idea: In non-post-selected schemes, vacuum, and multiphoton components are errors that exist in an orthogonal space to the qubit subspace, which has a weight η given by the single-photon component of any created qubit. Those errors are classical and as such can be teleported with unit fidelity. The unconditional classical fidelity bound $\mathcal{F}_\eta$ calculated in [227] is therefore defined as the linear combination between detecting a classical state with probability $1-\eta$ and detecting the pure qubit with probability η, giving $\mathcal{F}_\eta = (1-\eta) + \eta\frac{2}{3} = 1 - \frac{\eta}{3}$ and reduces to the 2/3 bound for pure states. In our case, the qubit fraction η in the fidelity bound $\mathcal{F}_\eta$ is given by the heralding efficiency of OPOIIb, which in our case is equal to $\eta = 71.2 \pm 1.5\%$. This sets $\mathcal{F}_\eta = 76.3 \pm 0.5\%$, which is achievable in our system, although with a smaller conditioning window, as visible in fig. 5.8 (b). The measured fidelity reaches $78.6^{+0.5}_{-0.1}\,\% > \mathcal{F}_\eta$ for a conditioning window equal to $\Delta = 1/4$. This constitutes a first assessment of using our experiment for unconditional conversion for other than Fock encodings. Next to adapting the discrete mode, the hybrid Bell-sate measurement would have to be adapted too.

In conclusion, we have presented the first not post-selected optical qubit converter, which converts information from the Fock basis to the cat-state basis. The successful outcome of this experiment was accompanied by a comprehensive theoretical analysis of the results, making the measurement and analysis components crucial aspects of this thesis work. The classical threshold of such a conversion was assessed theoretically and exceeded experimentally with an average fidelity above 79% over the Bloch sphere. The results of this experiment were published in 2023 [37].

5.7 Key results

- Achieving the full potential of quantum networks requires the ability to convert information between different platforms and encoding schemes. This chapter focuses on contributing to the latter aspect.
- Hybrid entanglement was created and used in a teleportation-based scheme to convert a discrete input qubit into a continuous output qubit. Discrete here means a superposition between vacuum and single-photon components while continuous refers to the superposition of even and odd cat states. We use the hybrid BSM, explained in the previous chapter. This experiment needs three-fold-coincidence events and uses homodyne conditioning.
- To asses the success of the protocol, a new teleportation threshold, valid for mixed input states, was derived and found to be $\mathcal{F}' = 0.741$. Furthermore, the process matrix approach was used, which analyses the mapping of input to output qubits. In the chosen basis its first matrix element has to fulfill $\chi[0,0] > 0.5$ for the process to be considered quantum.
- Both methods require input and output qubits to have equally sized density matrices. We therefore project the output qubit onto the cat basis. This process is not trace-preserving, leading to unnormalized states.
- The process matrix of the unnormalized input and output states is calculated with convex programming to have the element $\chi[0,0] = 0.578 > 0.5$, describing a quantum process.
- The fidelities between input and output states are all above the classical threshold $\mathcal{F}'$, with an average value of 79% over the Bloch sphere.
- With this we presented the first not post-selected optical qubit converter. The results were published in 2023 [37].

Chapter 6

Experimentally verifiable criteria of non-Gaussian coherences

Contents

In this chapter, we will discuss the emergence of non-Gaussian coherences in quantum states. The wave-like nature of particles, as demonstrated by quantum coherences, forms the foundation of our understanding of quantum mechanics. This phenomenon has also played a crucial role in the development of laser technologies and is of fundamental interest in quantum error correction. Here, we develop a threshold that can certify the Non-Gaussianity of coherences in a quantum state. In the **first section** we will discuss the main idea of quantum resource theory. Resource theory separates operations into free (or easy) operations and resource (or hard) operations. We can therefore formulate Non-Gaussianity as a resource theory in the **second section** and use this notion to develop a criterion to compute a threshold for non-Gaussian coherences. Furthermore, the idea of building a hierarchy of thresholds is introduced and our chosen hierarchy is motivated. In the **third section**, this hierarchy of thresholds is applied to two experimentally generated states. This is followed by a discussion about the experimental results and an outlook for the verification of a broader class of non-Gaussian coherences in the **fourth section**. The **fifth section** summarized the key results. The theory was developed in close collaboration with Lukáš Lachman from the Palacký University Olomouc, and a paper about the results is in preparation.

6.1 Quantum resource theory and coherences

In the last chapters, we have seen many attributes of experimental quantum states that render them useful in protocols: purity, entanglement, basis-state orthogonality, fidelity, and production rate. Deciding which properties of a state are useful in a quantum system is not always straightforward, resulting in the development of *resource theories* in quantum information theory [244]. In these theories, certain operators are considered easy and any state that can be created by applying those operations on a fully mixed state is considered a *free state*. A state that cannot be created within this set of operations is called a *resource state* and is deemed especially valuable. Which operations are considered as "free" can be adapted to the experimental capabilities. We can recast quantum teleportation in the framework of resource theory: if the set of free operators is defined to contain local unitary operations and classical communication (LOCC), then entangled states cannot be created by operations within this set. Therefore, entangled states are considered a resource, that unlock new quantum operations, which in this case would be quantum teleportation. Another example of a resource theory has been discussed in section 2.4, where free operators form the Clifford group and non-Clifford resource states have to be used to enable error correction [88]. While resource theories do not restrict the definition of free operations, a subset of operations that can be *efficiently simulated on a classical computer* is often used. Famous examples are the resource theory of purity and the resource theory of entanglement.

While these theories are basis-independent, one can also define the resource theory of coherence, which is basis-dependent and was first formulated by J. Aberg in 2006 [245]. Quantum coherences lie at the basic understanding of quantum mechanics by showing the wave nature of particles and have enabled the development of laser technologies. Moreover, they are at the heart of quantum information manipulation, enabling superposition and entanglement [246]. Additionally, coherences are of fundamental interest in quantum error correction, where Bosonic qubits are encoded in infinite Hilbert spaces. Error correction requires high quality and stable logical qubits, both factors that translate directly to the coherences in the physical system. In this context, the *resource theory of coherences* defines any diagonal state in a fixed basis and their coherent mixtures $\sum_i p_i |i\rangle \langle i|$ as free states. The free operations capable of creating those states are defined such that they cannot increase the coherence of a state. How coherent a state is, can be quantified via a *coherence measure*, which is defined by a function $\mathcal{C}$ [247].

In this work we present a modification to the before-mentioned resource theory, connecting it to the notion of Non-Gaussianity. Especially in single-mode quantum optics, this is a natural definition of free operations (see section 2.3). Naturally, we will choose the Fock states as a basis, in which coherences have to be verified. Coherences can be either scram-

bled over the whole Hilbert space of a system, forming strongly non-local correlations, or can be localized as the interference term between two Fock state probabilities. Although both possibilities are equally relevant, we will focus on the localized case, which translates to the target state

$$|\text{target}\rangle = \frac{1}{\sqrt{2}}(|n_1\rangle) + e^{i\phi}\,|n_2\rangle). \tag{6.1}$$

To connect coherence resource theory with non-Gaussian theory, we need to construct a criterion that can only be verified by quantum coherences, it should not be satisfied by any Fock state, as they do not exhibit any coherences. This indicates that we will consider the highly non-Gaussian Fock states as "trivial" in the study of non-Gaussian coherences, as also suggested by A. Streltsov et al. [246]. This can be reformulated as restricting the coherence-inducing non-Gaussianity to be located in the system's dynamics.

With this approach, we can now consider *non-Gaussian coherences*, purely induced by *non-Gaussian dynamics* (see section 2.2 and section 2.3). The general idea is depicted in fig. 6.1, where non-Gaussian dynamics are applied on an input state, which can include Gaussian or non-Gaussian states. The dynamics create coherences in these states, which can be measured and judged by the criterion we will develop in this chapter.
Furthermore, our goal is to develop a non-Gaussian coherence criterion that features a *hierarchical structure*, allowing states to be ranked from less valuable to more valuable. In quantum information, hierarchies are not a fixed concept and can be thought of as sorting criteria. A commonly employed hierarchy is the entanglement hierarchy, where states are organized based on the number of entangled particles or the intricacy of their entanglement

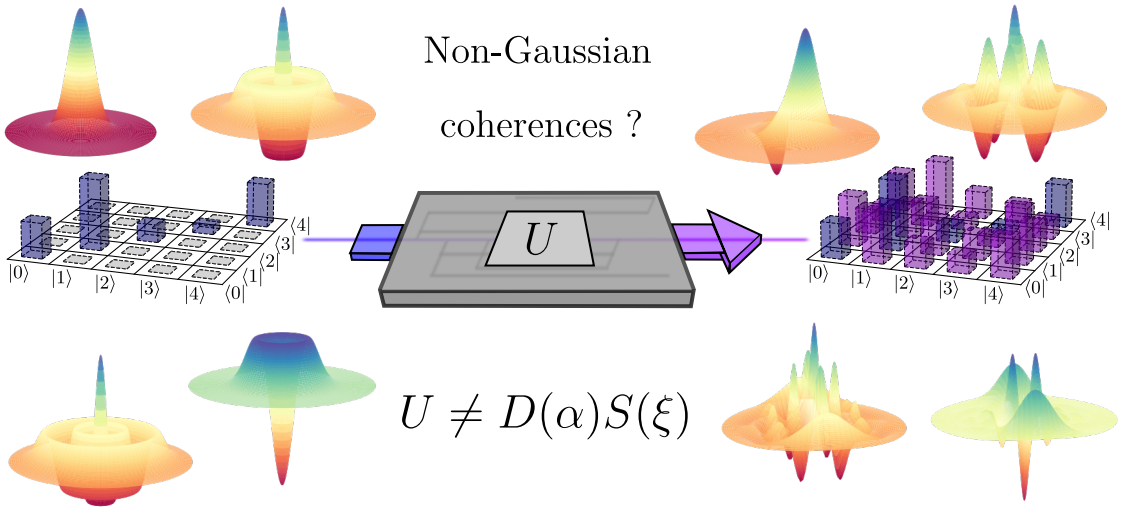

Figure 6.1: The creation of non-Gaussian coherences is shown. On the left, any purely Wigner-symmetric input state enters a system that applies a unitary transformation U on this mode. If this operation cannot be described by the general Gaussian dynamics of a displacement $D(\alpha)$ and squeezing $S(\xi)$ operation, then non-Gaussian coherences can be measured in the output state.

structure. Generally, states can be arranged hierarchically according to their relevance, usefulness, or performance in various applications. By selecting a specific hierarchy, we effectively determine which states are more valuable or challenging to achieve experimentally. This can be visualized as a ladder, where increased experimental complexity propels the state to a higher rank on the hierarchy ladder. Consequently, this corresponds to a ladder of thresholds that a state must surpass to advance to the subsequent stage on the ladder. A formal definition of this hierarchization procedure shall be developed in the next section.

6.2 Building a hierarchy and choosing free states

In this section, we develop the theoretical framework of a non-Gaussian coherence criterion in the **first subsection**. For this, we first discuss the definition of a hierarchy. We present the *Stellar hierarchy*, which forms a hierarchy of non-Gaussian states and use it to generalize the idea of hierarchies in non-Gaussian criteria. In the **second subsection**, we will devise on which state property shall be evaluated by the hierarchical criterion. This depends on the envisioned target state ordering. Given this ordering, two possible hierarchy definitions are discussed: one that is based on the maximal Fock excitation in the system and another, that is based on the maximal distance between the two Fock states forming the target superposition. Both hierarchies are developed and applied to different examples of target states. Finally, the hierarchy resulting in higher thresholds is chosen.

6.2.1 State hierarchies in quantum mechanics

As explained in e.g. [248], a hierarchy criterion follows certain properties. For the sake of the explanation, we review here the famous example of non-Gaussian states hierarchy: the so-called Stellar hierarchy.

6.2.1.1 Stellar hierarchy

Here, we will sketch the stellar hierarchy by summarizing the results of Chabaud et al. that are relevant for us [248]. The goal is to characterize quantum states in terms of their Non-Gaussianity in a way that is invariant under Gaussian operations. In this way, ranks $r \in [0, \infty]$ are defined, where $r = 0$ corresponds to Gaussian states. Each state is formulated in the stellar function $F^\star_\psi(\alpha)$ of a state $|\psi\rangle$, which corresponds to the function

$$F^\star_\psi(\alpha) = e^{|\alpha|^2/2} \langle \alpha^* | \psi \rangle = \sum_n^\infty \psi_n \frac{\alpha^n}{\sqrt{n!}}, \tag{6.2}$$

where α is the coherent state amplitude and $\psi_n = \langle n|\psi\rangle$. It represents the projection of the state onto the basis of coherent states. This representation is unique up to a global phase,

such that two states are deemed equivalent if they have the same stellar representation. The stellar rank of a state is then defined as the number of zero points in the Husimi Q-function

$$Q_\psi(\alpha) = \frac{1}{\pi} e^{-|\alpha|^2} |F^\star_\psi(\alpha^*)|^2, \tag{6.3}$$

which is equivalent to the zero-crossings of the Wigner function. This automatically gives each Fock state $|n\rangle$ a stellar rank of $r = n$. The stellar hierarchy is equivalent to the minimal number of photon additions N to create a state of rank $r = N$. Moreover, mixing of any states with a stellar rank $r < N$ cannot create a state with $r \geq N$.

6.2.1.2 General formulation of a hierarchy of states

Let us extract the general properties of hierarchies via the example of the stellar hierarchy. To formulate a hierarchy, a set of *target states* has to be defined. Next, *properties* have to be found, that enable the envisioned ordering of the target states.

In the stellar hierarchy, the target states are the pure Fock states and the property is the number of zero points of the Husimi Q-function. Moreover, the goal of the Stellar hierarchy is to verify the Non-Gaussianity of a state. Therefore, Gaussian dynamics on any convex mixture of states with a certain rank should not be able to create a higher-ranked state.

Here, we see the connection to section 6.1, defining Gaussian dynamics as free operations. For each rank $r = k$ of the hierarchy, all target states of $r < k$ are included in a set $\{|f\rangle_0, |f\rangle_1, ..., |f\rangle_{k-1}\}$ that we call the *basis set* of pure free states. Besides, we require this set to be convex, allowing for coherent superpositions with arbitrary weights between members of this set. In the example of the Stellar hierarchy, this set of states for rank $r = 3$ would be all the target states of lower ranks $\{|0\rangle, |1\rangle, |2\rangle\}$ including their coherent superposition $c_0 |0\rangle + c_1 |1\rangle + c_2 |2\rangle$.

Following resource theory, arbitrary free operations can be applied to this basis set, such that a linear combination of the basis set together with all allowed free operations applied to those combinations, from the set of *pure free states*. From this set, any statistical mixtures can be created, forming the full *set of free states* F_k, where to be a proper hierarchy, this set of states for $r = k$ has to be included in next ranks $F_k \subset F_{k+1} \subset F_{k+2}$....

We can now write any set of free states from the basis states $|f\rangle_k$ becoming a general pure free state $|G\rangle_i^F$, such that

$$\text{Free Gaussian states of rank } r < k \qquad \rho_k^{F,G} = \sum_i^{k-1} p_i \, |G\rangle_i^F \, \langle G|_i^F \,,$$

$$|G\rangle_j^F = \sum_j^{k-1} S(\xi) D(\alpha) c_j \, |f\rangle_j \,, \tag{6.4}$$

$$\text{Free classical states of rank } r < k \qquad \rho_k^{F,C} = \sum_i^{k-1} p_i \, |C\rangle_i^F \, \langle C|_i^F \,,$$

$$|C\rangle_j^F = \sum_j^{k-1} D(\alpha) c_j \, |f\rangle_j \,. \tag{6.5}$$

Here, we have also allowed for the set of free classical states $\rho_k^{F,C}$, applying only displacement to the basis states. In fact, hierarchies for non-classicality are not common. They should be seen as a first step to test each hierarchy: If a state beats the non-classical threshold of rank k, then the non-Gaussian threshold of rank k can be tested[1].

Next, a property P has to be defined. This property is the measure, i.e. evaluates the performance of any state in the context of the defined hierarchy. In the case of the stellar hierarchy, the property is the number of zero points in the Husimi Q-function. In this case, the property is unchanged by the target states of the hierarchy but we can also imagine a set of properties P_t adapted to the target rank in the hierarchy.
We require that the property P_t is maximized if applied to its target state $|\text{target}\rangle_t$, such that $P_t(|\text{target}\rangle_t) = \max_\rho P_t(\rho)$ over all possibles states ρ.
To judge if a state ρ' achieves a certain rank t, the threshold value of the free states of this rank has to be computed. The best possible value any free Gaussian (classical) state can achieve, creates a set of thresholds for the target state $|\text{target}\rangle_t$

$$T_{t,k}^{F,G} = \max_{\rho_k \in F_k^G} P_t(\rho_k), \tag{6.6}$$

$$T_{t,k}^{F,C} = \max_{\rho_k \in F_k^C} P_t(\rho_k). \tag{6.7}$$

Here the maximization over the set of free states F includes maximizing over the superpositions weights c_j, the squeezing ξ and the displacement α as well as the statistical mixing weights p_i of eq. (6.4) or (6.5).

[1] We note here, that the non-classical thresholds are strictly lower than the non-Gaussian ones for the same rank. It can however happen, that a non-classical threshold for rank $r = 5$ is harder to beat than a non-Gaussian threshold of rank $r = 1$.

Any state ρ', tested against the free states of the target state $|\text{target}_t\rangle$ could achieve ranks $k = 1$ to $k = t$. For this, ρ' has to achieve a higher value of the property $P_t(\rho')$ than $T_{t,k}^{F,G}$ ($T_{t,k}^{F,C}$), such that $P_t(\rho') > T_{t,k}^{F,G}$. If the state lies above the tested threshold $T_{t,k}^{F,G}$ it has (at least) rank k. In cases where the state does not exceed the $k = 1$ threshold, the result remains inconclusive. The selection of free states and the property to measure are crucial decisions that largely depend on the objective of the hierarchy. Subsequently, our choices of features will be elaborated upon.

6.2.2 Coherence based hierarchies

Our goal is to build a hierarchy that quantifies coherences in the Fock basis. As discussed in section 6.1, the free operations in our system are defined to be all Gaussian (classical) operations. While this choice is the same as in the Stellar hierarchy, we choose a different property that we evaluate for creating thresholds.

Measuring non-Gaussian (-classical) coherences requires us to build a criterion that is not verified by non-Gaussian states without coherences: the Fock states. After having defined the property, we will choose an ordering of target states and discuss two possible sets of free states and therefore hierarchies that enable this ordering[2]. One is based on the Fock-state excitation, similar to the Stellar hierarchy, while the other is based on the length of a quantum superposition. We will finally argue why we chose the latter for our experimental states.

6.2.2.1 The chosen property: local coherence measure

A properly defined measure of local coherences between two Fock excitations should be maximized by the ideal target state of eq. (6.1), which we recall to be

$$|\text{target}\rangle = \frac{1}{\sqrt{2}}(|n_1\rangle + e^{i\phi}|n_2\rangle).$$

For this, we can define the operator S

$$S(\phi,\theta)_{n_1,n_2} = \sin(\theta)[\cos(\phi)X_{n_1,n_2} + \sin(\phi)Y_{n_1,n_2}] + \cos(\theta)Z_{n_1,n_2}, \tag{6.8}$$

which is equivalent to a projective measurement of a qubit on a Bloch sphere with poles $|n_1\rangle$ and $|n_2\rangle$. The angle θ is the colatitude concerning the $z-$axis and ϕ is the longitude

[2] We do not claim that these are the only two possible sets of free states. They are the simplest and therefore most logical sets to consider in our view.

concerning the $x-$axis. Here, the Pauli matrices have to be defined for the corresponding state-space n_1 and n_2, shifting their matrix values to the corresponding Fock basis as in

$$X_{n_1,n_2} = |n_1\rangle\langle n_2| + |n_2\rangle\langle n_1|, \tag{6.9}$$

$$Y_{n_1,n_2} = i|n_1\rangle\langle n_2| - i|n_2\rangle\langle n_1|, \tag{6.10}$$

$$Z_{n_1,n_2} = |n_1\rangle\langle n_1| - |n_2\rangle\langle n_2|. \tag{6.11}$$

The local coherence measure $\mathcal{C}$ of any state ρ can then be defined as applying S on the state and fetching the highest coherences around the Bloch equator $\theta = \pi/2$:

$$\mathcal{C}_{n_1,n_2}(\rho) = \frac{1}{2}\left(\max_{\phi} \mathrm{Tr}[S(\phi, \frac{\pi}{2})_{n_1,n_2}\ \rho] - \min_{\phi} \mathrm{Tr}[S(\phi, \frac{\pi}{2})_{n_1,n_2}\ \rho]\right). \tag{6.12}$$

We can interprete this as an interferometric measurement with a phase scan ϕ, where $\mathcal{C}$ would be the contrast of the fringes. As such, $\mathcal{C} \in [0, 1]$ and ϕ is not fixed here such that we are only interested in the absolute value of the coherences. The target state will achieve the ideal value of unity.

6.2.2.2 Target state ordering

In the previous subsubsection, we established a measure of coherences $\mathcal{C}$. To conceive a hierarchy, we must first determine the ordering of coherences $\mathcal{C}_{n_1,n_2}$ with different n_1, n_2, assuming $n_2 > n_1$. As previously mentioned, this is analogous to assessing the difficulty of creating coherences between different fock states.
We aim at an ordering of the form

$$\begin{aligned}
&r = k && |\mathrm{target}\rangle_k = \frac{1}{\sqrt{2}}(|n_1\rangle + |n_2\rangle) && \text{with} && \mathcal{C}_{n_1,n_2},\\
&r = k-1 && |\mathrm{target}\rangle_{k-1} = \frac{1}{\sqrt{2}}(|n_1\rangle + |n_2 - 1\rangle) && \text{with} && \mathcal{C}_{n_1,n_2-1},\\
&\ldots\\
&r = 1 && |\mathrm{target}\rangle_1 = \frac{1}{\sqrt{2}}(|n_1\rangle + |n_1 + 1\rangle) && \text{with} && \mathcal{C}_{n_1,n_1+1},
\end{aligned} \tag{6.13}$$

where the last superposition occurs for the rank $r = 1$. This ordering can be achieved by choosing two different target state properties for the hierarchy definition: the two most striking features of the target order for superposition between n_1 and n_2, that can define its rank, are either the *maximal Fock excitation* n_2 or the *maximal length of the superposition* $n_2 - n_1$. Both of these properties can be used to order the target states as in eq. (6.13).

By choosing one of these properties our hierarchy will include more states than the ones in eq. (6.13)). The extend of this set can generally increase the threshold value of each rank. A hierarchy can therefore be evaluated by this threshold value for different ranks, as in eq.

(6.6) or eq. (6.7). If one hierarchy consistently gives a higher threshold for different ranks, it should be chosen.
We will now formally present two hierarchies, based on the maximal excitation or length in the target superposition.

6.2.2.3 Free states based on the maximal Fock excitation

One can achieve the desired ordering of the target states based on their maximal Fock excitation in the system n_2, which we call here N-hierarchy. This idea is physically grounded, as creating higher-order Fock states is experimentally hard. With the maximal Fock excitation n_2 being the dominant property, any lower excitation should be free, such that the set of basis states $|f\rangle$ for the state of rank $r = n_2$ enlarges to

$$\begin{aligned}
&r = n_2 - 1 \quad |f\rangle_{n_2-1} = \frac{1}{\sqrt{2}}(|x\rangle + |n_2 - 1\rangle) \quad x \in [0, n_2 - 1],\\
&r = n_2 - 2 \quad |f\rangle_{n_2-2} = \frac{1}{\sqrt{2}}(|x\rangle + |n_2 - 2\rangle) \quad x \in [0, n_2 - 2],\\
&\ldots\\
&r = 1 \qquad |f\rangle_1 = \frac{1}{\sqrt{2}}(|0\rangle + |1\rangle),\\
&r = 0 \qquad |f\rangle_0 = |0\rangle\,.
\end{aligned} \tag{6.14}$$

The full set of pure free states for the N-hierarchy includes superpositions of the above basis states $|f\rangle$, to which free operations can be applied. The set of free states is then containing any statistical mixtures of the set of pure free states. As such, the set of basis states can be written in a simpler form, here exemplary for the non-Gaussian set of free states

$$\begin{aligned}
&\text{set of free states } F_{n_2}^{N,G} \text{ for} \quad r = n_2 \quad |f\rangle_j \in \{|0\>, |1\>, |2\>, |3\> ..., |n_2 - 1\rangle\},\\
&\rho_{n_2}^{N,G} = \sum_{i=0}^{n_2-1} p_i \, |G\rangle_i^F \langle G|_i^F \qquad |G\rangle_i^{N,G} = \sum_j^N S(\xi)D(\alpha)c_j \, |f\rangle_j\,.
\end{aligned} \tag{6.15}$$

Written in this form, we see that the pure free states of the rank $r = n_2$ are composed of any displaced and squeezed superposition of Fock states, while excluding the maximal Fock excitation n_2 of the target state of this rank. This set of free states is equivalent to the one of the Stellar hierarchy. Nonetheless, our definition of the N-hierarchy has a different property to define thresholds: the coherence measure. Applied to those states the threshold for the rank $r = n_2$ can be calculated as

$$T_{t,n_2}^{N,G} = \max_{\rho_{n_2} \in F_{n_2}^{N,G}} \mathcal{C}_t(\rho_{n_2}), \tag{6.16}$$

$$T_{t,n_2}^{N,C} = \max_{\rho_{n_2} \in F_{n_2}^{N,C}} \mathcal{C}_t(\rho_{n_2}), \tag{6.17}$$

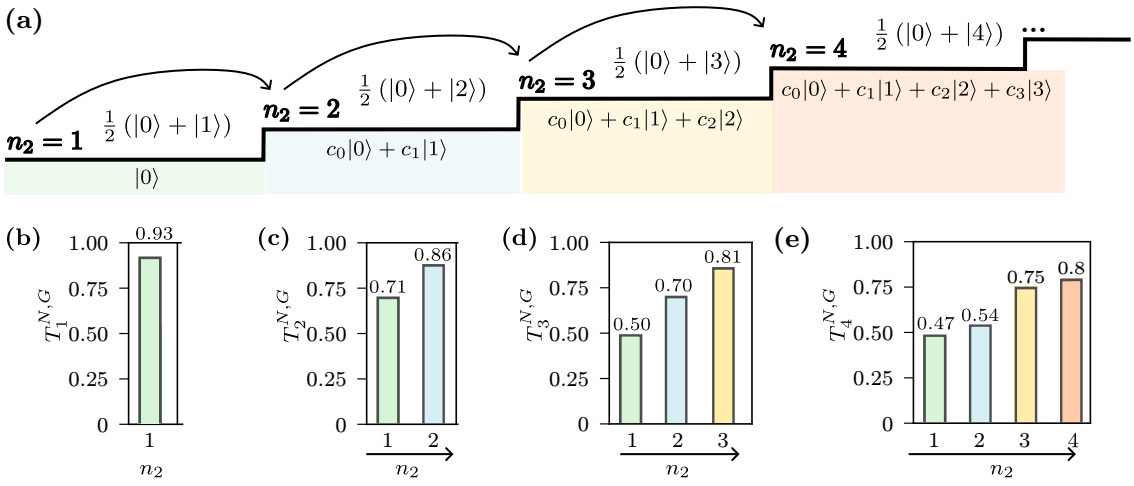

Figure 6.2: In **(a)** the N-hierarchy for the length of superpositions of the form $\propto |0\rangle + |N\rangle$ is shown. Above each stair of this hierarchy, the ideal target state is shown, while below, the set of basis states for the corresponding rank is explicitly written. The threshold for each hierarchy rank n_2 is calculated by optimizing over the set of free operations applied to the set of basis states, that can be mixed classically. For each target state $\propto |0\rangle + |N\rangle$, all threshold values are given in **(b)-(e)**.

where the target state, and therefore maximal rank $n_2 = t$ is defined by the target state's n_1, n_2.

The N-hierarchy for the example of a maximal value of $n_2 = 4$ is shown in fig. 6.2 (a). The hierarchy is drawn as a staircase with the target states sitting on each stair and all basis states hovering below this stair. The threshold values for each target state are shown in (b)-(e) for all possible ranks n_2.
Let us now turn to the length of the target superposition as another criterion to order the hierarchy.

6.2.2.4 Free states based on the maximal length of superpositions

In the previous approach, the maximal Fock state excitation in the system was chosen as an ordering parameter for the target states. In the present approach, we follow a different idea, using the length L of the superposition state $\propto |n_1\rangle + |n_2\rangle$, named the L-hierarchy.

Given that we now choose to prioritize the length, we should see all states $\propto |m\rangle + |m+l\rangle$ as equal such that we can define the additional basis states as follows

$$\begin{aligned} |f\rangle_{l,m} &= \frac{1}{\sqrt{2}}(|m\rangle + |m+l\rangle), \\ |f\rangle_{l-1,m} &= \frac{1}{\sqrt{2}}(|m\rangle + |m+l-1\rangle), \\ &... \\ |f\rangle_{1,m} &= \frac{1}{\sqrt{2}}(|m\rangle + |m+1\rangle), \\ |f\rangle_{0,m} &= |m\rangle\,, \end{aligned} \tag{6.18}$$

where we set $m \in [0, N_{\max} - l]$. This set of basis states is only dependent on the difference between n_1 and n_2 such that we can write the set of free states as

$$\begin{aligned} &\text{set of free states } F^{L,G}_{l,m} \text{ for} \quad r = l \quad \text{and} \quad m \in [0, N_{\max} - l] \\ &|f\rangle_j \in \{|0\rangle\,, |1\rangle\,, |2\rangle\,, |3\rangle\,..., |N_{\max}\rangle\}, \\ &\rho^{L,G}_{l,m} = \sum_{i=0}^{N_{\max}-l} p_i\, |G\rangle^L_{i,m}\, \langle G|^L_{i,m} \qquad |G\rangle^{L,G}_{i,m} = \sum_{j=m}^{m+l} S(\xi)D(\alpha)c_j\, |f\rangle_j\,. \end{aligned} \tag{6.19}$$

We have once again further simplified the set of basis states. Comparing this set to that of the N-hierarchy in eq. (6.15), we can see that the only difference the number of states per rank allowed.

While in the N-hierarchy the rank $r = 1$ only permits for the basis state $|0\rangle$, the L-hierarchy allows for $|0\rangle\,, |1\rangle\,, ... |N_{\max} - l\rangle$, where $N_{\max}$ can be arbitrarily high.
Even if we set $N_{\max} = n_2$, the example of the lowest rank of the L-hierarchy will still include Fock states up to the target state value n_2, while the N-hierarchy will always only consider vacuum. Therefore, we note that the L-hierarchy is a generalisation of the N-hierarchy.

The threshold for each rank $r = l$ has now also to be maximized over the running variable m, such that

$$T^{L,G}_{t,l} = \max_m \max_{\rho_l \in F^{L,G}_{l,m}} \mathcal{C}_t(\rho_l), \tag{6.20}$$

$$T^{L,C}_{t,l} = \max_m \max_{\rho_l \in F^{L,C}_{l,m}} \mathcal{C}_t(\rho_l), \tag{6.21}$$

where the target t is defined by the target state's n_1, n_2. In fig. 6.3 we set $N_{\max} = 4$ and evaluate the hierarchy up to $l = 4$. Importantly, we observe that in (d) and (e), the threshold values are higher than the ones of the N-hierarchy. This has been numerically

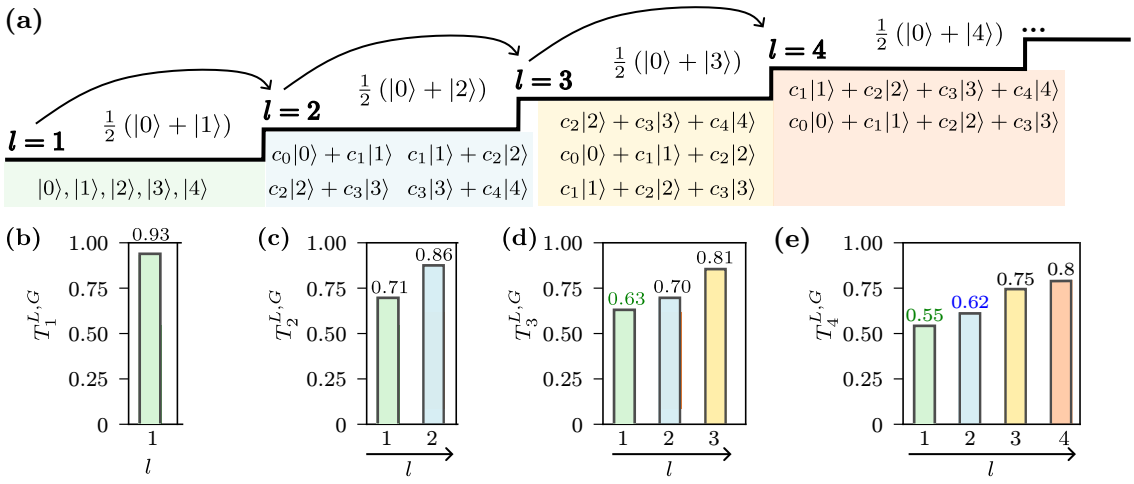

Figure 6.3: In **(a)** the L-hierarchy for the length of superpositions of the form $\propto |0\rangle + |N\rangle$ is shown. Above each stair of this hierarchy, the ideal target state is shown, while below the set of basis states for $N_{\max} = 4$ is explicitly written. The threshold for each hierarchy step l is calculated by optimizing over the set of free operations applied to the set of basis states, that can be mixed classically. For each target state $\propto |0\rangle + |N\rangle$, all thresholds are shown in **(b)-(e)**. Each threshold of rank $r = l$ is optimized over the set of free states, defined by the basis states shown in the same color. The bright green and blue numbers in (d) and (e) mark where this threshold lies above the N-hierarchy.

verified for multiple values n_1, n_2 and seems to consistently be the case for $n_1 = 0$.

Moreover, we remark that after numerical checks, N_{max} for $n_1 = 0$ does not have to be restricted in the L-hierarchy, as the highest threshold is always given for $m = 0$.
We can therefore set $N_{max} \to \infty$ if $n_1 = 0$, thereby being able to test the threshold against an infinite Hilbert space.

6.2.2.5 Hierarchy discussion

If we compare fig. 6.2 and fig. 6.3, we observe several trends. First, we see that the maximal threshold, meaning the threshold of the maximal rank l is steadily decreasing for target states with higher n_2.
This has been numerically checked for $n_1 = 0$ and n_2 up to $n_2 = 7$ but seems to be consistently the case also for $n_1 \neq 0$. It leads to the somehow counter-intuitive fact, that non-Gaussian (classical) coherences are harder to achieve, if one wants to produce $\propto |0\rangle + |1\rangle$ than $\propto |0\rangle + |5\rangle$. This monotonic decrease mirrors the importance of higher and longer superpositions. It shows that they are harder to produce with Gaussian operations and is valid for both hierarchies. Experimentally this can be explained as follows: given small displacement and squeezing, a coherent superposition of vacuum and single photon can be created with high fidelity. This will raise the threshold to verify any non-Gaussian coherence between those states. On the other hand, displacement and squeezing will always create unwanted excitations if one wants to create coherence between for example a two-photon

and a five-photon state. These unwanted excitations will lower the maximal achievable coherence value, thereby lowering the threshold.

Moreover, we see that for the case of $n_1 = 0$, the L-hierarchy produces harder or equivalent thresholds, especially when comparing (d) and (e) of fig. 6.2 and fig. 6.3, where the value where the L-hierarchy exceeds the N-hierarchy threshold is indicated by color. As $n_1 = 0$ corresponds to our experimental states, we will use the L-hierarchy.

Before proceeding we briefly discuss how to calculate each threshold. The calculation of the threshold values requires a global optimization over many parameters: the squeezing and its phase, the displacement, and the weights of the basis state superposition. We do not have to optimize over statistical mixtures of basis states, as a linear function, defined on a convex set is always optimal on the boundary of the convex set due to the *Bauer maximum principle*, formulated in 1958 [249, 250]. To compute the thresholds for each rank, we have to consider all possible basis states. For each basis state, we optimize over the squeezing, the displacement amplitude, and the angle between displacement and squeezing. Moreover, we optimize the coefficient weights of the superposition. The threshold values of all basis states are compared and the maximum value is defined as the threshold.
This problem requires a global optimization algorithm. We choose the combination of a bound-constrained *Nelder-Mead* minimization, together with basinhopping as implemented in `scipy` [251]. Basin-hopping [252] is an iterative optimization algorithm that finds the global minimum of a smooth function by randomly perturbing coordinates, performing local minimization, and accepting or rejecting the new minimum based on the function value. All parameters and snippets of this code are given in section 8.3. Due to the stochastic behavior of the minimization algorithm, we run each each optimization at least ten times, to consider the solution converged. Note that one can never completely be sure to obtain a global solution. Moreover, all values are cross-checked with the calculation of Lukáš Lachman, who uses a different approach.

6.3 Coherence in experimental states

6.3.1 Introduction

Creating high-quality coherences experimentally can be very challenging or very easy, depending on the physical platform. In the example of atomic systems, high fidelity rotations between atomic levels via laser pulses [253] or a combination of radiofrequency and microwave magnetic fields [254] enable the creation of coherences in d-level systems [255], which can be read out with high fidelity and even mapped onto photonic states [256]. These approaches are limited to qubit systems, where higher-order Fock states are not available. To see non-Gaussian coherences in the Fock basis beyond coherences between $|0\rangle$ and $|1\rangle$,

the mode of the atomic system should be described by a quantum harmonic oscillator. For this, the motional state of ions or atoms is used [257] and microwave pulses can decrease or increase the excitation of the motional state. As previously mentioned, the creation of a Fock state or a coherence between two Fock states is equivalently hard. Similarly, in superconducting systems, a cavity-qubit coupled system can use projective qubit measurements to create Fock states and their coherences in the cavity mode, although only with post-selection [258]. Fock states and their coherences have also been shown to exist in bulk acoustic-wave resonators [259]. Although all those approaches can create high-quality quantum coherences, their measurement is based on a projection on only a few operators [3], from which the density matrix is reconstructed. While this leads to trustworthy measurements of Fock number probabilities, equivalent to the diagonal elements of the density matrix, a faithful reconstruction of the off-diagonal elements requires a phase scan rather than a few projective measurements.

We will see with the example of the coherence between $\propto |0\rangle + |1\rangle$, that already small loss and de-phasing can reduce the coherences drastically, such that high confidence in the measured coherences is absolutely necessary. For this, we use the qubit model of chapter 5, given in eq. (5.10) and (5.11), for balanced qubits. First, we can assume a pure state ($c_{vac} = 0$, $c_{sp} = 1$, $c_{tp} = 0$) and find that phase noise with a standard deviation of maximally $\Delta_\phi = 0.37$ rad can be allowed, reducing the coherences to $C_{0,1} = 0.933$, equal to the non-Gaussian threshold. This is equivalent to a maximal allowed phase noise of 5.9 % and reduces to a maximal allowed phase noise of 3 % if we consider losses of 5 % ($c_{vac} = 0.05$, $c_{sp} = 0.95$, $c_{tp} = 0$) in the system. The maximally allowed phase noise in percentage is calculated by taking $\Delta_\phi/(2\pi)$.
In fig. 6.4 we show the phase noise and loss combinations that allow a balanced qubit with coherences between $n_1 = 0$ and $n_2 \in \{1, 2, 3, 4\}$ to surpass the the non-Gaussian threshold. Once loss or phase-noise are increased, the threshold cannot be reached anymore such that those qubits do not have non-Gaussian coherences.
With those stringent requirements on the quality of the system, a significant uncertainty in the measurement and readout can render a confident verification of non-Gaussian coherences very challenging. In contrast, optical systems are better suited in terms of measurement and offer a fine-grained highly reliable full tomographic reconstruction of the state, leading to high confidence in the off-diagonal elements. High-quality Fock states in optics can only be produced to date via optical parametric oscillators, as detailed in chapter 3. These systems initially emit Gaussian states and therefore need non-Gaussian measurements to be lifted into Non-Gaussianity. Inducing coherences in these states is non-trivial and different from atomic or superconducting systems requires additional resources that have to exhibit non-Gaussian dynamics.

[3] Most often the parity operator is used.

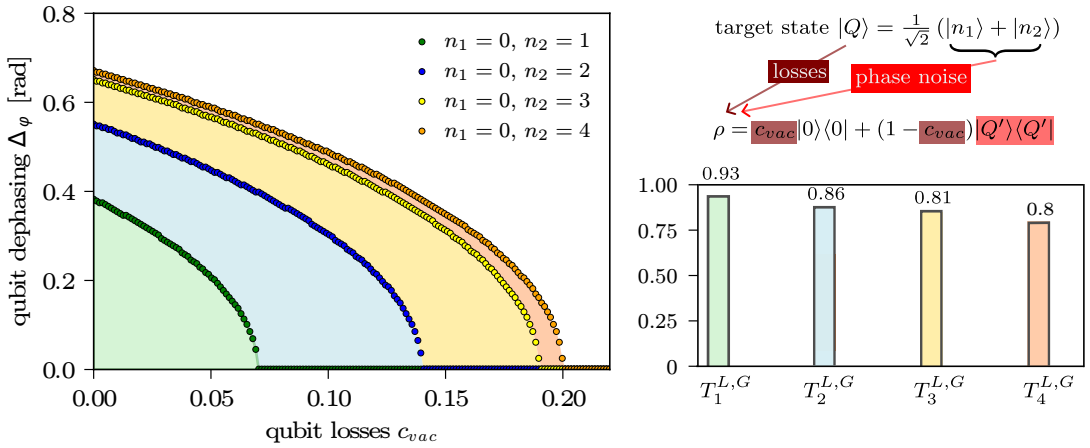

Figure 6.4: The maximally allowed combinations of phase-noise and losses to reach the Non-Gaussian threshold of highest rank are calculated for qubits ranging from $n_2 = 1$ to $n_2 = 4$. We assume losses and dephasing to be the only sources of error. On the left side the plot areas, where the qubit can reach coherences up to its threshold are colored. Markers correspond to simulated values. The corresponding color and threshold value for each qubit and clarified to the right side of the plot.

Therefore, the faithful generation of high-quality Fock states in optics does not guarantee the Non-Gaussianity of coherences in the Fock basis.

We will test experimentally generated states in superpositions of $\propto |0\rangle + |1\rangle$ and $\propto |0\rangle + |2\rangle$ against their non-Gaussian (classical) coherence threshold.
We first explain how the experimental states are created and then apply the non-Gaussian coherence criteria to these states. We calculate different threshold values by taking into account additional information about the density matrix and show the performance of our experimental states against these thresholds. Finally, we present an alternative criterion, which evaluates qubit coherences rather than general coherences.

6.3.2 Experimental state creation

The first set of states we want to test are the input qubits for the qubit converter we presented in chapter 5. The experimental setup is shown again for completeness in fig. 6.5 (a). The type-II OPOIIb creates two-mode squeezed light and is pumped at a low threshold of around 2 mW. The degenerate signal and idler photons at 1064 nm can be separated on a polarizing beam-splitter. Upon detection of n idler photons on high-efficiency superconducting nanowire single-photon detectors (SNSPD 1), the creation of a Fock state n on the signal path is heralded. The generated state is emitted into a well-defined spatio-temporal mode due to filtering in the heralding mode, with a bandwidth of about 60 MHz. The signal is characterized via a high-efficiency homodyne detection and reconstructed by a maximum-likelihood algorithm. To create a superposition of the form $c_0 |0\rangle + c_1 e^{i\varphi} |1\rangle$, a weak displacement is applied on the heralding mode. The phase φ is defined by the rel-

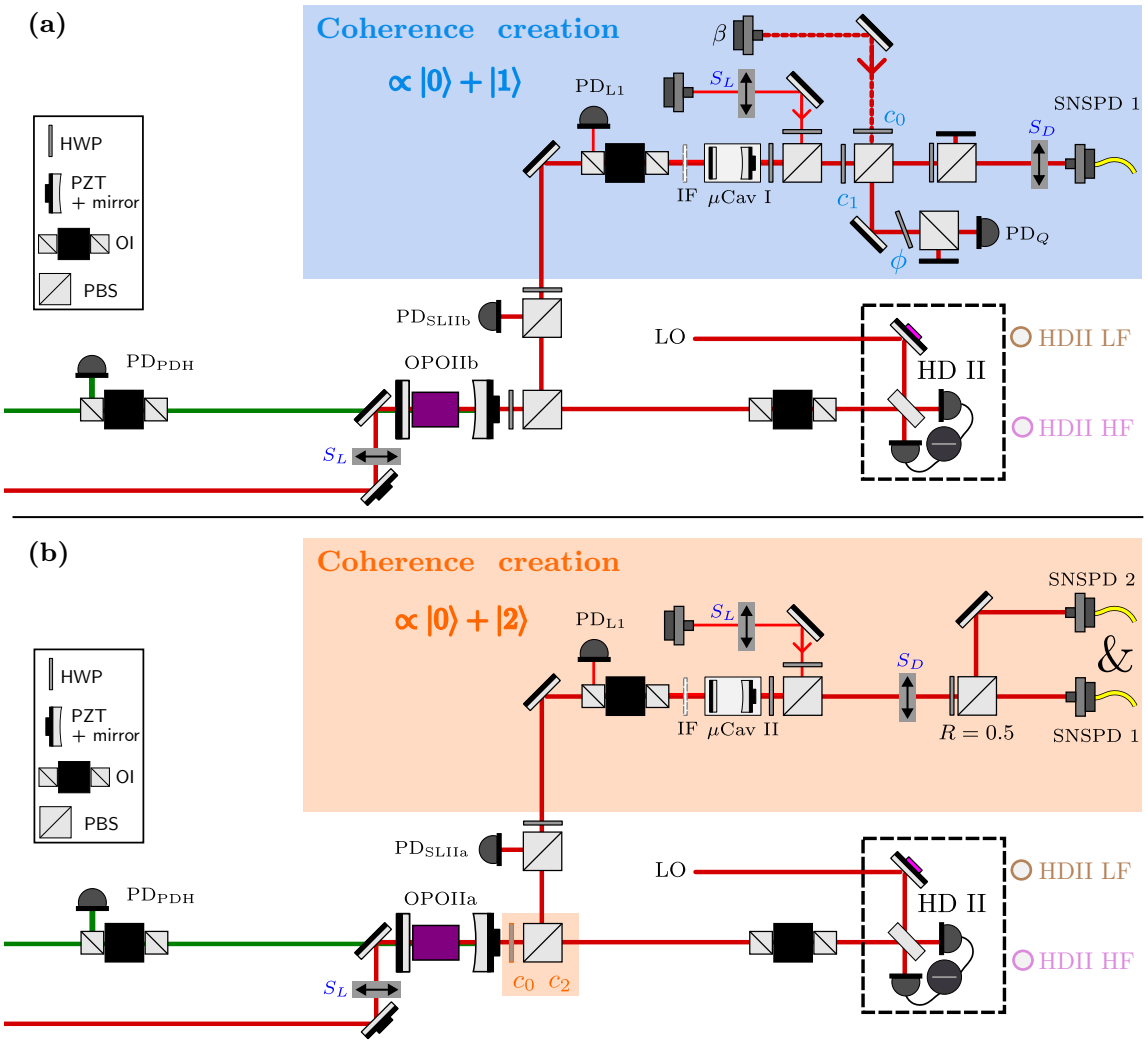

Figure 6.5: The experimental setups for the creation of two types of Fock-state coherences are shown. In **(a)** the creation of a superposition of the form $\propto |0\rangle + |1\rangle$ is depicted. The coherence is created by a displacement beam β that interferes with the heralding path of OPOIIb after filtering by an interferential filter (IF) and the micro-cavity (μCav). The superposition phase is locked on the interference fringe between displacement and heralding path ϕ and the weights of this superposition can be controlled by the two respective HWPs, controlling the merging weight of each path. The output state is measured with a homodyne detector. In **(b)** the creation setup of a superposition $\propto |0\rangle + |2\rangle$ is shown. Here, the heralding path of OPOIIa is split into two after filtering, enabling two on-off SNSPD detectors to monitor the path. If both SNSPDs click within a small time window, then a two-photon state has been heralded with high probability. Tuning the HWP after OPOIIa can correlate signal and idler beams instead of perfectly separating them, creating correlations in their photon-number distribution. Those correlations can be analyzed via homodyne detection.

ative phase between the displacement and heralding path, whereas the weights c_0, c_1 can be controlled by the relative count rates between the two paths. Upon one heralding click, the signal state is projected onto the desired superposition, with a maximal single-photon heralding efficiency of 72%. For a more detailed explanation and modeling of this process, we refer to subsection 5.2.3.

We use the state proportional to $\propto |0\rangle - |1\rangle$, as it showed the best performances of our data set. In fig. 6.5 (b), the setup to create a superposition of the form $\propto |0\rangle + |2\rangle$ is shown. The two-mode squeezing of OPOIIa is not ideally separated into signal and idler but rather mixed by a ratio $x\%$. This induces correlations that can, upon a heralding detection of two photons with two SNSPDs, create a coherent superposition of Fock states in the weak pump limit. This experiment was conducted in the group and we make use of the data set used in the paper *Optical Synthesis of Large-Amplitude Squeezed Coherent-State Superpositions with Minimal Resources* by K. Huang et al. [32]. We interpret these cat states of an amplitude around $\alpha = 1.73$ as a good approximation of the target superposition. For this data set, the coincidence window of the two on-off detection events of SNSPD1 and SNSPD2 was set to 0.8 ns. This reduces the rate of the experiment to 200 Hz, as discussed in subsection 5.2.4. The ideal setting of the half-wave plate in 6.5 (b), which controls the mixing ratio, is at an angle of 2.5°, corresponding to a mixing of signal and idler by 5.6 %. We do, however, test the full set of states available to us, independent of the mixing ratio.

Our states have a maximal fidelity with the ideal qubit of $\mathcal{F}_1 = 82.1\%$ and $\mathcal{F}_2 = 83.1\%$ without post-selection and are therefore among the purest photonic qubits created to-date. Their Wigner functions and density matrices are visible in fig. 6.6 (a)-(c) for the superposition of vacuum and a single photon and (e)-(g) for the superposition of vacuum and two-photon components. Given the high overlap with the ideal superposition state, we will test the non-Gaussian coherence criterion on them and then present strategies to refine this criterion.

6.3.3 Absolute and conditional criteria on experimental states

6.3.3.1 Absolute coherence criterion

Now that our experimental states are created we can test them against the calculated non-Gaussian (-classical) *absolute coherence criterion* of fig. 6.3. As discussed in subsection 6.2.2, we will choose the L-hierarchy due to its higher thresholds. The maximal values free states can obtain, and therefore the thresholds to beat are given in table 6.1. Before calculating the coherences $\mathcal{C}$ of our experimental states this table allows us to make important observations. As analyzed in chapter 5, the phase noise of our superpositions between vacuum and single photon is on average $\Delta_\phi = 0.707$ rad, which is above the tolerable phase

Table 6.1: Here the thresholds for quantum non-Gaussian and non-classical coherences for the target coherences $\mathcal{C}_{01}$ and $\mathcal{C}_{02}$ are given. While the first has only one rank, the latter has two ranks in the hierarchy of coherences, given by the number of l.

rank	threshold $T^{L,C}_{1,l}$	threshold $T^{L,G}_{1,l}$	threshold $T^{L,C}_{2,l}$	threshold $T^{L,G}_{2,l}$
$l = 1$	0.86	0.93	0.52	0.71
$l = 2$	none	none	0.78	0.86

noise of 0.37 rad for lossless states, calculated in subsection 6.3.1. Given that our system has losses and phase noise above the calculated limit, we cannot expect those states to beat the non-Gaussian coherence threshold.
This phase-noise limitation is not present in the superposition of vacuum and two-photon components, as these are created via phase-stable two-mode squeezed states and include no additional phase lock. Only the losses should hinder us from surpassing the non-Gaussian coherence threshold. We calculate that states with losses below 14 %, under the assumption of no phase noise, can beat the highest non-Gaussian coherence threshold for the rank $l = 2$.

In fig. 6.6, we can see representative states of all measured coherent states.
In the first row (a)-(c) the state $\propto |0\rangle - |1\rangle$ is shown, while in the second row (e)-(g) the state $\propto |0\rangle + |2\rangle$ is depicted. In (d) the threshold for absolute non-Gaussian (in orange) and non-classical (in turquoise) coherences is shown, together with the experimental coherence value $\mathcal{C}_{0,1}^{\text{exp}} = 0.66$, represented by a dashed line and a star marker. In (h) the threshold for absolute non-Gaussian and non-classical coherences are shown for both ranks $l = 1$ and $l = 2$. The experimental coherence value $\mathcal{C}_{0,2}^{\text{exp}} = 0.72$ is depicted by a dashed line and a diamond marker. The absolute non-Gaussian threshold of the first rank $l = 1$ is beaten, while the second rank $l = 2$ is not reached.

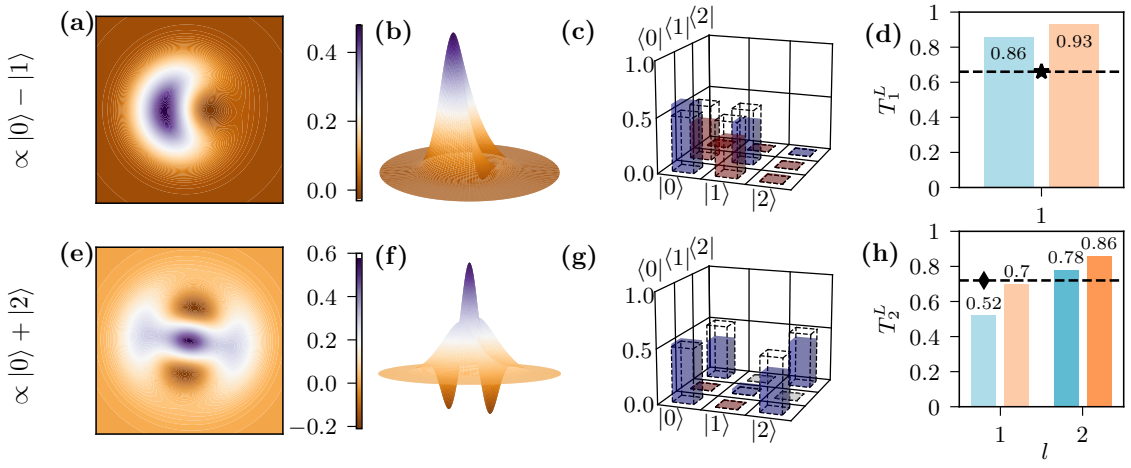

Figure 6.6: The experimental input states and their performance on the absolute non-Gaussian (classical) coherence threshold are shown. In **(a)** to **(c)** the top and 3D view of the Wigner function of the experimental state $\propto |0\rangle - |1\rangle$ and its density matrix are shown. The dotted lines in (c) indicate the ideal state. In **(d)** the coherence $\mathcal{C}_{0,1}$ of this state is shown in dashed lines and marked with a star against the absolute non-classical (in turquoise) and non-Gaussian (in orange) threshold. **e** to **g** show the top and 3D view of the Wigner function of the experimental state $\propto |0\rangle + |2\rangle$ and its corresponding density matrix. In **(h)** the coherence $\mathcal{C}_{0,2}$ of this state is shown in dashed lines and marked with a diamond against the absolute non-classical (in turquoise) and non-Gaussian (in orange) thresholds for the ranks $l = 1$ and $l = 2$.

This can be explained by the residual 4% single photon component in the experimental state, due to the imperfect heralding detectors and 2% higher order Fock components. Moreover, we do observe small phase noise, which can be due to the laser's small phase fluctuations, changing the squeezing axis. This results in a small phase averaging in the squeezing and therefore reduces the purity of the output state [260]. Moreover, we find that the qubit is unbalanced, which contributes also to the lowering of the maximal achievable coherences.

Given how stringent the "absolute" non-Gaussian coherence criterion presented so far is, we discuss two possible additional criteria necessitating additional accessible information of the measured density matrix. These criteria are equivalent but less strong non-Gaussian (-classical) coherence criteria and can be seen as steps towards the absolute criterion. For these criteria, we will only use the strongest hierarchy, allowing for the maximal set of free states to compute the thresholds.

6.3.3.2 Conditional coherence criteria

Instead of using only the operator S of eq. (6.8) we will take additional properties of the experimental states into account. Each additional property can be seen as a new dimension, added to the absolute criterion, forming a *conditional criterion*. This new dimension adds a restriction to the set of free states, intuitively making it harder for this set to reach high values. There is no restriction as to which property can be chosen, such that we can test which one is the best choice for our target states [261].

Let us call the additional measurements S_i' and the new properties that are tested with each new measurement P_i'. The new d-dimensional overall property P_c can then be written as a convex linear combination of all measured properties, such that

$$P_c^{\{g_i\}} = \sum_i g_i P_i', \tag{6.22}$$

where g_i are the weights over this convex sum. Any threshold derived from this convex sum is a conditional non-Gaussian (classical) coherence criterion, as it is conditioned on $i \neq 1$ dimensions. Note that the weights g_i are determined by optimizing them for each experimental input state, such that the threshold can be computed as

$$T_{t,k}^{F,G} = \max_{\rho_k \in F_k^G} P_c^{\{g_i\}}(\rho_k), \tag{6.23}$$

$$T_{t,k}^{F,C} = \max_{\rho_k \in F_k^C} P_c^{\{g_i\}}(\rho_k). \tag{6.24}$$

For our states, we will use two types of additional measurements. The first is a simple Fock state m projection P_m and the second a projection P_{n+} on all Fock states from a certain excitation n onward

$$P_m = |m\rangle \langle m| , \tag{6.25}$$

$$P_{n+} = \sum_{i=n}^{\infty} P_n. \tag{6.26}$$

We propose to first try a *second dimension* P_{n_2} as defined in eq. (6.25) and adapted to our experimental states $\propto |0\rangle + |n_2\rangle$. Each threshold value is therefore a linear combination of $g_0 P_{n_2} + g_1 \mathcal{C}_{n_1,n_2}$, optimized over g_0 and g_1, shown in fig. 6.7. While some of our experimental states $\propto |0\rangle + |2\rangle$ exceeds this two-dimensional conditional coherence threshold in (b), the experimental state $\propto |0\rangle - |1\rangle$ in (a) does not succeed.

This is why we add a *third dimension* for the experimental state $\propto |0\rangle - |1\rangle$, consisting of P_{2+} as defined in eq. (6.26). All threshold values can now be computed with linear combinations of $g_0 P_1 + g_1 \mathcal{C}_{0,1} + g_2 P_{2+}$. This results in a 3d plot, shown in fig. 6.8 (a), where the threshold is plotted against the more-than-two-photon and single-photon probability. The experimental state has $P_{2+} = 0.02$, which corresponds to a 2D cut through (a), shown in light grey. This cut is plotted in (b), where the three-dimensional criterion is shown as a two-dimensional criterion with one dimension fixed. While the experimental state lies above the non-classical threshold it does not beat the non-Gaussian threshold.

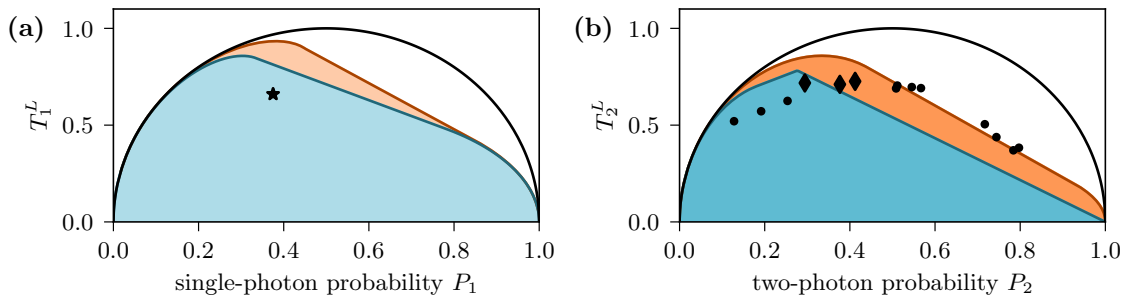

Figure 6.7: Two-dimensional conditional non-Gaussian (-classical) coherence threshold. In **(a)** the non-Gaussian threshold T_1^L is plotted against the single photon probability P_1. This imposes a physical boundary on all possible states, shown as a half-circle in black. The non-Gaussian (in orange) and non-classical (in turquoise) thresholds change with P_1, where the maximal value is equal to the absolute threshold. The experimental state is shown as a star. In **(b)** we see a similar figure but with the second dimension P_2. All experimental states are plotted as round markers, except for three diamonds, which surpassed the first-ranked threshold of fig. 6.6

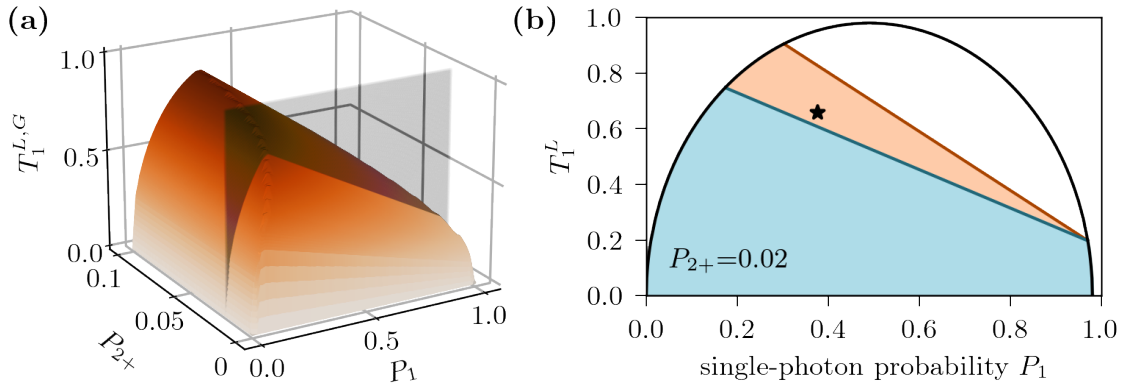

Figure 6.8: Three-dimensional conditional non-Gaussian (-classical) coherence threshold for the experimental state $\propto |0\rangle - |1\rangle$. In **(a)** the non-Gaussian threshold $T_1^{L,G}$ is plotted against the single photon probability P_1 and the higher Fock population probability P_{2+}. We take a 2D slice of this 3D plot, corresponding to our experimental value $P_{2+} = 0.02$. This 2D cut is shown in **(b)**, where the black line shows the physical boundary for all states. The experimental state is shown as a star.

Therefore, we can see that adding additional dimensions can help improving the performance of experimental states, but at the price of making the threshold dependent on something that is not a coherence, thereby deviating from the pure definition of non-Gaussian (-classical) coherences.
Instead of adding dimensions to the coherence criterion, we can also construct a qubit-coherence criterion, valuing all superpositions instead of trying to achieve the maximal coherence for the balanced superposition.

6.3.4 Qubit-coherence criterion

In this subsection, we shift our perspective and focus on qubit coherences. Contrary to the method employed for absolute coherences, a qubit may have unbalanced weights. This imbalance diminishes the achievable maximum coherences. By adopting a coherence measure that accommodates this discrepancy, we have to consider both n_1 and n_2. We can therefore define a new target state

$$|\text{target}\rangle_Q = \cos(\theta)\,|n_1\rangle + e^{i\phi}\sin(\theta)\,|n_2\rangle\,, \tag{6.27}$$

differing from the previous target state of eq. (6.1) by its freedom of θ. This freedom is mirrored by an adapted measure. For this, we do not change the operator S of eq. (6.8), but change the definition of the local coherence measure to a set value of θ

$$\mathcal{G}^{\theta}_{n_1,n_2}(\rho) = \max_{\phi} \text{Tr}[S(\theta,\phi)_{n_1,n_2}\rho]. \tag{6.28}$$

In opposition to the coherence measure $\mathcal{C}$, the qubit-coherence measure has different limits $\mathcal{G} \in [-1, 1]$. It is equivalent to a Mach–Zehnder interferometer, where both its phase and splitting ratio are fixed, before the measurement is realized.
Fixing the phase ϕ will not penalize the set of free states as there are enough degrees of freedom that can align their maximal value on this phase. Given that we can fix both phases, this measurement is projective. The threshold can be calculated as

$$T_{t,k}^{F,G}(\theta) = \max_{\rho_k \in F_k^G} \mathcal{G}_t^\theta(\rho_k), \tag{6.29}$$

$$T_{t,k}^{F,C}(\theta) = \max_{\rho_k \in F_k^C} \mathcal{G}_t^\theta(\rho_k), \tag{6.30}$$

where t is determined by the target state's n_1, n_2.
We will in the following apply the qubit-coherence non-Gaussian and non-classical threshold on the experimental state $\propto |0\rangle + |2\rangle$, as it has already shown promising performances in the previous thresholds.
The threshold can be calculated for different angles θ and the corresponding plot is shown in fig. 6.9. We see that the threshold has a minimum for certifying qubit-non-Gaussian coherences around $\theta = 0.4 \times \pi/2$. We can define this as the minimal requirement to call a qubit non-Gaussian. In the inset of fig. 6.9 two of our experimental states are plotted as dotted lines, where the diamond markers beat the threshold.
We can see that around and at the *minimal requirement for qubit-non-Gaussian coherences*, both states beat the threshold, thereby verifying said coherences.

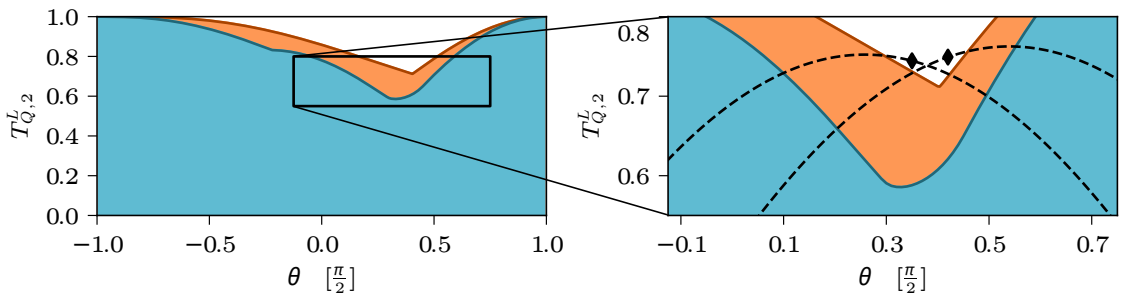

Figure 6.9: Qubit non-Gaussian (-classical) coherence threshold for the experimental state $\propto |0\rangle + |2\rangle$. The threshold $T^L_{Q,2}$ is plotted against the qubit phase θ. The inset shows the development of the non-Gaussian (orange) and non-classical (blue) thresholds around their respective minima. The dotted lines represent two experimental states that show non-Gaussian qubit coherences, marked by the diamond positions.

6.4 Discussion

A local non-Gaussian and non-classical coherence criterion within a hierarchical framework has been established. The non-Gaussian threshold completely depends on the target state definition and the property one wants to evaluate. In our case, this hierarchy is founded on the difference $n_2 - n_1$ between the target coherences of the state $\propto |n_1\rangle + |n_2\rangle$. The absolute criterion was then modified to create a set of conditional criteria, which take into account additional state dimensions such as the Fock state probabilities n_2 or n_1. Furthermore, an alternative approach was presented, focusing on qubit-coherences instead of perfectly balanced superpositions.
By testing those criteria on highly non-Gaussian experimental resource states, we have highlighted the challenges associated with non-Gaussian coherence verification in optics, particularly when contrasted with non-Gaussian verification based on Fock state probabilities.

Nonetheless, Non-Gaussianity over the whole Bloch-sphere is implicitly assumed in the theory of Non-Gaussianity such that its results are only valid if this feature can be maintained. In the experiment, this study has made us even more vigilant of phase noise and can be used to quantify an improvement in our system. Especially for the superposition of vacuum and single-photon components, we should be able to decrease the phase noise by improving the fringe visibility and increasing the PID micro-controller voltage resolution and algorithm. This work is ongoing and will serve for future experiments, as presented in the next chapter. In the context of theory development, a natural progression would involve incorporating non-local coherences. This extension would enable the inclusion of cat-states and GKP-states within this framework.

6.5 Key results

We have presented a criterion with a hierarchy of thresholds that can verify non-Gaussian and non-classical coherences in comparison to a target state superposition of the two Fock states n_1 and n_2.
These thresholds are based on the notion of coherence resource theory and non-Gaussianity and therefore have operational relevance, given the connection of Gaussianity to classical computing.
Our main findings can be summarized as follows:

- We have tested this criteria on state-of-the-art optical qubits with $n_1 = 0$, $n_2 = 1$ and $n_1 = 0$, $n_2 = 2$. Although these states are generally non-Gaussian, their coherences do not show absolute non-Gaussianity such that the criterion can be adapted by adding different Fock state probabilities, resulting in conditional criteria.

- With the conditional criteria, we find that the experimental superposition $\approx |0\rangle + |2\rangle$ surpasses the conditional non-Gaussian and $\approx |0\rangle + |1\rangle$ the conditional non-Classical threshold.

- The final approach we presented allowed for any qubit superposition to be the target and is closer to the use case in computing and communication where phase scans are seldom applied before the final measurement. We find that the experimental state $\approx |0\rangle + |2\rangle$ surpasses the minimal requirement of this threshold.

Chapter 7

Proposal: Towards the generation of GKP states

Contents

In this last chapter, we want to give an outlook and discuss new projects that can enhance our experimental capability. Using OPOs, heralding with SNSPDs and homodyne conditioning we have discussed the creation of high-quality single-photon, two-photon, and cat states of an amplitude around $\alpha = 1$ in chapter 3. The indistinguishably of those output states enable the generation of hybrid entanglement, discussed in chapter 4 and led to the experimental demonstration of information conversion from a single-photon qubit of to a cat-state qubit in chapter 5. Analyzing the Non-Gaussianity of the coherences we can create in the laboratory in chapter 6 has shown, that there is room for higher quality states which can be achieved by improving phase-noise and increasing the escape efficiency.

Here we will discuss how those improvements can enable the creation of GKP states thereby providing more of an experimentalist's view of their introduction in chapter 2. In the **first section** we recall the definition of ideal and approximate GKP states and introduce the stabilizer expectation value as a quantitative measure for the quality of GKP states. In the **second section** we give a short overview of experimentally created GKP states. The **third section** then introduces our envisioned setup and we simulate the kind of states we can produce. The feasibility of this experiment is discussed in the **fourth section**. This chapter is concluded by the **fifth section**, summarizing the key results.

7.1 Error-correctability of pure GKP states

7.1.1 Ideal GKP state

In chapter 2 we have introduced ideal GKP states (eq. (2.234) and (2.235)) as the coherent superposition of momentum or position eigenvectors in phase space, which we recall to be written as

$$|\text{GKP}_x^{id}\rangle = \sum_{s\in\mathbb{Z}} D((ns+k)\frac{\gamma}{\sqrt{2\hbar}})\,|x=0\rangle = \sum_{k\in\mathbb{Z}} D(\alpha(ns+k))\,|x=0\rangle\,,$$
$$|\text{GKP}_p^{id}\rangle = \sum_{k\in\mathbb{Z}} D((ns+k)\frac{i2\hbar\pi}{n\gamma\sqrt{2\hbar}})\,|p=0\rangle = \sum_{k\in\mathbb{Z}} D(\beta(ns+k))\,|p=0\rangle\,,$$

where n is the dimension of a qudit ($n=2$ is a qubit, $n=3$ is a qutrit ...), k the logical eigenstate $k \in [0, n-1]$ and γ the GKP amplitude, which can be translated into two displacement amplitudes α and β, which are both uniquely defined by γ. Those states are celebrated for their good error correctability, which was explained in subsubsection 2.4.3.2. We want to first discuss the ideal GKP states for the square GKP, rectangular GKP (with $\lambda = 1.3$), and hexagonal GKP state. We recall their definitions, which are given in eq. (2.309)-(2.311) for the displacement amplitudes, and here for the amplitude γ of the ideal GKP states

Square GKP	$\gamma = \sqrt{\frac{2\pi\hbar}{n}},$	(7.1)
Rectangular GKP	$\gamma = \lambda\sqrt{\frac{2\pi\hbar}{n}} \quad \lambda > 0,$	(7.2)
Hexagonal GKP	$\gamma = \sqrt{\frac{2\pi\hbar}{n\sqrt{3}}}.$	(7.3)

In order to visualize that they are indeed stabilized by the squared Pauli-X and Pauli-Z gates (eq. (2.308)), we want to plot the marginal distribution of the GKP state against the binning of the stabilizers.

7.1.2 Stabilizer and Pauli gate binning

The binning corresponds to regions in position or momentum which are associated to positive weights (blue) or a negative weights (red). Those weights are multiplied with the integrated marginal distribution, such that the overall sum of this process give the expectation value of the operator on the state.

As the GKP states are eigenstates of both *stabilizers* with eigenvalues +1, we expect the peaks in their marginal distributions to only be in blue regions. In order to find the binning size, we can apply the stabilizers on the quadratures

$$S_z^\dagger \hat{x} S_z = \hat{x} - n\gamma, \tag{7.4}$$

$$S_x^\dagger \hat{p} S_x = \hat{p} - \frac{2\pi\hbar}{\gamma}. \tag{7.5}$$

A state is stabilized, or unchanged, if a shift by the above value leaves the GKP states in the blue bins. Therefore eq. (7.4) and (7.5) has to correspond to the width of two bins, one blue and one red, such that a shift by this value shifts the state into the next blue bin. We can calculate the binning sizes for the stabilizers to be

$$2n\gamma \mathrm{bin}_x = n\gamma \quad \Leftrightarrow \quad \mathrm{bin}_x = \frac{1}{2}, \tag{7.6}$$

$$2n\gamma \mathrm{bin}_p = \frac{2\pi\hbar}{\gamma} \quad \Leftrightarrow \quad \mathrm{bin}_p = \frac{\pi\hbar}{n\gamma^2}, \tag{7.7}$$

where we choose to write position and momentum in multiples of γ. If we now write bin_p in terms of eq. (7.2), we find $\mathrm{bin}_p = \mathrm{bin}_x/\lambda^2$. The same logic can be applied to the binning for the *Pauli gates*, such that we find the overall binnings

$$\text{Stabilizer binning} \qquad \mathrm{bin}_x = \frac{1}{2} \quad \mathrm{bin}_p = \frac{1}{2\lambda^2}, \tag{7.8}$$

$$\text{Pauli binning} \qquad \mathrm{bin}_x = 1 \quad \mathrm{bin}_p = \frac{1}{\lambda^2}. \tag{7.9}$$

The ideal GKP state is plotted in fig. 7.1 for the squared GKP state. For better visibility we choose to shift the plots of the rectangular and hexagonal GKP state into section 8.4 (fig. 8.1 and fig. 8.2).
Here we are always plotting the logical computational basis $|0\rangle_L$ and $|1\rangle_L$.

Independently of the type of GKP, the marginal distributions of the two plotted states are completely in the +1-region (blue) for both stabilizers. As such, they are clearly eigenvectors of the stabilizers with eigenvalues +1. For the Pauli Z gate binning they are either completely in the +1-region for $|0\rangle_L$ or in the −1-region (red) for $|1\rangle_L$, showing that they are the ± 1 eigenvectors of the Z gate. Logically, they are completely mixed for the Pauli X gate.

However, the GKP states we have plotted so far are not physical as they have infinite energy. This is easily visible in each of the above mentioned figures, where a two-dimensional integration of the Wigner function does not normalize to one but rather to infinity.

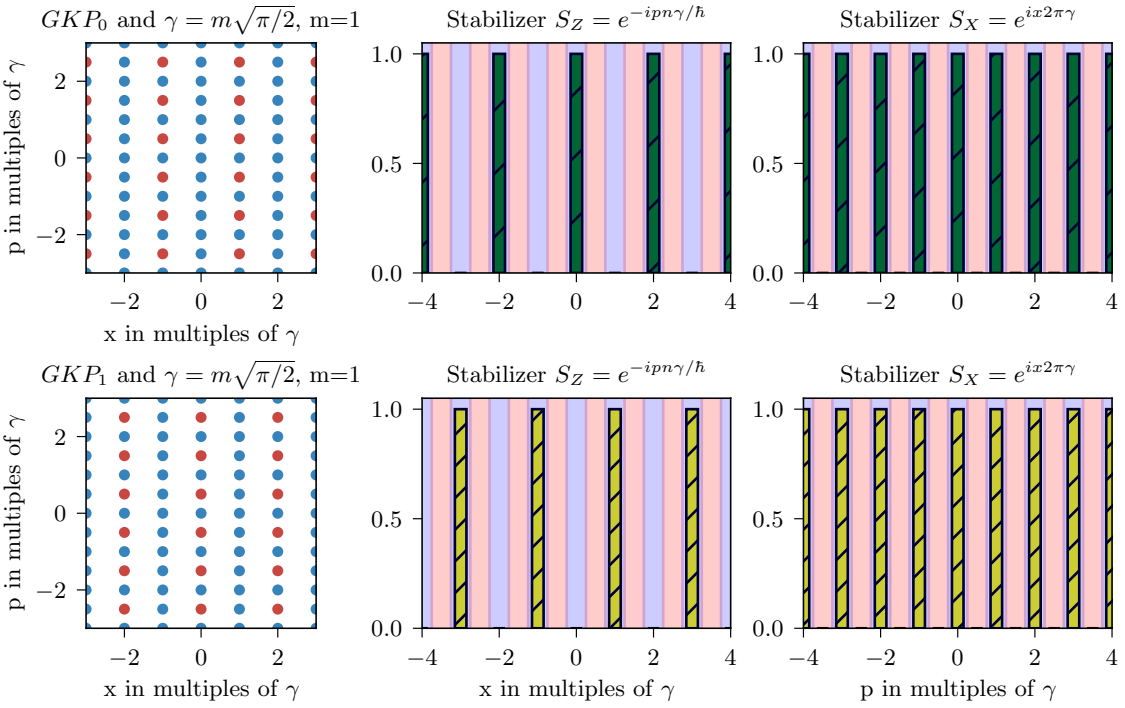

(a) Stabilizers on the GKP logical basis

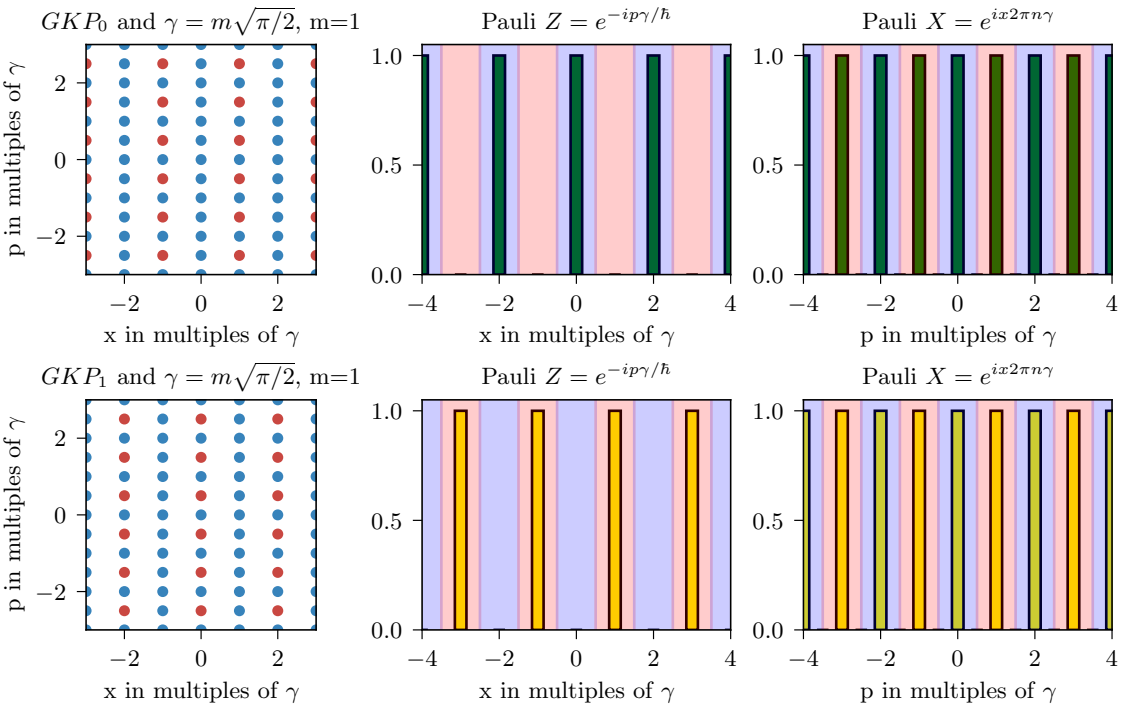

(b) Pauli gates on the GKP logical basis

Figure 7.1: The ideal square GKP state is plotted in multiples of γ for $n = 2$ and $\hbar = 0.5$ for the logical $|0\rangle_L$ and $|1\rangle_L$ state. It is an eigenvector of both stabilizers with eigenvalue $+1$, visible as all peaks of the marginal position and momentum distribution lie in the blue area in **(a)**, representing an eigenvalue of $+1$. We can see that the logical states are eigenvectors of the Pauli Z gate, with eigenvalues $+1$ and -1 in **(b)**, where the red bins represent -1.

7.1.3 Ideal physical GKP state

In eq. (2.236) we have given the physical approximation of an ideal GKP state, which we recall is

$$|\text{GKP}^{\kappa}\rangle = N_k \sum_{s\in\mathbb{Z}} e^{-0.5(ns+k)^2\kappa^2\alpha^2} D(\alpha(ns+k))S(\xi)\,|0\rangle\,,$$

where N_k is the normalization constant. We see that in the limit $(\xi,\kappa)\to(\infty,0)$ the ideal GKP states are recovered. Physical achievable states have finite (ξ,κ), such that we need a way to assess their quality.

7.1.4 Quality criterion of GKP states

The question of how to asses the quality of a GKP state is not trivial to answer because the general quality of a GKP state depends strongly on the envisioned error-correction code. To the best of our understanding, the only code-independent way to verify the GKP-ness of a state is via the calculation of the expectation value of its stabilizers, which ideally gives $+1$ for both stabilizers. We will therefore use the *stabilizer expectation values* as a quantitative measure for the quality of approximate GKP states.

We plot the square approximate square GKP state in figure 7.2, for a squeezing of $\xi = 0.24$ and an envelope $\kappa = 0.2$. The approximate rectangular and hexagonal GKP states are plotted in the appendix (section 8.4 fig. 8.3 and fig. 8.4). Here, the expectation values of stabilizers and Pauli gates are directly given in each plot.

One important observation is that for physical GKP states, the two logical states do not have the same quality for the same values κ,ξ. This indicates, that the error correctability over the whole Bloch sphere is not the same. This is an interesting point, as we remind ourselves that we are still talking about pure states. It can be explained by components of the state living outside the defined Hilbert space of the Bloch sphere, and is very similar to our discussion in chapter 5 about non-preserved traces. In order to have a good error-correctability over the whole Bloch sphere, the values κ,ξ have to approach their ideal values, which makes those states hard to achieve experimentally. We will now discuss existing experimental implementations of GKP states.

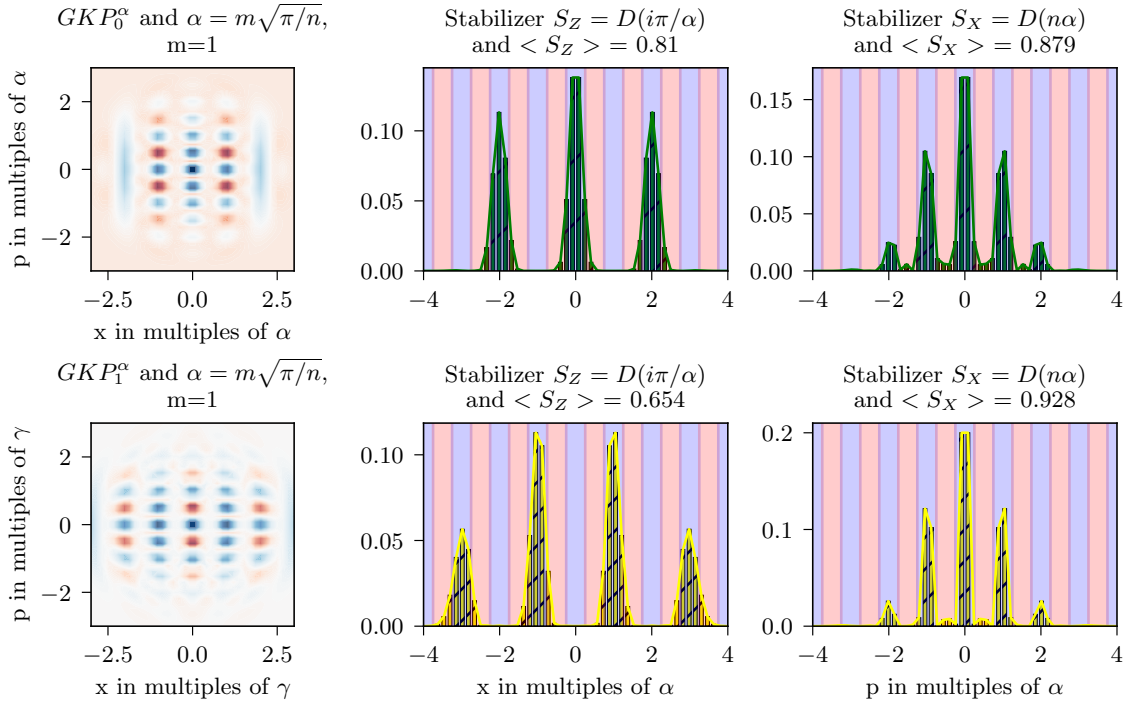

(a) Stabilizers on the GKP logical basis

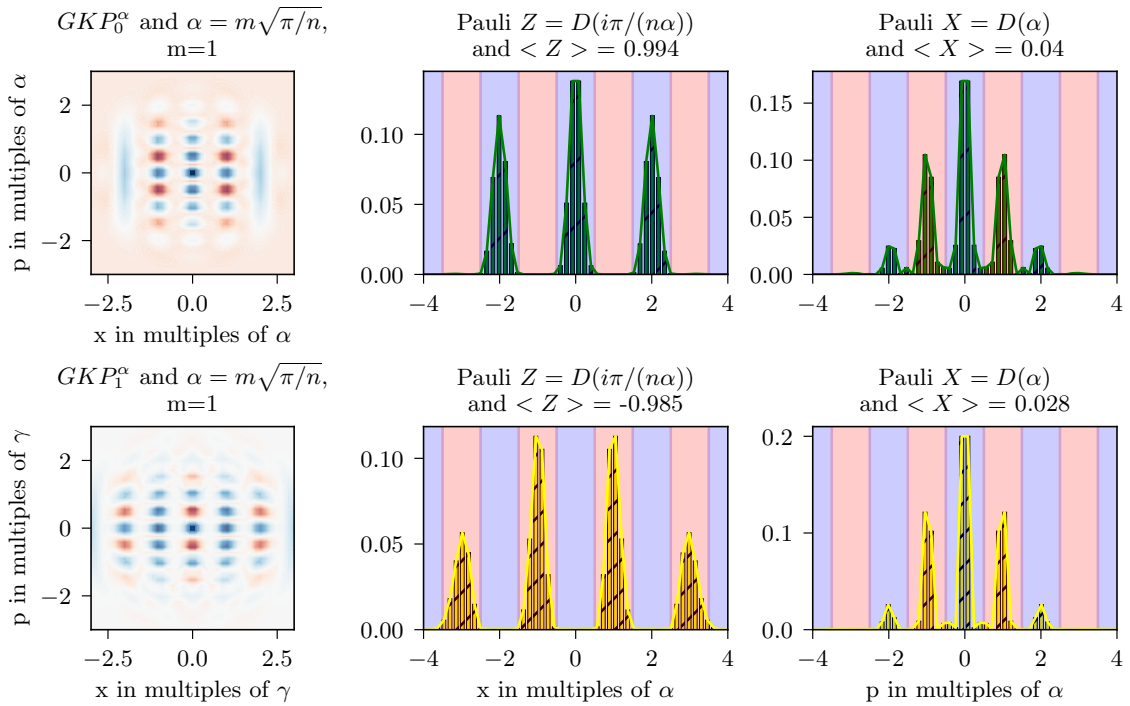

(b) Pauli gates on the GKP logical basis

Figure 7.2: The physical version of the ideal squared GKP state is plotted in multiples of α for $n = 2$ and $\hbar = 0.5$ for the logical $|0\rangle_L$ and $|1\rangle_L$ state with parameters $\kappa = 0.2$ and $\xi = 0.45$. It is an eigenvector of both stabilizers with eigenvalue $\to +1$, visible as all peaks of the marginal position and momentum distribution lie in the blue area in **(a)**, representing an eigenvalue of $+1$. We can see that the logical states are eigenvectors of the Pauli Z gate, with eigenvalues $\to +1$ and $\to -1$ in **(b)**, where the red bins represent -1.

7.2 Experimentally created GKP states so far

High-quality GKP states have been produced experimentally for the first time in 2018 with trapped ions by C. Flühmann et al. [262] and have been improved upon by the same group in 2019 and 2022 [263, 264]. In superconducting circuits, they were first achieved in 2020 by P. Campagne-Ibarcq [265] and since repeated three times [266–268]. The small number of groups in trapped ions and superconducting circuits that can produce a GKP state can do this with astonishing precision, as visible in fig. 7.3. Those states show a large qualitative resemblance to the physical GKP codes and have been shown to be usable beyond the break-even point (see definition in subsubsection 2.4.2.1).

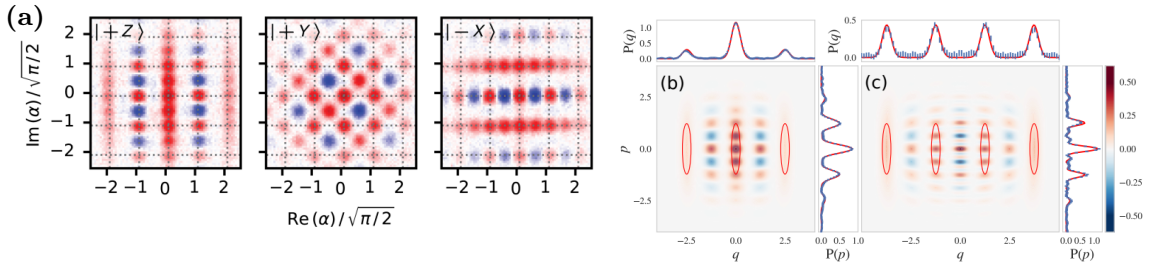

Figure 7.3: Two examples of experimentally generated GKP states are shown. **(a)** is produced on a superconducting platform and taken from [267]. **(b)** and **(c)** are on a trapped ion platform and taken from [263].

In photonics, the GKP state is hard to achieve, as precise control of coherences and high Fock excitations in the system is required. The first version of an optical GKP state was published in 2024 by S. Konno et al. [269] using photonic capabilities similar to ours. In fig. 7.4 the experimental setup in (a) is shown. Two OPO sources are used, that emit single-mode squeezing. A small fraction of this squeezed output is used for heralding, creating an odd cat-state if the pumping is in the right regime. This is equivalent to our setup for OPOI and gives states similar to the ones presented in subsection 3.2.3.

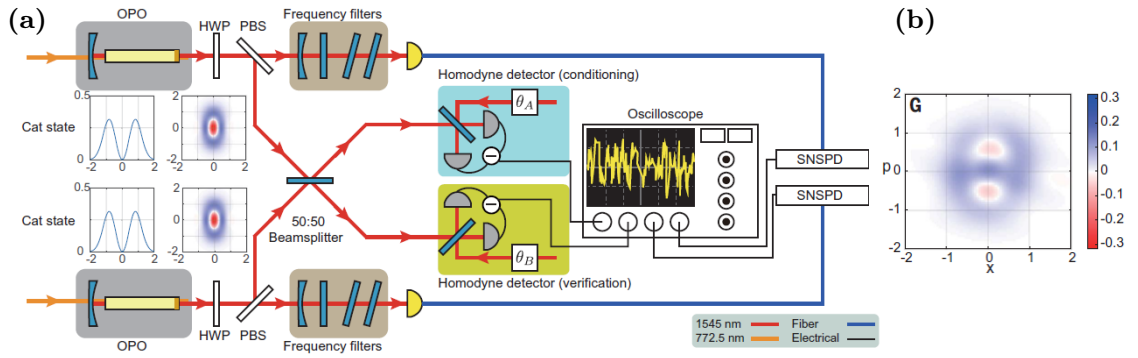

Figure 7.4: The first optical GKP state with **(a)** the experimental setup and **(b)** the measured GKP state. Figures are taken from [269].

Those two odd cats are interfering on a 50:50 beamsplitter and one output arm of this beamsplitter is used for homodyne conditioning. Here the conditioning, different than in chapter 4, is done on both quadrature and phase, which are set to $\theta = 0$ and $x = 0$ with a conditioning window of $\Delta = 0.3$. The experimental output state is then verified via homodyne detection and its reconstruction (without any loss correction) is shown in fig. 7.4 (b). In this paper the expectation value of the stabilizer S_x is measured to be $\langle S_x \rangle = 0.170$. The second stabilizer S_z is not measured and instead the Pauli gate $-Z$ is used as a stabilizer. This can be done if one aims to verify that a logical $|1\rangle_L$ state is created, which indeed is the $+1$ eigenstate of the $-Z$ operator and the S_x stabilizer. While this stabilizer pair $S_x, -Z$ can serve as a test of how close the system is to the logical $|1\rangle_L$ state, it does not indicate if the logical $|1\rangle_L$ state can be used as a qubit - for this the expectation value of S_z has to be measured. This setup is, therefore, a hybrid between a $n = 1$ and $n = 2$ GKP state space, having a qubit character for the bit-flip and a single-state behavior for the phase-flip.

We can simulate the output of this setup without losses and phase noise for simplification. Because we do not know the cat amplitude, we guess it from fig. 7.4 (a) to be $\alpha = 0.7i$. Upon perfect conditioning, we find that we can visually reproduce the results in fig. 7.5. Moreover, this state is close to an eigenstate of $-Z$ with an eigenvalue $\langle Z \rangle = -0.707$ and is intermediately stabilized by the stabilizer S_x with an expectation value $\langle S_x \rangle = 0.46$.

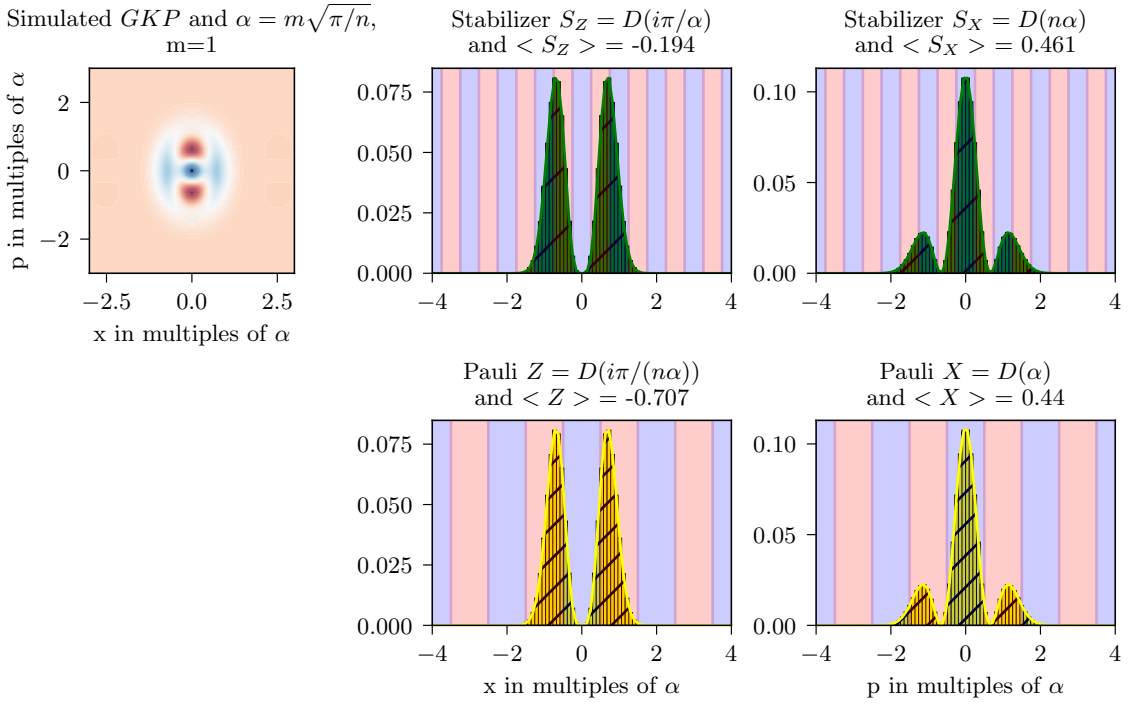

Figure 7.5: Here the simulated result of the setup used for the creation of the experimental state in the paper of S. Konno et al. [269] is shown. We set $n = 2$. Losses and phase noise were not taken into account.

Those values would reduce if our simulation would take into account phase noise and losses, such that we can consider that we have a good tool to simulate an ideal experimental case. We also note, that the input state was assumed to be a perfect odd cat state and not a single-mode photon subtracted squeezed vacuum. In the following, we want to use a different setup and simulate how an experimental state could look with this setup.

7.3 A setup to increase our non-Gaussian capability

7.3.1 Motivation: Simulations on a simplified model

The setup we are considering was proposed for the creation of four-headed cat states in 2020 by J. Hastrup et al. [270]. We adapt the setup to our experimental capabilities by exchanging photon-number resolution with homodyne conditioning, shown in fig. 7.6.
Here two even cat states of amplitude α and $\alpha e^{i\phi}$ interfere on a beamsplitter with variable reflectivity R. The variable reflectivity is equivalent to allowing for different input cat sizes. One of the two beamsplitter output modes is used to project the other mode onto a GKP state via homodyne conditioning with variable phase θ. We use a local optimization with the Python package *scipy* with the Nelder-Mead minimization algorithm to find the best settings of those parameters. In table 7.1 the free and set parameters for the simulation are shown, where the optimization is allowed on the free parameters.
Depending on the minimization function we define, two different types of states can be found. In fig. 7.7 (a), the simulated state is a rotated and slightly higher quality version of our simulation in fig. 7.5.

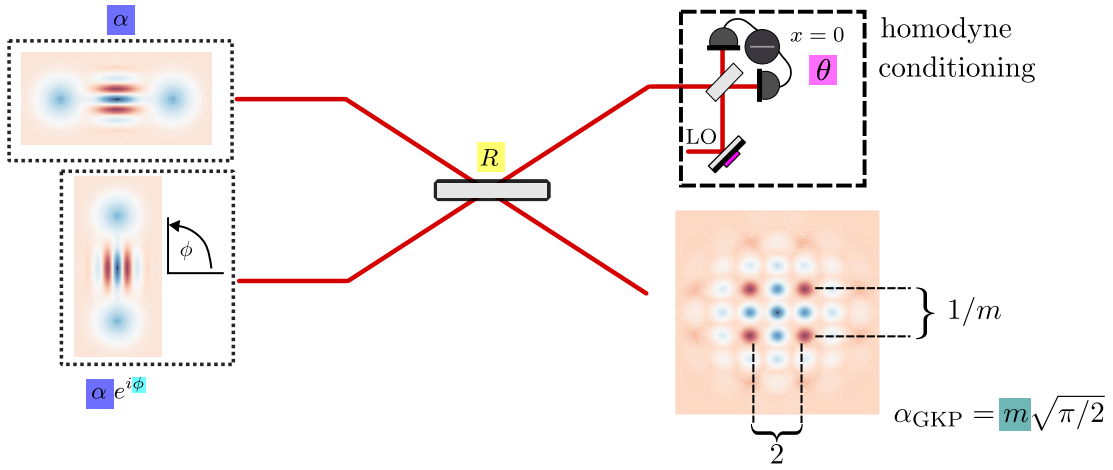

Figure 7.6: A simplification of the proposed setup is shown. Two ideal even cat states with a free relative phase ϕ between their amplitudes are interfering on a beamsplitter with reflectivity R. The homodyne conditioning on $x = 0$ and a phase θ should then project the output state on a GKP state. We show in color which parameters we optimize in our simulation: The cat amplitude α, the phase between the two cat states ϕ, the reflectivity R, the conditioning phase θ and the binning proportionality factor for the measurement of the stabilizers m.

Table 7.1: Here we show the parameters that are tunable in our simulation of the simplified setup shown in fig. 7.6. For all simulations, only pure input states are considered, such that the losses are $L = 0$. To avoid parasitic effects from a too-small density matrix size, we simulate all results for Fock excitations of up to 20 photons. The homodyne efficiency is set to one, such that an ideal projection is possible. After fixing those parameters, we run an optimization algorithm over the free parameters, which include the cat amplitude α, the relative phase between the two input cat amplitudes ϕ, the mixing ratio R on the beamsplitter, the homodyne phase θ and the GKP target spacing m.

free parameters	cat amplitude α homodyne phase θ	relative phase ϕ GKP parameter m	mixing R
set parameters	Losses $L = 0$	Fock dimension dim= 21	efficiency HD $\eta_{\text{HD}} = 1$

This state has stabilizers $S_Z, -X$ and is therefore not usable for full error correction. On the other hand, the state obtained in (b) is more interesting because it shows relatively good expectation values for both stabilizers $\langle S_z \rangle = 0.66$ and $\langle S_x \rangle = 0.68$. Unfortunately, this state has similar expectation values for both Pauli gates X and Z. This means that this approximate GKP state is not a pure state of the GKP Bloch sphere as it would need to be of the form $\sqrt{0.678}\,|1\rangle_L + \sqrt{0.631}\,|-\rangle_L$, which is not a normalized state. The same problem occurs if one wants to formulate this state as a mixed state. Therefore we can see that this state is not fully living in the GKP Bloch sphere but has support outside of this Hilbert space. We are not sure how error correction can work on a state that is only partially a GKP state, such that we have to change this simplified circuit.

From our optimization, we see that this is the closest this setup can come to an ideal GKP state, hinting at the fact that we might need other input states than even cat states.

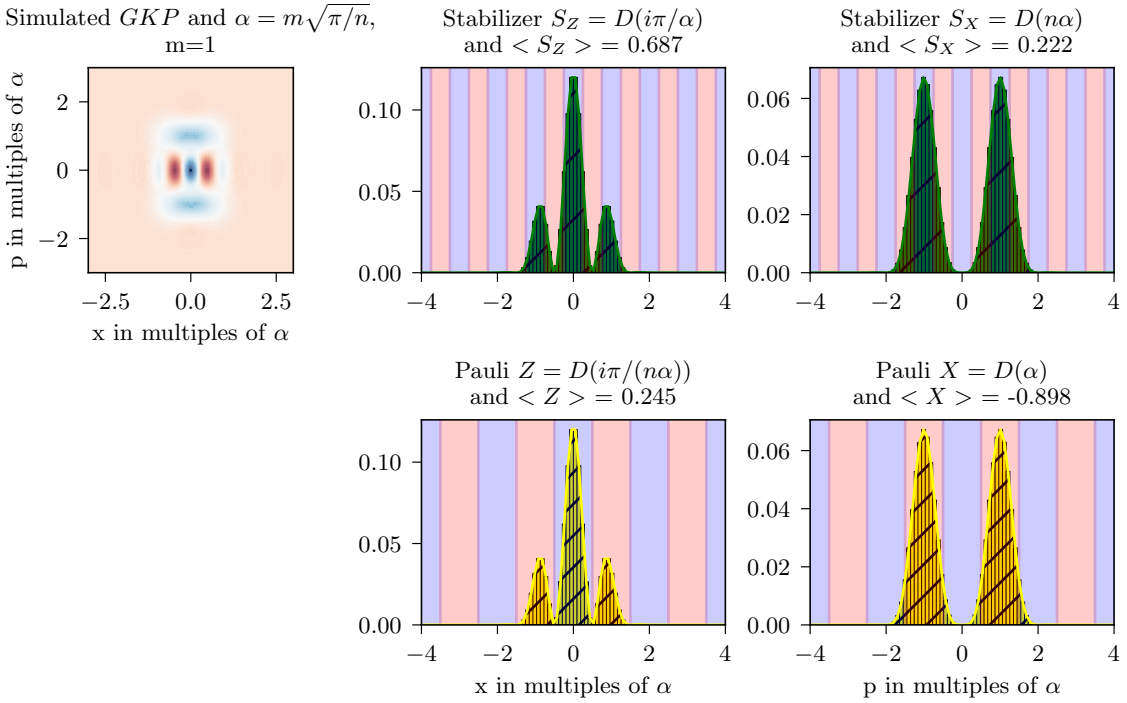

(a) Optimization no1. $\alpha = 1.4$,$\phi = 1.56$ rad, $R = 0.8$, $\theta = 0$,$m = 1$.

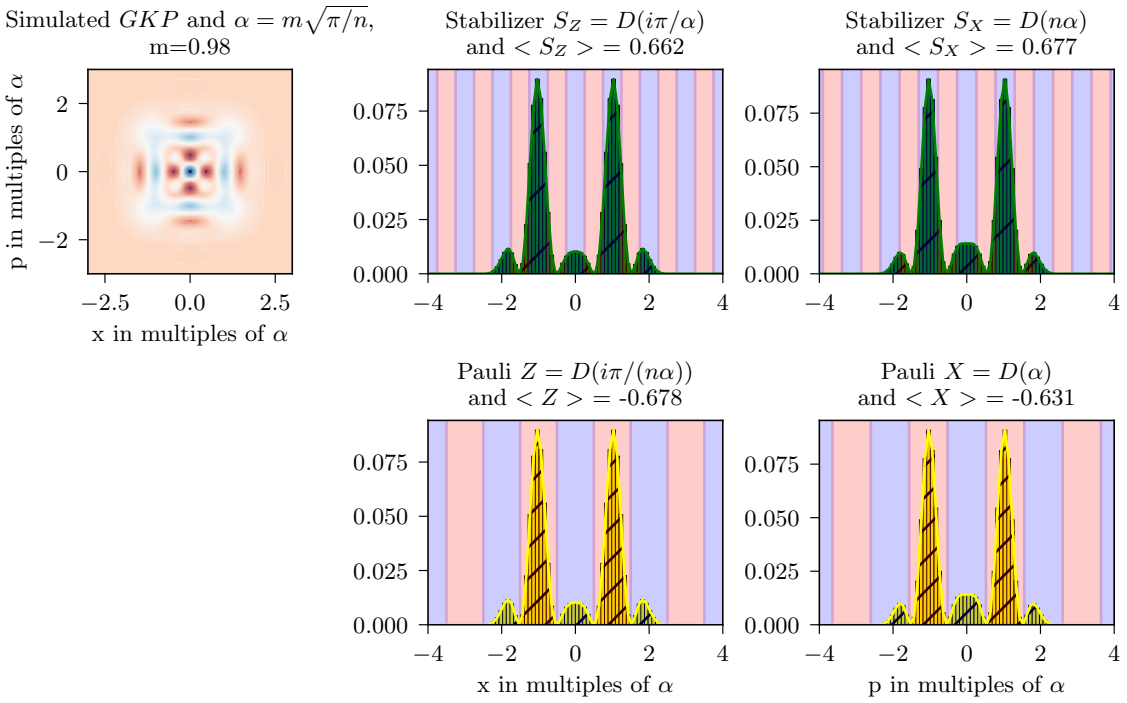

(b) Optimization no2. $\alpha = 1.83$,$\phi = \pi/2$ rad, $R = 0.47$, $\theta = 0$,$m = 0.98$.

Figure 7.7: The optimal results of the simplified setup are shown. Two cat states of amplitude α and phase-difference ϕ are interfering on a beamsplitter with reflectivity R. One mode of this beamsplitter is used for homodyne conditioning on the quadrature $x = 0$ and the phase θ. The output state after conditioning is plotted on the left of the two optimization results **(a)** and **(b)**. In (a) we see that no real grid appeared such that this state is close to a shared eigenstate of S_Z and $-X$. In (b) the state shows reasonable eigenvalues for both stabilizers S_x and S_z and is therefore closer to an ideal GKP state.

7.3.2 Modeling the GKP-creation setup

Here we take inspiration from M. Eaton, R. Nehra, and O. Pfister [271] and H. M. Vasconcelos, L. Sanz, and S. Glancy [272] who propose squeezed cat states as input states. We therefore consider an updated setup, visible in fig. 7.8. We see the main change to the previous setup in the input states of (a), which are squeezed even cat states.

The experimental setup to produce those states is shown in (b) and is equivalent to the setup for the creation of a superposition between vacuum and two-photon components in chapter 6.

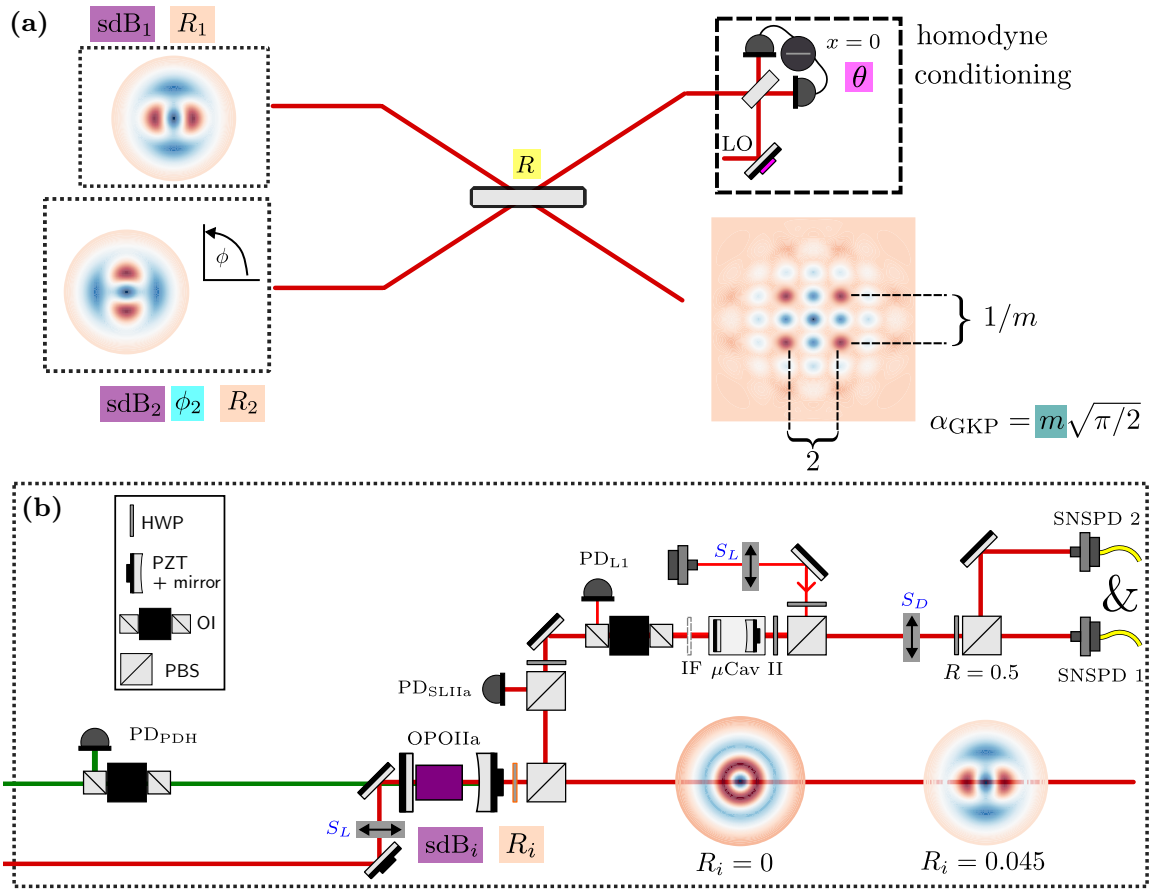

Figure 7.8: The simulation model of the experimental setup is shown. In **(a)** two squeezed even cat states interfere on a beamsplitter with mixing reflectivity R, where one path is used for homodyne conditioning of $x = 0$ at a phase θ. The state of the other beamsplitter port is then ideally projected onto a GKP state with target amplitude α_{GKP}. All free parameters in our optimization are shown in color. This includes the creation parameters of the squeezed even cat states, shown in **(b)**. Here a type-II OPO is producing two-mode squeezing of a strength sdB_i. The orthogonal signal and idler output modes are mixed via an HWP and a PBS, modeled by a tapping ratio R_i. The tapped heralding path is subsequently filtered via a micro-cavity and an interferential filter (IF) such that only a single mode can be detected on the SNSPDs. The two SNSPDs act as an imperfect two-photon projection of a photon number resolution detector. Dependent on the tapping ratio R_i a two-photon state ($R_i = 0$) can be tuned towards a squeezed cat state.

Table 7.2: Here we show the parameters that are tunable in our simulation of the experimental setup shown in fig. 7.8. We allow for an imperfect escape efficiency in both OPOs, which can be modeled by the losses L_1, L_2. To avoid parasitic effects from a too-small density matrix size we simulate all results for Fock excitations of up to 20 photons. The homodyne efficiency as well as the SNSPD efficiency are variable but are not included in the optimization. After fixing those parameters, we run an optimization algorithm over the free parameters, which include the initial OPO squeezing sdB, the relative phase between the two squeezed states ϕ_2, the tapping ratios R_1, R_2, the mixing ratio R on the beamsplitter, the homodyne phase θ and the GKP target spacing m.

free parameters	squeezing $\text{sdB}_1 = \text{sdB}_2$ mixing R	2x tapping ratio R_i homodyne phase θ	relative phase ϕ_2 GKP parameter m
set parameters	Losses L_1, L_2 efficiency η_{HD}	Fock dimension: 21	efficiency η_{SNSPD}

Turning the HWP after the OPO corresponds to a tapping ratio R_i, which mixes the signal and idler polarizations, thereby creating coherences. The output states range from a two-photon state for $R_i = 0$ to a squeezed even cat state with amplitudes between $\alpha = 1.3 - 1.7$ and a squeezing ranging from 3-4 dB. Experimental results of those states, having been created with the current OPOIIa, have been published by K. Huang et al. [32]. There, a fidelity of maximally 68% with the ideal squeezed cat state was measured. In our simulations, we want to create two of those squeezed cat states with a variable phase between their amplitudes. We account for the imperfect escape efficiency of the OPO by allowing for losses L_i. The two SNSPDs are each modeled to have an efficiency η_{SNSPD}. In fig. 7.8 (a), the free parameters of the simulation are visible.

The before-mentioned two-mode-squeezing strength sdB_i and tapping ratio R_i as well as the relative phase between the two cat amplitudes ϕ_2 are optimized together with the mixing reflectivity R, the homodyne phase θ and the targeted GKP amplitude via the parameter m. The parameters of the simulation are given in table 7.2. Here, we use the same optimization algorithm as in the previous subsection but due to the increased complexity, the optimization result is sub-optimal, such that we fine-tune it by hand. We note, that allowing for different squeezings sdB_1 and sdB_2 is equivalent to changing the mixing reflectivity R, such that we can reduce the parameter space by setting $\text{sdB}_1 = \text{sdB}_2$. We optimize the parameters first for the lossless case and then apply realistic losses $L_1 = L_2 = 0.1$, reduce the homodyne efficiency to $\eta_{HD} = 0.85$ and each SNSPD efficiency to $\eta_{\text{SNSPD}} = 0.5$.

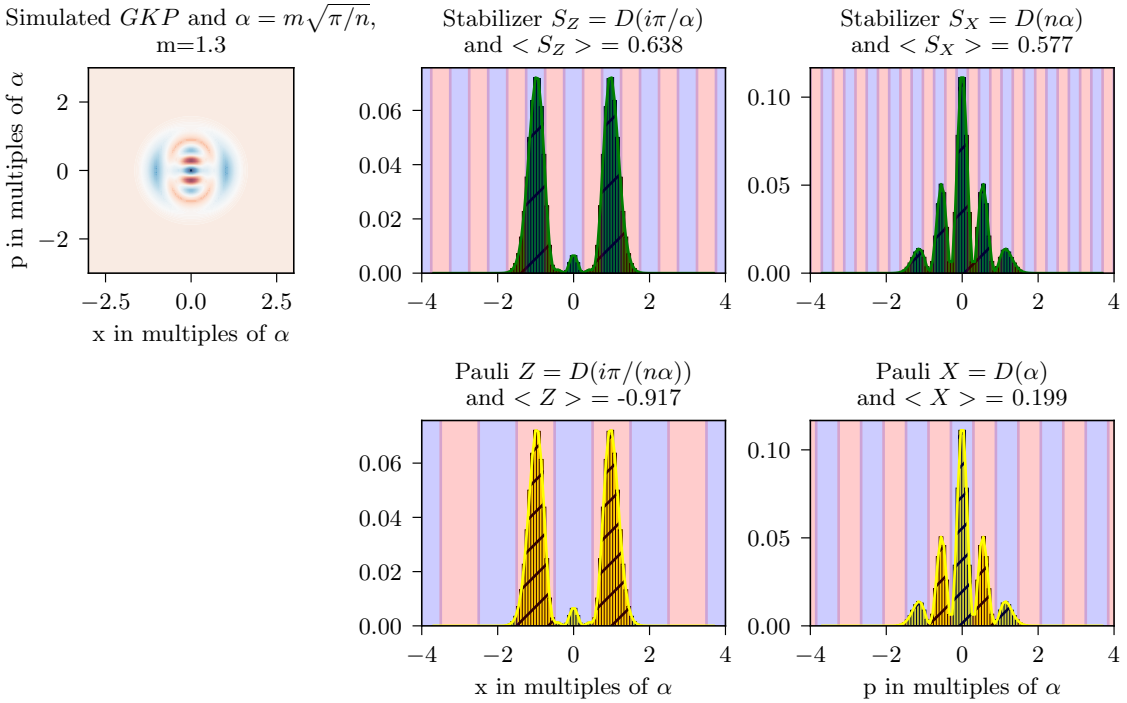

(a) Optimization no1: sdB=2.2, $R_1 = 0.05$, $R_2 = 0.05$, $\phi_2 = \pi/2$, $R = 0.3$, $\theta = \pi/2$, $m = 1.3$. With $L_1 = L_2 = 0$, $\eta_{\text{HD}} = 1$, $\eta_{\text{SNSPD}} = 1$

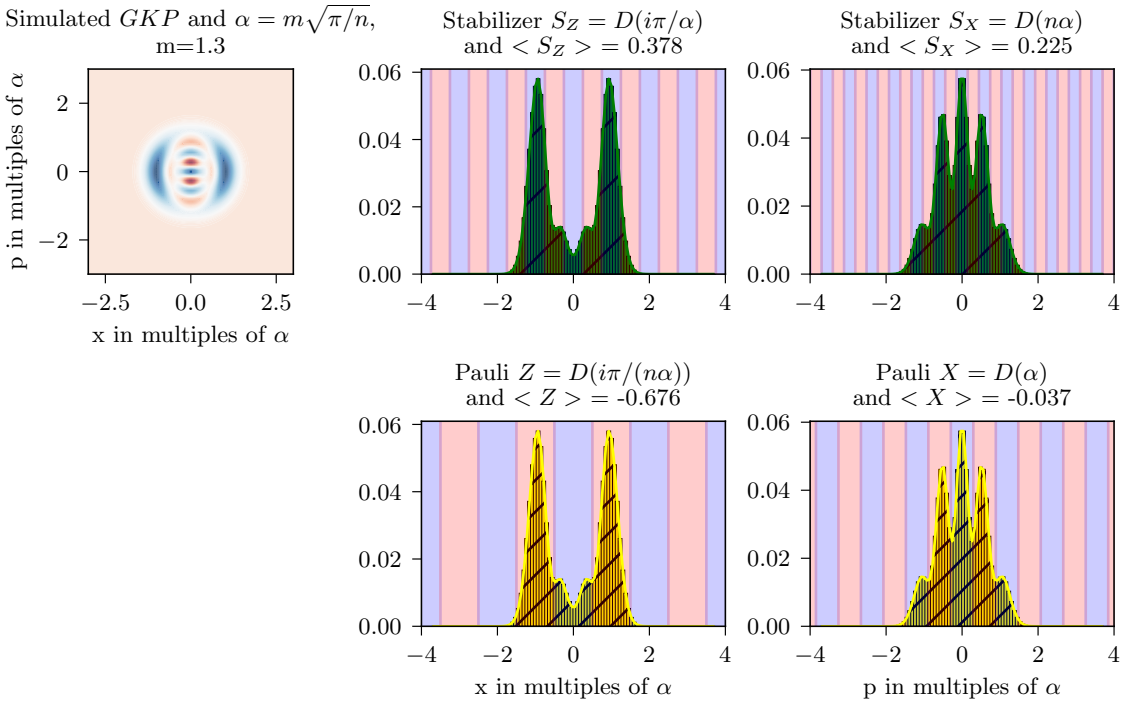

(b) Optimization no1: sdB=2.2, $R_1 = 0.05$, $R_2 = 0.05$, $\phi_2 = \pi/2$, $R = 0.3$, $\theta = \pi/2$, $m = 1.3$. With $L_1 = L_2 = 0.1$, $\eta_{\text{HD}} = 0.85$, $\eta_{\text{SNSPD}} = 0.5$

Figure 7.9: An optimized outcome of the simulated experimental setup is shown without losses in **(a)** and with losses in **(b)**. The outcome was optimized for the case without losses and left unchanged when losses were applied. This state approximates the logical $|1\rangle_L$ GKP state, visible in the Pauli Z expectation value $\langle Z \rangle = -0.917$ in (a) but still has some unwanted non-zero expectation value in the Pauli X operation.

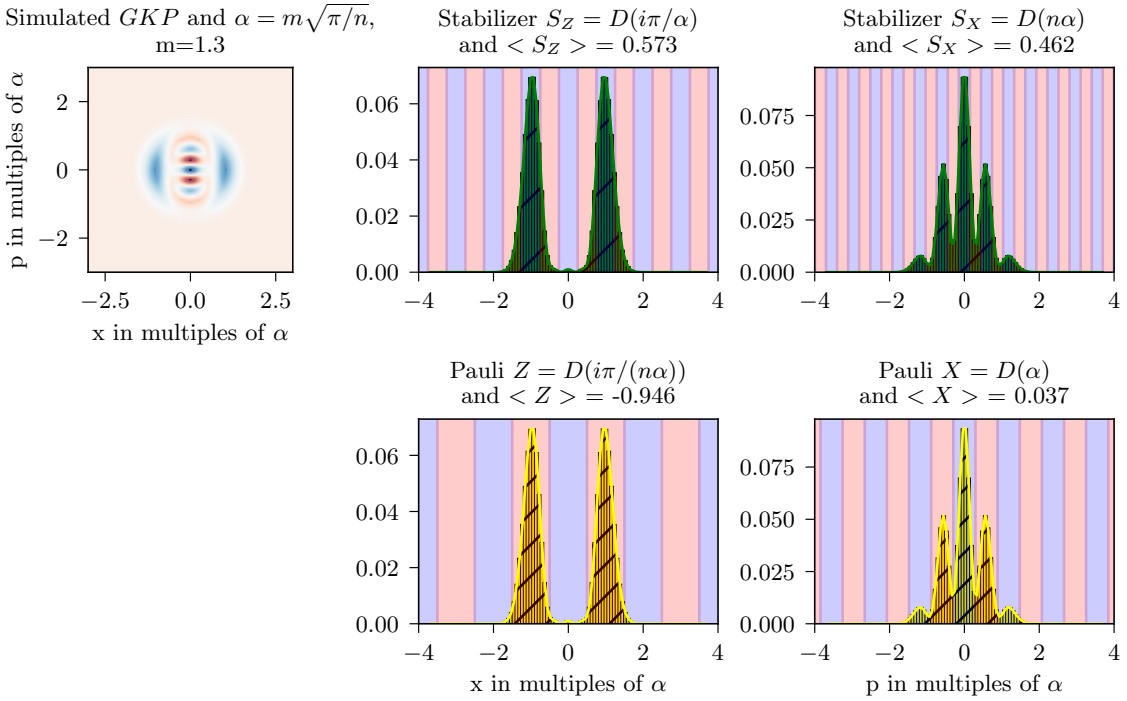

(a) Optimization no2: sdB=4.0, $R_1 = 0.05$, $R_2 = 0.1$, $\phi_2 = \pi/2$, $R = 0.3$, $\theta = \pi/2$, $m = 1.3$. With $L_1 = L_2 = 0$, $\eta_{\text{HD}} = 1$, $\eta_{\text{SNSPD}} = 1$

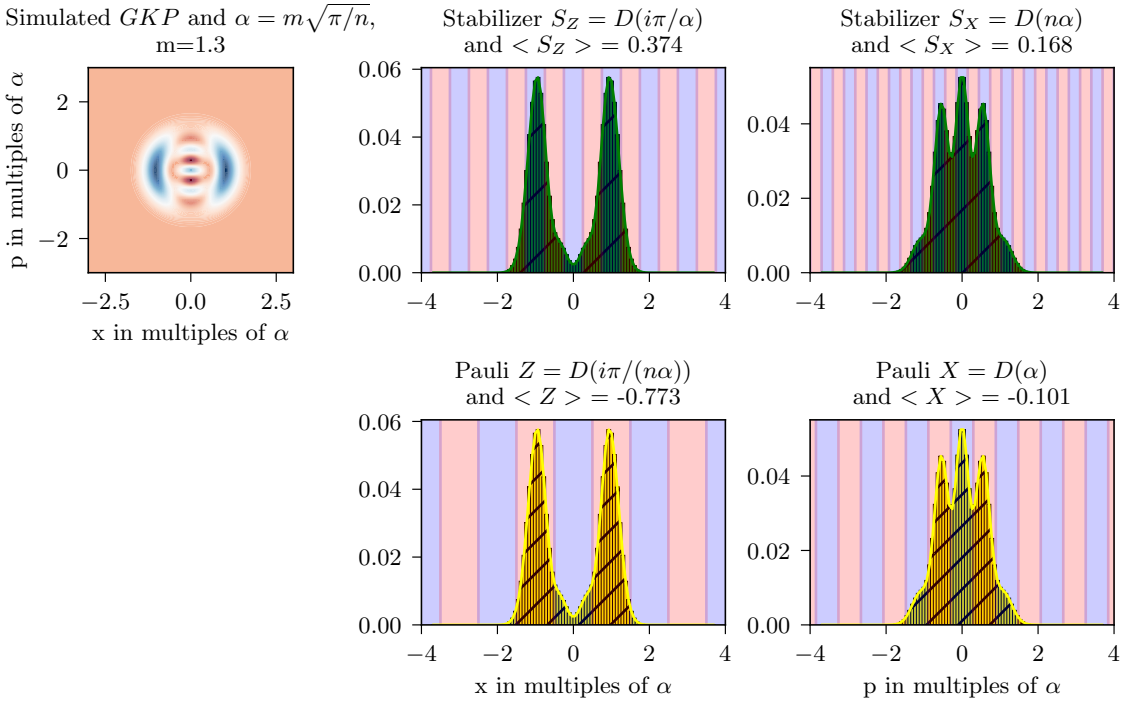

(b) Optimization no2: sdB=4.0, $R_1 = 0.05$, $R_2 = 0.1$, $\phi_2 = \pi/2$, $R = 0.3$, $\theta = \pi/2$, $m = 1.3$. With $L_1 = L_2 = 0.1$, $\eta_{\text{HD}} = 0.85$, $\eta_{\text{SNSPD}} = 0.5$

Figure 7.10: An alternative optimized outcome of the simulated experimental setup is shown without losses in **(a)** and with losses in **(b)**. The outcome was optimized for the case without losses and left unchanged when losses were applied. This state approximates the logical $|1\rangle_L$ GKP state, visible in the Pauli Z expectation value $\langle Z\rangle = -0.946$ in (a).

We present two different optimization results in figures 7.9 and 7.10. In both cases, the states were optimized on the lossless case such that applying losses can quantify how much they worsen our states. In both lossless cases (fig. 7.9 (a) and fig.7.10 (a)), we achieve reasonable expectation values for the stabilizers. They differ in their Pauli X and Z eigenvalues, which should ideally add up to unity in absolute values, such that the full state can be described by the logical GKP state space. We see in fig. 7.9 (a), that this is not the case, such that a small part of the state will be defined outside the logical basis. By allowing for slightly lower stabilizer expectation values in fig. 7.10 (a), we can create a state that is fully described by the GKP Bloch sphere.
Applying losses to both cases leaves those characteristics unchanged, but reduces the absolute value of both stabilizer and Pauli expectation values. Surprisingly, even realistic experimental loss in detection and state creation leaves an important part of the peak structure intact.

Before attempting its experimental realization, this simulation has to be extended. Especially the effect of phase noise on the homodyne measurement and the phase ϕ_2 have to be considered. Moreover, here we have assumed a perfect coincidence window of the two SNSPD heralding events for the creation of the squeezed cat states. Nonzero coincidence windows have to be taken into account as they will add loss to the system. Finally, a finite conditioning window and phase-noise on the homodyne phase lock of θ have to be taken into account. Those final simulations should be optimized for the realistic, not the ideal system, such that a potent optimization algorithm has to be used.

7.3.3 Modelling a binomial code state

The setup we presented in fig. 7.8 can be used to create a binomial logical code state $|0\rangle_L$ of the first order (see Bosonic rotation codes), which is almost equivalent to a four-headed cat state of low amplitude. Those two states can be written as

$$\text{Binomial code:} \qquad |0\rangle_L = \frac{1}{\sqrt{2}}(|0\rangle + |4\rangle), \tag{7.10}$$

$$\text{4-headed cat code:} \qquad |0\rangle_L \propto |\alpha\rangle + |-\alpha\rangle + |i\alpha\rangle + |-i\alpha\rangle\,. \tag{7.11}$$

In fig. 7.11 we can see the ideal four-headed cat state of amplitude $\alpha = 1.5$ in (a). It closely resembles the logical zero binomial state in (b) and those two states show a fidelity overlap of 99.2%. We can simulate how faithfully our experimental model can produce such a state, visible in (c) for no losses, and find an overlap of 98% with either of the ideal states. We can now allow for the same losses as in the GKP consideration, such that $L_1 = L_2 = 0.1$, $\eta_{\text{HD}} = 0.85$ and $\eta_{\text{SNSPD}} = 0.5$. To adapt for those losses, we can slightly increase the squeezing and find that we can maintain an overlap of 62% with both target states. Here we can adapt the losses in the simulation to our experimental parameters of $L_1 = 0.15$ and

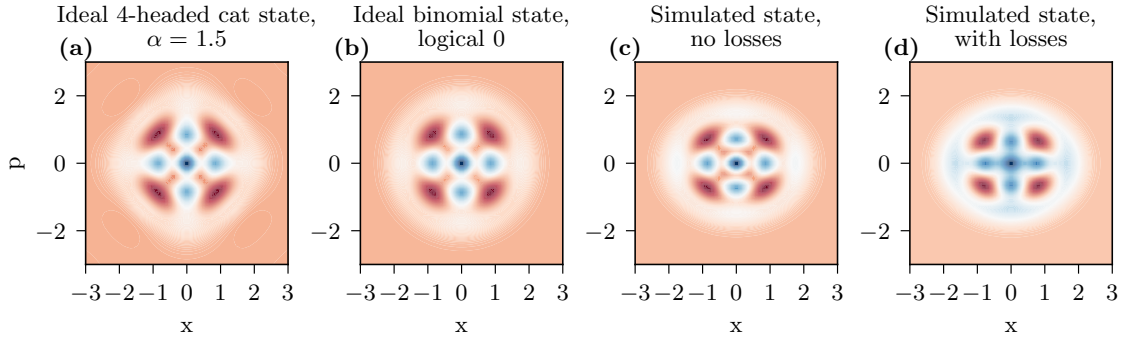

Figure 7.11: In **(a)** the ideal four-headed cat state with an amplitude of $\alpha = 1.5$ is shown. This state has an overlap of 99.2% with the logical zero binomial code state, shown in **(b)**. For no losses and perfect detection efficiencies we can recreate (a) and (b) with an overlap of 98% by using the parameters sdB= 0.2, $R_1 = 0.014$, $R_2 = 0.004$, $\phi_2 = \pi/2$, $R = 0.2$ and $\theta = \pi/2$, visible in **(c)**. For losses of $L_1 = L_2 = 0.1$, $\eta_{\text{HD}} = 0.85$ and $\eta_{\text{SNSPD}} = 0.5$ we can reproduce a 62% overlap with the ideal state by increasing the squeezing to sdB= 0.4.

$L_2 = 0.26$ and optimize the fidelity overlap between the binomial state and the simulated state. The result of this optimization is shown in fig. 7.12. If we enforce the experimental parameters $\eta_{\text{HD}} = 0.85$, $\eta_{\text{SNSPD}} = 0.5$, $L_1 = 0.15$ and $L_2 = 0.26$ we can still achieve an overlap of 53% of the resulting state with the ideal binomial state. However, reducing the amplitude of the four-headed cat state to $\alpha = 1.2$ enables an overlap of 60% between the simulated and ideal state.

We can therefore see the creation of an approximate binomial code or four-legged cat state as a valuable first step towards the creation of a GKP state and can consider using our

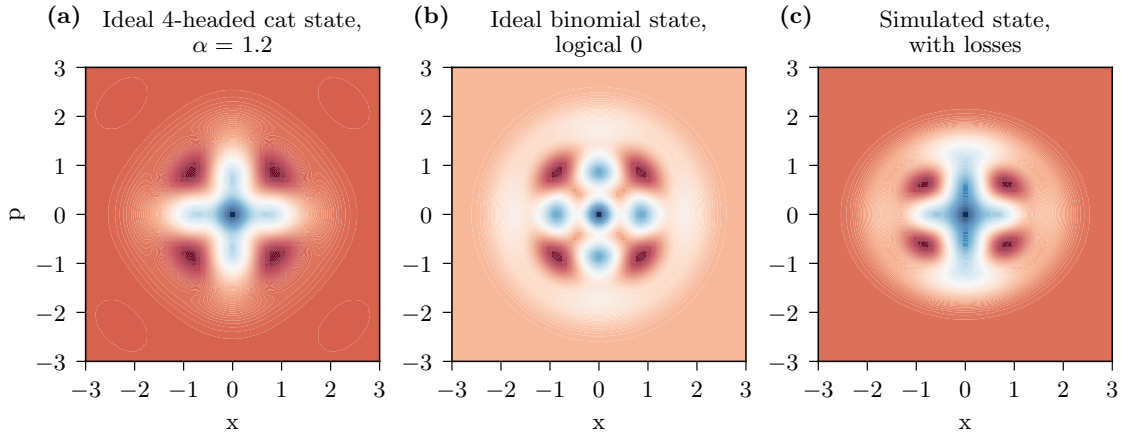

Figure 7.12: In **(a)** the ideal four-headed cat state with an amplitude of $\alpha = 1.2$ is shown. This state has an overlap of 75.1% with the logical zero binomial code state, shown in **(b)**. For our experimental losses of $L_1 = 0.15$,$L_2 = 0.26$, $\eta_{\text{HD}} = 0.85$ and $\eta_{\text{SNSPD}} = 0.5$ we can reproduce a 53% overlap with the ideal binomial state and a 60% overlap with the ideal four-legged cat stat. The parameters are set to: sdB= 0.2, $R_1 = 0.008$, $R_2 = 0$, $\phi_2 = \pi/2$, $R = 0.324$ and $\theta = \pi/2$.

current resources. As for GKP states, improving the losses in our system would benefit the state quality greatly. In the next section, we will discuss possible improvements in the system that can reduce the losses.

7.4 Experimental GKP feasibility

The proposed setup in fig. 7.8 includes two OPOII sources, four SNSPD detectors, and two homodyne detectors. Those resources are readily available in the lab. The current losses in our system, equivalent to the inefficiency due to the escape efficiency $1-\eta$, are $L_1 = 0.15$ for OPOIIa and $L_2 = 0.26$ for OPOIIb. One OPO, together with two SNSPDs will be used to create squeezed even cat states. Those cat states have already been created for OPOIIa in our lab [32]. This resource state is needed two times, resulting in the full use of all available SNSPDs in our setup. Moreover, a coincidence window has to be set between those four SNSPD detection events, which should result in a single trigger pulse to record the homodyne conditioning trace and the homodyne measurement that will analyze the output state. This four-fold coincidence can be programmed on the coincidence detector *IDQuantique ID900*, which we already used in chapter 5 and which has four input possibilities. Moreover, one new phase lock has to be added. The homodyne conditioning phase cannot be allowed to scan, but has to be locked, which was already demonstrated in our setup in 2018 [35]. Additionally, we need to be able to control the relative phase ϕ between the two OPOs, which is equivalent to locking the relative phase between the two pump beams. Luckily the two pump beams have a constant relative phase relation because they are coming from the same laser beam. Consequently, we can use a beamsplitter with a relative phase between reflected and transmitted output of $\pi/2$ [177, 273]. This does not give us any flexibility in the phase or the reflectivity, but all our simulations so far suggested, that the phase is ideal at $\pi/2$. As far as we see, all possible setups with a flexible reflectivity would involve a polarizing beam-splitter. Because we need the two input beams impinging on the beamsplitter to interfere, and interference is only possible if the beams have the same polarization, we would effectively add losses with this kind of setup, which is why we do not consider it.

If we install one additional phase lock on the homodyne we could use the components on our experimental optical table today to try and create four-legged cat states. To attempt GKP states, the losses created inside the OPOs have to be reduced. As mentioned above, the current losses are measured to be $L_1 = 0.15$ for OPOIIa and $L_2 = 0.26$ for OPOIIb, with an output coupler transmission of $T = 0.1$ for both. The efficiency of the output state can then be calculated via the escape efficiency of the OPO $\eta = T/(T+L)$. We can therefore increase the output coupler transmission T to reduce the effective losses, but at the price of increasing the bandwidth of the output state, calculated with eq. (3.39). In a first step, we can use an output coupler with transmission $T' = 0.15$, which we already

have in stock. This would reduce the losses to $L_1^{'} = 0.11$ and $L_2^{'} = 0.19$ and lead to an OPO bandwidth of 90-94 MHz. Given our analysis in subsection 3.1.4, we expect that this mismatch between the OPO and homodyne bandwidth reduces the homodyne detection efficiency by maximally 1%. The micro-cavities, which were built to be 4-5 times wider than the OPO bandwidth could also support this change. We do however expect that the count rate will be an important factor, given that we can expect an overall lower count rate than in chapter 5, below the Hz level. As such a possible improvement could be to buy commercial etalon fabry-perot cavities for the filtering on the heralding path[1] that have higher transmission performances and would allow for higher count rates. Moreover, we can also re-consider changing the homodyne circuit, not to increase its bandwidth, but to increase its clearance at low frequencies of up to 20-30 MHz, as our analysis in chapter 3 has identified this range to be the most crucial to improve the homodyne efficiency.

[1] For example from *LightMachinery*

7.5 Conclusion and key results

In this chapter, we discussed a possible experimental setup, that can enable us to create GKP, binomial, or four-legged cat states. It includes the creation of two squeezed even cat states with an OPOII and two SNSPDs each. Those states with a phase difference of $\pi/2$, are then impinging on a beamsplitter with reflectivity R. One beamsplitter output is used for homodyne conditioning, such the other beamsplitter output is projected onto the target state. The main results are:

- Our simulations of the proposed setup, including losses and detector imperfections, suggest that we can create a four-legged cat state of 60% fidelity with an ideal state of amplitude $\alpha = 1.2$ with our current experimental capabilities.
- For this, one additional phase lock needs to be installed, controlling the phase of the homodyne conditioning.
- An increased fidelity four-legged cat state, binomial state as well as GKP states are within reach of our current experiment, if we choose to exchange the output coupler of both OPOs, thereby increasing their escape efficiency.

The next steps on the experiment and in terms of simulations are identified to be

- We want to exchange the OPO output couplers. Currently, we have output couplers with a transmission of $T = 0.15$ in stock in the lab.
- Other proposed improvements include the reduction of losses on the homodyne detection by a new circuit design that focuses on higher clearance at frequencies up to 20-30 MHz. The count rate of the experiment could also be improved by reducing the losses on the heralding path via commercially available filtering cavities.
- The simulation will be made more complete, to include phase noise on the OPO lock, the four-fold-coincidence window, and the conditioning window.
- We want to develop an optimization, that tolerates small deviations from the parameters, such that the output change is robust to experimental imperfections.

Chapter 8

Appendix

Contents

8.1 Hermite polynomials

The Hermite polynomials used in this work are defined as (physicist's version)

$$\begin{aligned} H_{n+1}(x) &= 2xH_n(x) - 2nH_{n-1}(x), \\ H_0(x) &= 1, \\ H_1(x) &= 2x, \\ H_2(x) &= 4x^2 - 2. \end{aligned} \tag{8.1}$$

8.2 Measuring cavity parameters

Here we give the formulas in order to measure the length L, free spectral range FSR and bandwidth $\Delta\nu$ of a cavity. For this we slightly misalign the beam onto the cavity, such that we see at least one higher order mode TEM_{nm} (mostly TEM_{01}) appear. While sweeping the cavity two successive FSR should appear within the same sweep, labeled I and II. The center of the peak is called c^j_{nm}, where j is either I or II. The radius of curvature of the mirror (ROC) is assumed to be know. The length and finesse of the cavity can then be calculated as

$$L = \mathrm{ROC}(1 - \cos^2(\pi \frac{c^I_{01} - c^I_{00}}{c^{II}_{00} - c^I_{00}})), \tag{8.2}$$

$$F = \frac{1}{2}\left(\frac{c^I_{00}}{w^I_{00}} + \frac{c^{II}_{00}}{w^{II}_{00}}\right), \tag{8.3}$$

where w is the FWHM of the targeted peak. The calculated length will be the length of the cavity for one round trip, meaning $2L$ in the case of a Fabry-Perot cavity. Calculating the FSR from the length enables an easy calculation of the bandwidth.

8.3 Optimization algorithm for non-Gaussian coherences

Here we draft the combinations of optimization algorithms that were used to calculate the non-Gaussian coherence thresholds. For this the package *scipy.optimize* was used. The squeezing and displacement function are defined first:

```
from scipy.linalg import expm
from sympy.physics.quantum.dagger import Dagger
import numpy as np

def a(dim):
    #annihilation matrix
    return np.diag([np.sqrt(i+1) for i in range(0,dim)],1)


def Displacement(dim,alpha):
    #Displacement matrix
    aM = a(dim-1)
    D = expm(alpha * Dagger(aM) - np.conjugate(alpha) * aM)
    return D

def SqM(sdB,ph,dim):
    #squeezing matrix
    dim = dim-1
    z = np.log(10)/20*sdB*np.exp(1j*ph)
    M = np.conjugate(z)/2*np.matmul(a(dim),a(dim))-
        z/2*np.matmul(qs.Dagger(a(dim)),qs.Dagger(a(dim)))
    return expm(M)
```

We can then define the function to minimize, here shown for the non-Gaussian coherences between $|n_1\rangle$ and $|n_2\rangle$:

```
def FockKet(Fock,Sum):
    vec = np.zeros(Sum)
    vec[Fock] = 1
    return vec

def CN1N2(params,N1,N2,VecFocks,dim):
    '''
    Calculates the effect of Gaussian dynamics on a Fock superposition defined via
        VecFocks for the rho element N1N2
    params --> alphaR,sdB,phasesdB,input weights of VecFocks the code varies
    N1,N2 --> Superposition you are targeting
    VecFocks --> vector with Fock states of interest, for example
        np.array([0,1,2]) optimizes over the weights of the superposition 0+1+2
```

```
    dim --> Fock state maximal dimension
    '''
    alphaR, sdB, ph = params[:3]
    ketin = params[3:]

    if len(ketin) != len(VecFocks)-1:
        print("Difference in defined fock space, please review ketin and VecFocks")
        return
    vec_in = np.zeros(dim)
    for i in range(0,len(ketin)):
        vec_in += ketin[i]*FockKet(VecFocks[i],dim)
    if len(ketin) == 0:
        vec_in = FockKet(VecFocks[-1],dim)
    else:
        vec_in +=np.sqrt(1-np.sum(np.array(ketin)**2))
        *FockKet(VecFocks[len(VecFocks)-1],dim)
    Donket = np.matmul(SqM(sdB,ph,dim),np.matmul(Displacement(dim,alphaR),vec_in))
    return np.round(2*abs(Donket[N1]*Donket[N2]),7)

def CN1N2_min(params,N1,N2,VecFocks,dim):
    #function to minimize
    return (1-CN1N2(params,N1,N2,VecFocks,dim))**2
```

We can now finally write the optimization function

```
from scipy.optimize import minimize, basinhopping

def GiveAbsoluteNonGThreshold_bound(N1,N2,VecFocks,dim):
    #initial parameters
    aR_init = 0
    sdb_init = 0
    ph_init = 0
    ketin_init = [0]*(len(VecFocks)-1)
    param_init = [aR_init,sdb_init,ph_init,ketin_init]
    param_init = flatten_list(param_init)
    #blounds
    bnds = [(-5, 5), (0, 10), (0,2*np.pi)]
    bnds.extend([(0, 1)] * (len(VecFocks)-1))

    result0 = basinhopping(CN1N2_min,param_init,niter= 300,niter_success=20,
        T=5.0, stepsize=1,minimizer_kwargs={'args' :
        (N1,N2,VecFocks,dim),"method": "Nelder-Mead","bounds":bnds})
    fitted_params0 = result0.x
    C = CN1N2(fitted_params0,N1,N2,VecFocks,dim)
```

```
    print("Normalization VecFocks", np.sum(fitted_params0[3:]**2))
    return C, fitted_params0
```

Here we try all possible basis states by hand, by changing the input "VecFocks". We choose dimension 20 for our simulations. Here a typical function call is shown

```
GiveAbsoluteNonGThreshold_bound(0,4,np.array([0,1,2,3]),20)
```

where we output the threshold for the target state $\propto |0\rangle + |1\rangle$, given the basis state $c_0 |0\rangle + c_1 |1\rangle + c_2 |2\rangle + c_3 |3\rangle$. Each run takes maximally half a minute with those settings.
We note, that the above optimization is somehow a "brute-force" optimization. Especially for higher dimensional target states it might take too long to be practical. For this we envision the use of a more elegant optimization, for example with the package *SMT*, which has a potent optimization algorithm [274, 275].

8.4 Supporting GKP figures

Here additional plots of chapter 7 are to be found. The ideal GKP states are plotted in fig. 8.1 for the rectangular GKP state and in fig. 8.2 for the hexagonal GKP state. The physical ideal GKP states are plotted in fig. 8.3 for the rectangular GKP state and in fig. 8.4 for the hexagonal GKP state.

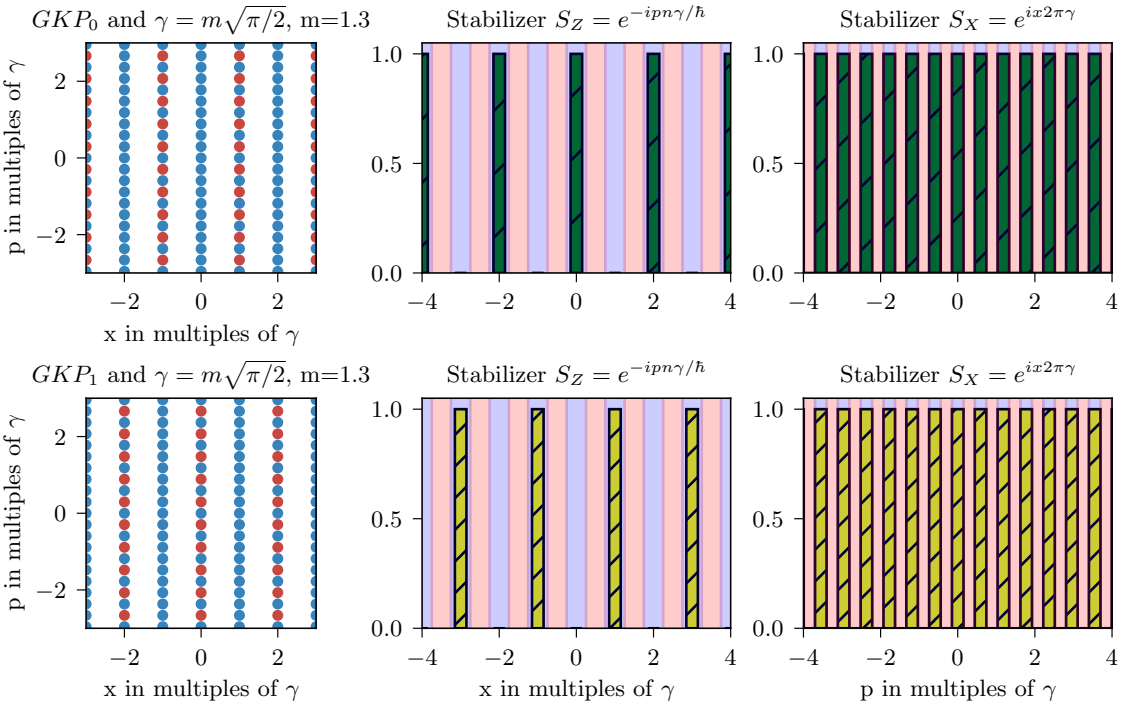

(a) Stabilizers on the GKP logical basis

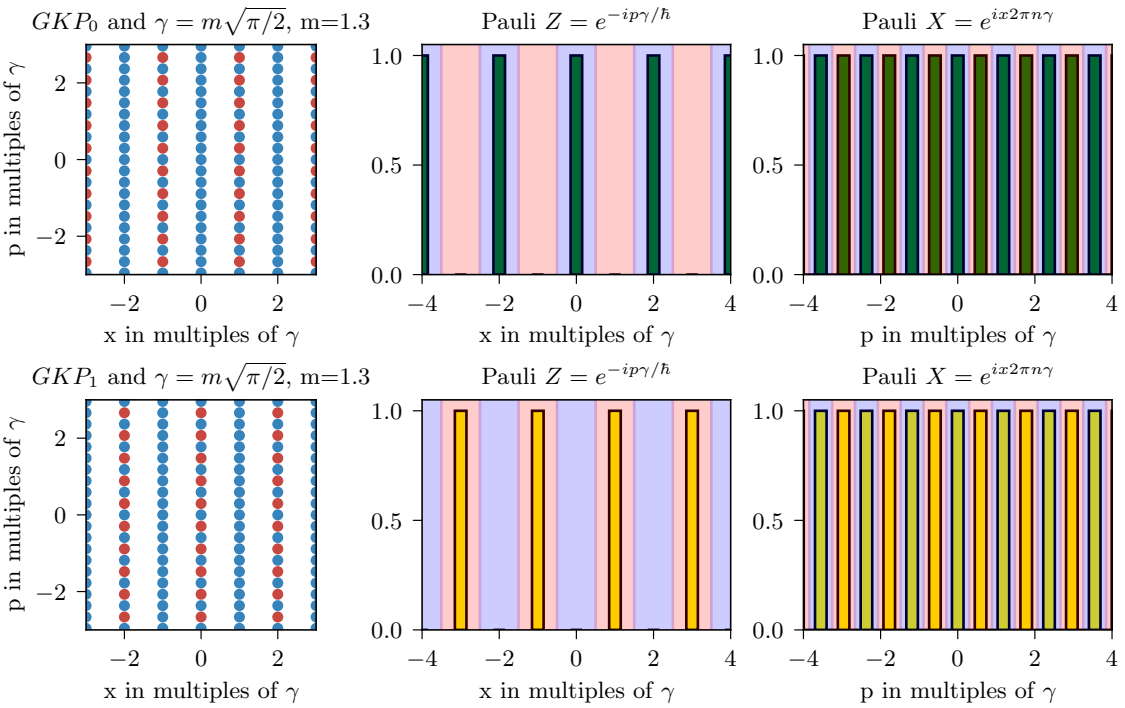

(b) Pauli gates on the GKP logical basis

Figure 8.1: The ideal rectangular GKP state with $\lambda = 1.3$ is plotted in multiples of γ for $n = 2$ and $\hbar = 0.5$ for the logical $|0\rangle_L$ and $|1\rangle_L$ state. It is an eigenvector of both stabilizers with eigenvalue $+1$, visible as all peaks of the marginal position and momentum distribution lie in the blue area in **(a)**, representing an eigenvalue of $+1$. We can see that the logical states are eigenvectors of the Pauli Z gate, with eigenvalues $+1$ and -1 in **(b)**, where the red bins represent -1.

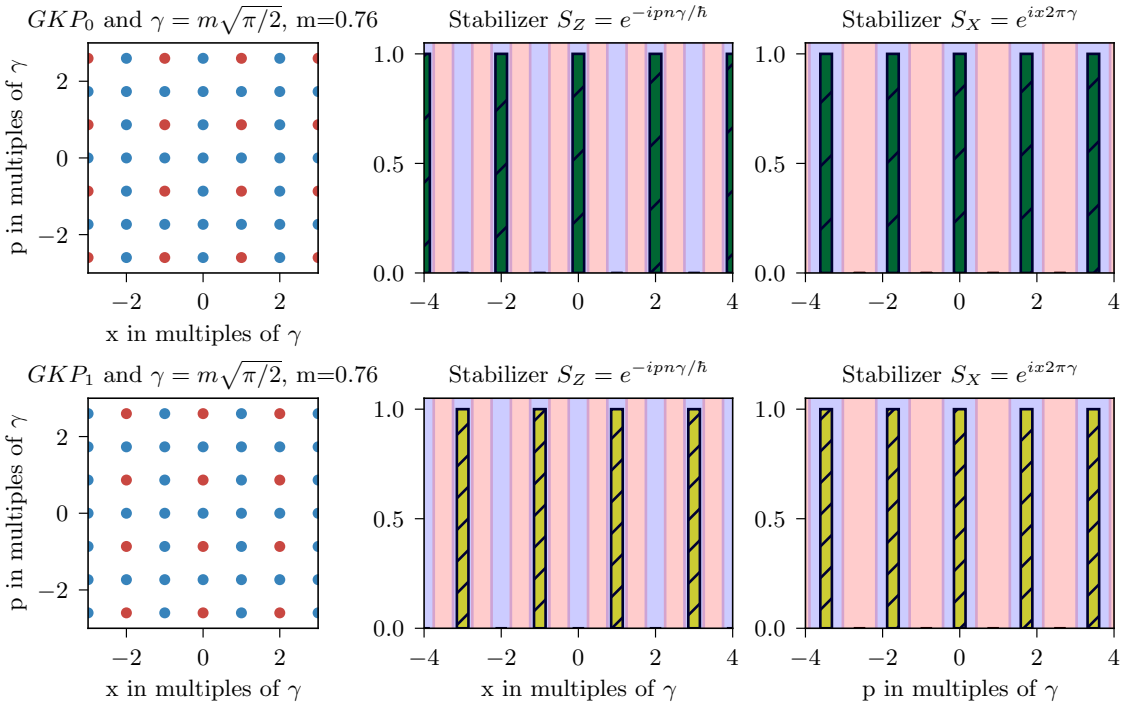

(a) Stabilizers on the GKP logical basis

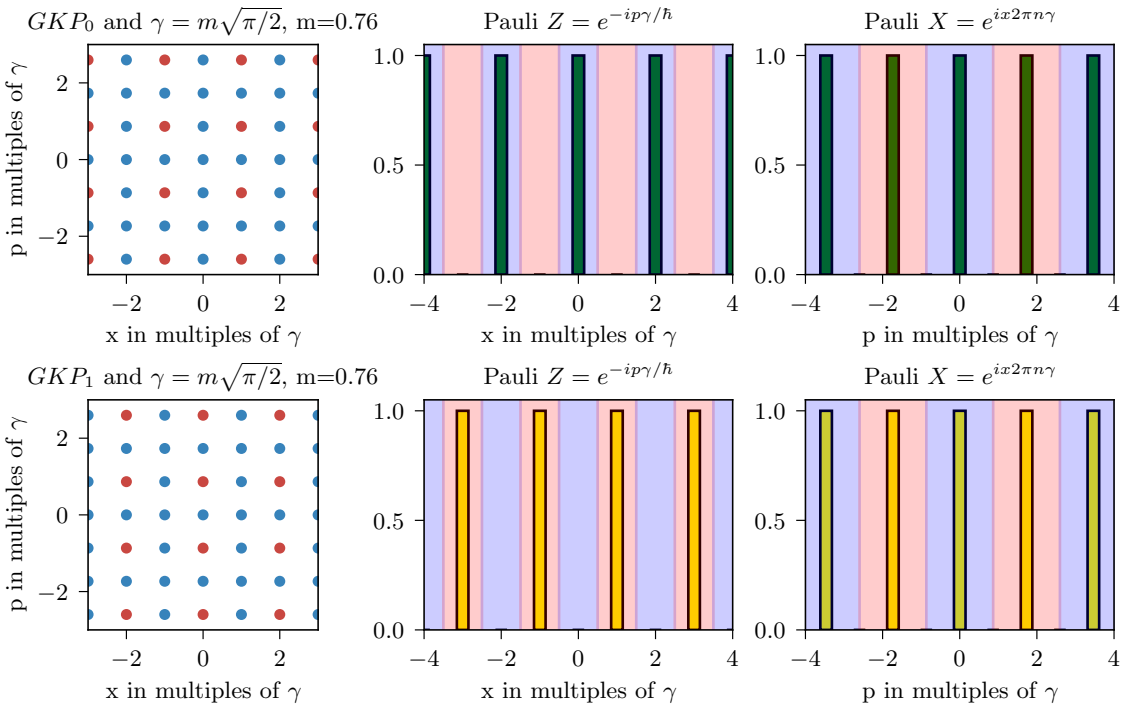

(b) Pauli gates on the GKP logical basis

Figure 8.2: The ideal hexagonal GKP state is plotted in multiples of γ for $n = 2$ and $\hbar = 0.5$ for the logical $|0\rangle_L$ and $|1\rangle_L$ state. It is an eigenvector of both stabilizers with eigenvalue $+1$, visible as all peaks of the marginal position and momentum distribution lie in the blue area in **(a)**, representing an eigenvalue of $+1$. We can see that the logical states are eigenvectors of the Pauli Z gate, with eigenvalues $+1$ and -1 in **(b)**, where the red bins represent -1.

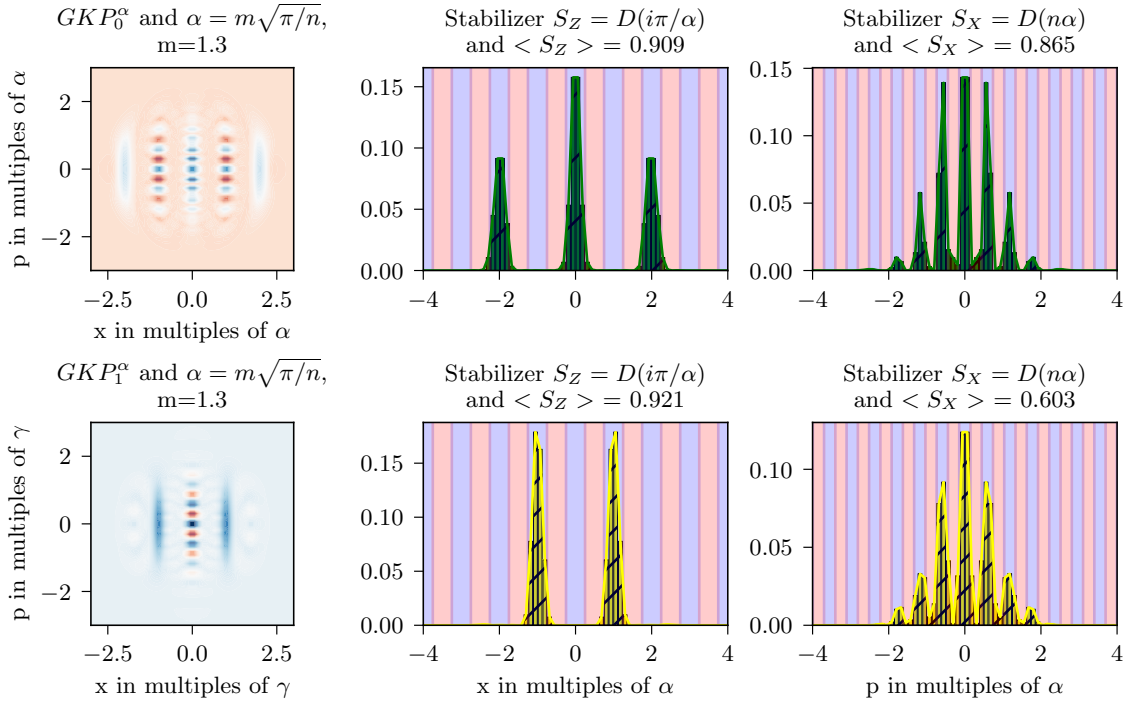

(a) Stabilizers on the GKP logical basis

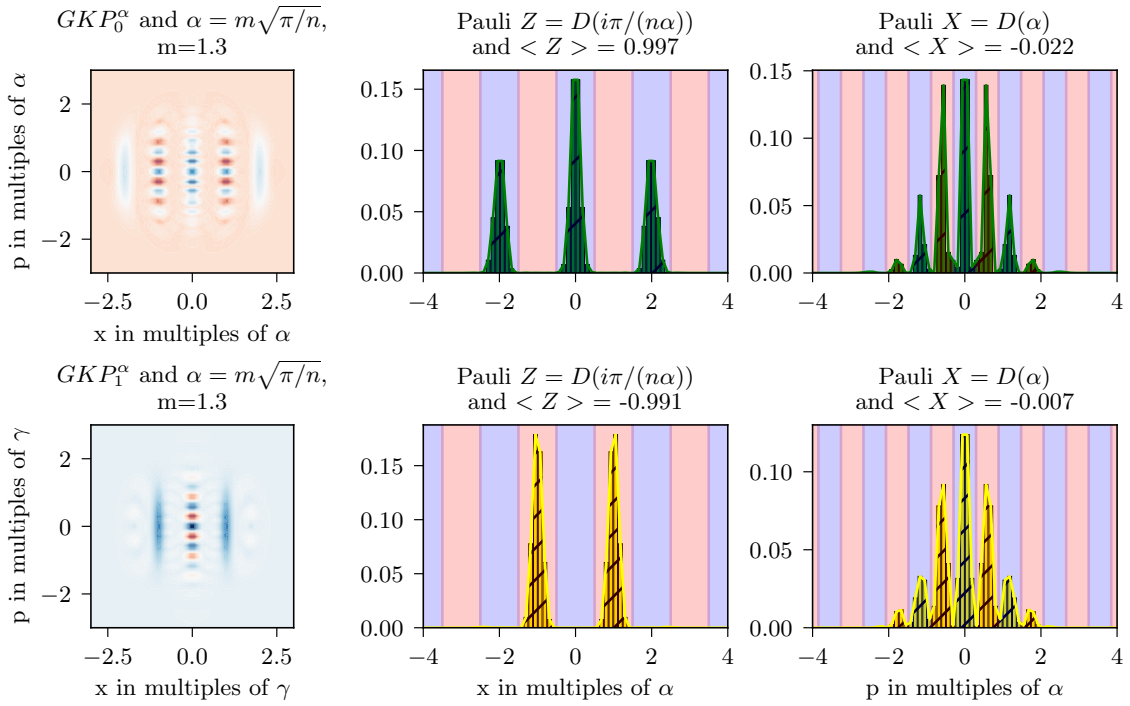

(b) Pauli gates on the GKP logical basis

Figure 8.3: The physical version of the ideal rectangular GKP state with $\lambda = 1.3$ is plotted in multiples of α for $n = 2$ and $\hbar = 0.5$ for the logical $|0\rangle_L$ and $|1\rangle_L$ state with parameters $\kappa = 0.2$ and $\xi = 0.45$. It is an eigenvector of both stabilizers with eigenvalue $\to +1$, visible as all peaks of the marginal position and momentum distribution lie in the blue area in **(a)**, representing an eigenvalue of $+1$. We can see that the logical states are eigenvectors of the Pauli Z gate, with eigenvalues $\to +1$ and $\to -1$ in **(b)**, where the red bins represent -1.

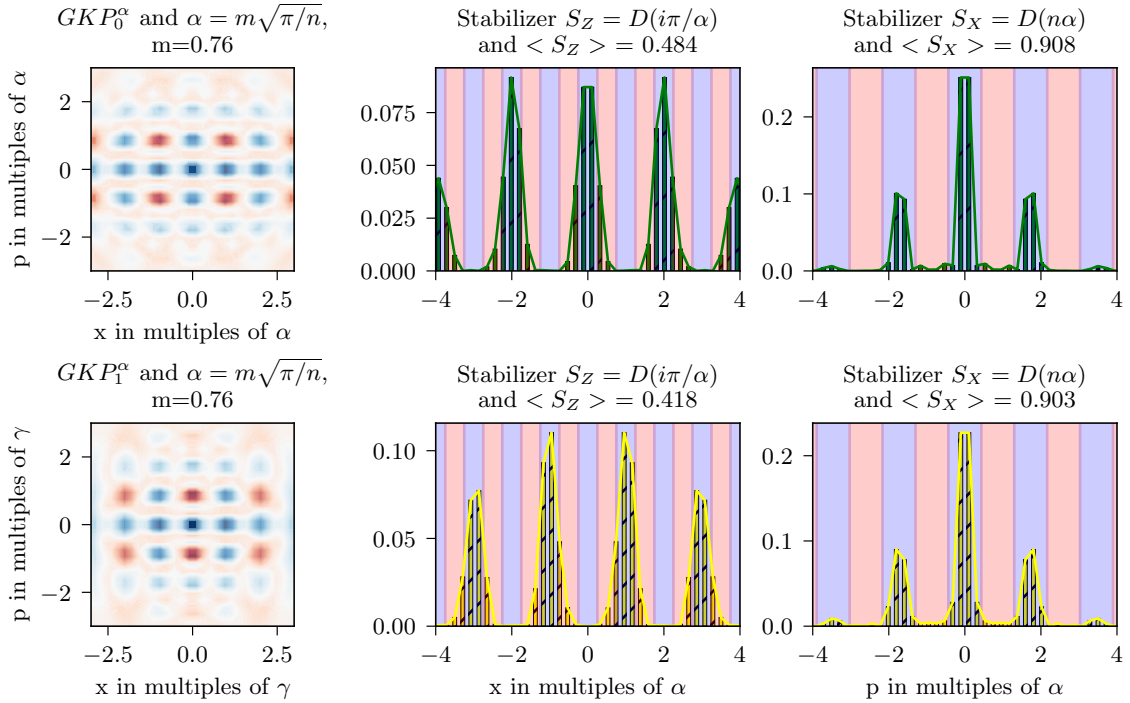

(a) Stabilizers on the GKP logical basis

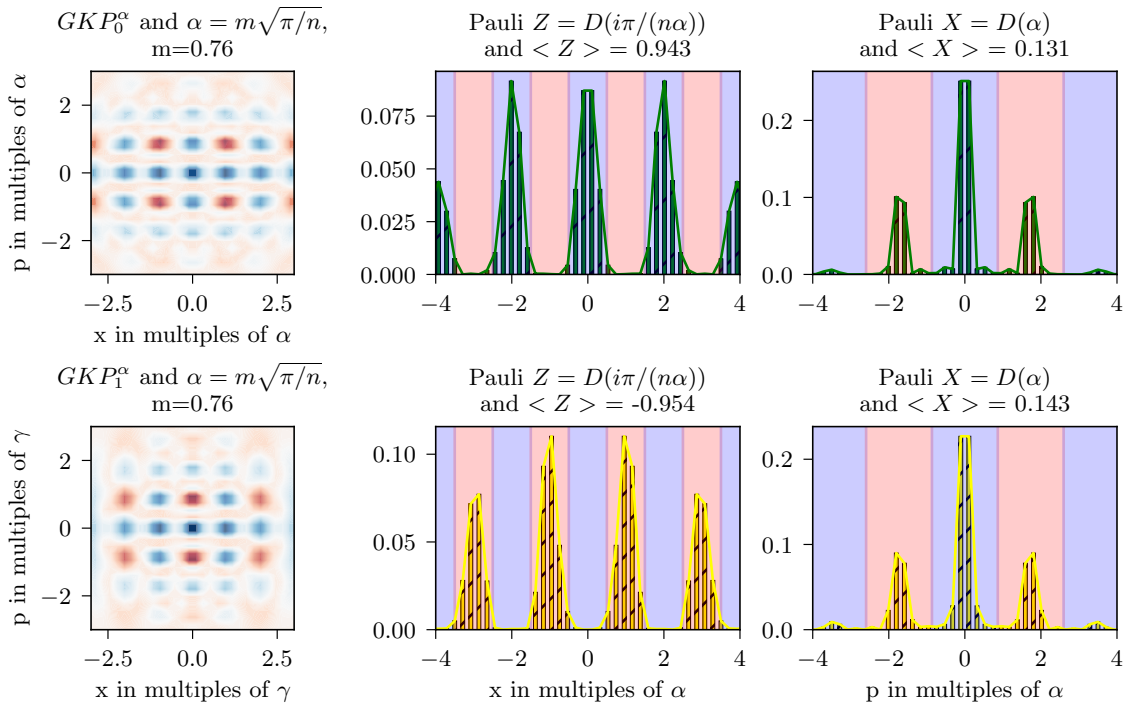

(b) Pauli gates on the GKP logical basis

Figure 8.4: The physical version of the ideal hexagonal GKP state is plotted in multiples of α for $n = 2$ and $\hbar = 0.5$ for the logical $|0\rangle_L$ and $|1\rangle_L$ state with parameters $\kappa = 0.2$ and $\xi = 0.45$. It is an eigenvector of both stabilizers with eigenvalue $\to +1$, visible as all peaks of the marginal position and momentum distribution lie in the blue area in **(a)**, representing an eigenvalue of $+1$. We can see that the logical states are eigenvectors of the Pauli Z gate, with eigenvalues $\to +1$ and $\to -1$ in **(b)**, where the red bins represent -1.

Bibliography

[1] W. Heisenberg. "Über den anschaulichen Inhalt der quantentheoretischen Kinematik und Mechanik". In: *Zeitschrift für Physik* 43.3–4 (Mar. 1927), pp. 172–198. ISSN: 1434-601X. DOI: 10.1007/bf01397280.

[2] N. David Mermin. "Could Feynman Have Said This?" In: *Physics Today* 57.5 (May 2004), pp. 10–11. ISSN: 1945-0699. DOI: 10.1063/1.1768652.

[3] Ivan H. Deutsch. "Harnessing the Power of the Second Quantum Revolution". In: *PRX Quantum* 1.2 (Nov. 2020), p. 020101. ISSN: 2691-3399. DOI: 10.1103/prxquantum.1.020101.

[4] A. Einstein, B. Podolsky, and N. Rosen. "Can Quantum-Mechanical Description of Physical Reality Be Considered Complete?" In: *Physical Review* 47.10 (May 1935), pp. 777–780. ISSN: 0031-899X. DOI: 10.1103/physrev.47.777.

[5] J. S. Bell. "On the Einstein Podolsky Rosen paradox". In: *Physics Physique Fizika* 1.3 (Nov. 1964), pp. 195–200. ISSN: 0554-128X. DOI: 10.1103/physicsphysiquefizika.1.195.

[6] Olivier Darrigol. "'Shut up and contemplate!': Lucien Hardy⊠s reasonable axioms for quantum theory". In: *Studies in History and Philosophy of Science Part B: Studies in History and Philosophy of Modern Physics* 52 (Nov. 2015), pp. 328–342. ISSN: 1355-2198. DOI: 10.1016/j.shpsb.2015.10.002.

[7] Wojciech Hubert Zurek. "Decoherence, einselection, and the quantum origins of the classical". In: *Reviews of Modern Physics* 75.3 (May 2003), pp. 715–775. ISSN: 1539-0756. DOI: 10.1103/revmodphys.75.715.

[8] Warren Nagourney, Jon Sandberg, and Hans Dehmelt. "Shelved optical electron amplifier: Observation of quantum jumps". In: *Physical Review Letters* 56.26 (June 1986), pp. 2797–2799. ISSN: 0031-9007. DOI: 10.1103/physrevlett.56.2797.

[9] Stuart J. Freedman and John F. Clauser. "Experimental Test of Local Hidden-Variable Theories". In: *Physical Review Letters* 28.14 (Apr. 1972), pp. 938–941. ISSN: 0031-9007. DOI: 10.1103/physrevlett.28.938.

[10] Alain Aspect, Philippe Grangier, and Gérard Roger. "Experimental Tests of Realistic Local Theories via Bell's Theorem". In: *Physical Review Letters* 47.7 (Aug. 1981), pp. 460–463. ISSN: 0031-9007. DOI: 10.1103/physrevlett.47.460.

[11] Ryszard Horodecki et al. "Quantum entanglement". In: *Reviews of Modern Physics* 81.2 (June 2009), pp. 865–942. ISSN: 1539-0756. DOI: 10.1103/revmodphys.81.865.

[12] Simon Kochen and E. P. Specker. "The Problem of Hidden Variables in Quantum Mechanics". In: *Ernst Specker Selecta*. Birkhäuser Basel, 1990, pp. 235–263. ISBN: 9783034892599. DOI: 10.1007/978-3-0348-9259-9_21.

[13] N. David Mermin. "Hidden variables and the two theorems of John Bell". In: *Reviews of Modern Physics* 65.3 (July 1993), pp. 803–815. ISSN: 1539-0756. DOI: 10.1103/revmodphys.65.803.

[14] Robert Raussendorf. "Contextuality in measurement-based quantum computation". In: *Physical Review A* 88.2 (Aug. 2013), p. 022322. ISSN: 1094-1622. DOI: 10.1103/physreva.88.022322.

[15] Anatole Kenfack and Karol yczkowski. "Negativity of the Wigner function as an indicator of non-classicality". In: *Journal of Optics B: Quantum and Semiclassical Optics* 6.10 (Aug. 2004), pp. 396–404. ISSN: 1741-3575. DOI: 10.1088/1464-4266/6/10/003.

[16] W. K. Wootters and W. H. Zurek. "A single quantum cannot be cloned". In: *Nature* 299.5886 (Oct. 1982), pp. 802–803. ISSN: 1476-4687. DOI: 10.1038/299802a0.

[17] P Feynman Richard. "There's Plenty of Room at the Bottom". In: *Annual Meeting of the American Physical Society,(1959), December 29*. 1959.

[18] William D. Phillips. "Nobel Lecture: Laser cooling and trapping of neutral atoms". In: *Reviews of Modern Physics* 70.3 (July 1998), pp. 721–741. ISSN: 1539-0756. DOI: 10.1103/revmodphys.70.721.

[19] Daniel F Walls. "Squeezed states of light". In: *nature* 306.5939 (1983), pp. 141–146.

[20] R Miller et al. "Trapped atoms in cavity QED: coupling quantized light and matter". In: *Journal of Physics B: Atomic, Molecular and Optical Physics* 38.9 (Apr. 2005), S551–S565. ISSN: 1361-6455. DOI: 10.1088/0953-4075/38/9/007.

[21] Alexandre Blais et al. "Circuit quantum electrodynamics". In: *Reviews of Modern Physics* 93.2 (May 2021), p. 025005. ISSN: 1539-0756. DOI: 10.1103/revmodphys.93.025005.

[22] David Deutsch. "Quantum theory, the Church–Turing principle and the universal quantum computer". In: *Proceedings of the Royal Society of London. A. Mathematical and Physical Sciences* 400.1818 (1985), pp. 97–117.

[23] Samuel L. Braunstein and Carlton M. Caves. "Statistical distance and the geometry of quantum states". In: *Physical Review Letters* 72.22 (May 1994), pp. 3439–3443. ISSN: 0031-9007. DOI: 10.1103/physrevlett.72.3439.

[24] Vittorio Giovannetti, Seth Lloyd, and Lorenzo Maccone. "Quantum Metrology". In: *Physical Review Letters* 96.1 (Jan. 2006), p. 010401. ISSN: 1079-7114. DOI: 10.1103/physrevlett.96.010401.

[25] Luca Pezzè et al. “Quantum metrology with nonclassical states of atomic ensembles”. In: *Reviews of Modern Physics* 90.3 (Sept. 2018), p. 035005. ISSN: 1539-0756. DOI: 10.1103/revmodphys.90.035005.

[26] Clémentine Rouvière et al. “Ultra-sensitive separation estimation of optical sources”. In: *Optica* 11.2 (Jan. 2024), p. 166. ISSN: 2334-2536. DOI: 10.1364/optica.500039.

[27] Charles H. Bennett and Gilles Brassard. “Quantum cryptography: Public key distribution and coin tossing”. In: *Theoretical Computer Science* 560 (Dec. 2014), pp. 7–11. ISSN: 0304-3975. DOI: 10.1016/j.tcs.2014.05.025.

[28] Hadriel Mamann et al. “Quantum cryptographic protocol implementation using a highly-efficient cold-atom-based quantum memory”. In: *CLEO 2023*. CLEO FS. Optica Publishing Group, 2023. DOI: 10.1364/cleo_fs.2023.ff2a.3.

[29] Stefano Pirandola and Samuel L. Braunstein. “Physics: Unite to build a quantum Internet”. In: *Nature* 532.7598 (Apr. 2016), pp. 169–171. ISSN: 1476-4687. DOI: 10.1038/532169a.

[30] Olivier Morin. “Non-Gaussian states and measurements for quantum information”. Theses. Université Pierre et Marie Curie - Paris VI, Dec. 2013. URL: https://theses.hal.science/tel-01066655.

[31] Olivier Morin et al. “Remote creation of hybrid entanglement between particle-like and wave-like optical qubits”. In: *Nature Photonics* 8.7 (June 2014), pp. 570–574. ISSN: 1749-4893. DOI: 10.1038/nphoton.2014.137.

[32] K. Huang et al. “Optical Synthesis of Large-Amplitude Squeezed Coherent-State Superpositions with Minimal Resources”. In: *Physical Review Letters* 115.2 (July 2015), p. 023602. ISSN: 1079-7114. DOI: 10.1103/physrevlett.115.023602.

[33] H. Le Jeannic et al. “Slowing Quantum Decoherence by Squeezing in Phase Space”. In: *Physical Review Letters* 120.7 (Feb. 2018), p. 073603. ISSN: 1079-7114. DOI: 10.1103/physrevlett.120.073603.

[34] Hanna Le Jeannic et al. “High-efficiency WSi superconducting nanowire single-photon detectors for quantum state engineering in the near infrared”. In: *Optics Letters* 41.22 (Nov. 2016), p. 5341. ISSN: 1539-4794. DOI: 10.1364/ol.41.005341.

[35] A. Cavaillès et al. “Demonstration of Einstein-Podolsky-Rosen Steering Using Hybrid Continuous- and Discrete-Variable Entanglement of Light”. In: *Physical Review Letters* 121.17 (Oct. 2018), p. 170403. ISSN: 1079-7114. DOI: 10.1103/physrevlett.121.170403.

[36] Giovanni Guccione et al. “Connecting heterogeneous quantum networks by hybrid entanglement swapping”. In: *Science Advances* 6.22 (May 2020). ISSN: 2375-2548. DOI: 10.1126/sciadv.aba4508.

[37] Tom Darras et al. “A quantum-bit encoding converter”. In: *Nature Photonics* 17.2 (Dec. 2022), pp. 165–170. ISSN: 1749-4893. DOI: 10.1038/s41566-022-01117-5.

[38] C. Fabre and N. Treps. “Modes and states in quantum optics”. In: *Reviews of Modern Physics* 92.3 (Sept. 2020), p. 035005. ISSN: 1539-0756. DOI: 10.1103/revmodphys.92.035005.

[39] Gilbert Grynberg et al. *Introduction to Quantum Optics: From the Semi-classical Approach to Quantized Light*. Cambridge University Press, Sept. 2010. ISBN: 9780511778261. DOI: 10.1017/cbo9780511778261.

[40] V. Rosenhaus. “Infinite symmetries and conservation laws”. In: *Journal of Mathematical Physics* 43.12 (Dec. 2002), pp. 6129–6150. ISSN: 1089-7658. DOI: 10.1063/1.1517394.

[41] Mattia Walschaers. “Non-Gaussian Quantum States and Where to Find Them”. In: *PRX Quantum* 2.3 (Sept. 2021), p. 030204. ISSN: 2691-3399. DOI: 10.1103/prxquantum.2.030204.

[42] M. Kempe et al. “Spatial and temporal transformation of femtosecond laser pulses by lenses and lens systems”. In: *Journal of the Optical Society of America B* 9.7 (July 1992), p. 1158. ISSN: 1520-8540. DOI: 10.1364/josab.9.001158.

[43] Aabid Patel et al. “Non-paraxial polarization spatio-temporal coupling in ultrafast laser material processing”. In: *Laser & Photonics Reviews* 11.3 (Mar. 2017). ISSN: 1863-8899. DOI: 10.1002/lpor.201600290.

[44] Thomas F. Jordan and E. C. G. Sudarshan. “Lie Group Dynamical Formalism and the Relation between Quantum Mechanics and Classical Mechanics”. In: *Reviews of Modern Physics* 33.4 (Oct. 1961), pp. 515–524. ISSN: 0034-6861. DOI: 10.1103/revmodphys.33.515.

[45] Denys I. Bondar et al. “Operational Dynamic Modeling Transcending Quantum and Classical Mechanics”. In: *Physical Review Letters* 109.19 (Nov. 2012), p. 190403. ISSN: 1079-7114. DOI: 10.1103/physrevlett.109.190403.

[46] Lluís Masanes, Thomas D. Galley, and Markus P. Müller. “The measurement postulates of quantum mechanics are operationally redundant”. In: *Nature Communications* 10.1 (Mar. 2019). ISSN: 2041-1723. DOI: 10.1038/s41467-019-09348-x.

[47] George W. Mackey. “Quantum Mechanics and Hilbert Space”. In: *The American Mathematical Monthly* 64.8 (Oct. 1957), p. 45. ISSN: 0002-9890. DOI: 10.2307/2308516.

[48] Fattah Sakuldee, Philip Taranto, and Simon Milz. “Connecting commutativity and classicality for multitime quantum processes”. In: *Physical Review A* 106.2 (Aug. 2022), p. 022416. ISSN: 2469-9934. DOI: 10.1103/physreva.106.022416.

[49] Habib Salehi. "Stone's Theorem for a Group of Unitary Operators Over a Hilbert Space". In: *Proceedings of the American Mathematical Society* 31.2 (Feb. 1972), p. 480. ISSN: 0002-9939. DOI: 10.2307/2037557.

[50] V I Tatarskiĭ. "The Wigner representation of quantum mechanics". In: *Soviet Physics Uspekhi* 26.4 (Apr. 1983), pp. 311–327. ISSN: 0038-5670. DOI: 10.1070/pu1983v026n04abeh004345.

[51] Renan Cabrera et al. "Efficient method to generate time evolution of the Wigner function for open quantum systems". In: *Physical Review A* 92.4 (Oct. 2015), p. 042122. ISSN: 1094-1622. DOI: 10.1103/physreva.92.042122.

[52] Shunlong Luo. "Heisenberg uncertainty relation for mixed states". In: *Physical Review A* 72.4 (Oct. 2005), p. 042110. ISSN: 1094-1622. DOI: 10.1103/physreva.72.042110.

[53] Asher Peres. "Separability Criterion for Density Matrices". In: *Physical Review Letters* 77.8 (Aug. 1996), pp. 1413–1415. ISSN: 1079-7114. DOI: 10.1103/physrevlett.77.1413.

[54] Hassan Shapourian et al. "Entanglement Negativity Spectrum of Random Mixed States: A Diagrammatic Approach". In: *PRX Quantum* 2.3 (Sept. 2021), p. 030347. ISSN: 2691-3399. DOI: 10.1103/prxquantum.2.030347.

[55] J Eisert, F G S L Brandão, and K M R Audenaert. "Quantitative entanglement witnesses". In: *New Journal of Physics* 9.3 (Mar. 2007), pp. 46–46. ISSN: 1367-2630. DOI: 10.1088/1367-2630/9/3/046.

[56] Filip Rozpędek et al. "Optimizing practical entanglement distillation". In: *Physical Review A* 97.6 (June 2018), p. 062333. ISSN: 2469-9934. DOI: 10.1103/physreva.97.062333.

[57] Jian-Wei Pan et al. "Experimental entanglement purification of arbitrary unknown states". In: *Nature* 423.6938 (May 2003), pp. 417–422. ISSN: 1476-4687. DOI: 10.1038/nature01623.

[58] Paul G. Kwiat et al. "Experimental entanglement distillation and 'hidden' nonlocality". In: *Nature* 409.6823 (Feb. 2001), pp. 1014–1017. ISSN: 1476-4687. DOI: 10.1038/35059017.

[59] Hao Jeng et al. "Entanglement properties of a measurement-based entanglement distillation experiment". In: *Physical Review A* 99.4 (Apr. 2019), p. 042304. ISSN: 2469-9934. DOI: 10.1103/physreva.99.042304.

[60] Michael Gaida and Matthias Kleinmann. "Seven definitions of bipartite bound entanglement". In: *Journal of Physics A: Mathematical and Theoretical* 56.38 (Aug. 2023), p. 385302. ISSN: 1751-8121. DOI: 10.1088/1751-8121/aceecc.

[61] Beatrix C. Hiesmayr. "Free versus bound entanglement, a NP-hard problem tackled by machine learning". In: *Scientific Reports* 11.1 (Oct. 2021). ISSN: 2045-2322. DOI: 10.1038/s41598-021-98523-6.

[62] R. Simon. "Separability Criterion for Gaussian States". In: *Quantum Information with Continuous Variables*. Springer Netherlands, 2003, pp. 155–172. ISBN: 9789401512589. DOI: 10.1007/978-94-015-1258-9_14.

[63] Tamás Vértesi and Nicolas Brunner. "Disproving the Peres conjecture by showing Bell nonlocality from bound entanglement". In: *Nature Communications* 5.1 (Nov. 2014). ISSN: 2041-1723. DOI: 10.1038/ncomms6297.

[64] M. Hillery et al. "Distribution functions in physics: Fundamentals". In: *Physics Reports* 106.3 (Apr. 1984), pp. 121–167. ISSN: 0370-1573. DOI: 10.1016/0370-1573(84)90160-1.

[65] Thomas Curtright, Tsuneo Uematsu, and Cosmas Zachos. "Generating all Wigner functions". In: *Journal of Mathematical Physics* 42.6 (June 2001), pp. 2396–2415. ISSN: 1089-7658. DOI: 10.1063/1.1366327.

[66] Kathleen S. Gibbons, Matthew J. Hoffman, and William K. Wootters. "Discrete phase space based on finite fields". In: *Physical Review A* 70.6 (Dec. 2004), p. 062101. ISSN: 1094-1622. DOI: 10.1103/physreva.70.062101.

[67] Arthur O Pittenger and Morton H Rubin. "Wigner functions and separability for finite systems". In: *Journal of Physics A: Mathematical and General* 38.26 (June 2005), pp. 6005–6036. ISSN: 1361-6447. DOI: 10.1088/0305-4470/38/26/012.

[68] Ingemar Bengtsson and Karol Zyczkowski. *Geometry of Quantum States: An Introduction to Quantum Entanglement*. Cambridge University Press, May 2006. ISBN: 9780511535048. DOI: 10.1017/cbo9780511535048.

[69] Tsung-Yen Lee, Chun-Yaung Lu, and Chia-Chun Chou. "Moving Boundary Truncated Grid Method: Application to the Time Evolution of Distribution Functions in Phase Space". In: *The Journal of Physical Chemistry A* 125.1 (Dec. 2020), pp. 476–491. ISSN: 1520-5215. DOI: 10.1021/acs.jpca.0c09525.

[70] Austin T. Green and Craig C. Martens. "Zombie cats on the quantum–classical frontier: Wigner–Moyal and semiclassical limit dynamics of quantum coherence in molecules". In: *The Journal of Chemical Physics* 159.20 (Nov. 2023). ISSN: 1089-7690. DOI: 10.1063/5.0177421.

[71] Leslie E Ballentine. *Quantum Mechanics: A Modern Development*. WORLD SCIENTIFIC, Nov. 2014. ISBN: 9789814578592. DOI: 10.1142/9038.

[72] Stephen D. Bartlett et al. "Efficient Classical Simulation of Continuous Variable Quantum Information Processes". In: *Physical Review Letters* 88.9 (Feb. 2002), p. 097904. ISSN: 1079-7114. DOI: 10.1103/physrevlett.88.097904.

[73] A. Mari and J. Eisert. "Positive Wigner Functions Render Classical Simulation of Quantum Computation Efficient". In: *Physical Review Letters* 109.23 (Dec. 2012), p. 230503. ISSN: 1079-7114. DOI: 10.1103/physrevlett.109.230503.

[74] Ryuji Takagi and Quntao Zhuang. "Convex resource theory of non-Gaussianity". In: *Physical Review A* 97.6 (June 2018), p. 062337. ISSN: 2469-9934. DOI: 10.1103/physreva.97.062337.

[75] Eric Chitambar and Gilad Gour. "Quantum resource theories". In: *Reviews of Modern Physics* 91.2 (Apr. 2019), p. 025001. ISSN: 1539-0756. DOI: 10.1103/revmodphys.91.025001.

[76] Eric R. Anschuetz et al. "Interpretable Quantum Advantage in Neural Sequence Learning". In: *PRX Quantum* 4.2 (June 2023), p. 020338. ISSN: 2691-3399. DOI: 10.1103/prxquantum.4.020338.

[77] Robert Alicki and Ronnie Kosloff. "Introduction to Quantum Thermodynamics: History and Prospects". In: *Thermodynamics in the Quantum Regime*. Springer International Publishing, 2018, pp. 1–33. ISBN: 9783319990460. DOI: 10.1007/978-3-319-99046-0_1.

[78] Marcos Rigol, Vanja Dunjko, and Maxim Olshanii. "Thermalization and its mechanism for generic isolated quantum systems". In: *Nature* 452.7189 (Apr. 2008), pp. 854–858. ISSN: 1476-4687. DOI: 10.1038/nature06838.

[79] Evaldo M. F. Curado et al. "Helstrom Bound for Squeezed Coherent States in Binary Communication". In: *Entropy* 24.2 (Jan. 2022), p. 220. ISSN: 1099-4300. DOI: 10.3390/e24020220.

[80] Daniel Gottesman, Alexei Kitaev, and John Preskill. "Encoding a qubit in an oscillator". In: *Physical Review A* 64.1 (June 2001), p. 012310. ISSN: 1094-1622. DOI: 10.1103/physreva.64.012310.

[81] J. Eli Bourassa et al. "Fast Simulation of Bosonic Qubits via Gaussian Functions in Phase Space". In: *PRX Quantum* 2.4 (Oct. 2021), p. 040315. ISSN: 2691-3399. DOI: 10.1103/prxquantum.2.040315.

[82] Takaya Matsuura, Hayata Yamasaki, and Masato Koashi. "Equivalence of approximate Gottesman-Kitaev-Preskill codes". In: *Physical Review A* 102.3 (Sept. 2020), p. 032408. ISSN: 2469-9934. DOI: 10.1103/physreva.102.032408.

[83] L. García-Álvarez, A. Ferraro, and G. Ferrini. "From the Bloch Sphere to Phase-Space Representations with the Gottesman–Kitaev–Preskill Encoding". In: *Mathematics for Industry*. Springer Singapore, Oct. 2020, pp. 79–92. ISBN: 9789811551918. DOI: 10.1007/978-981-15-5191-8_9.

[84] Michael A. Nielsen and Isaac L. Chuang. *Quantum Computation and Quantum Information: 10th Anniversary Edition*. Cambridge University Press, June 2012. ISBN: 9780511976667. DOI: 10.1017/cbo9780511976667.

[85] Olivier Pfister. "Continuous-variable quantum computing in the quantum optical frequency comb". In: *Journal of Physics B: Atomic, Molecular and Optical Physics* 53.1 (Nov. 2019), p. 012001. ISSN: 1361-6455. DOI: 10.1088/1361-6455/ab526f.

[86] Jan Provazník et al. "Benchmarking photon number resolving detectors". In: *Optics Express* 28.10 (May 2020), p. 14839. ISSN: 1094-4087. DOI: 10.1364/oe.389619.

[87] Lior Cohen et al. "Absolute calibration of single-photon and multiplexed photon-number-resolving detectors". In: *Physical Review A* 98.1 (July 2018), p. 013811. ISSN: 2469-9934. DOI: 10.1103/physreva.98.013811.

[88] Julien Niset, Jaromír Fiurášek, and Nicolas J. Cerf. "No-Go Theorem for Gaussian Quantum Error Correction". In: *Physical Review Letters* 102.12 (Mar. 2009), p. 120501. ISSN: 1079-7114. DOI: 10.1103/physrevlett.102.120501.

[89] Stephen D. Bartlett and Barry C. Sanders. "Universal continuous-variable quantum computation: Requirement of optical nonlinearity for photon counting". In: *Physical Review A* 65.4 (Mar. 2002), p. 042304. ISSN: 1094-1622. DOI: 10.1103/physreva.65.042304.

[90] M. Ohliger, K. Kieling, and J. Eisert. "Limitations of quantum computing with Gaussian cluster states". In: *Physical Review A* 82.4 (Oct. 2010), p. 042336. ISSN: 1094-1622. DOI: 10.1103/physreva.82.042336.

[91] Seth Lloyd and Samuel L. Braunstein. "Quantum Computation over Continuous Variables". In: *Physical Review Letters* 82.8 (Feb. 1999), pp. 1784–1787. ISSN: 1079-7114. DOI: 10.1103/physrevlett.82.1784.

[92] Timo Hillmann et al. "Universal Gate Set for Continuous-Variable Quantum Computation with Microwave Circuits". In: *Physical Review Letters* 125.16 (Oct. 2020), p. 160501. ISSN: 1079-7114. DOI: 10.1103/physrevlett.125.160501.

[93] Benjamin J. Brown. "A fault-tolerant non-Clifford gate for the surface code in two dimensions". In: *Science Advances* 6.21 (May 2020). ISSN: 2375-2548. DOI: 10.1126/sciadv.aay4929.

[94] Shunya Konno et al. "Non-Clifford gate on optical qubits by nonlinear feedforward". In: *Physical Review Research* 3.4 (Oct. 2021), p. 043026. ISSN: 2643-1564. DOI: 10.1103/physrevresearch.3.043026.

[95] Steven M. Girvin. "Introduction to Quantum Error Correction and Fault Tolerance". In: *SciPost Phys. Lect. Notes 70 (2023)* (Nov. 2021). DOI: 10.21468/SciPostPhysLectNotes.70. arXiv: 2111.08894 [quant-ph].

[96] Hein M. et al. “Entanglement in graph states and its applications”. In: *Proceedings of the International School of Physics “Enrico Fermi”* 162 (2006), pp. 115–218. ISSN: 0074-784X. DOI: 10.3254/978-1-61499-018-5-115.

[97] Emanuel Knill and Raymond Laflamme. “Theory of quantum error-correcting codes”. In: *Physical Review A* 55.2 (Feb. 1997), pp. 900–911. ISSN: 1094-1622. DOI: 10.1103/physreva.55.900.

[98] Arne L. Grimsmo, Joshua Combes, and Ben Q. Baragiola. “Quantum Computing with Rotation-Symmetric Bosonic Codes”. In: *Physical Review X* 10.1 (Mar. 2020), p. 011058. ISSN: 2160-3308. DOI: 10.1103/physrevx.10.011058.

[99] Linshu Li et al. “Cat Codes with Optimal Decoherence Suppression for a Lossy Bosonic Channel”. In: *Physical Review Letters* 119.3 (July 2017), p. 030502. ISSN: 1079-7114. DOI: 10.1103/physrevlett.119.030502.

[100] Arne L. Grimsmo and Shruti Puri. “Quantum Error Correction with the Gottesman-Kitaev-Preskill Code”. In: *PRX Quantum* 2.2 (June 2021), p. 020101. ISSN: 2691-3399. DOI: 10.1103/prxquantum.2.020101.

[101] Jacob Hastrup et al. “Measurement-free preparation of grid states”. In: *npj Quantum Information* 7.1 (Jan. 2021). ISSN: 2056-6387. DOI: 10.1038/s41534-020-00353-3.

[102] Kosuke Fukui, Akihisa Tomita, and Atsushi Okamoto. “Analog Quantum Error Correction with Encoding a Qubit into an Oscillator”. In: *Physical Review Letters* 119.18 (Nov. 2017), p. 180507. ISSN: 1079-7114. DOI: 10.1103/physrevlett.119.180507.

[103] Christophe Vuillot et al. “Quantum error correction with the toric Gottesman-Kitaev-Preskill code”. In: *Physical Review A* 99.3 (Mar. 2019), p. 032344. ISSN: 2469-9934. DOI: 10.1103/physreva.99.032344.

[104] Julien Laurat. “Génération d’états non-classiques et intrication en variables continues à l’aide d’un oscillateur paramétrique optique”. Theses. Université Pierre et Marie Curie - Paris VI, Sept. 2004. URL: https://theses.hal.science/tel-00007442.

[105] A. Ashkin et al. “Optically-induced refractive index inhomogeneities in LiNbO3 and LiTaO3”. In: *Applied Physics Letters* 9.1 (July 1966), pp. 72–74. ISSN: 1077-3118. DOI: 10.1063/1.1754607.

[106] Ansgar Hellwig. “Nonlinear optical and photorefractive properties of periodically poled channel waveguides in lithium niobate”. PhD thesis. Universitätsbibliothek, 2011.

[107] Golnoush Shafiee et al. “Nonlinear power dependence of the spectral properties of an optical parametric oscillator below threshold in the quantum regime”. In: *New Journal of Physics* 22.7 (July 2020), p. 073045. ISSN: 1367-2630. DOI: 10.1088/1367-2630/ab9a87.

[108] Feng Guo et al. “Dielectric frame, Sellmeier equations, and phase-matching properties of the monoclinic acentric crystal $GdCa_4O(BO_3)_3$”. In: *Optics Letters* 41.22 (Nov. 2016), p. 5290. ISSN: 1539-4794. DOI: 10.1364/ol.41.005290.

[109] Georges H. Wagnière and Stanislaw Woźniak. “Nonlinear Optical Properties”. In: *Encyclopedia of Spectroscopy and Spectrometry*. Elsevier, 2017, pp. 375–387. DOI: 10.1016/b978-0-12-803224-4.00232-6.

[110] M. Yamada et al. “First-order quasi-phase matched LiNbO3 waveguide periodically poled by applying an external field for efficient blue second-harmonic generation”. In: *Applied Physics Letters* 62.5 (Feb. 1993), pp. 435–436. ISSN: 1077-3118. DOI: 10.1063/1.108925.

[111] James Schneeloch et al. “Introduction to the absolute brightness and number statistics in spontaneous parametric down-conversion”. In: *Journal of Optics* 21.4 (Feb. 2019), p. 043501. ISSN: 2040-8986. DOI: 10.1088/2040-8986/ab05a8.

[112] Kai-Hong Luo et al. “Direct generation of genuine single-longitudinal-mode narrowband photon pairs”. In: *New Journal of Physics* 17.7 (Aug. 2015), p. 073039. ISSN: 1367-2630. DOI: 10.1088/1367-2630/17/7/073039.

[113] M. J. Collett and C. W. Gardiner. “Squeezing of intracavity and traveling-wave light fields produced in parametric amplification”. In: *Physical Review A* 30.3 (Sept. 1984), pp. 1386–1391. ISSN: 0556-2791. DOI: 10.1103/physreva.30.1386.

[114] C. W. Gardiner and M. J. Collett. “Input and output in damped quantum systems: Quantum stochastic differential equations and the master equation”. In: *Physical Review A* 31.6 (June 1985), pp. 3761–3774. ISSN: 0556-2791. DOI: 10.1103/physreva.31.3761.

[115] Ryan Wagner et al. “Direct measurement of radiation pressure and circulating power inside a passive optical cavity”. In: *Optics Express* 26.18 (Aug. 2018), p. 23492. ISSN: 1094-4087. DOI: 10.1364/oe.26.023492.

[116] Takao Aoki, Go Takahashi, and Akira Furusawa. “Squeezing at 946nm with periodically poled KTiOPO4”. In: *Optics Express* 14.15 (2006), p. 6930. ISSN: 1094-4087. DOI: 10.1364/oe.14.006930.

[117] E. S. Polzik, J. Carri, and H. J. Kimble. “Atomic spectroscopy with squeezed light for sensitivity beyond the vacuum-state limit”. In: *Applied Physics B Photophysics and Laser Chemistry* 55.3 (Sept. 1992), pp. 279–290. ISSN: 1432-0649. DOI: 10.1007/bf00325016.

[118] Ling-An Wu, Min Xiao, and H. J. Kimble. “Squeezed states of light from an optical parametric oscillator”. In: *Journal of the Optical Society of America B* 4.10 (Oct. 1987), p. 1465. ISSN: 1520-8540. DOI: 10.1364/josab.4.001465.

[119] Nur Ismail et al. "Fabry-Pérot resonator: spectral line shapes, generic and related Airy distributions, linewidths, finesses, and performance at low or frequency-dependent reflectivity". In: *Optics Express* 24.15 (July 2016), p. 16366. ISSN: 1094-4087. DOI: 10.1364/oe.24.016366.

[120] Tom Darras. "Quantum teleportation-based protocols with hybrid entanglement of light". Theses. Sorbonne Université, June 2021. URL: https://theses.hal.science/tel-03712015.

[121] Adam Libson et al. "Simple method for locking birefringent resonators". In: *Optics Express* 23.3 (Feb. 2015), p. 3809. ISSN: 1094-4087. DOI: 10.1364/oe.23.003809.

[122] FJ Raab and SE Whitcomb. "Estimation of special optical properties of a triangular ring cavity". In: *LIGO-T920004* (1992).

[123] Shailendhar Saraf, Robert L. Byer, and Peter J. King. "High-extinction-ratio resonant cavity polarizer for quantum-optics measurements". In: *Applied Optics* 46.18 (May 2007), p. 3850. ISSN: 1539-4522. DOI: 10.1364/ao.46.003850.

[124] H. Kogelnik and T. Li. "Laser Beams and Resonators". In: *Applied Optics* 5.10 (Oct. 1966), p. 1550. ISSN: 1539-4522. DOI: 10.1364/ao.5.001550.

[125] Dana Z. Anderson. "Alignment of resonant optical cavities". In: *Applied Optics* 23.17 (Sept. 1984), p. 2944. ISSN: 1539-4522. DOI: 10.1364/ao.23.002944.

[126] Thomas Corbitt, Nergis Mavalvala, and Stan Whitcomb. "Optical cavities as amplitude filters for squeezed fields". In: *Physical Review D* 70.2 (July 2004), p. 022002. ISSN: 1550-2368. DOI: 10.1103/physrevd.70.022002.

[127] Michael Steve Stefszky et al. "Generation and detection of low-frequency squeezing for gravitational-wave detection". PhD thesis. Australian National University, 2012.

[128] Shigenori Moriwaki et al. "Frequency Discrimination Method Making Use of Polarization Selectivity of Triangular Optical Cavity". In: *Applied Physics Express* 2.1 (Dec. 2008), p. 016501. ISSN: 1882-0786. DOI: 10.1143/apex.2.016501.

[129] Ian N. Ross et al. "Analysis and optimization of optical parametric chirped pulse amplification". In: *Journal of the Optical Society of America B* 19.12 (Dec. 2002), p. 2945. ISSN: 1520-8540. DOI: 10.1364/josab.19.002945.

[130] Karl Johan Åström. "Control system design lecture notes for me 155a". In: *Department of Mechanical and Environmental Engineering University of California Santa Barbara* 333 (2002).

[131] D. A. Shaddock, M. B. Gray, and D. E. McClelland. "Frequency locking a laser to an optical cavity by use of spatial mode interference". In: *Optics Letters* 24.21 (Nov. 1999), p. 1499. ISSN: 1539-4794. DOI: 10.1364/ol.24.001499.

[132] Namisha Chabbra et al. "High stability laser locking to an optical cavity using tilt locking". In: *Optics Letters* 46.13 (June 2021), p. 3199. ISSN: 1539-4794. DOI: 10.1364/ol.427615.

[133] Eric D. Black. "An introduction to Pound–Drever–Hall laser frequency stabilization". In: *American Journal of Physics* 69.1 (Jan. 2001), pp. 79–87. ISSN: 1943-2909. DOI: 10.1119/1.1286663.

[134] L. Neuhaus et al. "PyRPL (Python Red Pitaya Lockbox) — An open-source software package for FPGA-controlled quantum optics experiments". In: *2017 Conference on Lasers and Electro-Optics Europe & European Quantum Electronics Conference (CLEO/Europe-EQEC)*. 2017, pp. 1–1. DOI: 10.1109/CLEOE-EQEC.2017.8087380.

[135] Hanna Le Jeannic. "Optical Hybrid Quantum Information processing". Theses. Université Pierre et Marie Curie - Paris VI, Dec. 2016. URL: https://theses.hal.science/tel-01665496.

[136] Jürgen Appel et al. "Electronic noise in optical homodyne tomography". In: *Physical Review A* 75.3 (Mar. 2007), p. 035802. ISSN: 1094-1622. DOI: 10.1103/physreva.75.035802.

[137] Jake Biele et al. "Shot-noise limited homodyne detection for MHz quantum light characterisation in the 2 µm band". In: *Optics Express* 30.5 (Feb. 2022), p. 7716. ISSN: 1094-4087. DOI: 10.1364/oe.450217.

[138] Yaojiang Chen et al. "Dynamic model and bandwidth characterization of InGaAs/-GaAsSb type-II quantum wells PIN photodiodes". In: *Optics Express* 26.26 (Dec. 2018), p. 35034. ISSN: 1094-4087. DOI: 10.1364/oe.26.035034.

[139] Fabien Bonnet. "Etude de la condensation et de l'évaporation de l'hélium dans les milieux poreux: effets du confinement et du désordre". PhD thesis. Université Joseph-Fourier-Grenoble I, 2009.

[140] Andrew J. Kerman et al. "Electrothermal feedback in superconducting nanowire single-photon detectors". In: *Physical Review B* 79.10 (Mar. 2009), p. 100509. ISSN: 1550-235X. DOI: 10.1103/physrevb.79.100509.

[141] Lixing You. "Superconducting nanowire single-photon detectors for quantum information". In: *Nanophotonics* 9.9 (June 2020), pp. 2673–2692. ISSN: 2192-8606. DOI: 10.1515/nanoph-2020-0186.

[142] Di Zhu et al. "Superconducting nanowire single-photon detector with integrated impedance-matching taper". In: *Applied Physics Letters* 114.4 (Jan. 2019). ISSN: 1077-3118. DOI: 10.1063/1.5080721.

[143] A. Bahgat Shehata et al. "Effect of temperature on superconducting nanowire single-photon detector noise". In: *SPIE Proceedings*. Ed. by Manijeh Razeghi, Dorota S. Temple, and Gail J. Brown. SPIE, Aug. 2015. DOI: 10.1117/12.2188234.

[144] Sebastian M. F. Raupach, Mariia Sidorova, and Alexej D. Semenov. "Photon number dependent afterpulsing in superconducting nanostrip single-photon detectors". In: *Physical Review B* 108.5 (Aug. 2023), p. 054507. ISSN: 2469-9969. DOI: 10.1103/physrevb.108.054507.

[145] Olivier Morin et al. "Quantum State Engineering of Light with Continuous-wave Optical Parametric Oscillators". In: *Journal of Visualized Experiments* 87 (May 2014). ISSN: 1940-087X. DOI: 10.3791/51224.

[146] A. I. Lvovsky. *Squeezed Light*. Jan. 2015. DOI: 10.1002/9781119009719.ch5.

[147] Hanna Le Jeannic. "Optical Hybrid Quantum Information processing". PhD thesis. Paris 6, 2016.

[148] Ulysse Chabaud, Pierre-Emmanuel Emeriau, and Frédéric Grosshans. "Witnessing Wigner Negativity". In: *Quantum* 5 (June 2021), p. 471. ISSN: 2521-327X. DOI: 10.22331/q-2021-06-08-471.

[149] A I Lvovsky. "Iterative maximum-likelihood reconstruction in quantum homodyne tomography". In: *Journal of Optics B: Quantum and Semiclassical Optics* 6.6 (May 2004), S556–S559. ISSN: 1741-3575. DOI: 10.1088/1464-4266/6/6/014.

[150] Philippe Faist and Renato Renner. "Practical and Reliable Error Bars in Quantum Tomography". In: *Physical Review Letters* 117.1 (July 2016), p. 010404. ISSN: 1079-7114. DOI: 10.1103/physrevlett.117.010404.

[151] Christian Schwemmer et al. "Systematic Errors in Current Quantum State Tomography Tools". In: *Physical Review Letters* 114.8 (Feb. 2015), p. 080403. ISSN: 1079-7114. DOI: 10.1103/physrevlett.114.080403.

[152] E. S. Tiunov et al. "Experimental quantum homodyne tomography via machine learning". In: *Optica* 7.5 (May 2020), p. 448. ISSN: 2334-2536. DOI: 10.1364/optica.389482.

[153] Sanjaya Lohani et al. "Machine learning assisted quantum state estimation". In: *Machine Learning: Science and Technology* 1.3 (July 2020), p. 035007. ISSN: 2632-2153. DOI: 10.1088/2632-2153/ab9a21.

[154] William Blanzeisky and Pádraig Cunningham. "Algorithmic Factors Influencing Bias in Machine Learning". In: *Machine Learning and Principles and Practice of Knowledge Discovery in Databases*. Springer International Publishing, 2021, pp. 559–574. ISBN: 9783030937362. DOI: 10.1007/978-3-030-93736-2_41.

[155] Shi-Hai Wei et al. "Towards Real-World Quantum Networks: A Review". In: *Laser and amp; Photonics Reviews* 16.3 (Jan. 2022). ISSN: 1863-8899. DOI: 10.1002/lpor.202100219.

[156] Zhonghui Li et al. “Entanglement-Assisted Quantum Networks: Mechanics, Enabling Technologies, Challenges, and Research Directions”. In: *IEEE Communications Surveys and amp; Tutorials* 25.4 (2023), pp. 2133–2189. ISSN: 2373-745X. DOI: 10.1109/comst.2023.3294240.

[157] Koji Azuma et al. “Quantum repeaters: From quantum networks to the quantum internet”. In: *Reviews of Modern Physics* 95.4 (Dec. 2023), p. 045006. ISSN: 1539-0756. DOI: 10.1103/revmodphys.95.045006.

[158] Peter W. Shor and John Preskill. “Simple Proof of Security of the BB84 Quantum Key Distribution Protocol”. In: *Physical Review Letters* 85.2 (July 2000), pp. 441–444. ISSN: 1079-7114. DOI: 10.1103/physrevlett.85.441.

[159] John F. Clauser et al. “Proposed Experiment to Test Local Hidden-Variable Theories”. In: *Physical Review Letters* 23.15 (Oct. 1969), pp. 880–884. ISSN: 0031-9007. DOI: 10.1103/physrevlett.23.880.

[160] B. Hensen et al. “Loophole-free Bell inequality violation using electron spins separated by 1.3 kilometres”. In: *Nature* 526.7575 (Oct. 2015), pp. 682–686. ISSN: 1476-4687. DOI: 10.1038/nature15759.

[161] Marissa Giustina et al. “Significant-Loophole-Free Test of Bell’s Theorem with Entangled Photons”. In: *Physical Review Letters* 115.25 (Dec. 2015), p. 250401. ISSN: 1079-7114. DOI: 10.1103/physrevlett.115.250401.

[162] Lynden K. Shalm et al. “Strong Loophole-Free Test of Local Realism”. In: *Physical Review Letters* 115.25 (Dec. 2015), p. 250402. ISSN: 1079-7114. DOI: 10.1103/physrevlett.115.250402.

[163] Simon Storz et al. “Loophole-free Bell inequality violation with superconducting circuits”. In: *Nature* 617.7960 (May 2023), pp. 265–270. ISSN: 1476-4687. DOI: 10.1038/s41586-023-05885-0.

[164] Johannes Handsteiner et al. “Cosmic Bell Test: Measurement Settings from Milky Way Stars”. In: *Physical Review Letters* 118.6 (Feb. 2017), p. 060401. ISSN: 1079-7114. DOI: 10.1103/physrevlett.118.060401.

[165] Wenjamin Rosenfeld et al. “Event-Ready Bell Test Using Entangled Atoms Simultaneously Closing Detection and Locality Loopholes”. In: *Physical Review Letters* 119.1 (July 2017), p. 010402. ISSN: 1079-7114. DOI: 10.1103/physrevlett.119.010402.

[166] Charles H. Bennett et al. “Teleporting an unknown quantum state via dual classical and Einstein-Podolsky-Rosen channels”. In: *Physical Review Letters* 70.13 (Mar. 1993), pp. 1895–1899. ISSN: 0031-9007. DOI: 10.1103/physrevlett.70.1895.

[167] Dik Bouwmeester et al. “Experimental quantum teleportation”. In: *Nature* 390.6660 (Dec. 1997), pp. 575–579. ISSN: 1476-4687. DOI: 10.1038/37539.

[168] S. Pirandola et al. “Advances in quantum teleportation”. In: *Nature Photonics* 9.10 (Sept. 2015), pp. 641–652. ISSN: 1749-4893. DOI: 10.1038/nphoton.2015.154.

[169] Xiao-Min Hu et al. “Progress in quantum teleportation”. In: *Nature Reviews Physics* 5.6 (May 2023), pp. 339–353. ISSN: 2522-5820. DOI: 10.1038/s42254-023-00588-x.

[170] M. Żukowski et al. “‘“Event-ready-detectors”’ Bell experiment via entanglement swapping”. In: *Physical Review Letters* 71.26 (Dec. 1993), pp. 4287–4290. ISSN: 0031-9007. DOI: 10.1103/physrevlett.71.4287.

[171] Jian-Wei Pan et al. “Experimental Entanglement Swapping: Entangling Photons That Never Interacted”. In: *Physical Review Letters* 80.18 (May 1998), pp. 3891–3894. ISSN: 1079-7114. DOI: 10.1103/physrevlett.80.3891.

[172] M. Pompili et al. “Realization of a multinode quantum network of remote solid-state qubits”. In: *Science* 372.6539 (Apr. 2021), pp. 259–264. ISSN: 1095-9203. DOI: 10.1126/science.abg1919.

[173] S. L. N. Hermans et al. “Qubit teleportation between non-neighbouring nodes in a quantum network”. In: *Nature* 605.7911 (May 2022), pp. 663–668. ISSN: 1476-4687. DOI: 10.1038/s41586-022-04697-y.

[174] V. Krutyanskiy et al. “Entanglement of Trapped-Ion Qubits Separated by 230 Meters”. In: *Physical Review Letters* 130.5 (Feb. 2023), p. 050803. ISSN: 1079-7114. DOI: 10.1103/physrevlett.130.050803.

[175] Tim van Leent et al. “Entangling single atoms over 33 km telecom fibre”. In: *Nature* 607.7917 (July 2022), pp. 69–73. ISSN: 1476-4687. DOI: 10.1038/s41586-022-04764-4.

[176] Matthias J. Bayerbach et al. “Bell-state measurement exceeding 50% success probability with linear optics”. In: *Science Advances* 9.32 (Aug. 2023). ISSN: 2375-2548. DOI: 10.1126/sciadv.adf4080.

[177] Mitsuyoshi Yukawa, Hugo Benichi, and Akira Furusawa. “High-fidelity continuous-variable quantum teleportation toward multistep quantum operations”. In: *Physical Review A* 77.2 (Feb. 2008), p. 022314. ISSN: 1094-1622. DOI: 10.1103/physreva.77.022314.

[178] Jie Zhao et al. “Enhancing quantum teleportation efficacy with noiseless linear amplification”. In: *Nature Communications* 14.1 (Aug. 2023). ISSN: 2041-1723. DOI: 10.1038/s41467-023-40438-z.

[179] M. D. Barrett et al. “Deterministic quantum teleportation of atomic qubits”. In: *Nature* 429.6993 (June 2004), pp. 737–739. ISSN: 1476-4687. DOI: 10.1038/nature02608.

[180] M. Riebe et al. “Deterministic quantum teleportation with atoms”. In: *Nature* 429.6993 (June 2004), pp. 734–737. ISSN: 1476-4687. DOI: 10.1038/nature02570.

[181] Carlos A. González-Gutiérrez and Juan Mauricio Torres. "Atomic Bell measurement via two-photon interactions". In: *Physical Review A* 99.2 (Feb. 2019), p. 023854. ISSN: 2469-9934. DOI: 10.1103/physreva.99.023854.

[182] Stephan Welte et al. "A nondestructive Bell-state measurement on two distant atomic qubits". In: *Nature Photonics* 15.7 (May 2021), pp. 504–509. ISSN: 1749-4893. DOI: 10.1038/s41566-021-00802-1.

[183] Jorge Miguel-Ramiro, Alexander Pirker, and Wolfgang Dür. "Optimized Quantum Networks". In: *Quantum* 7 (Feb. 2023), p. 919. ISSN: 2521-327X. DOI: 10.22331/q-2023-02-09-919.

[184] Koji Azuma et al. "Tools for quantum network design". In: *AVS Quantum Science* 3.1 (Feb. 2021). ISSN: 2639-0213. DOI: 10.1116/5.0024062.

[185] Mingtao Cao et al. "Efficient reversible entanglement transfer between light and quantum memories". In: *Optica* 7.10 (Oct. 2020), p. 1440. ISSN: 2334-2536. DOI: 10.1364/optica.400695.

[186] Stefano Duranti et al. *Efficient cavity-assisted storage of photonic qubits in a solid-state quantum memory*. 2023. DOI: 10.48550/ARXIV.2307.03509.

[187] L.-M. Duan et al. "Long-distance quantum communication with atomic ensembles and linear optics". In: *Nature* 414.6862 (Nov. 2001), pp. 413–418. ISSN: 1476-4687. DOI: 10.1038/35106500.

[188] Zong-Quan Zhou et al. "Photonic Integrated Quantum Memory in Rare-Earth Doped Solids". In: *Laser & Photonics Reviews* 17.10 (Aug. 2023). ISSN: 1863-8899. DOI: 10.1002/lpor.202300257.

[189] Nicolas Sangouard et al. "Quantum repeaters with entangled coherent states". In: *Journal of the Optical Society of America B* 27.6 (May 2010), A137. ISSN: 1520-8540. DOI: 10.1364/josab.27.00a137.

[190] S. Omkar et al. "Highly photon-loss-tolerant quantum computing using hybrid qubits". In: *Physical Review A* 103.3 (Mar. 2021), p. 032602. ISSN: 2469-9934. DOI: 10.1103/physreva.103.032602.

[191] Harald Herrmann et al. "Post-selection free, integrated optical source of non-degenerate, polarization entangled photon pairs". In: *Optics Express* 21.23 (Nov. 2013), p. 27981. ISSN: 1094-4087. DOI: 10.1364/oe.21.027981.

[192] S. J. van Enk, N. Lütkenhaus, and H. J. Kimble. "Experimental procedures for entanglement verification". In: *Physical Review A* 75.5 (May 2007), p. 052318. ISSN: 1094-1622. DOI: 10.1103/physreva.75.052318.

[193] David R. M. Arvidsson-Shukur et al. "Quantum advantage in postselected metrology". In: *Nature Communications* 11.1 (July 2020). ISSN: 2041-1723. DOI: 10.1038/s41467-020-17559-w.

[194] Natasha Tomm et al. “A bright and fast source of coherent single photons”. In: *Nature Nanotechnology* 16.4 (Jan. 2021), pp. 399–403. ISSN: 1748-3395. DOI: 10.1038/s41565-020-00831-x.

[195] Morteza Moradi et al. “CHSH Bell tests for optical hybrid entanglement”. In: *New Journal of Physics* 26.3 (Mar. 2024), p. 033019. ISSN: 1367-2630. DOI: 10.1088/1367-2630/ad2d40.

[196] Ruslan Hummatov et al. “Fast transition-edge sensors suitable for photonic quantum computing”. In: *Journal of Applied Physics* 133.23 (June 2023). ISSN: 1089-7550. DOI: 10.1063/5.0149478.

[197] Élie Gouzien et al. “Scheme for the generation of hybrid entanglement between time-bin and wavelike encodings”. In: *Physical Review A* 102.1 (July 2020), p. 012603. ISSN: 2469-9934. DOI: 10.1103/physreva.102.012603.

[198] Samuel L. Braunstein and A. Mann. “Measurement of the Bell operator and quantum teleportation”. In: *Physical Review A* 51.3 (Mar. 1995), R1727–R1730. ISSN: 1094-1622. DOI: 10.1103/physreva.51.r1727.

[199] Robert H. Hadfield. “Single-photon detectors for optical quantum information applications”. In: *Nature Photonics* 3.12 (Dec. 2009), pp. 696–705. ISSN: 1749-4893. DOI: 10.1038/nphoton.2009.230.

[200] Adriana E. Lita et al. “Development of Superconducting Single-Photon and Photon-Number Resolving Detectors for Quantum Applications”. In: *Journal of Lightwave Technology* 40.23 (Dec. 2022), pp. 7578–7597. ISSN: 1558-2213. DOI: 10.1109/jlt.2022.3195000.

[201] Helstrom. *Quantum Detection and Estimation Theory*. Elsevier Science and Technology Books, 1976. ISBN: 9780080956329.

[202] V. D’Auria et al. “Effect of the heralding detector properties on the conditional generation of single-photon states”. In: *The European Physical Journal D* 66.10 (Oct. 2012). ISSN: 1434-6079. DOI: 10.1140/epjd/e2012-30351-6.

[203] U. Leonhardt and H. Paul. “Measuring the quantum state of light”. In: *Progress in Quantum Electronics* 19.2 (Jan. 1995), pp. 89–130. ISSN: 0079-6727. DOI: 10.1016/0079-6727(94)00007-l.

[204] Adriana E. Lita, Aaron J. Miller, and Sae Woo Nam. “Counting near-infrared single-photons with 95% efficiency”. In: *Optics Express* 16.5 (2008), p. 3032. ISSN: 1094-4087. DOI: 10.1364/oe.16.003032.

[205] Gershon Kurizki et al. “Quantum technologies with hybrid systems”. In: *Proceedings of the National Academy of Sciences* 112.13 (Mar. 2015), pp. 3866–3873. ISSN: 1091-6490. DOI: 10.1073/pnas.1419326112.

[206] Morten Kjaergaard et al. “Superconducting Qubits: Current State of Play”. In: *Annual Review of Condensed Matter Physics* 11.1 (Mar. 2020), pp. 369–395. ISSN: 1947-5462. DOI: 10.1146/annurev-conmatphys-031119-050605.

[207] Samuel L. Braunstein and Peter van Loock. “Quantum information with continuous variables”. In: *Reviews of Modern Physics* 77.2 (June 2005), pp. 513–577. ISSN: 1539-0756. DOI: 10.1103/revmodphys.77.513.

[208] Jeremy L. O’Brien, Akira Furusawa, and Jelena Vučković. “Photonic quantum technologies”. In: *Nature Photonics* 3.12 (Dec. 2009), pp. 687–695. ISSN: 1749-4893. DOI: 10.1038/nphoton.2009.229.

[209] Hai-Tao Tu et al. “High-efficiency coherent microwave-to-optics conversion via off-resonant scattering”. In: *Nature Photonics* 16.4 (Feb. 2022), pp. 291–296. ISSN: 1749-4893. DOI: 10.1038/s41566-022-00959-3.

[210] Xu Han et al. “Microwave-optical quantum frequency conversion”. In: *Optica* 8.8 (Aug. 2021), p. 1050. ISSN: 2334-2536. DOI: 10.1364/optica.425414.

[211] Srujan Meesala et al. *Quantum entanglement between optical and microwave photonic qubits*. 2023. DOI: 10.48550/ARXIV.2312.13559.

[212] B. B. Blinov et al. “Observation of entanglement between a single trapped atom and a single photon”. In: *Nature* 428.6979 (Mar. 2004), pp. 153–157. ISSN: 1476-4687. DOI: 10.1038/nature02377.

[213] Rikizo Ikuta et al. “Polarization insensitive frequency conversion for an atom-photon entanglement distribution via a telecom network”. In: *Nature Communications* 9.1 (May 2018). ISSN: 2041-1723. DOI: 10.1038/s41467-018-04338-x.

[214] E. Togan et al. “Quantum entanglement between an optical photon and a solid-state spin qubit”. In: *Nature* 466.7307 (Aug. 2010), pp. 730–734. ISSN: 1476-4687. DOI: 10.1038/nature09256.

[215] W. B. Gao et al. “Observation of entanglement between a quantum dot spin and a single photon”. In: *Nature* 491.7424 (Nov. 2012), pp. 426–430. ISSN: 1476-4687. DOI: 10.1038/nature11573.

[216] Xiao-Feng Shi. “Quantum logic and entanglement by neutral Rydberg atoms: methods and fidelity”. In: *Quantum Science and Technology* 7.2 (Apr. 2022), p. 023002. ISSN: 2058-9565. DOI: 10.1088/2058-9565/ac18b8.

[217] Raustin Reyes et al. “Complete Bell state measurement of diamond nuclear spins under a complete spatial symmetry at zero magnetic field”. In: *Applied Physics Letters* 120.19 (May 2022). ISSN: 1077-3118. DOI: 10.1063/5.0088155.

[218] Hyunseok Jeong et al. “Generation of hybrid entanglement of light”. In: *Nature Photonics* 8.7 (June 2014), pp. 564–569. ISSN: 1749-4893. DOI: 10.1038/nphoton.2014.136.

[219] Demid V. Sychev et al. “Entanglement and teleportation between polarization and wave-like encodings of an optical qubit”. In: *Nature Communications* 9.1 (Sept. 2018). ISSN: 2041-1723. DOI: 10.1038/s41467-018-06055-x.

[220] K. Huang et al. “Microcontroller-based locking in optics experiments”. In: *Review of Scientific Instruments* 85.12 (Dec. 2014). ISSN: 1089-7623. DOI: 10.1063/1.4903869.

[221] Jonas S. Neergaard-Nielsen et al. “Optical Continuous-Variable Qubit”. In: *Physical Review Letters* 105.5 (July 2010), p. 053602. ISSN: 1079-7114. DOI: 10.1103/physrevlett.105.053602.

[222] Francisco E. Veiras, Liliana I. Perez, and María T. Garea. “Phase shift formulas in uniaxial media: an application to waveplates”. In: *Applied Optics* 49.15 (May 2010), p. 2769. ISSN: 1539-4522. DOI: 10.1364/ao.49.002769.

[223] S. Massar and S. Popescu. “Optimal Extraction of Information from Finite Quantum Ensembles”. In: *Physical Review Letters* 74.8 (Feb. 1995), pp. 1259–1263. ISSN: 1079-7114. DOI: 10.1103/physrevlett.74.1259.

[224] F. Basso Basset et al. “Quantum teleportation with imperfect quantum dots”. In: *npj Quantum Information* 7.1 (Jan. 2021). DOI: 10.1038/s41534-020-00356-0.

[225] Peter J. Mosley et al. “Experimental Realization of Maximum Confidence Quantum State Discrimination for the Extraction of Quantum Information”. In: *Physical Review Letters* 97.19 (Nov. 2006), p. 193601. DOI: 10.1103/physrevlett.97.193601.

[226] Sarah Croke et al. “Maximum Confidence Quantum Measurements”. In: *Physical Review Letters* 96.7 (Feb. 2006), p. 070401. DOI: 10.1103/physrevlett.96.070401.

[227] Shuntaro Takeda et al. “Deterministic quantum teleportation of photonic quantum bits by a hybrid technique”. In: *Nature* 500.7462 (Aug. 2013), pp. 315–318. DOI: 10.1038/nature12366.

[228] E. Bagan et al. “Optimal full estimation of qubit mixed states”. In: *Physical Review A* 73.3 (Mar. 2006), p. 032301. ISSN: 1094-1622. DOI: 10.1103/physreva.73.032301.

[229] E. Bagan et al. “Purity Estimation with Separable Measurements”. In: *Physical Review Letters* 95.11 (Sept. 2005), p. 110504. ISSN: 1079-7114. DOI: 10.1103/physrevlett.95.110504.

[230] V Al Osipov, H-J Sommers, and K Życzkowski. “Random Bures mixed states and the distribution of their purity”. In: *Journal of Physics A: Mathematical and Theoretical* 43.5 (Jan. 2010), p. 055302. ISSN: 1751-8121. DOI: 10.1088/1751-8113/43/5/055302.

[231] G. M. D’Ariano and L. Maccone. “Quantum Tomography of Optical Devices”. In: NASA. NASA CONFERENCE PUBLICATION (pp. 529-534)., 1998.

[232] Joel Yuen-Zhou et al. “The process matrix and how to determine it: quantum process tomography”. In: *Ultrafast Spectroscopy*. IOP Publishing, Sept. 2014. DOI: 10.1088/978-0-750-31062-8ch1.

[233] Charles H. Baldwin, Amir Kalev, and Ivan H. Deutsch. “Quantum process tomography of unitary and near-unitary maps”. In: *Physical Review A* 90.1 (July 2014), p. 012110. DOI: 10.1103/physreva.90.012110.

[234] Irene Bongioanni et al. “Experimental quantum process tomography of non-trace-preserving maps”. In: *Physical Review A* 82.4 (Oct. 2010), p. 042307. DOI: 10.1103/physreva.82.042307.

[235] J. L. O’Brien et al. “Quantum Process Tomography of a Controlled-NOT Gate”. In: *Physical Review Letters* 93.8 (Aug. 2004), p. 080502. DOI: 10.1103/physrevlett.93.080502.

[236] Jaromír Fiurášek and Zdeněk Hradil. “Maximum-likelihood estimation of quantum processes”. In: *Physical Review A* 63.2 (Jan. 2001), p. 020101. DOI: 10.1103/physreva.63.020101.

[237] Miroslav Ježek, Jaromír Fiurášek, and Zdeněk Hradil. “Quantum inference of states and processes”. In: *Physical Review A* 68.1 (July 2003), p. 012305. DOI: 10.1103/physreva.68.012305.

[238] Michael Garstka, Mark Cannon, and Paul Goulart. “COSMO: A Conic Operator Splitting Method for Convex Conic Problems”. In: *Journal of Optimization Theory and Applications* 190.3 (Aug. 2021), pp. 779–810. DOI: 10.1007/s10957-021-01896-x.

[239] Michael A Nielsen. “A simple formula for the average gate fidelity of a quantum dynamical operation”. In: *Physics Letters A* 303.4 (Oct. 2002), pp. 249–252. DOI: 10.1016/s0375-9601(02)01272-0.

[240] Alexei Gilchrist, Nathan K. Langford, and Michael A. Nielsen. “Distance measures to compare real and ideal quantum processes”. In: *Physical Review A* 71.6 (June 2005), p. 062310. DOI: 10.1103/physreva.71.062310.

[241] Marcus Reindl et al. “All-photonic quantum teleportation using on-demand solid-state quantum emitters”. In: *Science Advances* 4.12 (Dec. 2018). ISSN: 2375-2548. DOI: 10.1126/sciadv.aau1255.

[242] F. Basso Basset et al. “Entanglement Swapping with Photons Generated on Demand by a Quantum Dot”. In: *Physical Review Letters* 123.16 (Oct. 2019), p. 160501. ISSN: 1079-7114. DOI: 10.1103/physrevlett.123.160501.

[243] Hyukjoon Kwon and Hyunseok Jeong. “Generation of hybrid entanglement between a single-photon polarization qubit and a coherent state”. In: *Physical Review A* 91.1 (Jan. 2015), p. 012340. ISSN: 1094-1622. DOI: 10.1103/physreva.91.012340.

[244] Michal Horodecki and Jonathan Oppenheim. "(Quantumness in the context of) resource theories". In: *International Journal of Modern Physics B* 27.01n03 (Nov. 2012), p. 1345019. ISSN: 1793-6578. DOI: 10.1142/s0217979213450197.

[245] Johan Aberg. *Quantifying Superposition*. 2006. DOI: 10.48550/ARXIV.QUANT-PH/0612146.

[246] Alexander Streltsov, Gerardo Adesso, and Martin B. Plenio. "Colloquium: Quantum coherence as a resource". In: *Reviews of Modern Physics* 89.4 (Oct. 2017), p. 041003. ISSN: 1539-0756. DOI: 10.1103/revmodphys.89.041003.

[247] Alexander Streltsov et al. "Maximal coherence and the resource theory of purity". In: *New Journal of Physics* 20.5 (May 2018), p. 053058. ISSN: 1367-2630. DOI: 10.1088/1367-2630/aac484.

[248] Ulysse Chabaud, Damian Markham, and Frédéric Grosshans. "Stellar Representation of Non-Gaussian Quantum States". In: *Physical Review Letters* 124.6 (Feb. 2020), p. 063605. ISSN: 1079-7114. DOI: 10.1103/physrevlett.124.063605.

[249] Heinz Bauer. "Minimalstellen von Funktionen und Extremalpunkte". In: *Archiv der Mathematik* 9.4 (Nov. 1958), pp. 389–393. ISSN: 1420-8938. DOI: 10.1007/bf01898615.

[250] Martin Kružík. "Bauer's maximum principle and hulls of sets". In: *Calculus of Variations and Partial Differential Equations* 11.3 (Nov. 2000), pp. 321–332. ISSN: 1432-0835. DOI: 10.1007/s005260000047.

[251] Pauli Virtanen et al. "SciPy 1.0: Fundamental Algorithms for Scientific Computing in Python". In: *Nature Methods* 17 (2020), pp. 261–272. DOI: 10.1038/s41592-019-0686-2.

[252] David J. Wales and Jonathan P. K. Doye. "Global Optimization by Basin-Hopping and the Lowest Energy Structures of Lennard-Jones Clusters Containing up to 110 Atoms". In: *The Journal of Physical Chemistry A* 101.28 (July 1997), pp. 5111–5116. ISSN: 1520-5215. DOI: 10.1021/jp970984n.

[253] T. P. Harty et al. "High-Fidelity Preparation, Gates, Memory, and Readout of a Trapped-Ion Quantum Bit". In: *Physical Review Letters* 113.22 (Nov. 2014), p. 220501. ISSN: 1079-7114. DOI: 10.1103/physrevlett.113.220501.

[254] R. Srinivas et al. "High-fidelity laser-free universal control of trapped ion qubits". In: *Nature* 597.7875 (Sept. 2021), pp. 209–213. ISSN: 1476-4687. DOI: 10.1038/s41586-021-03809-4.

[255] Martin Ringbauer et al. "A universal qudit quantum processor with trapped ions". In: *Nature Physics* 18.9 (July 2022), pp. 1053–1057. ISSN: 1745-2481. DOI: 10.1038/s41567-022-01658-0.

[256] Valentin Magro et al. “Deterministic freely propagating photonic qubits with negative Wigner functions”. In: *Nature Photonics* 17.8 (Apr. 2023), pp. 688–693. ISSN: 1749-4893. DOI: 10.1038/s41566-023-01196-y.

[257] C. Flühmann and J. P. Home. “Direct Characteristic-Function Tomography of Quantum States of the Trapped-Ion Motional Oscillator”. In: *Physical Review Letters* 125.4 (July 2020), p. 043602. ISSN: 1079-7114. DOI: 10.1103/physrevlett.125.043602.

[258] W. Wang et al. “Converting Quasiclassical States into Arbitrary Fock State Superpositions in a Superconducting Circuit”. In: *Physical Review Letters* 118.22 (June 2017), p. 223604. ISSN: 1079-7114. DOI: 10.1103/physrevlett.118.223604.

[259] Yiwen Chu et al. “Creation and control of multi-phonon Fock states in a bulk acoustic-wave resonator”. In: *Nature* 563.7733 (Nov. 2018), pp. 666–670. ISSN: 1476-4687. DOI: 10.1038/s41586-018-0717-7.

[260] J. Arnbak et al. “Compact, low-threshold squeezed light source”. In: *Optics Express* 27.26 (Dec. 2019), p. 37877. ISSN: 1094-4087. DOI: 10.1364/oe.27.037877.

[261] Luca Innocenti, Lukáš Lachman, and Radim Filip. “Coherence-Based Operational Nonclassicality Criteria”. In: *Physical Review Letters* 131.16 (Oct. 2023), p. 160201. ISSN: 1079-7114. DOI: 10.1103/physrevlett.131.160201.

[262] C. Flühmann et al. “Sequential Modular Position and Momentum Measurements of a Trapped Ion Mechanical Oscillator”. In: *Physical Review X* 8.2 (Apr. 2018), p. 021001. ISSN: 2160-3308. DOI: 10.1103/physrevx.8.021001.

[263] C. Flühmann et al. “Encoding a qubit in a trapped-ion mechanical oscillator”. In: *Nature* 566.7745 (Feb. 2019), pp. 513–517. ISSN: 1476-4687. DOI: 10.1038/s41586-019-0960-6.

[264] Brennan de Neeve et al. “Error correction of a logical grid state qubit by dissipative pumping”. In: *Nature Physics* 18.3 (Feb. 2022), pp. 296–300. ISSN: 1745-2481. DOI: 10.1038/s41567-021-01487-7.

[265] P. Campagne-Ibarcq et al. “Quantum error correction of a qubit encoded in grid states of an oscillator”. In: *Nature* 584.7821 (Aug. 2020), pp. 368–372. ISSN: 1476-4687. DOI: 10.1038/s41586-020-2603-3.

[266] Alec Eickbusch et al. “Fast universal control of an oscillator with weak dispersive coupling to a qubit”. In: *Nature Physics* 18.12 (Oct. 2022), pp. 1464–1469. ISSN: 1745-2481. DOI: 10.1038/s41567-022-01776-9.

[267] V. V. Sivak et al. “Real-time quantum error correction beyond break-even”. In: *Nature* 616.7955 (Mar. 2023), pp. 50–55. ISSN: 1476-4687. DOI: 10.1038/s41586-023-05782-6.

[268] Marina Kudra et al. “Robust Preparation of Wigner-Negative States with Optimized SNAP-Displacement Sequences”. In: *PRX Quantum* 3.3 (July 2022), p. 030301. ISSN: 2691-3399. DOI: 10.1103/prxquantum.3.030301.

[269] Shunya Konno et al. “Logical states for fault-tolerant quantum computation with propagating light”. In: *Science* 383.6680 (Jan. 2024), pp. 289–293. ISSN: 1095-9203. DOI: 10.1126/science.adk7560.

[270] Jacob Hastrup, Jonas Schou Neergaard-Nielsen, and Ulrik Lund Andersen. “Deterministic generation of a four-component optical cat state”. In: *Optics Letters* 45.3 (Jan. 2020), p. 640. ISSN: 1539-4794. DOI: 10.1364/ol.383194.

[271] Miller Eaton, Rajveer Nehra, and Olivier Pfister. “Non-Gaussian and Gottesman–Kitaev–Preskill state preparation by photon catalysis”. In: *New Journal of Physics* 21.11 (Nov. 2019), p. 113034. ISSN: 1367-2630. DOI: 10.1088/1367-2630/ab5330.

[272] H. M. Vasconcelos, L. Sanz, and S. Glancy. “All-optical generation of states for “Encoding a qubit in an oscillator””. In: *Optics Letters* 35.19 (Sept. 2010), p. 3261. ISSN: 1539-4794. DOI: 10.1364/ol.35.003261.

[273] M. W. Hamilton. “Phase shifts in multilayer dielectric beam splitters”. In: *American Journal of Physics* 68.2 (Feb. 2000), pp. 186–191. ISSN: 1943-2909. DOI: 10.1119/1.19393.

[274] Mohamed Amine Bouhlel et al. “A Python surrogate modeling framework with derivatives”. In: *Advances in Engineering Software* (2019), p. 102662. ISSN: 0965-9978. DOI: https://doi.org/10.1016/j.advengsoft.2019.03.005.

[275] P. Saves et al. “SMT 2.0: A Surrogate Modeling Toolbox with a focus on Hierarchical and Mixed Variables Gaussian Processes”. In: *Advances in Engineering Sofware* 188 (2024), p. 103571. DOI: https://doi.org/10.1016/j.advengsoft.2023.103571.